Energy and information in fluorescence with superconducting circuits

Nathanaël Pierre Cottet

THÈSE DE DOCTORAT

de l'Université de recherche Paris Sciences et Lettres
PSL Research University

École Normale Supérieure

Énergie et information dans la fluorescence de circuits
supraconducteurs

Ecole doctorale n°564

PHYSIQUE EN ÎLE DE FRANCE

Spécialité PHYSIQUE

COMPOSITION DU JURY :

M. PEKOLA Jukka
Aalto University, Rapporteur

M. POP Ioan
Karlsruhe Institute of Technology, Rapporteur

M. RAIMOND Jean-Michel
Sorbonne Université, Président du jury

Mme. DRÉAU Anaïs
Université de Montpellier, Membre du jury

M. WHITNEY Robert
Université Grenoble Alpes, Membre du jury

Soutenue par Nathanaël **COTTET**
le 20 Novembre 2018

Dirigée par **Benjamin HUARD**

To my teachers

ABSTRACT

This experimental thesis explores energetic and informational aspects of the fluorescence emitted by superconducting circuits. A quantum bit interacting with a resonant drive exchanges quanta of energy during absorption and emission cycles. Using low- noise amplification and linear detection of microwave light, we have developed a measurement setup to record the energy and complex amplitude of the fluorescence field and realized three experiments based on the record of fluorescence.

First, we have realized and demonstrated a transfer of energy between two resonant drives. Owing to the properties of stimulated emission, the direction and magnitude of energy transfer can be controlled by the phase of a quantum superposition of qubit states.

Second, we have used the information contained in fluorescence to implement a new readout scheme for superconducting circuits without the help of any ancillary quantum system. The circuit, directly coupled to the environment, encodes quantum information in a well-protected subspace and is read using the fluorescence of a strongly coupled transition.

Finally, we have explored the interplay between information and energy in the quantum regime by realizing an autonomous Maxwell's demon. The demon is a cavity measuring the system, a superconducting qubit. Work is extracted in the form of a stimulated photon emitted by the qubit and is directly measured using our fluorescence measurement setup. It is linked with the variations of the system's internal energy. Using independent measurements, the transfer of information from the system to the demon is quantified. In particular, we demonstrated the quantum signatures of the demon when the system is initialized in a quantum superposition.

RÉSUMÉ

Cette thèse expérimentale explore les aspects énergétiques et informationnels de la fluorescence émise par des circuits supraconducteurs. Un bit quantique échange des quanta d'énergie avec une onde résonante lors de cycles d'émission et d'absorption. Nous avons développé un système de mesure basé sur l'amplification bas bruit et la détection linéaire de la lumière micro-onde pour mesurer l'énergie et l'amplitude complexe du champ de fluorescence, et réalisé trois expériences basées sur la mesure de fluorescence.

Premièrement nous avons réalisé et démontré le transfert d'énergie entre deux impulsions lumineuses résonantes. Grâce aux propriétés de l'émission stimulée, la direction et l'amplitude du transfert d'énergie sont contrôlées par la phase d'une superposition d'états quantiques.

Deuxièmement, nous avons utilisé l'information contenue dans la fluorescence pour réaliser un nouveau type de lecture d'un circuit supraconducteur sans l'aide d'un système quantique auxiliaire. Le circuit, directement couplé à l'environnement, encode l'information quantique dans un sous-espace bien isolé et est lu grâce à la fluorescence d'une transition fortement couplée.

Enfin, nous avons exploré le lien entre information et énergie dans le régime quantique en réalisant un démon de Maxwell autonome. Le démon est une cavité mesurant le système, un qubit supraconducteur. Le travail est extrait sous la forme d'un photon stimulé émis par le qubit et est directement mesurée par notre système de mesure de fluorescence. Il est relié aux variations de l'énergie interne du qubit. Le transfert d'information du système vers le démon est quantifié par des mesures indépendantes. En particulier nous avons démontré la présence de signatures quantique du démon quand le système est initialisé dans une superposition d'états quantiques.

ACKNOWLEDGMENTS

En sortant de Licence il y a plus de six ans, je n'imaginais pas qu'un simple stage de fin d'année m'emporterait si loin dans une aventure tant humaine que scientifique, qui me mena, à la découverte des circuits supraconducteurs, de Paris à Lyon en passant par le Maryland. Durant ces trois années de thèse, j'ai eu le privilège d'interagir avec beaucoup de personnes, scientifiques ou non, sans qui ce travail n'aurait pas été le même, et auxquelles il n'est que justice de rendre hommage ici.

I would like to start by thanking the members of the thesis committee: my two "rapporteurs", Jukka Pekola and Ioan Pop, for their careful reading of my manuscript, their report, corrections and questions; the "président du jury", Jean-Michel Raimond, whose teaching of Quantum Physics 1.0.1 is in large part responsible for my interest in the strange world of quantum mechanics; Anaïs Dréau and Robert Whitney for shedding the light of their expertise in quantum optics and quantum thermodynamics on my work.

Un immense merci à Benjamin Huard pour ces années passées sous ton aile. Tu as été un soutien sans failles et constant, dans les meilleurs moments comme les mauvais, où j'ai su que je pouvais compter sur toi. Je suis fier d'avoir travaillé avec une personne qui a de telles qualités scientifiques et humaines. J'ai énormément appris à tes côtés, l'exigence scientifique, le fait de ne pas faire de concessions avec les résultats expérimentaux, la précision dans l'écriture des articles. Tu m'as donné le virus des discussions au tableau et des expériences qui puisent dans la théorie et tu prouves qu'il est possible d'associer un haut niveau scientifique avec une excellente ambiance de travail. Thank you Vladimir Manucharyan for agreeing so quickly to let me spend a year in your group. I really enjoyed working with you and learning about fluxonium circuits, highly inductive chains, and superconducting circuits in general. I particularly appreciated the opportunity to discuss various topics with you, as well as your enthusiasm for new ideas and experiments.

Je tiens à remercier tous les membres de l'équipe Qelec, maintenant Qcircuits, qui ont fait et font toujours de ce groupe un environnement de travail aussi chaleureux et motivant. Merci à François Mallet, qui m'a tant appris en ingénierie micro-ondes et à Zaki Leghtas pour m'avoir transmis le goût des chats et des processus non-linéaires, et pour la joie communicative avec laquelle tu fais de la physique. Merci à Sebastien Jezouin d'avoir partagé avec moi tes conseils et ta rigueur expérimentale, pour les innombrables discussions sur le démon de Maxwell ou la thermodynamique quantique, à Landry Bretheau et Philippe Campagne-Ibarcq qui m'ont mis le pied à l'étrier au début de mon stage de master quand je ne connaissais presque rien à l'expérience. Merci à Danijela Markovic pour ses explications sur le JPC et m'avoir fait découvrir la rakija, Quentin Ficheux avec qui j'ai partagé les joies de la rédaction de thèse et autant de discussions scientifiques que de bonnes rigolades, Théau Peronnin, toujours prêt à partager de nouvelles idées d'expériences et de projets, Raphaël Lescanne pour sa sérénité et son sens de l'aventure, Jeremy Stevens et Antoine Essig qui reprennnent le flambeau du groupe et avec qui il est super de travailler comme de boire des bières au Ninkasi. Merci aussi aux théoriciens avec lesquels j'ai collaboré au cours des différents projets et donc l'apport scientifique a été indéniable. Au sein de l'équipe Quantic, Pierre

CONTENTS

CONTENTS

INTRODUCTION

And the light shineth in the darkness; and the darkness comprehendeth it not.

Genesis

If the whole universe has no meaning, we should never have found out that it has no meaning: just as, if there were no light in the universe and therefore no creatures with eyes, we should never know it was dark. Dark would be without meaning.

C.S Lewis

Few physical entities have played as an important role as light in our discovery of the laws of Nature. In the history of science many examples show how the underlying regularity of particular phenomenons has been unravelled thanks to careful, repeated observations relying on the most developed sense of mankind: vision. The measurement of the light emitted by planets and stars, first with bare eyes, later on using lenses, telescopes and cameras, is the core of astronomy. It lead to the first planetary models, Galileo's observation of craters on the moon using a telescope, the confirmation of Einstein's general relativity and the discovery of the universe expansion by the red shift of far galaxies. The use of interferometers has led to the experimental refutation of the theory of ether by Michelson and Morley thus paving the way to Einstein's special relativity, and now to the recent discovery of gravitational waves, contractions of space-time propagating in the universe. The development of optical lenses have guided tremendous progress in the observation of small structures, with magnifying glasses showing the inner composition of minerals and microscopes shedding light on the constituents of passive and living forms. The measurement of light is not constrained in the visible range but in a whole spectrum from gamma rays emitted by stars to the microwave background, which is a remnant of the first light emitted in the universe 13.8 billion years ago.

All these examples - and the many more not mentioned here - rely on precise, though complex, types of light-matter interaction. In fact it is because light interacts with matter that is carries *information* about it. The fact that microscopic objects such as molecules or atoms interact with light have been acknowledge since the 19th century. These systems can absorb or emit *energy* in the form of photons, particles of light, whose energy is proportional to the light frequency. Because of these interactions the emitted *fluorescence* light is correlated to the system and hence carries a signature of its dynamics. When the energy levels are quantized the exchanges with light occur

at precisely defined frequencies. A quantum system initially at rest is excited into an unstable state by an incoming photon with the right energy. After a while it relaxes towards a lower-energy state by reemitting light in a *spontaneous emission* process. If a resonant photon arrives before the system has relaxed it can trigger *stimulated emission* by forcing the system back to a low-energy state [1]. By carefully changing the amount of light sent on the system it is possible to generate non-classical states of matter such as quantum superpositions. Light is thus a way to control and measure the energy states of quantum systems. Photons being quantum particles, light can itself be used as a carrier of quantum information, inside cavities [2] or while propagating between two nodes [3, 4] or even between the ground and a satellite [5].

This thesis is devoted to the experimental study of the energy and information contained in the fluorescence emitted by superconducting circuits. Artificial atoms based on superconducting circuits have proved their worth for studying the fundamentals of quantum mechanics [6–8] as well as processing quantum information [9]. With them, we investigated experimentally three different topics involving fluorescence. First, we present the experimental measurement of time-resolved spontaneous and stimulated emission using quantum-limited detectors microwave detectors and use this effect to perform and characterize a transfer of power controlled by the phase of a quantum superposition. Second, we use the information carried by fluorescence photons to read the state of a quantum bit without resorting to an ancillary system, in a process similar to atomic physics experiments. Third, we study of the role of energy and information in the interactions between a quantum system and its environment, a question at the center of the blooming field of quantum thermodynamics. We carried out a Maxwell's demon experiment in the quantum domain, where the demon is a quantum object acquiring information about the state of a quantum system and uses it autonomously to cyclically extract work from a heat bath in apparent violation of the second law of thermodynamics. This paradox is solved when considering the thermodynamical cost of information processing. Using fluorescence measurements we directly probe the work extracted by the demon, but also determine the transfers of energy and information between the system and demon exhibiting quantum signatures. The power transfer and Maxwell's demon experiments were realized at the École Normale Supérieure, France, and the fluorescence readout experiment was carried out at the Joint Quantum Institute, University of Maryland, USA.

1.1 ARTIFICIAL ATOMS: TRANSMON AND FLUXONIUM CIRCUITS

The experiments presented in this thesis are based on two distinct artificial atoms, a transmon circuit embedded in a microwave cavity and a fluxonium circuit in a microwave waveguide. This section gives a quick overview of the generalities of superconducting circuits and describes the characteristics and properties of each circuit.

1.1.1 *Building blocks of superconducting circuits*

When certain materials are cooled down below a critical temperature they acquire the property of conducting current without opposing any resistance. This effect, called superconductivity is a macroscopic manifestation of quantum mechanics. Due to interactions in the material, electrons form pairs, called Cooper pairs, which condensate
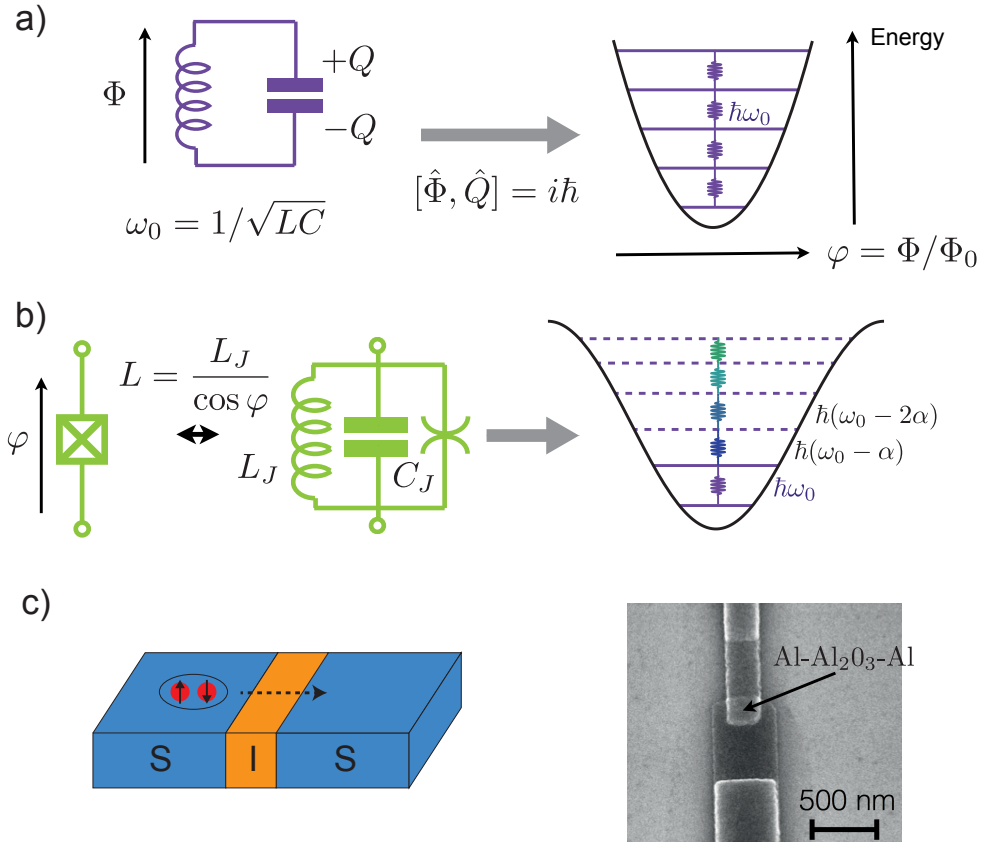
Figure 1.1: Building blocks of superconducting circuits. a) A linear oscillator described by the generalized flux and charge results after quantization into evenly spaced energy levels, represented in the magnetic potential energy (see text). The flux quantum is $\Phi_0 = h/2e$ with e the electron charge. b) Electrical symbol of a Josephson junction, a lossless non-linear element whose inductance depends on the flux. It can be decomposed as a capacitance C_J and a linear inductance L_J in parallel with a purely non-linear element represented by the spider symbol. After quantization non-evenly spaced energy levels are obtained so that it becomes possible to address two states specifically. c) Schematic representation and SEM image of a junction. Two superconductors (S) are separated by an insulating barrier (I) across which Cooper pairs can tunnel.

into the same quantum state. Thanks to the dramatic reduction of losses an LC circuit formed of superconducting capacitance and inductance is thus able to conserve excitations for a long time and is expected to behave quantum-mechanically. Such a quantum linear oscillator has evenly spaced energy levels (see Fig. 1.1a). If we drive it with light it will reach a classical state similar to light being trapped between two mirrors. To generate non-classical states it is necessary to add a non-linear element. The Josephson junction, made of two superconductors separated by a thin insulating barrier, is a non-linear lossless inductance [10]. A circuit containing one or several junctions thus acquires unevenly spaced energy levels (see Fig. 1.1b) and hence acts as an engineered atom [11]. By sending light at precise frequencies it becomes possible to address arbitrary transitions between energy levels and therefore prepare quantum states. Besides, the fabrication of Josephson non-linearities can be used to realize non-linear operations on light such as frequency conversion and parametric amplification [12].

In order to stay in the ground state of the superconductor it is necessary for the circuit energy level spacing hf (with h the Planck constant) to be smaller than the superconducting energy gap Δ. Aluminum junctions, where the insulator layer is made of aluminum oxide are the most commonly used because they combine a good versatility with well-controlled fabrication procedures. For bulk aluminum, $\Delta = h \times 82$ GHz [13]. Therefore the frequencies of superconducting circuits lie in the microwave range, typically between $1 - 20$ GHz. In order to avoid effects due to temperature it is necessary to reach the limit $\hbar\omega \gg k_B T$ with $\hbar = h/(2\pi)$ the reduced Planck constant, $\omega = 2\pi f$ the circuit angular frequency, k_B the Boltzmann constant and T the temperature. To fulfill this condition the circuits are cooled near 10 mK at the lower stage of a dilution refrigerator [14].

Electrical circuits are generally characterized by the current i flowing through a branch and the voltage v across them. Another possible representation uses the generalized flux and charge variables [11, 15]. By analogy with the magnetic flux threading a coil ran by a current and the electrical charge appearing on the plates of a capacitance under a voltage, the generalized flux and charge are defined by the time integrals

$$
\begin{aligned}
\Phi(t) &= \int_{-\infty}^{t} v(t') \mathrm{d}t' \\
Q(t) &= \int_{-\infty}^{t} i(t') \mathrm{d}t' \ .
\end{aligned}
\tag{1.1}
$$

For a branch, the flux and charge observe $\{\Phi, Q\} = \pm 1$. We can thus proceed to the canonical quantization by replacing Φ and Q by the operators $\hat{\Phi}$ and $\hat{Q}$ verifying $[\hat{\Phi}, \hat{Q}] = \pm i\hbar$ according to the sign of the Poisson bracket[1]. In the following we will omit the hats on quantum operators unless necessary to distinguish them from classical variables. In many cases it is convenient to use dimensionless variables. To do so we normalize the flux and charge operators by the flux quantum $\Phi_0 = h/2e$ and the charge unit carried by one Cooper pair $2e$ and obtain

$$
\begin{aligned}
\varphi &= 2\pi \frac{\Phi}{\Phi_0} \\
n &= \frac{Q}{2e} \ .
\end{aligned}
\tag{1.2}
$$

This defines the phase and reduced charge operators φ and n, giving respectively the superconducting phase difference across the branch and the number of Cooper pairs having crossed the branch.

The Hamiltonians of a capacitance, inductance and Josephson junction can easily be expressed by computing their internal energy and expressing it as a function of φ and n. For a capacitance C it reads

$$
\boxed{H_{\mathrm{C}} = 4E_C(n - n_g)^2, \quad E_C = \frac{e^2}{2C}} \ .
\tag{1.3}
$$

where n_g is a charge offset on the capacitor plate due to external electric fields. Note the factor 4 in front of the charging energy E_C due to the fact that charge is carried by Cooper pairs. For an inductance L the Hamiltonian is

$$
\boxed{H_{\mathrm{L}} = E_L \frac{\varphi^2}{2}, \quad E_L = \frac{(\Phi_0/2\pi)^2}{L}} \ .
\tag{1.4}
$$

---

[1] This change of sign depends on the inductive or capacitive nature of the branch. For a complete derivation see [11].

The junction's dynamics corresponds to a phase-dependent inductance $L(\varphi) = L_J/\cos(\varphi)$. Its Hamiltonian is thus

$$H_{\mathrm{JJ}} = -E_J \cos \varphi, \quad E_J = \frac{(\Phi_0/2\pi)^2}{L_J} \qquad (1.5)$$

with L_J the Josephson inductance of the junction related to the critical current I_c by

$$L_J = \frac{\Phi_0}{2\pi I_c} \ . \qquad (1.6)$$

The junction's inductance depends on its dimensions and tunnel barrier properties. The bigger the junction, the larger the critical current and the smaller L_J. Typically the junction's inductance is contained between $0.1 - 20$ nH. Due to its architecture the Josephson junction also possesses an intrinsic capacitance C_J.

   These blocks can be combined at will to design interesting Hamiltonians. In particular it is possible to design quantum systems for which the change of energy levels is associated to a change of the charge carriers number $\langle n \rangle$ in a capacitance plate.

1.1.2 *Transmon circuit*

The results presented in the first and third parts of this thesis are based on a 3D transmon circuit, a charge qubit adapted from the Cooper pair box [16, 17] and shown in Fig. 1.2. The transmon circuit is nowadays one of the very promising candidates for the realization of quantum machines able to manipulate quantum information with few errors [18, 19]. It consists of a single junction shunted by two large antennas realizing a capacitance C_a. Taking into account the junction's capacitance C_J, the total shunting capacitance is $C = C_a + C_J$. This design sets up two independent islands separated by the insulating barrier of the junction through which Cooper pairs can tunnel. The circuit eigenstates are defined by the precise values of $\langle n \rangle$ and a jump from one state $|j\rangle$ to $|j \pm 1\rangle$ is associated with a Cooper pair tunneling from one island to the other.

   Such a device is naturally sensitive to charge noise, variations of the offset charge due to unwanted external electric fields. It can be modeled by the charge offset n_g associated to a noisy gate voltage V_g (Fig 1.2a). The circuit Hamiltonian thus reads

$$H_{\mathrm{CBP}} = 4E_C(n - n_g)^2 - E_J \cos \varphi, \qquad (1.7)$$

known as the Cooper-pair box Hamiltonian, from the original charge qubit design where n_g was indeed an external parameter controlled by a voltage [20]. Here, we consider n_g to be a variable fluctuating around 0. A change of n_g modifies the Hamiltonian and thus its eigenenergies. For a quantum system this means that charge noise induces dephasing and therefore decoherence (see Sec. 2.1.2 for the precise effects of dephasing). To overcome this issue we design the circuit in the *transmon regime* so that $E_J > 50E_C$. In this limit the transition frequencies, whose energy dependence with n_g decays exponentially with E_C/E_J, are essentially independent on n_g and we can write

$$\boxed{H_{\mathrm{transmon}} = 4E_C n^2 - E_J \cos \varphi} \ . \qquad (1.8)$$

The operators n and φ are conjugate variables. By analogy with a particle in movement, we can represent the state of the circuit by a fictitious particle of position φ and momentum n moving in the potential energy $E_p(\varphi) = -E_J \cos \varphi$ which is 2π-periodic
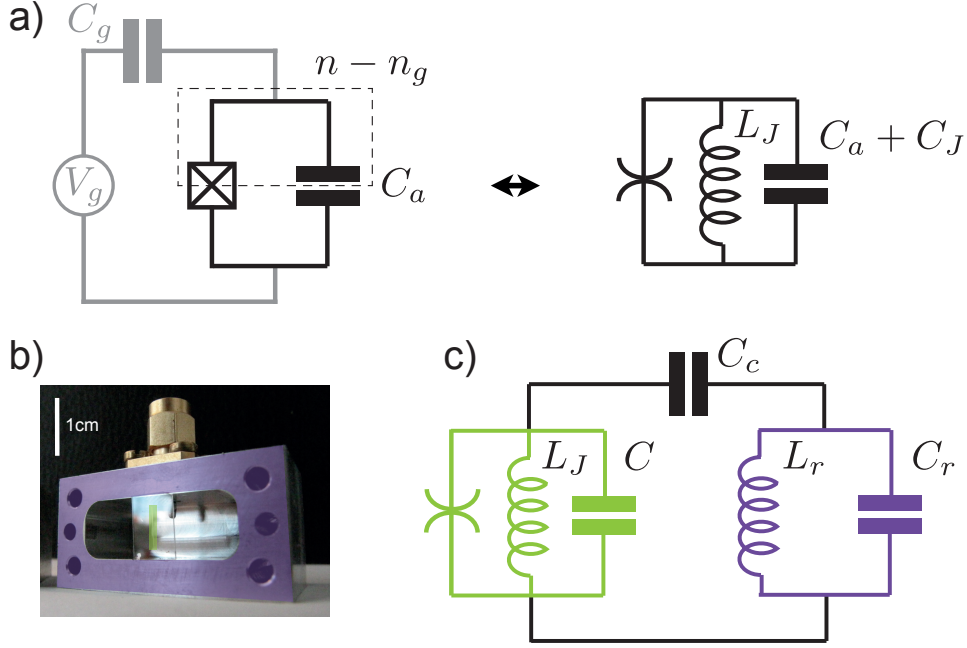
Figure 1.2: Transmon artificial atom. a) Electrical circuit of the transmon, equivalent to a non-linear oscillator. A noisy gate voltage V_g modifies the charge offset n_g on the island highlighted by the dotted rectangle with the result of producing dephasing. This issue is overcome when C_a is large enough ($E_J > 50E_C$). b) Picture of a transmon deposited on the central sapphire chip (green) embedded into an aluminum cavity (purple) and c) electrical circuit of a transmon (green) capacitively coupled to a linear resonator (purple).

and minimum in 0. Therefore φ is defined modulo 2π and its conjugate variable n takes integer values. When in an energy state below E_J, the particle is trapped and its position φ is delocalized in the well. By symmetry around 0 we thus have $\langle \varphi \rangle = 0$. The expansion of the cosine term near 0 at the second order gives the approximate expression

$$H_{\text{transmon}} \approx 4E_C n^2 + E_J \frac{\varphi^2}{2} - E_J \frac{\varphi^4}{24} \; . \tag{1.9}$$

The two first terms correspond to a linear oscillator with the angular frequency

$$\boxed{\omega_p = \frac{1}{\hbar} \sqrt{8 E_C E_J}} \; . \tag{1.10}$$

The diagonalization of the transmon Hamiltonian can be done exactly. It yields to energy levels $|j\rangle$ getting closer in energy as we go to higher levels. The transition frequency between two successive levels $|j\rangle$ and $|j+1\rangle$ is given by $E_{j+1} - E_j = \hbar\omega_p - jE_C$. By driving the circuit only at ω_p we thus only address the first two eigenstates that we can rewrite as the ground $|g\rangle$ and excited $|e\rangle$ states.

In our experiments the 3D transmon is embedded into a 3D cavity and is therefore capacitively coupled to an LC oscillator representing the first resonance mode of the cavity of angular frequency $\omega_r = \sqrt{1/L_r C_r}$ (see Fig. 1.2c). Physically, the coupling enables the cavity and transmon to exchange excitations. If we restrict ourselves to the first two states of the transmon the Hamiltonian describing the coupling is the Jaynes-Cummings Hamiltonian

$$H = \hbar\omega_p |e\rangle\langle e| + \hbar\omega_r a^\dagger a + \hbar g \left(a\sigma_+ + a^\dagger \sigma_- \right) \tag{1.11}$$

with a the annihilation operator of a photon in the resonator, g the coupling constant and $\sigma_- = |g\rangle\langle e|$ (respectively $\sigma_+ = |e\rangle\langle g|$) the lowering (raising) operator of the transmon. In the large detuning limit $\Delta = \omega_p - \omega_r \gg g$ the qubit and cavity cannot exchange excitations. Instead the quantum state of one shifts the resonance frequency of the other. It yields the *dispersive* Hamiltonian

$$\boxed{H = \hbar\omega_q |e\rangle\langle e| + \hbar\omega_c a^\dagger a - \hbar\chi a^\dagger a |e\rangle\langle e|} \ . \tag{1.12}$$

The energy levels have been slightly renormalized by the qubit-cavity coupling (Lamb shift) so we renamed ω_q the effective qubit angular frequency and ω_c the effective cavity angular frequency. For a transmon the exact computation of the dispersive shift has to take into account the higher excited levels whose interaction with the cavity is not negligible. It gives

$$\hbar\chi = 2E_C \frac{g^2}{\Delta^2} \ . \tag{1.13}$$

The dispersive coupling between the qubit and the cavity is used in the third part of the thesis to transfer information from the transmon to the cavity in a quantum thermodynamics experiment. The cavity is indeed commonly used as a measurement apparatus of the transmon energy states. This point, less central in this thesis, is discussed in Appendix B.

When the cavity is open on a transmission line with a decay rate κ the fluorescence light emitted by the transmon is strongly filtered by the cavity with the effect of reducing the rate at which photons are emitted by the circuit. This phenomenon known as the Purcell effect [21] is used to increase the lifetime of superconducting circuits [22]. The precise computation of the Purcell rate, the emission rate of fluorescence in the line, is challenging, as it involves the careful simulation of the electromagnetic coupling between the line and the circuit. However for transmons there is an approximate formula giving the order of magnitude of the Purcell effect that one can derive by coupling the cavity to a transmission line terminated by an impedance matched. It gives[2]

$$\Gamma_{\text{Purcell}} \approx \kappa \frac{g^2}{\Delta^2} \ . \tag{1.14}$$

In our experiments we largely enhance the cavity coupling to the line κ and reduce the detuning Δ as much as possible while staying in the dispersive regime in order to maximize the Purcell rate.

1.1.3 *Fluxonium circuit*

The fluxonium circuit has been introduced more recently [24, 25] as another way of getting rid of charge offsets to improve coherence by inductively shunting the junction by a large inductance L (Fig. 1.3). We use this circuit in the second part of this thesis to realize a qubit readout based on fluorescence. Our fluxonium is a 3D version where the junction is in addition shunted like a transmon by the capacitance C_a coming from two large antennas [26]. It can thus be referred to as an "inductively shunted transmon", where the junction is also capacitively shunted by the total capacitance $C = C_a + C_J$. The electrical circuit is represented in Fig. 1.3a). The loop formed by the junction

---

2 In all generality, when the Josephson junction is connected to an admittance $Y(\omega)$ we obtain [23] $\Gamma_{\text{Purcell}} = \frac{2\mathrm{Re}(Y(\omega_q))}{\mathrm{Im}(Y'(\omega_q))}$.

and the inductance enables to phase bias the junction by applying a magnetic flux
. An external magnetic flux thus generates the flux offset Φ_{ext}, giving the following
fluxonium Hamiltonian

$$H = 4E_C n^2 - E_J \cos\left(\varphi - \varphi_{\text{ext}}\right) + E_L \varphi^2 \tag{1.15}$$

where we defined $\varphi_{\text{ext}} = 2\pi\Phi_{\text{ext}}/\Phi_0$. The quantity Φ_{ext}/Φ_0 gives the number of flux
quanta threading the loop. Because the two sides of the junction are directly connected
through the inductance there is no offset charge $n_g = 0$. Moreover the potential energy
$E_{(\varphi)} = -E_J \cos\left(\varphi - \varphi_{\text{ext}}\right) + E_L \varphi^2$ is not 2π-periodic like the transmon. As a result φ
is defined on the whole real axis and n is not quantized. Physically it means that the
cloud of Cooper pairs is free to move continuously within the circuit hence inducing
continuous changes of the charge difference between the two sides of the junction. This
is in contrast with transmons, where the charge changes only by tunneling of integer
numbers of Cooper pairs through the tunnel barrier.
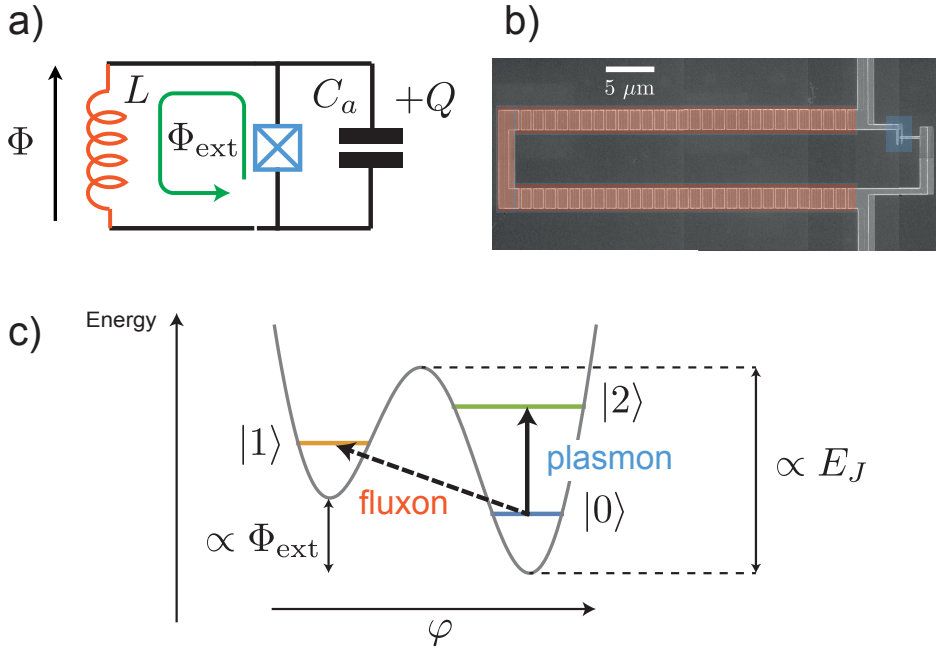
Figure 1.3: Fluxonium artificial atom. a) Electrical circuit of the fluxonium. The junction (blue)
is shunted by both a linear inductance L (red) and an additional capacitance coming
from the antennas. b) SEM image of the junction (blue) and superinductance made
of an array of large junctions (red, see text). c) Potential energy and first eigenstates
for $E_C = h \times 0.74$ GHz, $E_J = h \times 9.4$ GHz and $E_L = h \times 2.1$ GHz. Intra-well
transitions are due to plasmonic excitations similar to transmon exictations while
inter-well transitions are due to fluxons tunneling in/out of the loop. The energy
barrier separating two consecutive wells is set by E_J and the relative position of
the wells is controlled by the external flux Φ_{ext}.

If one tries to fabricate the linear inductance using the geometric inductance of a wire,
the length of wire required to obtain $E_J \gg E_L$ would result in the wire self-capacitance
largely overcoming the shunting capacitance, thus an effective charging energy E_C
orders of magnitude below E_J. This would result in large quantum fluctuations of n
and thus in the impossibility to build a qubit [24]. To avoid this issue we use the large
kinetic inductance of Josephson junctions by making a chain of large junctions to realize

a superinductance. The phase difference φ along the chain is uniformly distributed between the N junctions composing it. The phase difference between the two islands of junction composing the chain is thus φ/N. Assuming all the chain junctions have the same inductance L_J^c the total inductance of the chain L is obtained by summing over all the junction's inductances

$$L = \sum_{i=1}^{N} \frac{L_J^c}{\cos(\varphi/N)} \approx L_J^c \sum_{i=1}^{N} \left(1 + \frac{\varphi^2}{2N^2}\right) = NL_J^c + L_J^c \frac{\varphi^2}{2N} \tag{1.16}$$

where we have developed the cosine term for $\varphi/N \ll 1$. The chain's non-linearity thus scales as $1/N$ while its inductance scales as N. In practice we fabricate an array of large junctions so that $L_J^c \approx 0.1$ nH and N is between a few 100 to a few 10000. A picture of the chain is represented in Fig. 1.3b).

The fluxonium circuits exhibits two types of transitions represented in Fig. 1.3c). *Plasmon* transitions occur between two eigenstates localized in the same well. The mean position $\langle\varphi\rangle$ of the fictitious particle does not change so this transition is associated to a change of charge. These transitions are therefore equivalent to transmon transitions. The frequency of a plasmon transition between two consecutive states is hence approximatively given by the plasmon frequency $\sqrt{8E_J E_C}/\hbar$. Like in transmons, plasmon transitions are "strongly allowed" transitions because the wavefunctions of the eigenstates of the same well overlap strongly (a more precise treatment of this point is made in Sec. 4.1.3). On the other hand, inter-well transitions are in addition associated to a change of the position $\langle\varphi\rangle$ of the fictitious particle. It is associated to *fluxons* tunneling in or out of the superconducting loop. Because of the large energy barriers separating two wells, fluxon transitions are "strongly forbidden transitions" (see Sec. 4.1.3).

The fluxonium circuit is particularly suited to the realization of a qubit readout by fluorescence because we can use a plasmon transition to readout the state of a logical qubit encoded into a fluxon transition, expected to have a longer lifetime. We embedded the fluxonium in a 3D waveguide so that we can send and collect microwave light to and from it. It is important to stress that unlike many other fluxonium designs [27–29] there is no resonator coupled to the circuit. In this matter, our circuit here is really the equivalent of a single atom trapped by lasers in free space.

1.2 FLUORESCENCE MEASUREMENT IN MICROWAVES

The central point of this thesis is the measurement of the fluorescence emitted by a superconducting circuit when it interacts with one or several near-resonant drives. The evolution of a driven atom and its emission of light has been long known and well studied experimentally in the optical domain by the atomic physics community [1, 30]. The fluorescence of superconducting circuits was first measured thanks to low-noise signal amplification [31–33] and has been used in recent experiments to unravel quantum trajectories of a qubit [34, 35], study the role of post-selection [36] or perform autonomous feedback [35]. In this thesis we re-express the theoretical predictions made about fluorescence in the input-output formalism which is more adapted to the manipulation of microwave light [34, 37, 38]. In particular we recover the expression of spontaneous and stimulated emission and perform a time-resolved measurement of fluorescence, where we monitor directly the exchanges of electromagnetic field amplitude

and energy between the atom and the drive (Chap. 2). We use this effect to design a quantum machine where a superposed qubit controls the direction of energy transfers (Chap. 3).

1.2.1 *Fluorescence field and photons*

Detectors in the microwave range are particularly suited to the measurement of the complex field amplitude, because the time oscillations of the electromagnetic field are slow enough for the detectors to resolve them. On the contrary the direct measurement of microwave photons is challenging due to their much smaller energy than optical photons. Instead, we reconstruct the mean number of photons in the fluorescence field from the outcomes of heterodyne detection, which is the acquisition of the two field quadratures. This technique allows us to measure simultaneously both the field complex amplitude and the number of photons.

Let us consider the basic, though central in this work, example of a qubit coupled to a transmission line a. The incoming wave is represented by the annihilation operator a_{in} of a photon propagating *towards* the qubit. Similarly the outgoing wave is represented by the operator a_{out}. These operators have the dimension or $\sqrt{\text{Hz}}$ because the fields considered are propagating. Under the action of the drive the qubit undergoes Rabi oscillations and in doing so exchanges energy with its environment. The input-output relation [11, 37] allows to express the outgoing wave in terms of the incoming one and of the operators of the qubit. Considering that the qubit oscillates in the (x, z) plane of the Bloch sphere, the fluorescence field amplitude $\langle a_{\text{out}} \rangle$ and photon rate $\langle a_{\text{out}}^\dagger a_{\text{out}} \rangle$ are given by

$$
\begin{aligned}
\langle a_{\text{out}} \rangle &= \alpha_{\text{in}} - \sqrt{\Gamma_a} \langle \sigma_- \rangle \\
\langle a_{\text{out}}^\dagger a_{\text{out}} \rangle &= \alpha_{\text{in}}^2 + \Gamma_a \frac{1 + \langle \sigma_z \rangle}{2} - \frac{\Omega}{2} \langle \sigma_x \rangle
\end{aligned}
\tag{1.17}
$$

with $\alpha_{\text{in}} = \langle a_{\text{in}} \rangle$ the complex amplitude of the incoming drive, assumed to be a real positive number, Γ_a the decay rate of the qubit into the line a, $\sigma_- = (\sigma_x - i\sigma_y)/2$, $\sigma_{x,y,z}$ the Pauli matrices of the qubit along x, y and z, and $\Omega = \sqrt{\Gamma_a} \alpha_{\text{in}}$ the Rabi frequency induced by the drive in a. The fluorescence field complex amplitude is the sum of the incoming drive amplitude α_{in} (which is reflected) and of the amplitude of the field emitted by the qubit, which is proportional to the annihilation operator σ_-. The input-ouput relation for the field thus gives us the *scattering* relation of the qubit. The photon rate is composed of the reflected incoming photon rate α_{in}^2 with two additional terms due to the qubit. The first one is equal to the probability to find the qubit in the excited state times its decay rate. It originates from the *spontaneous emission* of the qubit. The second one is proportional to the drive amplitude α_{in} since it scales as the Rabi frequency Ω. Suppose that the drive α_{in} realizes a π-pulse on the qubit between the excited $|e\rangle$ and ground $|g\rangle$ states. Then the integral of this term over time is $-\int_{|e\rangle}^{|g\rangle} \Omega \langle \sigma_x \rangle \mathrm{d}t/2 = 1$, meaning that the qubit emitted one quantum of energy exactly. It corresponds to the photon emitted by *stimulated emission*.

It is possible to distinguish experimentally between spontaneous and stimulated emission by adding a second transmission line b and measuring fluorescence in transmission, where light is sent through b and collected in a, or in reflection, where light is both sent and collected in a, as represented in Fig. 1.4a). Indeed if $\alpha_{\text{in}} = 0$ then the
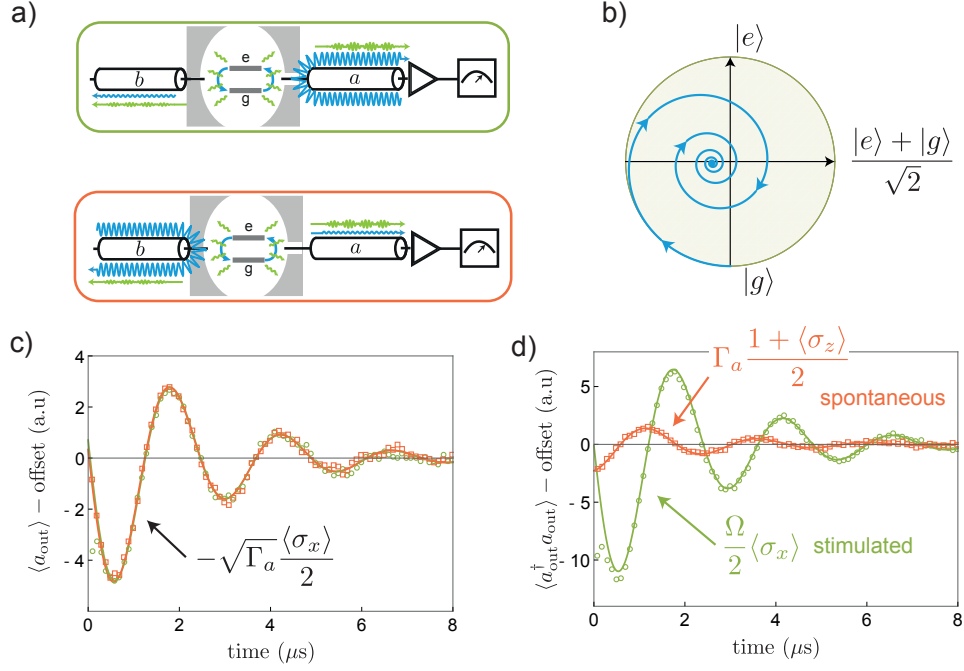
Figure 1.4: Time-resolved fluorescence of a superconducting qubit undergoing Rabi oscillations. a) When driven in reflection (green box) or in transmission (red box), a qubit undergoes Rabi oscillations b) represented in the (x, z) plane of the Bloch sphere. c) The oscillatory parts of the field complex amplitude $\langle a_{\text{out}} \rangle$ measured as a function of time in transmission (red squares) and in reflection (green circles) are the same and given by $-\sqrt{\Gamma_a}\langle \sigma_x \rangle/2$. The theory is represented by the plain line (bottom). d) Measured photon rate $\langle a_{\text{out}}^\dagger a_{\text{out}} \rangle$ for the same experiment. The two time evolutions are in phase quadrature. The transmitted photon rate is given by the spontaneous emission term $\Gamma_a(1 + \langle \sigma_z \rangle)/2$. In the limit $\Omega \gg \Gamma_a$ the reflected photons are mostly due to stimulated emission and evolve as $\Omega\langle \sigma_x \rangle/2$ (plain lines). Here $\Omega = 2\pi \times 0.41$ MHz and $\Gamma_a = 2\pi \times 0.072$ MHz.

only non-zero term is spontaneous emission. On the other hand if we set $\Omega \gg \Gamma_a$ the reflected photon rate contains mostly stimulated emission. We directly measured the time-resolved evolution of the fluorescence signal emitted by a qubit driven either in transmission or in reflection and undergoing Rabi oscillations. Note that the qubit is here embedded in a far detuned cavity which can be left out of the study. The results of the measurement, where α_{in} and $|\alpha_{\text{in}}|^2$ have been subtracted if needed in order to keep only the oscillatory parts of fluorescence, are represented in Fig. 1.4. Owing to the qubit's inner dynamics, the fluorescence signal oscillates in time. The field amplitude oscillates with the same amplitude and phase whether the qubit is driven in transmission or in reflection (Fig. 1.4c). However there is a clear difference between the time evolutions of the reflected and transmitted number of photons (Fig. 1.4d). According to the expression of the photon rate by the input-output relation, they oscillate in phase quadrature with different amplitudes, the transmitted photons containing spontaneous emission only while the reflected ones being mostly made of stimulated emission. It is important to stress that due to our procedure used for the reconstruction of the photon number presented in Sec. 2.4, the data showed in Fig. 1.4 are reconstructed from the *same* measurement records, where the only change is the way the measurement records are averaged. The fact that a simple post-processing allows us to reconstruct either an

identical behavior (for the complex amplitude) or two totally different evolutions (for the photon number) of fluorescence in transmission and in reflection is remarkable.

1.2.2 *Power transfer controlled by a quantum superposition*

The name "stimulated emission" used to designate the term $\Omega\langle\sigma_x\rangle/2$ in the output photon rate Eq. (1.17) does not really cover its whole effects. Indeed, this term also represents the coherent *absorption* of energy from the drive when the qubit is oscillating towards a higher-energy state. Since its amplitude is proportional to the Rabi drive amplitude $\Omega = \sqrt{\Gamma_a}\alpha_{\mathrm{in}}$ its phase might change with the phase of the drive. In general when using a single drive, this phase choice is hidden behind the fact that the qubit oscillates in the Bloch sphere around a direction set by the drive. In other words, the drive sets the phase of the quantum superpositions explored by the qubit during Rabi oscillations. If we add a second drive the phase difference between the incoming drive operator $\langle a_{\mathrm{in}}\rangle$ and the qubit operator $\langle \sigma_-\rangle$ becomes of first importance and can be detected when measuring the photon rate.
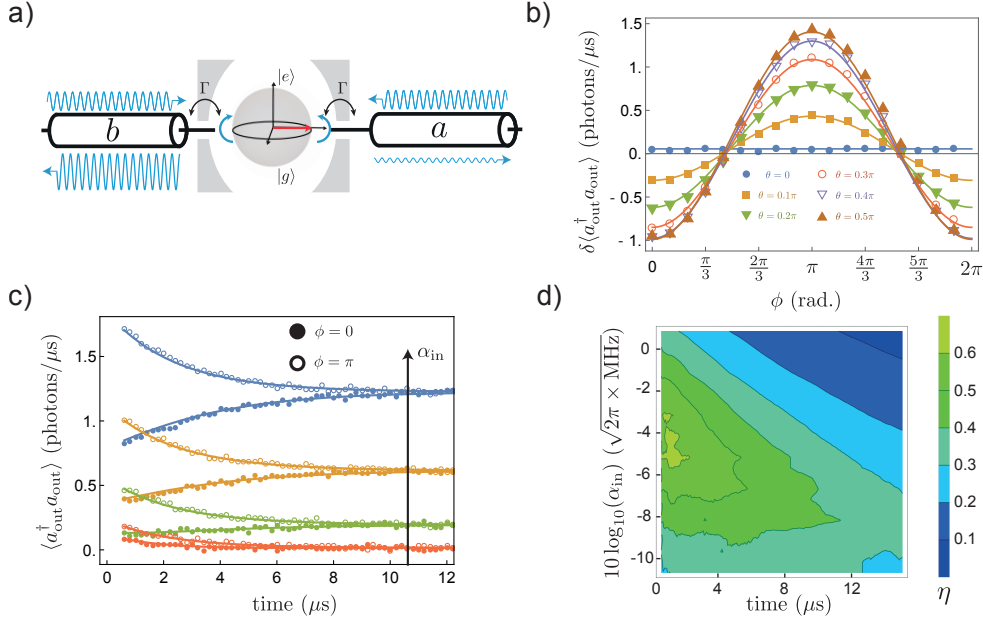
Figure 1.5: Transfer of power controlled by the phase of a superposition of states. a) Two drives in lines a and b in opposition of phase and with similar amplitudes are sent on resonance on the superposed qubit symmetrically coupled to the lines. The qubit absorbs energy from one and reemits it in the second with a sign determined by the phase of its quantum superposition. b) Measured evolution of the photon rate amplitude in a with the phase of the superposition (points). It exhibits a cosine behavior well reproduced by the theory (plain lines). c) Temporal measurement of the photon rate in a when the qubit is initially in $|e\rangle + e^{i\phi}|g\rangle$ with $\phi = 0$ (filled circles) and $\phi = \pi$ (empty circles) for different values of α_{in}. It follows the theoretical evolution predicted by Eq. (1.19). From the time evolution we extract the d) transfer efficiency (see text), reaching a maximum of 63%.

Based on this affirmation we conceived an experiment where the exchanges of energy between two drives are mediated by a qubit. Consider a qubit symmetrically coupled to two lines a and b with $\Gamma_a = \Gamma_b = \Gamma$. Two drives at qubit frequency of similar amplitude and in opposition of phase $\beta_{\mathrm{in}} = \langle b_{\mathrm{in}}\rangle = -\alpha_{\mathrm{in}}$ are simultaneously sent on the qubit

initialized in a superposed state $\sin(\frac{\theta}{2})|e\rangle + e^{i\phi}\cos(\frac{\theta}{2})|g\rangle$, as represented in Fig. 1.5a). The two drives interfer destructively at the level of the qubit whose only evolution is due to decoherence. Writing T_1 and T_2 the respective lifetime and coherence time of the qubit yields

$$
\begin{cases}
\langle\sigma_z\rangle(t) & = (1 - \cos(\theta))e^{-t/T_1} - 1 \\
\langle\sigma_x\rangle(t) & = \cos(\phi)\sin(\theta)e^{-t/T_2}
\end{cases}. \tag{1.18}
$$

From Eq. (1.17), the photon rates in a and b read

$$
\begin{cases}
\langle a_{\text{out}}^\dagger a_{\text{out}}\rangle(t) = \alpha_{\text{in}}^2 + \dfrac{\Gamma}{2}(1 - \cos(\theta))e^{-t/T_1} \\
\qquad\qquad\qquad - \cos(\phi)\sin(\theta)\sqrt{\Gamma}\alpha_{\text{in}}e^{-t/T_2} \\
\langle b_{\text{out}}^\dagger b_{\text{out}}\rangle(t) = \alpha_{\text{in}}^2 + \dfrac{\Gamma}{2}(1 - \cos(\theta))e^{-t/T_1} \\
\qquad\qquad\qquad + \cos(\phi)\sin(\theta)\sqrt{\Gamma}\alpha_{\text{in}}e^{-t/T_2}
\end{cases}. \tag{1.19}
$$

The stimulated emission term thus induces a net transfer of power from a to b whose direction is controlled by the parameter $\cos\phi$ coming from the phase of the quantum superposition. Physically, the two drives fight each other, one losing energy in trying to excite the qubit while the other one gains energy in trying to deexcite it. In Fig. 1.5b) we measure the amplitude of the photon rate decay $\delta\langle a_{\text{out}}^\dagger a_{\text{out}}\rangle = \langle a_{\text{out}}^\dagger a_{\text{out}}\rangle(t=0) - \alpha_{\text{in}}^2$ as a function of ϕ. We indeed find a cosine evolution from a situation where energy goes from a to b (maximized when $\phi = 0$) to energy going from b to a (maximized when $\phi = \pi$). The curves are not centered around zero because spontaneous emission is not directional. Its amount is increased when θ goes from 0 to $\pi/2$.

The total energy transfer needs to take into account the amount of reflected drive α_{in}^2. Depending on θ there exists an optimal drive amplitude maximizing the power transfer. Indeed if α_{in} is too large the directionality induced by the qubit becomes negligible in front of the reflected drive. On the other hand if α_{in} is too small, the qubit emission is dominated by spontaneous emission which is emitted symmetrically in both lines. Figure 1.5c) shows the experimental time evolution of $\langle a_{\text{out}}^\dagger a_{\text{out}}\rangle$ when the qubit is initialized with $\theta = \pi/2$, hence in $(|e\rangle + e^{i\phi}|g\rangle)/\sqrt{2}$, with $\phi = 0$ and $\phi = \pi$ for various values of α_{in}. At high amplitude (blue) stimulated emission is large but not enough to counter the reflected field, while a low amplitude (red) spontaneous emission dominates. At intermediate amplitudes (orange, green) directionality is enhanced. Obviously, because of qubit's decoherence, power transfer is reduced at long times and is maximal at $t = 0$. The transfer efficiency is defined as the difference between the photon rate emitted for $\phi = 0$ and $\phi = \pi$ normalized by the total photon rate

$$
\eta = \left| \frac{\int_0^{t_p} \langle a_{\text{out}}^\dagger a_{\text{out}}\rangle_{\phi=0}(t)\mathrm{d}t - \int_0^{t_p} \langle a_{\text{out}}^\dagger a_{\text{out}}\rangle_{\phi=\pi}(t)\mathrm{d}t}{\int_0^{t_p} \langle a_{\text{out}}^\dagger a_{\text{out}}\rangle_{\phi=0}(t)\mathrm{d}t + \int_0^{t_p} \langle a_{\text{out}}^\dagger a_{\text{out}}\rangle_{\phi=\pi}(t)\mathrm{d}t} \right|. \tag{1.20}
$$

Its experimental evolution for the qubit initially in $(|e\rangle \pm |g\rangle)/\sqrt{2}$ is represented in Fig. 1.5d) as a function of time and drive amplitude. We measure a maximal transfer efficiency of $\eta = 63\%$. Over time the efficiency decreases but stays over 50% for about 4 μs. This experiment demonstrates that quantum superpositions can be used as a control for power routing.

1.3   ARTIFICIAL ATOM DIRECTLY COUPLED TO THE ENVIRONMENT

Besides energy, fluorescence carries information about the system it has interacted with. This information propagating in the environment can be collected and used to measure the state of a quantum system. In general the interaction between a superconducting qubit and the environment is mediated by a far-detuned resonator dispersively coupled to the qubit. This architecture is inspired by cavity quantum electrodynamics (CQED) where an atom interacts with the photons of a cavity field [30, 39]. Similarly, circuit quantum electrodynamics (cQED) uses the interaction at the single photon level between a circuit and a cavity [40, 41]. For superconducting circuits the use of the cavity has many advantages. In the dispersive regime it filters the electromagnetic noise at qubit frequency (Purcell effect) with the result of increasing the coherence. On the other hand it is a good measurement apparatus and allows to perform fast, quantum non-demolition measurements[3]. In the second part of this thesis we study the feasibility of another option inspired from atomic physics systems such as cold atoms, trapped ions or colored centers in diamonds. In these systems, an atom is directly coupled to its environment and readout is made by collecting the light fluoresced by a short-lifetime transition [42]. The implementation of such a readout scheme in superconducting circuits might open possibilities for the future realization of quantum networks [43, 44]. We present the realization of the fluorescence readout of a fluxonium circuit in a cavity-free architecture, adapted to the specificities of microwave detectors. Owing to the orders of magnitude difference between different fluxonium transitions we maintain a good qubit coherence for a circuit directly coupled to its environment (Chap. 4). We characterize the readout by measuring the branching ratio of the readout transition and study the possibility of initializing the qubit by optical pumping (Chap. 5).

1.3.1   *Fluorescence readout*

The principle of our experimental realization of the fluorescence scheme is represented in Fig. 1.6a). The logical qubit is a long-lifetime transition $|0\rangle \leftrightarrow |1\rangle$ of the fluxonium, while a short-lifetime transition to a higher readout state $|R\rangle$ is used for readout. The circuit is embedded in a 3D waveguide acting as a low-pass filter to protect the qubit transition, whose frequency is below the cutoff, from spontaneous emission and is measured in reflection. To readout the state of the qubit, we measure the reflection coefficient $r = \frac{\langle a_{\text{out}} \rangle}{\langle a_{\text{in}} \rangle}$ near the transition frequency between $|0\rangle$ and $|R\rangle$, called the readout frequency ω_r. In contrast to the previous time-resolved measurements, the readout transition under the drive quickly reaches the steady-state of Rabi oscillations at Ω. The reflection coefficient r deduced from the input-output relation Eq. (1.17) is

$$ r = 1 - 2p_0 \frac{1 + 2i\frac{\delta}{\Gamma}}{1 + 4\left(\frac{\delta}{\Gamma}\right)^2 + 2\left(\frac{\Omega}{\Gamma}\right)^2} \tag{1.21} $$

with p_0 the population in $|0\rangle$, δ the drive-transition detuning and Γ the coupling rate of the readout transition to the line. Therefore measuring the reflection coefficient allows to retrieve the state of the qubit.

The dependence of the reflection coefficient for $p_0 \approx 1$ on detuning at various readout drive amplitudes Ω is represented in phase space in Fig. 1.6b). When δ is varied from

---

3 A quantum non-demolition measurement (QND) is such that two successive measurements will produce the same answers.
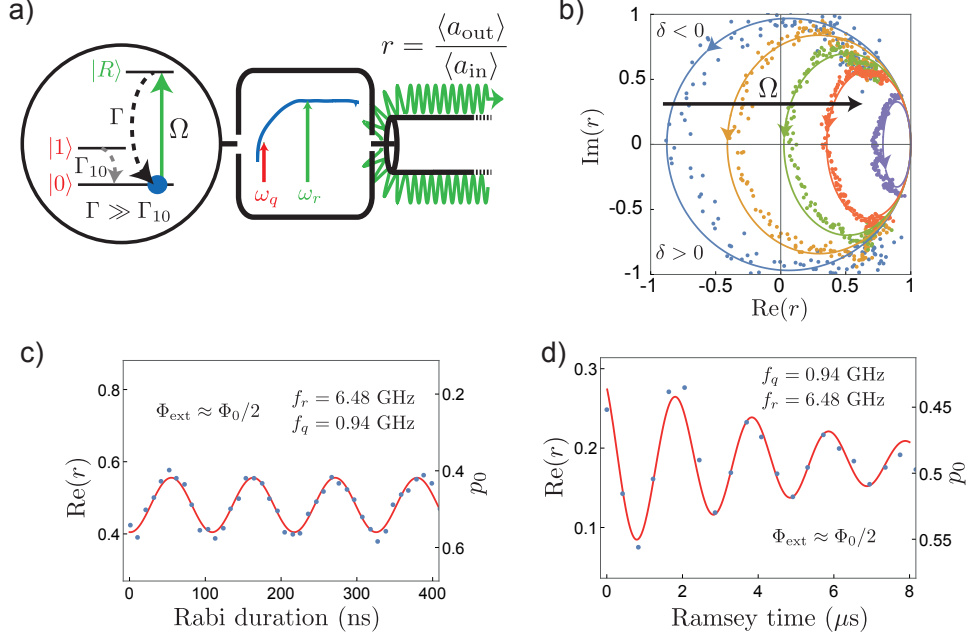
Figure 1.6: Fluorescence readout of a fluxonium circuit. a) The fluxonium, embedded in a 3D waveguide, is driven in reflection near readout transition $|0\rangle \leftrightarrow |R\rangle$ at frequency ω_r inducing the Rabi frequency Ω on the readout transition. The waveguide suppresses spontaneous emission of the logical qubit $\{|0\rangle, |1\rangle\}$. b) Reflection coefficient represented in phase space when the detuning δ is varied from negative values to positive values at various Ω. It describes ovals in phase space. At $\delta = 0$, the readout coefficient is on the real axis. c) Rabi oscillations of the qubit transition at half flux quantum measured by fluorescence. We perform a π-pulse in about 50 ns. The amplitude of the oscillations is lowered by thermal occupation of $|1\rangle$ at equilibrium. d) Ramsey oscillations at the same flux bias, giving $T_2 \approx 5\ \mu s$. Note that the readout power has been changed between figures c) and d), therefore the reflection coefficient changed as well (left axes). The reconstruction of the ground state population (right axes) takes it into account.

$-\infty$ to $+\infty$ the reflection coefficient describes an oval. At resonance $\delta = 0$ we have $r \in \mathbb{R}$. At low power $\Omega \ll \Gamma$, the reflection coefficient describes a circle between -1 and $+1$ in phase space, similarly to what we would obtain for a linear resonator. At higher amplitude the field saturates the readout transition with the result or distorting the circle into a smaller oval.

We now fix the readout frequency at $\delta = 0$ and its amplitude. The reflection coefficient is real and is equal to $1 - 2p_0 \times C$ where C is a constant determined by the drive amplitude. Therefore there is a simple scaling factor between the population and the measured reflection coefficient. In particular $r = 1$ corresponds to $p_0 = 0$. The interpretation is that physically when the logical qubit is in $|1\rangle$ the situation for the readout drive at ω_r is similar to an open termination in the transmission line. Figures 1.6c) and d) represent respectively Rabi and Ramsey oscillations of the qubit transition when the fluxonium is flux biased at half flux quantum $\Phi_{ext} = \Phi_0/2$. At this point the two central wells of the fluxonium potential energy are degenerate and the qubit frequency is independent on flux noise (at first order). We are able to apply a π-pulse on the qubit in about 50 ns and the measured coherence time is around $T_2 = 5\ \mu s$.

1.3.2 *Incoherent processes*

While real atoms are naturally well isolated from their environment, superconducting circuits, made of many atoms built on a substrate, are subjected to various loss channels. For instance losses can happen at the interface between the circuit and the substrate, where the electric field is constrained [45, 46]. Moreover, excitations of the superconductor called quasiparticles can dissipate the energy stored in the circuit by tunneling through the Josephson junctions composing the circuit [26, 27, 47]. Dissipation in the environment can be an inconvenient, as it degrades the quantum information stored in a quantum system, but can also be used when the system-environment interaction is well engineered [48–51]. A good example is optical pumping, where the joint action of a coherent drive and dissipation leads to the preparation of an atom in a target state with a good fidelity. We study several aspects induced by dissipation in the fluxonium circuit opened to the transmission line, in particular the branching ratio of the readout transition (see Fig. 1.7a), which induces a limitation of the quantum non-demolition property of the readout, and qubit initialization by optical pumping.

When the system is initially in the readout state $|R\rangle$, it might relax towards two "branches": either to $|0\rangle$ and in that case the readout transition stays bright, or to an ensemble of other states and in that case the readout transition becomes dark. This process is represented in Fig. 1.7a) and is characterized by the branching ratio, which is the ratio of the decay rates towards the two branches. It can be modeled by a fictitious unique state $|E\rangle$ (pictured by the dashed level line) to which the readout state decays with a rate Γ_{out} before eventually rejoining the ground state $|0\rangle$ with a rate Γ_{in}. The branching ratio is thus

$$\frac{\Gamma_r}{\Gamma_{\mathrm{out}}} \ . \tag{1.22}$$

The branching ratio gives the approximate number of photons radiated by the transition when it is driven, thus being in a "bright state", before decaying outside of the readout transition towards a "dark state". We develop a technique to measure the branching ratio from the transient evolution of the ground state population p_0 under a pump at the readout frequency ω_r. In the limit of a good readout $\Gamma_r \gg \Gamma_{\mathrm{out}}, \Gamma_{\mathrm{in}}$, the ground state is pumped out with a rate

$$\Gamma_{\mathrm{pump}} = \Gamma_{\mathrm{in}} + \frac{\Omega^2 \Gamma_{\mathrm{out}}}{\Gamma_r^2 + 2\Omega^2} \ . \tag{1.23}$$

The time evolution of p_0 when the fluxonium is driven at readout frequency ω_r is represented in Fig. 1.7b) for various values of Ω. It exhibits an exponential decrease of the population with time as the readout drive pumps population towards other states. Each experimental line is fitted with an exponential decay (lines) to extract the pumping time. Its evolution with Ω is represented in Fig. 1.7c). The error bars come from lifetime fluctuations over the course of the experiment that we interpret as being due to quasiparticles. The data (points) are fitted by the theoretical expression (red line) and give the experimental branching ratio

$$\frac{\Gamma_r}{\Gamma_{\mathrm{out}}} = 128 \pm 10 \ . \tag{1.24}$$

The error rate induced by the finite branching ratio is thus below 1%. The experimental branching ratio is well reproduced by simulations based on dielectric loss only with a quality factor $Q_{\mathrm{diel}} = 4.2 \times 10^5$.
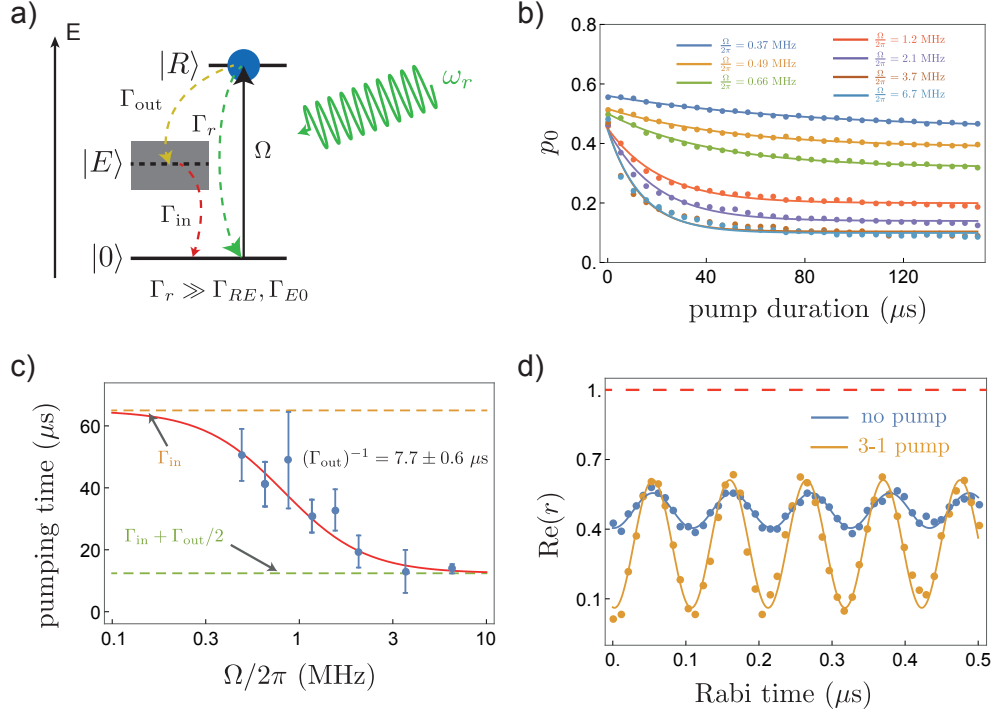
Figure 1.7: Pumping effects in superconducting circuits. a) Definition of the branching ratio $\Gamma_r/\Gamma_{\text{out}}$. Once in the readout state $|R\rangle$ the system can relax towards dark states (gray square, represented by the single state $|E\rangle$) with an effective rate Γ_{out}. b) Transient evolution of the ground state population under the readout drive. It decays exponentially due to the finite branching ratio, resulting in optical pumping of higher excited states. c) Evolution of the pumping time extracted from the transients with the Rabi amplitude Ω induced by the readout drive. Probably due to quasiparticles the lifetimes fluctuate in time, resulting in relatively large error bars. The theory (red line) gives the branching ratio $\Gamma_r/\Gamma_{\text{out}} = 128 \pm 10$. d) Example of qubit initialization by optical pumping. Time Rabi oscillations of the qubit are measured with the qubit initially either at thermal equilibrium (blue) or prepared by a pump applied between the qubit's excited state $|1\rangle$ and the readout state, in the experiment state $|3\rangle$ (orange).

Optical pumping is based on the same principle as pictured in Fig. 1.7a), population transits through a higher excited state thanks to a drive before decreasing towards the target state. We study three different schemes for optical pumping and their influence on decoherence. An example of qubit initialization is represented in Fig. 1.7d), where we measure time Rabi oscillations with or without qubit initialization by optical pumping of the transition between the qubit excited state $|1\rangle$ and the readout state, with the result of preparing the qubit in the ground state. The amplitude of Rabi oscillations is indeed greatly enhanced by the pump. These optical pumping schemes are promising but have to be enhanced to equal the state-of-the-art of qubit reset in superconducting circuits. A special circuit design optimizing this point could lead to an improvement of the pumping time and efficiency.

1.4 QUANTUM THERMODYNAMICS WITH SUPERCONDUCTING CIRCUITS

Finally, we use the fluorescence to carry out a quantum thermodynamics experiment. The tremendous improvements on the level of control and design of quantum systems since the second half of the 20th century have raised new fundamental questions. Among them, quantum thermodynamics investigates the flows of energy, in the form of heat and work, and entropy, carrying information, within quantum systems and between quantum systems and their environment. We implement and characterize an autonomous quantum Maxwell's demon (Chap. 6), where the demon is a quantum object acquiring information about a quantum system in order to extract work. Thanks to fluorescence measurement we directly measure the work extracted by the demon and link it to the independently determined internal energy variations of the system. Moreover we characterize the information acquired by the demon and show that it exhibits quantum signatures (Chap. 7).

1.4.1 *Heat and work in fluorescence*

The fluorescence photons emitted by a quantum system contain both work, a coherent source of energy, and heat, a stochastic form of energy. For fluorescence, work and heat are related respectively to the coherent I_{coh} and incoherent I_{incoh} emissions studied by Cohen-Tannoudji and coworkers in Ref. [1]. Thanks to our detection scheme we measure their time evolution and separate the two contributions of coherent and incoherent emission, or work and heat, to the photon rate.

In the photon rate $\langle a_{\mathrm{out}}^{\dagger} a_{\mathrm{out}} \rangle$ the coherent emission is the term corresponding to the square of the mean field amplitude $I_{\mathrm{coh}} = |\langle a_{\mathrm{out}} \rangle|^2$, the remaining part being due to incoherent emission. With Eq. (1.17) we have

$$
\begin{aligned}
I_{\mathrm{coh}} &= \alpha_{\mathrm{in}}^2 - \sqrt{\Gamma_a}\,\alpha_{\mathrm{in}}\langle\sigma_x\rangle + \frac{\Gamma_a}{4}\langle\sigma_x\rangle^2 \\
I_{\mathrm{incoh}} &= \frac{\Gamma_a}{2}\left(1 + \langle\sigma_z\rangle - \frac{\langle\sigma_x\rangle^2}{2}\right)
\end{aligned}
\tag{1.25}
$$

where we have kept the explicit dependence $\sqrt{\Gamma_a}\,\alpha_{\mathrm{in}}$ in front of $\langle\sigma_x\rangle$. The two first terms of coherent emission correspond to the reflected drive and stimulated emission, thus demonstrating that stimulated emission is a fully coherent process. The last term is the coherent part of spontaneous emission, proving that even though spontaneous emission is a stochastic process it contains a coherent part due to the fact that its emission is proportional to the population in the qubit's excited state. Work and heat are simply expressed by

$$
\begin{aligned}
\dot{W} &= \hbar\omega_q I_{\mathrm{coh}} \\
\dot{Q} &= \hbar\omega_q I_{\mathrm{incoh}}
\end{aligned}
\tag{1.26}
$$

where ω_q is the qubit angular frequency.

We measure the time evolutions of work and heat contained in the fluorescence photons emitted by an atom by acquiring simultaneously the field complex amplitude and the photon rate when the qubit is driven by two resonant drives, one in reflection and the other in transmission. In doing so the qubit always undergoes Rabi oscillations and the amount of stimulated emission (hence of coherent emission) is varied at will by changing the amplitude of the drive in reflection α_{in}. The total photon rate is
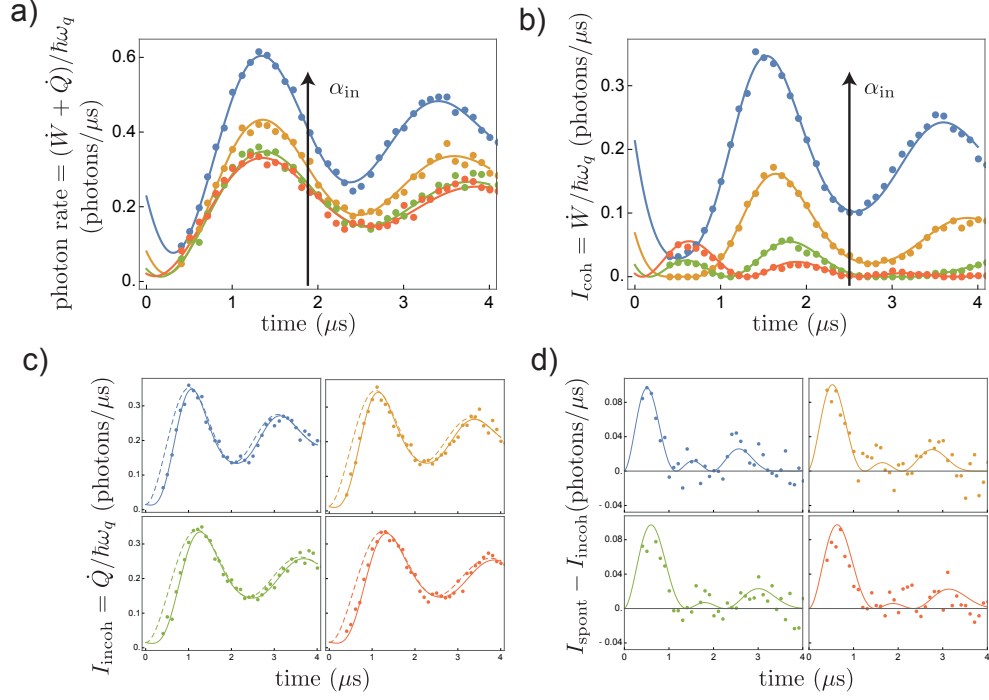
Figure 1.8: Dynamics of work and heat in fluorescence. a) Time-evolution of the total photon rate emitted by the qubit driven both in reflection and transmission for various reflection drive amplitudes. Raising α_{in} increases the amount of stimulated emission contained in the line. b) Coherent emission by the qubit. c) Incoherent emission by the qubit. This term is only due to spontaneous emission, but is clearly distinct from it (dashed line). Indeed, d) there is a non-zero contribution of spontaneous emission to stimulated emission (points, data and line, theory). Plots with the same colors correspond to the same drive amplitude α_{in}.

represented in Fig. 1.8a). It contains both coherent and incoherent emission. The coherent and incoherent parts are represented in Fig. 1.8b) and c), respectively. The data (points) are very well reproduced by the theoretical expressions (plain lines). In particular, the incoherent part clearly deviates from the total expression of spontaneous emission (dashed line on c). By subtracting the measured incoherent emission I_{incoh} from the theoretical spontaneous emission term I_{stim} we extract the coherent part of spontaneous emission. Importantly in the limit of large amplitude $\sqrt{\Gamma_a}\alpha_{\text{in}} \gg \Gamma_a$, spontaneous emission becomes negligible, thus incoherent emission, or heat, as well.

1.4.2 *Work extraction and information transfer in a quantum Maxwell's demon*

In 1867 Maxwell proposed an apparent paradox in the form of a thought experiment where a "demon" extracts work cyclically from a system coupled to a single heat bath in apparent violation of the second law of thermodynamics by acquiring information about the system and acting upon this information [52, 53]. This paradox stressed the profound link between information and thermodynamics. Versions of the Maxwell's demon in the quantum domain have been proposed and studied theoretically for the past thirty years [54–58]. We studied experimentally a quantum demon where the system is a transmon superconducting qubit dispersively coupled a cavity playing the demon.
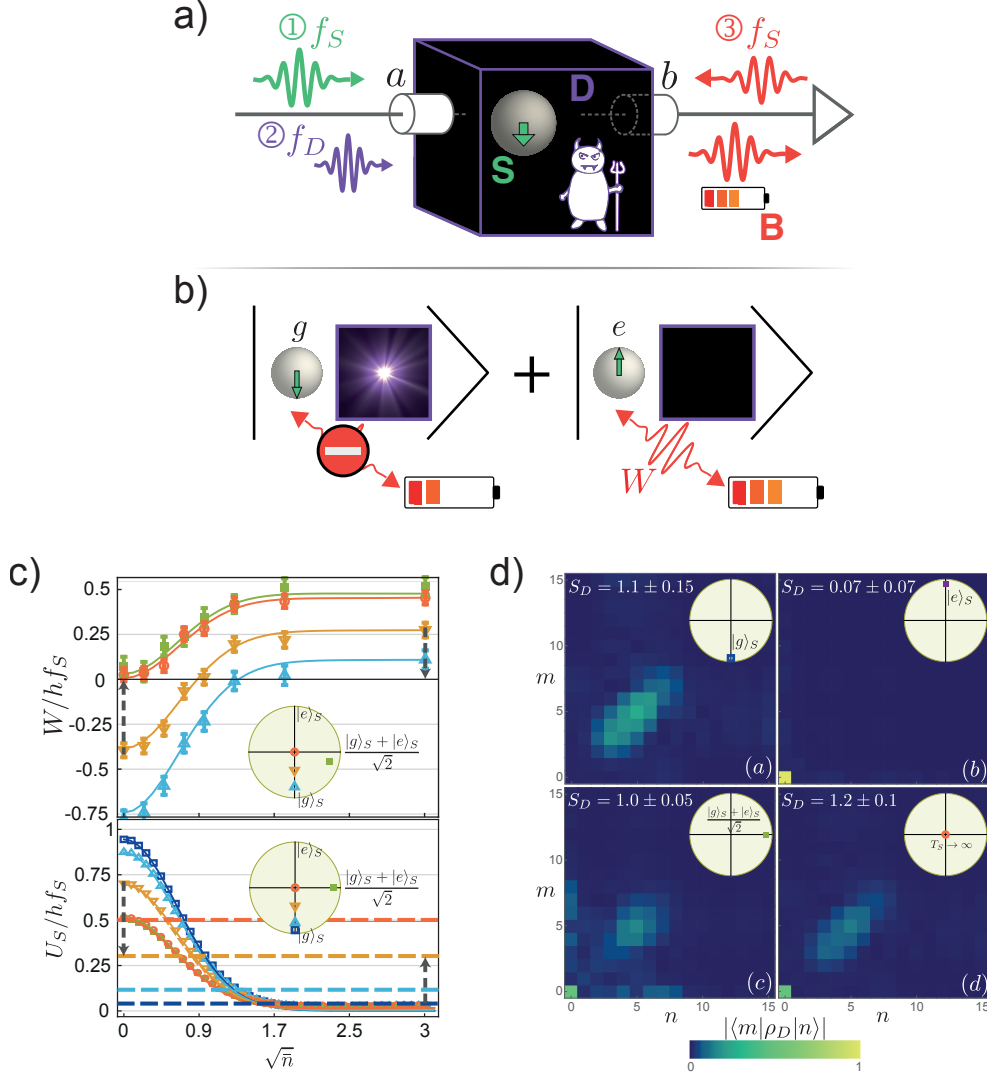
Figure 1.9: Autonomous quantum Maxwell's demon. a) After preparation by a pulse at f_S the system (transmon qubit) is measured by the demon (cavity) with a pulse at f_D populating the cavity conditionally on the qubit being in the ground state $|g\rangle$. This displacement prevents the qubit to interact with the battery, a π-pulse at f_S, when it is in $|g\rangle$, so that work is extracted when the qubit is excited. b) After the demon's measurement the cavity and qubit are entanglement if the latter was initialized in a superposed state. c) Extracted work W and qubit final internal energy U_S as a function of $\sqrt{\bar{n}}$. Work extraction is maximized at large values of $\bar{n}$, where the qubit ends up in the ground state. The equivalence between the extracted work and the qubit internal energy is represented by the dashed arrows. d) Cavity final internal state ρ_D represented in the Fock state basis. When the qubit is initialized in a superposed state the cavity exhibits coherences and is less entropic than the one corresponding to the qubit initialized in the maximally entropic state.

The principle of the experiment is shown in Fig. 1.9a). The system is first initialized in a thermal or superposed state by a pulse at its frequency f_S. Information about the state of the system in encoded into the demon's states by a pulse at demon frequency f_D. Because of the dispersive coupling this pulse is off resonant if the qubit is in the excited state $|e\rangle$ and populates the cavity with photons only if the qubit is in $|g\rangle$. Work is extracted by a π-pulse applied at f_S acting as a battery, which is resonant with the qubit when the cavity is in vacuum and off resonant otherwise. Depending on

the drive amplitude the populated cavity state overlaps with vacuum by an amount exponentially decreasing with $\bar{n}$ where $\bar{n}$ is the mean number of photons of the state. Because of this overlap the demon sometimes lets the qubit absorb a quantum of energy from the battery, resulting in a smaller (or even negative) extracted work W, with a lesser chance of making errors when $\bar{n} \gg 1$. When the qubit is initialized in a superposed state, the cavity and qubit are entangled after the pulse at f_D realizing the transfer of information, as represented in Fig. 1.9b).

Figure 1.9c) (top) shows the extracted work W determined by fluorescence measurement as a function of $\sqrt{\bar{n}}$. When $\bar{n}$ is small the demon does not distinguish properly between $|g\rangle$ and $|e\rangle$ and the qubit absorbs energy from the battery instead of providing it. At higher values of $\bar{n}$ work starts to be extracted, with a maximal amount of half a quantum of energy obtained for a qubit initialized in the maximally entropic state (red empty circles) or in the superposition $(|e\rangle + |g\rangle)\sqrt{2}$ (green squares, see inset). The extracted work compares very well to the variations of the qubit final internal energy U_S (Figure 1.9c) bottom) measured independently. The experimental results agree fully with the theoretical predictions (plain lines). Using the qubit as a measurement apparatus we realize a spectroscopy of the demon's state when it hosts $\bar{n} \approx 5$. We represent its state by the magnitude of the density matrix elements in the Fock states basis $|\langle m|\rho_D|n\rangle|$ in Fig. 1.9d) when the qubit was initialized near $|g\rangle$, $|e\rangle$, $(|e\rangle + |g\rangle)\sqrt{2}$ and the maximally entropic state. As expected the cavity hosts photons when the qubit is in $|g\rangle$ and does not when the qubit is in $|e\rangle$. When the qubit is initially in a superposed state the cavity exhibits the quantum signature of coherences of the density matrix $\langle 0|\rho_D|n\rangle \neq 0$, $n \geq 1$. Due to technical constraints the cavity state is entropic even when the qubit starts in $|g\rangle$. Nevertheless the cavity von Neuman entropy S_D is smaller for a superposed qubit than a thermal one. The results of this experiment demonstrate the use of superconducting circuits for studying thermodynamics in the quantum domain.

This thesis is divided in three parts. The first one is devoted to the theoretical and experimental study of fluorescence in the microwave domain. In Chap. 2 we recall the dynamics of an open qubit under a drive, explain how to reconstruct the number of fluorescence photons from the measurement outcomes of linear detectors, and present and implement a way to determine precisely the Purcell rate of a qubit to a line using fluorescence. Chapter 3 studies in details the experiment of power transfer between two drives. The second part investigates the fluorescence readout scheme to measure a fluxonium circuit. Chapter 4 explains the circuit design, optimal readout power and qubit measurement. Chap. 5 explores several aspects of decoherence in fluxoniums, notably the branching ratio of the readout transition and optical pumping. Finally, the third part is centered around quantum thermodynamics. Maxwell's demons in the quantum domain are studied theoretically in Chap. 6 and the different experimental platforms for realizing quantum demons are presented. Finally, Chap. 7 gives a comprehensive study of our experiment of a quantum mechanical Maxwell's demon.

Part I

QUBIT FLUORESCENCE

MEASURING THE FLUORESCENCE OF A QUBIT IN THE MICROWAVE DOMAIN

Over the past ten years fluorescence of superconducting atoms has been investigated using low-noise amplification, linear detection and power measurement. The fluorescence field and spontaneous emission of a qubit during its decay as a function of the initial state [31], its steady state response over a drive exhibiting the Mollow triplet [32] and coherent and incoherent emission [33] have been probed. The influence of post-selection on the qubit dynamics has been demonstrated using fluorescence measurement [36]. Owing to quantum-limited amplification, the information contained in the fluorescence field triggered experiments on the reconstruction of quantum trajectories [59, 60], and has been used to perform feedback [35].

This chapter recalls results on the interaction between a qubit and an environment modeled by a transmission line in the input-output formalism particularly suited to microwave light, and discusses the role of quantum-limited amplifiers and quantum detectors based on superconducting circuits. We derive the time-resolved expressions of the fluorescence complex amplitude and photon number and identify stimulated and spontaneous emission. Later we show how power measurement can be achieved using linear detectors and present a consistent way of determining the Purcell rate, the spontaneous emission rate of a qubit towards a transmission line, using time-resolved photon-number measurement.

2.1 DYNAMICS OF AN OPEN QUANTUM BIT

We recall in this section some important results on the dynamics of the simplest example of an open quantum system coupled: a two-level system coupled to the environment. We present how to compute its evolution when one discards the information lost in the environment using the Lindblad master equation, and describe in details the dynamics of an open qubit submitted to a drive, in particular the steady-state reached by the qubit under the conjugate actions of the drive and thermal bath. These results will be of first importance when we will use the fluorescence of a qubit transition to read the state of a fluxonium circuit in Chap. 4.

2.1.1 *Density matrix formalism*

When a quantum system interacts with uncontrolled degrees of freedom its state cannot be represented by a ket $|\psi\rangle$. Instead of a vector of the Hilbert space $\mathcal{H}$, we have to represent its state by a matrix ρ. The density matrix represents the knowledge that an observer has about a quantum system, and thus can differ from one observer to the other. In other words, the density matrix is the *best* guess an observer can make about the state of a quantum system *given the information* it has about the system, to successfully predict the outcome of an experiment. A density matrix is

- hermitian: $\rho^\dagger = \rho$

- positive semi-definite: $\forall X \in \mathcal{H}$, $X^T \rho X \geq 0$

- of unit trace: $\mathrm{Tr}(\rho) = 1$.

The two first properties ensure that ρ has real positive eigenvalues p_λ associated to the eigenstates $|X_\lambda\rangle$. With the unit trace of ρ they are interpreted as the classical probabilities to find the system in $|X_\lambda\rangle$. With $\rho = \sum_\lambda p_\lambda |X_\lambda\rangle\langle X_\lambda|$, the mean value of an operator $\hat{O}$ is then given by

$$\langle \hat{O} \rangle = \mathrm{Tr}(\rho \hat{O}) \ . \tag{2.1}$$

In the limit case of $p_\lambda = 1$, $p_{\lambda' \neq \lambda} = 0$, the system is in a pure state and can be represented by the ket $|X_\lambda\rangle$. Since its state is perfectly known it has a zero entropy. In general, one has to sum over all the possible states and by analogy with the classical Shannon entropy we get

$$S(\rho) = -\sum_\lambda p_\lambda \log p_\lambda = -\mathrm{Tr}(\rho \log \rho) \tag{2.2}$$

this is the Von Neumann entropy of a quantum system. For a two-level system the density matrix is a 2×2 matrix. In the $\{|e\rangle, |g\rangle\}$ basis it reads

$$\rho = \begin{pmatrix} \rho_{ee} & \rho_{eg} \\ \rho_{ge} & \rho_{gg} \end{pmatrix} \tag{2.3}$$

with $\rho_{gg} + \rho_{ee} = 1$ and $\rho_{ge} = \rho_{eg}^*$. It is equivalent to a spin $\frac{1}{2}$ ensemble possibly not entirely polarized. Any two-level system operator can be expressed in terms of the identity matrix and the Pauli matrices along the x, y and z-axes

$$\sigma_x = \begin{pmatrix} 0 & 1 \\ 1 & 0 \end{pmatrix}, \quad \sigma_y = \begin{pmatrix} 0 & -i \\ i & 0 \end{pmatrix}, \quad \sigma_z = \begin{pmatrix} 1 & 0 \\ 0 & -1 \end{pmatrix} \ . \tag{2.4}$$

For a qubit in ρ their mean values are

$$\begin{aligned}
x &= \langle \sigma_x \rangle = \rho_{eg} + \rho_{ge} = 2\mathrm{Re}(\rho_{eg}) \\
y &= \langle \sigma_y \rangle = i(\rho_{eg} - \rho_{ge}) = -2\mathrm{Im}(\rho_{eg}) \\
z &= \langle \sigma_z \rangle = \rho_{ee} - \rho_{gg}
\end{aligned} \tag{2.5}$$

By analogy with spins ensemble, we can represent the qubit state by a 3D vector, the Bloch vector, with coordinates (x, y, z). When the qubit is in a pure state, the vector norm is 1 and it is hence localized on a sphere of radius 1 called the Bloch sphere. When the qubit is in a mixed state the Bloch vector is inside the sphere (see Fig. 2.1a) and b)). An important particular case for this thesis is a qubit at thermal equlibrium with one or several heat bath. In equilibrium, $\rho_{eg}^{\mathrm{equ}} = \rho_{ge}^{\mathrm{equ}} = 0$ and the qubit has a certain probability to be in the excited state, given by the Maxwell-Boltzmann distribution

$$\rho_{ee}^{\mathrm{equ}} = \frac{1}{1 + e^{\hbar\omega_q/k_B T_{\mathrm{eff}}}} \tag{2.6}$$

where k_B is the Boltzmann constant, ω_q the qubit angular frequency and T_{eff} the effective qubit temperature. Note that since $\rho_{ee} + \rho_{gg} = 1$, it is always possible to define an effective temperature for the qubit. When $\rho_{ee} > \rho_{gg}$ this temperature becomes negative. In the case $k_B T_{\mathrm{eff}} \gg \hbar\omega_q$ the Bloch vector is in the center of the Bloch sphere and $\rho_{ee}^{\mathrm{equ}} = \rho_{gg}^{\mathrm{equ}} = \frac{1}{2}$ (Fig. 2.1c)).
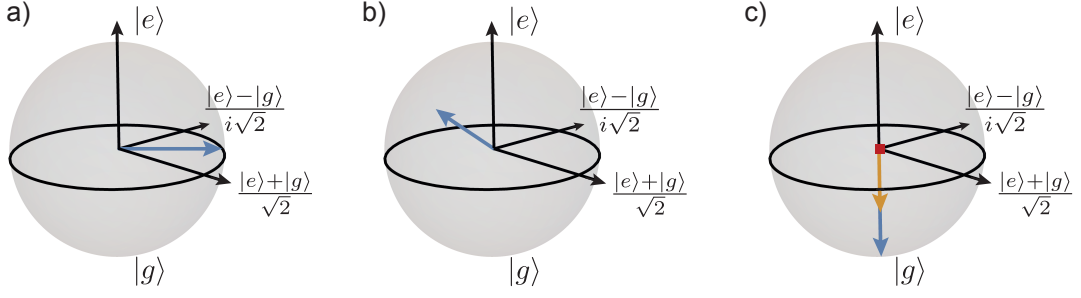
Figure 2.1: Bloch sphere representation: the qubit state can be represented as a 3-D vector that a) points towards the surface of the sphere when the qubit is in a pure state $|\psi\rangle$ or b) is inside the sphere when the qubit is in a mixed state. c) Qubit state at thermal equilibrium for $k_B T_{\text{eff}} \ll \hbar\omega_q$ (blue), $k_B T_{\text{eff}} \sim \hbar\omega_q$ (orange), and $k_B T_{\text{eff}} \gg \hbar\omega_q$ (red).

2.1.2 Decoherence and temperature: the Lindblad master equation

In general a quantum system is not fully isolated from the environment: it interacts in an uncontrolled manner with external degrees of freedom and eventually reaches an equilibrium, a process known as *decoherence*. From an information point a view, decoherence occurs because the observer cannot track the whole evolution of the ensemble formed of the system and environment, causing a loss of information. It is possible to recover a (sometimes large) part of this information by measuring how the state of the environment has been affected by the system of interest. In this case the trajectory followed by the quantum system strongly depends on the measurement outcomes [59]. We will focus here on the situation where the observer discards the information lost in the environment. The unconditional evolution of the density matrix can be put in the form of the Lindblad master equation [30]

$$\dot\rho = -\frac{i}{\hbar}[H,\rho] + \sum_i \gamma_i \mathcal{D}[O_i](\rho) \tag{2.7}$$

where H is the system Hamiltonian and $\mathcal{D}$ the Lindblad superoperator (also called Lindbladian). Given a jump operator O it reads

$$\mathcal{D}[O](\rho) = O\rho O^\dagger - \frac{1}{2}(\rho O^\dagger O + O^\dagger O\rho) . \tag{2.8}$$

The first term of the Lindblad master equation describes the deterministic evolution of the system with the Hamiltonian. The second term describes uncontrolled quantum jumps happening at a rate γ_i and dictated by the jump operators O_i. They directly come from the system-environment interaction.

For a two-level system the effect of the environment can be modeled using three jump operators only. A qubit initially in the excited state $|e\rangle$ eventually releases a quantum of energy and jumps down to $|g\rangle$ with a rate $\Gamma_\downarrow$. The jump operator associated to this process is naturally $|g\rangle\langle e| = \sigma_-$. Likewise the qubit can absorb a thermal photon from a heat bath and jump from the ground to the excited state. This happens with a rate $\Gamma_\uparrow$ and with a jump operator $|e\rangle\langle g| = \sigma_+$. When considering only one bath at temperature T, the up and down rates are related by the detailed balance

$$\frac{\Gamma_\uparrow}{\Gamma_\downarrow} = e^{-\hbar\omega_q/k_B T} . \tag{2.9}$$

Without any Hamiltonian evolution, $H = 0$, the up and down jumps cause an exponential relaxation of the qubit towards the thermal equilibrium described in Eq. (2.6)

$$\rho(t) = \begin{pmatrix} \rho_{ee}^{\text{equ}} + \left(\rho_{ee}(0) - \rho_{ee}^{\text{equ}}\right)e^{-\Gamma_1 t} & \rho_{eg}(0)e^{-\Gamma_1 t/2} \\ \rho_{ge}(0)e^{-\Gamma_1 t/2} & \rho_{gg}^{\text{equ}} + \left(\rho_{gg}(0) - \rho_{gg}^{\text{equ}}\right)e^{-\Gamma_1 t} \end{pmatrix} \tag{2.10}$$

with $\Gamma_1 = \Gamma_\downarrow + \Gamma_\uparrow$. When the qubit is coupled to several baths, one only need to sum all the rates and the relaxation stays exponential. This remarkable property does not necessarily hold true anymore for multi-level systems, where multi-exponential decays and non-thermal equilibrium steady-states are possible. It will be of first importance when we will study fluxonium circuits, where one cannot neglect higher excited states in the study (see Chap. 4). Apart from energy relaxation the environment can affect the phase of a qubit superposition. Experimentally, several effects are susceptible of operating such a pure dephasing. For instance a qubit is dispersively coupled to a cavity would suffer from cavity photon shot noise, inducing fluctuations of the qubit frequency. Flux-sensitive circuits, such as fluxonium, are naturally sensitive to magnetic flux noise. Pure dephasing is modeled by the brutal change of phase of a quantum superposition (phase flip). It is associated to the jump operator $\Gamma_\varphi \sigma_z/2$ since $\sigma_z(|e\rangle + |g\rangle) = |e\rangle - |g\rangle$.

2.1.3 *Bloch equations: steady-state and dynamical solutions*

The state of a qubit can be controlled by sending light on or near resonance with its transition frequency. When doing so, the qubit coherently exchanges energy with the drive and as a result undergoes rotations in the Bloch sphere. Let us consider a drive at frequency $\omega_d = \omega_q - \delta$. In the frame rotating at ω_d and with a judicious choice of the qubit eigenstates (or, equivalently, a choice of the drive phase), the effect of the drive detuned by δ is represented by the Hamiltonian

$$H_R = \hbar\frac{\delta}{2}\sigma_z - \hbar\frac{\Omega}{2}\sigma_y \ , \tag{2.11}$$

where Ω represents the strength of the drive. To write the equation of evolution of the qubit density matrix one has to take into account all the qubit decay channels as described previously in 2.1.2. At zero temperature it leads to the following master equation

$$\dot{\rho} = -\frac{i}{\hbar}[H_R, \rho] + \Gamma_1 \mathcal{D}[\sigma_-](\rho) + \frac{\Gamma_\varphi}{2}\mathcal{D}[\sigma_z](\rho) \ . \tag{2.12}$$

This equation can be expressed in terms of the expectation values $\langle\sigma_{x,y,z}\rangle$

$$\begin{cases} \langle\dot{\sigma_x}\rangle &= -\Omega\langle\sigma_z\rangle - \delta\langle\sigma_y\rangle - \Gamma_2\langle\sigma_x\rangle \\ \langle\dot{\sigma_y}\rangle &= \delta\langle\sigma_x\rangle - \Gamma_2\langle\sigma_y\rangle \\ \langle\dot{\sigma_z}\rangle &= \Omega\langle\sigma_x\rangle - \Gamma_1(1 + \langle\sigma_z\rangle) \end{cases} \tag{2.13}$$

with $\Gamma_2 = \Gamma_1/2 + \Gamma_\varphi$ the total dephasing rate. These equations are the well-known Bloch equations in the case of a detuned Rabi drive along the y-axis. In the steady-state, the qubit state is given by the expectation values [1]

$$
\begin{cases}
x_\infty(\Omega, \delta) &= \Gamma_1\Gamma_2\Omega \Big/ \left(\Gamma 1(\Gamma_2^2 + \delta^2) + \Gamma_2\Omega^2 \right) \\
y_\infty(\Omega, \delta) &= \Gamma_1\delta\Omega \Big/ \left(\Gamma 1(\Gamma_2^2 + \delta^2) + \Gamma_2\Omega^2 \right) \, . \\
z_\infty(\Omega, \delta) &= -1 + \Gamma_2\Omega^2 \Big/ \left(\Gamma 1(\Gamma_2^2 + \delta^2) + \Gamma_2\Omega^2 \right)
\end{cases}
\tag{2.14}
$$

Remarkably, the competition between decoherence and the coherent drive results in general in a qubit density matrix that exhibits coherences in contrast with a thermal state. At zero detuning, $y_\infty = 0$ and x_∞ reaches its maximum at $\Omega = \sqrt{\Gamma_1\Gamma_2}$ as represented Fig. 2.2. When $\Omega \gg \Gamma_2$ the Bloch vector converges towards the center of the Bloch sphere and the qubit ends up in the most entropic state $\rho_\infty = \frac{1}{2}(|e\rangle\langle e| + |g\rangle\langle g|)$.
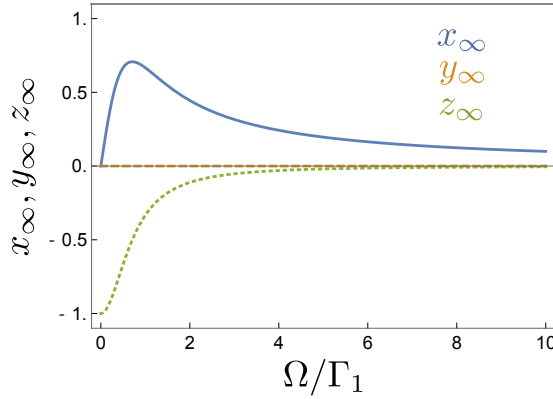
Figure 2.2: Evolution of the steady-state expectation values of σ_x (blue, plain), σ_y (orange, dashed) and σ_z (green, dotted) at zero detuning $\delta = 0$ with the Rabi drive amplitude Ω (in unit of Γ_1) for $\Gamma_\varphi = 0$.

In general the steady-state results from the competition between the detuning δ, that induces a rotation of the state along the z-axis of the Bloch sphere, and the drive strength Ω, that induces a rotation along the y-axis. An example of the evolution of the state with the detuning is represented in Fig. 2.3a) in the absence of pure dephasing $\Gamma_\varphi = 0$. Note that setting $\Gamma_\varphi \neq 0$ does not change the qualitative behavior of the qubit state. At very large detuning $\delta \gg \Omega$, the qubit is not excited by the drive. Fig. 2.3b) displays the line spanned by the steady-state in the Bloch sphere for various values of the Rabi drive. At fixed Ω, the Bloch vector trajectory given by Eq. (2.14) describes an ellipse in the plane rotated by the angle $\phi = -\arccos(\Omega/\Gamma_1)$ around the x-axis and that contains the bottom of the sphere. It is interesting to find under which condition the coherence of the qubit is maximized. For instance in Chap. 4, we will use the coherence of the steady-state of a qubit transition to read out the state of a fluxonium circuit, and maximizing the coherence leads to maximizing the amount of information extracted. The total coherence of the qubit is given by the norm of the Bloch vector projection on the equatorial plane $\sqrt{x_\infty^2 + y_\infty^2}$. When $\Omega \leq \sqrt{\Gamma_1\Gamma_2}$, the maximum amount of coherence is obtained for $\delta = 0$. At larger values of the drive

$\Omega \geq \sqrt{\Gamma_1 \Gamma_2}$, the coherence reaches a maximum for $\delta = \pm\Gamma_2\sqrt{\frac{\Omega^2}{\Gamma_1\Gamma_2} - 1}$. Interestingly, the maximum of coherence is constant and reads

$$\text{Max}(\sqrt{x_\infty^2 + y_\infty^2})_{\Omega \geq \sqrt{\Gamma_1\Gamma_2}} = \frac{1}{2}\sqrt{\frac{\Gamma_1}{\Gamma_2}} . \tag{2.15}$$

However, the direction of the Bloch vector at the maximum of coherence strongly depends on Ω: for $\Omega \leq \sqrt{\Gamma_1\Gamma_2}$ it is along the x-axis while when $\Omega \to \infty$, it is along the y-axis.
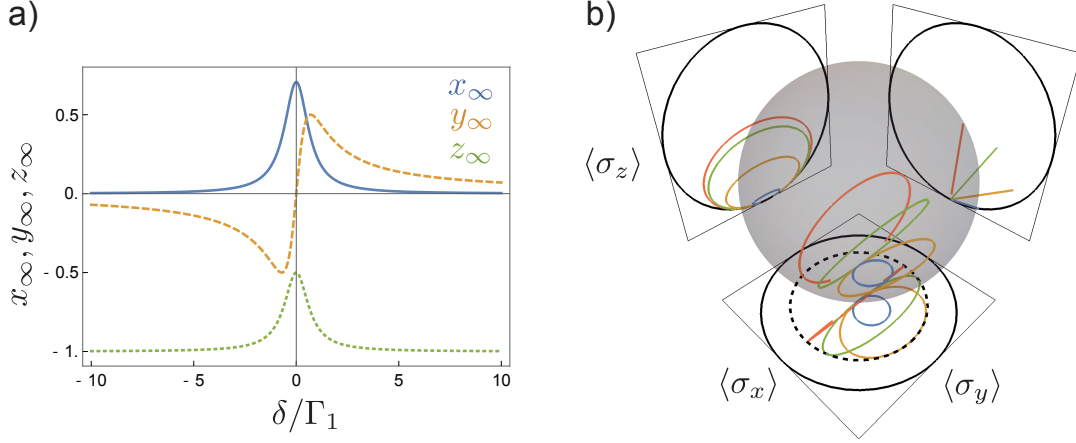
Figure 2.3: a) Evolution of the steady-state expectation values of σ_x (blue, plain), σ_y (orange, dashed) and σ_z (green, dotted) with the detuning δ at $\Omega = \Gamma_1/\sqrt{2}$ and $\Gamma_\varphi = 0$.
b) Lines spanned by the Bloch vector for varying detuning δ at $\Omega = \Gamma_1/5$ (blue), $\Gamma_1/\sqrt{2}$ (orange), $2\Gamma_1$ (green) and $10\Gamma_1$ (red) at $\Gamma_\varphi = 0$. The lines and the Bloch sphere are projected onto the three (x,y), (x,z) and (y,z) planes. The Bloch sphere projection is represented by the black circles of radius unity. The maximal value of coherence is represented by the dotted circle in the (x,y) plane, of radius $\frac{1}{2}\sqrt{\Gamma_1/\Gamma_2}$.

We now investigate the time-dependent solutions under a resonant drive. This will be the case experimentally in Sec. 2.6 and Chap. 7. When $\delta = 0$ and $\Omega \geq |\Gamma_1 - \Gamma_2|/2$, the qubit undergoes underdamped oscillations with

$$\begin{cases} \langle\sigma_x\rangle(t) &= x_\infty - \left(\frac{\Omega\langle\sigma_z\rangle^0 + \Gamma_R x_\infty}{\nu_R}\sin(\nu_R t)\right. \\ & \qquad\qquad\qquad \left. + x_\infty\cos(\nu_R t)\right)e^{-\Gamma_R t} \\ \langle\sigma_y\rangle(t) &= 0 \\ \langle\sigma_z\rangle(t) &= z_\infty + \left((\langle\sigma_z\rangle^0 - z_\infty)\cos(\nu_R t)\right. \\ & \qquad \left. + \frac{(\Gamma_R - \Gamma_1)\langle\sigma_z\rangle^0 - \Gamma_R z_\infty - \Gamma_1}{\nu_R}\sin(\nu_R t)\right)e^{-\Gamma_R t} \end{cases} \tag{2.16}$$

where $\Gamma_R = (\Gamma_1 + \Gamma_2)/2$ is the Rabi decay rate and

$$\nu_R = \sqrt{\Omega^2 - (\Gamma_1 - \Gamma_2)^2/4} \tag{2.17}$$

is the effective frequency of the Rabi oscillations. Here $\langle\sigma_z\rangle^0$ represents the initial state of the qubit that is assumed to be in a thermal state. When $\Omega \gg \Gamma_1, \Gamma_2$, we obtain $\nu_R \approx \Omega$, $z_\infty \approx x_\infty \approx 0$ and

$$
\begin{cases}
\langle\sigma_x\rangle(t) &= -\langle\sigma_z\rangle^0 \sin(\Omega t) \\
\langle\sigma_y\rangle(t) &= 0 \\
\langle\sigma_z\rangle(t) &= \langle\sigma_z\rangle^0 \cos(\Omega t)
\end{cases}
. \tag{2.18}
$$

The two observables σ_x and σ_z thus oscillate in phase quadrature.

2.2 FLUORESCENCE OF A QUBIT

So far we have focused on the qubit and on the effect of its coupling to the environment for its evolution. On the other hand, the presence of the qubit directly affects its electromagnetic environment. When the qubit is driven, it decays and emits radiation. Depending on type of the detector, the wave amplitude and phase of the emitted field and photon number can be directly detected. This emission can either be coherent and therefore seen as the result of elastic processes, or incoherent. We will study this distinction in more details and its link to thermodynamics in Chap. 7. In this section, we consider a qubit under a drive and derive the field and number of photons emitted in the environment. In doing so we recover well-studied results of quantum optics in atomic physics, but in a different frame. In particular we are able to express and detect the time-dependence of the fluorescence complex amplitude and photon number.

2.2.1 *Input-output relation*

Let us start with a simple model where a qubit of frequency ω_q is coupled to a transmission line a represented in Fig. 2.4. The transmission line is modeled as a bath containing a continuum of electromagnetic modes [61] at frequency ω propagating towards $(\leftarrow)$ or from $(\rightarrow)$ the qubit. As for the quantization of the electromagnetic field in a linear resonator, each mode is described by its annihilation operator $a_{\rightleftarrows}(\omega)$. In the time domain, the input (respectively output) field is represented by the annihilation operator $a_{\text{in}}(t)$ (resp. $a_{\text{out}}(t)$) given by the Fourier transform of the modes propagating towards (respectively from) the qubit [37]. Note that because we are dealing with propagating fields in the time domain, the annihilation/creation operators have the unit of $\sqrt{\text{Hz}}$.
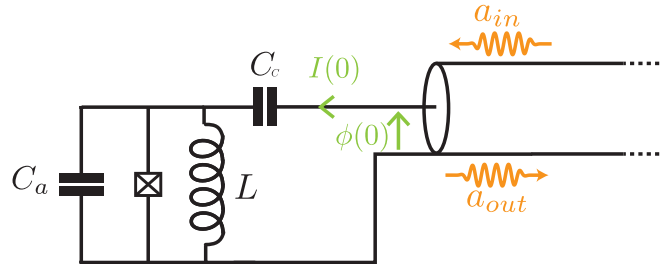
Figure 2.4: Input-output formalism. Model of a circuit capacitively coupled to a transmission line (for a transmon $L = \infty$). The input-ouput relation expresses the boundary condition of the input and ouput current and flux.

The coupling between the qubit and the line is modeled by the *Purcell rate* Γ_a at which the qubit spontaneously emits photons into the line. With this coupling the output field can be easily expressed in terms of the input field and qubit operators using the input-output formalism [11] as[1]

$$\boxed{a_{\text{out}} = a_{\text{in}} - \sqrt{\Gamma_a}\sigma_-} \tag{2.19}$$

with $\sigma_- = |g\rangle\langle e| = (\sigma_x - i\sigma_y)/2$. Importantly, the input-ouput relation can be found under other forms with phase terms in front of the modes and qubit operators. There is indeed a phase choice to do in the definition of a_{in} and a_{out} that determines the phase of the drive term due to a_{in} in the equations of evolution of the qubit.

2.2.2 Evolution under the drive: link with Bloch equations

From the point of view of the qubit the coupling to the transmission line has two effects: an Hamiltonian evolution due to the input field and an incoherent evolution due to the coupling to a continuum of degrees of freedom. The coherent evolution of the qubit is given by the Hamiltonian

$$H_d = \frac{\hbar\omega_q}{2}\sigma_z + i\hbar\sqrt{\Gamma_a}(a_{\text{in}} + a_{\text{in}}^\dagger)(\sigma_+ - \sigma_-) \tag{2.20}$$

where the phase of the second term is chosen consistently with the phase that had been set in the input-ouput relation. We will now restrict ourselves to the situation where the input field is described classically at frequency ω_d. In the laboratory frame a_{in} rotates at ω_d and can be replaced by a complex scalar: $a_{\text{in}} = \alpha_{\text{in}}e^{-i\omega_d t}$. Without loss of generality one can fix the phase of the input drive so that $\alpha_{\text{in}} \in \mathbb{R}^+$. To get rid of the rotating terms, one needs to go in the frame rotating at ω_d and apply the Rotating Wave Approximation (RWA), yielding to

$$H_R = \frac{\hbar\delta}{2}\sigma_z - \hbar\sqrt{\Gamma_a}\alpha_{\text{in}}\sigma_y \tag{2.21}$$

with $\delta = \omega_q - \omega_d$ the qubit-drive detuning. This is the same Hamiltonian as in Eq. (2.11) with

$$\boxed{\Omega = 2\sqrt{\Gamma_a}\alpha_{\text{in}}}\ . \tag{2.22}$$

Assuming that the transmission line is at zero temperature, the incoherent effect of the coupling to the line is represented by energy decay with a rate Γ_a due to spontaneous emission in the line, and therefore results in the term $\Gamma_a \mathcal{D}[\sigma_-]$ in the Lindblad master equation. We are hence back to the previous case where the qubit is described by the Bloch equations (2.13). If the qubit is also coupled to other uncontrolled degrees of freedom, the total decay rate of the qubit reads $\Gamma_1 = \Gamma_a + \Gamma_{\text{nr}}$ where Γ_{nr} is the qubit energy decay rate due to these non-radiative processes. The input-ouput relation (2.19) and the qubit Hamiltonian can be easily generalized to the case where the qubit is coupled to multiple transmission lines, with the propagating input/output fields $a_{\text{in,out}}^{(n)}$ and the Purcell rates $\Gamma_a^{(n)}$, $n \in \mathbb{N}$. If direct cross-talks between the lines are negligible, then the qubit entirely mediates the interaction between them and each line conserves its own input-ouput relation $a_{\text{out}}^{(n)} = a_{\text{in}}^{(n)} - \sqrt{\Gamma_a^{(n)}}\sigma_-$. However one has to take into account the

---

1 This is the series convention and will be always used in the following.

different phases ϕ_n of the drives in the computation of the qubit Hamiltonian, since the drives might interfere constructively or destructively, and can induce a rotation of the qubit around different directions of the Bloch sphere. Writing the drive amplitudes $\alpha_{\text{in}}^{(n)} = |\alpha_{\text{in}}^{(n)}|e^{i\phi_n}$ and assuming that all the drives are on resonance $\delta^{(n)} = 0$ the qubit Hamiltonian reads

$$H_R = -\hbar \left(\sum_n \sqrt{\Gamma_a^{(n)}} |\alpha_{\text{in}}^{(n)}| \cos(\phi_n) \right) \sigma_y - $$
$$\hbar \left(\sum_n \sqrt{\Gamma_a^{(n)}} |\alpha_{\text{in}}^{(n)}| \sin(\phi_n) \right) \sigma_x \ . \tag{2.23}$$

This relation will be used in the case of two drives either in phase or in opposition of phase in Chap. 3.

2.2.3 *Radiation of the qubit: spontaneous emission, stimulated emission*

When the drive induces Rabi oscillations of the qubit, it cyclically gives and receives energy to and from the qubit. On the other hand when the qubit decays from the excited to the ground state, it radiates energy. We express here in the microwave domain the well-studied results of the literature obtained for atoms probed by optical means [1]. The exchanges of energy between the atom and the field are represented by the rate of output photons $a_{\text{out}}^\dagger a_{\text{out}}$. Using the input-ouput relation Eq. (2.19) we get

$$a_{\text{out}}^\dagger a_{\text{out}} = a_{\text{in}}^\dagger a_{\text{in}} + \Gamma_a \sigma_+ \sigma_- - \sqrt{\Gamma_a}(a_{\text{in}}^\dagger \sigma_- + a_{\text{in}} \sigma_+) \ . \tag{2.24}$$

We can rewrite the second term as $\sigma_+ \sigma_- = \frac{1}{2}(1 + \sigma_z)$. The last term involves two products of the input field and qubit operators. Let us restrain ourselves to the previous case of a drive in a coherent state. We can rewrite the annihilation operator a_{in} as $a_{\text{in}} = \langle a_{\text{in}} \rangle + \delta a_{\text{in}} = \alpha_{\text{in}} + \delta a_{\text{in}}$. This defines the operator δa_{in} representing the quantum fluctuations of the drive. When the drive amplitude is much larger than its quantum fluctuations we obtain

$$a_{\text{in}} \sigma_+ = (\alpha_{\text{in}} + \delta a_{\text{in}})\sigma_+ \approx \alpha_{\text{in}} \sigma_+ \ . \tag{2.25}$$

This transformation allows us to express the output photon rate operator as

$$\boxed{a_{\text{out}}^\dagger a_{\text{out}} = a_{\text{in}}^\dagger a_{\text{in}} + \Gamma_a \frac{1 + \sigma_z}{2} - \sqrt{\Gamma_a} \alpha_{\text{in}} \sigma_x} \ . \tag{2.26}$$

The first term of this equation simply represents the rate of photons sent on the qubit. The second one is proportional to the probability to find the qubit in the excited state: it represents *spontaneous emission* of the qubit towards the line. By construction, we see that the last term is due to an interference between the reflected input drive and the electromagnetic field emitted by the qubit. To understand its meaning, let us consider a qubit coupled to one line only, hence one drive, in the limit case $\delta = 0$ and $\Omega = 2\sqrt{\Gamma_a}\alpha_{\text{in}} \gg \Gamma_1, \Gamma_2$. For this particular case the solutions of the Bloch equations are given by Eq. (2.18) and describe damped Rabi oscillations. If we integrate the mean value of the last term during the first half Rabi period and assume a qubit initially in $|g\rangle$ (hence $\langle \sigma_z \rangle^0 = -1$) we get

$$\int_{|g\rangle}^{|e\rangle} -\sqrt{\Gamma_a}\alpha_{\text{in}}\langle \sigma_x \rangle \mathrm{d}t \overset{\Omega \gg \Gamma_R}{\approx} -\int_0^{\pi/\Omega} \frac{\Omega}{2} \sin(\Omega t)\mathrm{d}t = -1 \ . \tag{2.27}$$
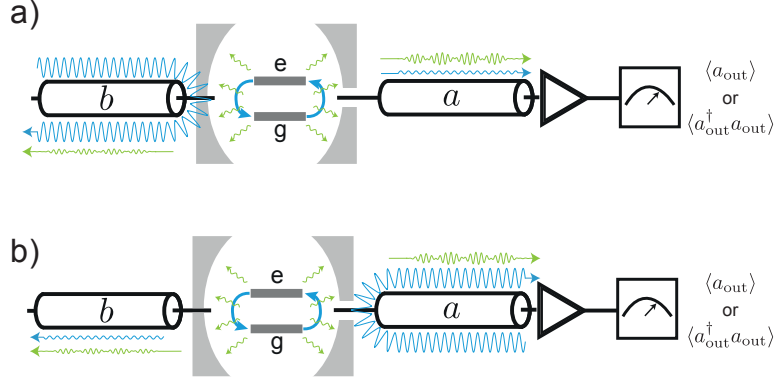
Figure 2.5: Fluorescence measurement in a) transmission and b) reflection. In transmission the drive is applied on the qubit through b and is reflected while the fluorescence field or photons are measured through a. In reflection the drive is applied through a and the measured fluorescence contains the contributions due to the drive.

Similarly integrating between $|e\rangle$ and $|g\rangle$ during the second half period would give $+1$. Therefore this last term represents the exchanges of quanta of energy between the drive and the qubit, and as such has to be interpreted as the *stimulated emission* term. This denotation will be used in the following to stress the link with quantum optics but we cannot forget that this term can be negative and then represents the absorption of energy from the drive. It is important to stress out that this distinction between spontaneous and stimulated emission arose when computing the photon rate operator $a_{\text{out}}^\dagger a_{\text{out}}$ and was absent in the expression of the ouput field operator a_{out}. Therefore the vocabulary of spontaneous and stimulated emissions should be reserved to the case of a photon number measurement and prevented when describing the measurement of the electromagnetic field amplitude.

This distinction appears very clearly if we consider two identical experiments where only the type of detector has been changed. We use the two-ports configuration represented Fig. 2.5, where the qubit is coupled to two lines a and b with the respective coupling rates Γ_a and Γ_b. We measure either the fluorescence field amplitude $\langle a_{\text{out}}\rangle$ or the photon rate $\langle a_{\text{out}}^\dagger a_{\text{out}}\rangle$ emitted by the qubit towards a during Rabi oscillations. The next section presents how such measurements can be performed experimentally in circuit-QED. The Rabi oscillations are induced by a drive sent either from a or b. Experimentally, we use a transmon qubit embedded in a far-detuned 3D aluminum cavity. Since we apply the drive at qubit frequency on the cavity, it is mostly reflected. The drive amplitudes in a and b, respectively α_{in} and β_{in}, are set so that $2\sqrt{\Gamma_b}\beta_{\text{in}} = 2\sqrt{\Gamma_a}\alpha_{\text{in}} = \Omega \gg \Gamma_1$. In transmission we have $a_{\text{in}} = 0$ and the only contribution to the output field and photons is due to the qubit. On the other hand in reflection, we have to take into account the presence of the reflected drive. We hence

obtain the following expressions for the field and the photon rate in transmission and in reflection

$$
\begin{cases}
\langle a_{\text{out}} \rangle^{\text{trans}} &= -\sqrt{\Gamma_a} \langle \sigma_- \rangle \\
\langle a_{\text{out}}^\dagger a_{\text{out}} \rangle^{\text{trans}} &= \Gamma_a \frac{1 + \langle \sigma_z \rangle}{2}
\end{cases}
$$

$$. \tag{2.28}$$

$$
\begin{cases}
\langle a_{\text{out}} \rangle^{\text{ref}} &= \alpha_{\text{in}} - \sqrt{\Gamma_a} \langle \sigma_- \rangle \\
\langle a_{\text{out}}^\dagger a_{\text{out}} \rangle^{\text{ref}} &= \alpha_{\text{in}}^2 + \Gamma_a \frac{1 + \langle \sigma_z \rangle}{2} - \frac{\Omega}{2} \langle \sigma_x \rangle
\end{cases}
$$
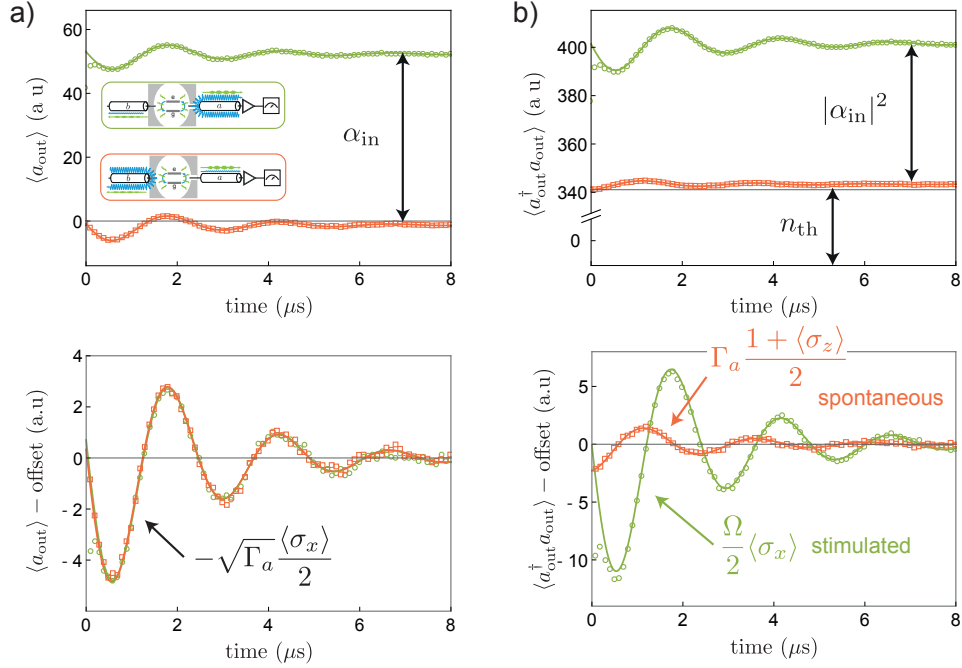
Figure 2.6: Time-resolved fluorescence of a superconducting atom undergoing Rabi oscillations. a) Field complex amplitude $\langle a_{\text{out}} \rangle$ measured as a function of time in transmission (red squares) and in reflection (green circles, see insets). The two signals are separated by the incoming field α_{in} reflected onto the cavity (top). After subtraction, we find the same oscillatory behavior, given by $-\sqrt{\Gamma_a} \langle \sigma_x \rangle / 2$ and represented by the plain line (bottom). b) Photon number rate $\langle a_{\text{out}}^\dagger a_{\text{out}} \rangle$ for the same experiment. The two signals are separated by α_{in}^2 and far above zero by an amount n_{th} corresponding to the average of the number of thermal photons added to the signal (top). They both oscillate in time but with different amplitudes and in phase quadrature. The evolution of the transmitted photons is given by the spontaneous emission term $\Gamma_a (1 + \langle \sigma_z \rangle)/2$. In the limit $\Omega \gg \Gamma_a$ the reflected photons are mostly due to stimulated emission and evolve as $\Omega \langle \sigma_x \rangle / 2$ (plain lines). Here $\Omega = 2\pi \times 0.41$ MHz and $\Gamma_a = 2\pi \times 0.072$ MHz.

For the field amplitude the only difference between transmission and reflection is an offset due to the reflected drive. For the energy however, there is a clear difference between transmission, where only spontaneous emission exists, and reflection, where both spontaneous and stimulated emission are present. The experimental results in transmission and reflection for the field and the energy as a function of time are represented in Fig. 2.6. When we measure $\langle a_{\text{out}} \rangle$ it does not matter whether we measure in transmission or in reflection: we obtain exactly the same signal up to an offset, in phase,

with the same amplitude. The only difference is the presence of the offset α_{in} present in reflection but not in transmission (Fig. 2.6a). However when we measure $\langle a_{\text{out}}^{\dagger} a_{\text{out}} \rangle$ we notice that the amplitude of the oscillations is larger in reflection than in transmission. Again, the photon rate measured in reflection has an offset due to α_{in}^2. Moreover, the two curves are largely above 0 by an amount n_{th} which corresponds to the number of thermal photons entering the detector (see Sec. 2.4). When the offsets are subtracted and the two curves put on top of each other we see that the two signals are in phase quadrature (Fig. 2.6b). Indeed, in transmission we see spontaneous emission only, hence oscillations of $\langle \sigma_z \rangle$. In reflection the stimulated emission term overcomes spontaneous emission since $\Omega \gg \Gamma_a$ and we mostly measure oscillations of $\langle \sigma_x \rangle$.

2.3 FLUORESCENCE MEASUREMENT IN OPTICS AND MICROWAVES

Several strategies can be used to measure the fluorescence of a superconducting circuit with a good accuracy, depending on the observable one aims to measure. Most of them rely on amplification of the signal at the quantum limit followed by a room-temperature detection setup, giving access to the distribution of the measured outcomes. Phase-sensitive amplification and homodyne detection is used when only one field quadrature $\text{Re}(a^{\dagger} e^{-i\varphi} + a e^{i\varphi})/\sqrt{2}$, $0 \le \varphi \le 2\pi$ contains the information of interest. The Josephson Parametric Amplifier (JPA) achieves such an amplification with a state-of-the-art gain of about 20 dB on a bandwidth of a few MHz, and a detection efficiency (the ratio between the quantum limited noise power and the experimental one) of 80 % [62–64]. Recently the bandpass of such devices has been increased by impedance matching to a few 100 MHz [65]. When two field quadratures need to be accessed simultaneously, phase-preserving amplification is required where the two orthogonal quadratures are amplified by the same amount. This process is described in the following for a Josephson Parametric Converter (JPC) [12, 66–69]. The JPC has typically the same quantum efficiency and the same gain-bandwidth product as the JPA[2]. Recently, a new kind of phase-preserving amplifier has been proposed and measured, where the non-linear amplifying medium is distributed along traveling waves instead of standing waves [71–73]. These Travelling Wave Parametric Amplifiers (TWPA) offer similar gain and quantum efficiencies as JPCs, but on a bandwidth of several GHz.

Linear amplification and detection is particularly suitable to the measurement of one or two quadratures of the field, but we will show in this section that they also lead to measuring the expectation value of the number of photons. However dedicated detectors also exist if one is only interested into measuring the photon number operator. The Josephson PhotoMultiplier (JPM) is based on a DC-biased Josephson junction and clicks when it receives one or more photons [74–76]. Recent experiments and proposals have also suggested to directly measure propagating microwave photons without destroying them. A photon bouncing on a resonant cavity coupled to a superposed qubit induces a phase shift of the qubit superposition. If this phase shift is set to π one can measure the parity of the photon number operator in a single-shot way [77, 78]. Such measurements naturally suffer from a small bandwidth as they are limited by the linewidth of the resonant cavity. An alternative is again to use traveling waves to increase the detection bandwidth. A detector where a propagating photon would induce small phase shifts in a chain of qubits has been proposed recently and is currently

---

2 Note that it is possible to use phase preserving amplifiers for measuring a single quadrature at the expense of half the signal-to-noise ratio [70], and to use the JPA in phase-preserving mode.

investigated with the promise of a bandwidth of several GHz [79]. It is also possible to detect the heating of a metal induced by microwave photons. For that one uses superconductor-normal-metal-superconductor (SNS) junctions [80, 81] or normal-meta-insulator-superconductor junctions [82]. The photons heat up the normal metal island and induces a change of its conductance. This change is detected by a frequency shift of the microwave resonator coupled to the island. Since the photons generate a heat current, these detectors are larger than the ones based on standing waves, an achieve a detection bandwidth of about 10-20 MHz. However they are still one or two orders of magnitude above the single-photon resolution. The different properties of microwave photons amplifiers and detectors are summarized in Table 2.1.

	Purpose	Bandwidth	Detection efficiency
JPA	Phase-sensitive amplifier	2 MHz to 200 MHz	≤ 84 [64] %
JPC	Phase-preserving amplifier	2 to 20 MHz	≤ 80 [67, 69] %
TWPA	Phase-preserving amplifier	3 GHz	≤ 75 [72] %
			Detection level
JPM	Photodetector	400 MHz	Single-photon (no photon number resolution) [74–76]
Qubit in cavity	Photodetector	1MHz	Single-photon / Photon parity [77, 78]
Bolometer	Photocounter	10 to 20 MHz	≥ 200 photons [81]

Table 2.1: State-of-the-art of microwave photons amplification and detection.

It is clear from Table 2.1 that microwave photodetectors still do not offer the resolution needed to measure stimulated and spontaneous emission of a superconducting qubit (corresponding to one photon at best), since either they only detect whether there are photons or not, or their sensitivity is too low. In this thesis, we use phase-preserving amplification of the field if needed, followed by heterodyne measurement. As we will see in the following, this method has the advantage of letting us reconstruct very easily the field quadratures and the number of photons. Even though this method achieves quantum optics measurements, it differs from usual optical measurements in the visible or near-visible range. This section is thus devoted to presenting the different challenges faced by the experimentalist when working with microwaves instead of optical frequencies, and how standard microwaves operations can be understood in terms of usual, textbook quantum optics [83].

2.3.1 *Of detectors and losses*

For an experimentalist the ways to measure the fluorescence of a system strongly depend on the frequency of operation. In the optical domain the frequency at which the electromagnetic field oscillates is so large that current electronics cannot resolve its time dependence straightforwardly by direct acquisition. However the photon energy is large and leads to the detection of energy at the single-photon level. On the contrary, in the microwave domain, fast electronics allows us to record time-resolved oscillations of the electromagnetic field while energy measurement down to the single-photon level remains challenging due to the low energy of photons, which is below $k_B \times 1$ K. More precisely, we investigate the case of a detection setup at room temperature, $T = 300$ K. Photodetection is usually based on the photoelectric effect, the excitation of charge carriers, electrons or holes, from a "dark" state to a "bright" state inducing a macroscopic current that can be measured. For instance it can consists of the jump of an electron from the valence band to a conduction band of a semiconductor, as represented in Fig. 2.7a). Photodetectors can also be based on charge carriers trapped in a potential, a quantum well or a quantum dot, and escaping it by photon absorption. The change of charge can either be directly detected, for instance by using an avalanche effect with multiple wells, or indirectly measured, by placing a two-dimensional electron or hole gas next to the trap. In any case, the typical energy scale of these systems is given by the energy band gap. For semiconductors the lowest gaps are of the order of 1 eV, corresponding to a frequency $\nu = (1 \text{ eV})/h \approx 250$ THz and a wavelength $\lambda \approx 1.2$ μm, therefore optical photons in the infrared[3]. The microwave signals used in superconducting circuits have a maximal frequency of about 20 GHz, and therefore do not have enough energy to excite an electronic transition from one band to the other. On the other hand, the fastest electronics up to now can digitize voltages oscillating at frequencies up to 100 GHz [84]. Moreover, non-linear elements at microwave frequencies allow one to perform frequency conversion of signals from the GHz range to the MHz range. As a result, the temporal oscillations of the electromagnetic field can be directly recorded for microwaves, while it remains impossible for optical photons where the electromagnetic field oscillates more than three orders of magnitude faster than the fastest digitizer[4]. Therefore detectors of optical photons naturally measure the photon number operator $a^\dagger a$ while detectors of microwave photons naturally measure the quadratures of the field $X = (a + a^\dagger)/\sqrt{2}$ and $P = i(a^\dagger - a)/\sqrt{2}$, as shown in Fig. 2.7b). As we will see in the following, this does not mean that it is impossible to measure the field quadratures of optical photons nor the number of photons of a microwave signals.

During their propagation in vacuum, optical fibers, or coaxial cables, the signals encounter losses. The losses can be modeled by an array of unbalanced beamsplitters, each one adding an extra field $h_{\text{loss}}^{(n)}$. The state of this field strongly depends on the frequency of the incoming signals. At room temperature $k_B T/h \approx 6$ THz, and for optical photons the fields added by the losses can be considered in the vacuum state. However at 10 GHz, the noise temperature corresponds to more than 600 thermal photons. If the signal outgoing from the quantum system contains only a few photons as it is often

---

3 Some semiconductors such at cadmium arsenide and indium antimonide can reach gaps as low as 0.1 eV, and hence appear as promising candidates to the detection of THz photons with a good efficiency. Bilayer graphene can also reach smaller gaps but its use as a microwave photocounter is still exploratory.

4 This does not mean that time-resolved measurements are impossible in the optical domain. It is actually possible to measure the correlation between two intensities with a time resolution below the nanosecond.
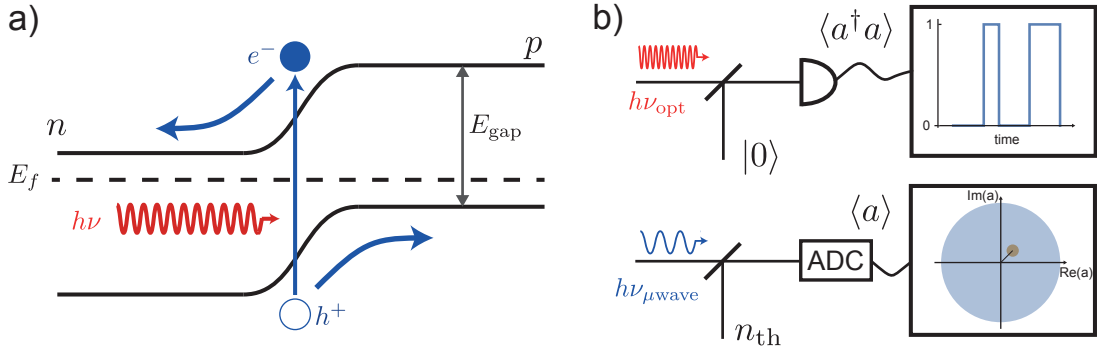
Figure 2.7: a) Example of photodetection in a semiconductor p-n junction. An incoming photon of energy $h\nu$ excites an electron from a valence band to a conduction band, generates an electron-hole pair and induces a current only if $h\nu \geq E_{\text{gap}}$.
b) Room temperature (top) optical / (bottom) microwave measurement in presence of losses: the signal losses are represented by beamsplitters that add modes to the signal, and can be considered in vacuum only if working at optical frequencies. At microwave frequencies, the signal (in orange) is hidden in the noise (in blue, not to scale) if it has not been amplified at low temperature, as shown by the circles representing the variance of the operators. Natural detectors measure $a^\dagger a$ for optical photons and a for microwave photons.

the case, it will be completely overcome by thermal noise. For this reason, despite the possible detrimental effect of amplifiers, it is crucial to amplify the microwave signals at low temperature before proceeding to the acquisition at room temperature, possibly at the quantum limit if needed.

2.3.2 Quadrature measurement in optics

Even though optical detectors measure the photon number operator it is possible to use a conjugation of beamsplitters and photodetectors to measure one or two quadratures of the field. The measurement of one field quadrature, called *homodyne* detection, is represented in Fig. 2.8a). The incoming field a is sent onto a beamsplitter together with a strong resonant drive b, the local oscillator (LO). Assuming a perfect beamsplitter, there is a $\pi/2$ phase difference between reflected and transmitted fields, energy is evenly split and the two output fields a_1 and a_2 are given by

$$\begin{cases} a_1 &= (a + ib)/\sqrt{2} \\ a_2 &= (ia + b)/\sqrt{2} \end{cases}. \tag{2.29}$$

The local oscillator is a large coherent field so we can approximate it by its mean value and write $b = \beta e^{-i\phi}$ with $\beta \gg 1 \in \mathbb{R}^+$. The two photodetectors measure the number of photons in ① and ②

$$\begin{cases} a_1^\dagger a_1 &= (a^\dagger a + \beta^2 + i\beta(a^\dagger e^{-i\phi} - a e^{i\phi}))/2 \\ a_2^\dagger a_2 &= (a^\dagger a + \beta^2 - i\beta(a^\dagger e^{-i\phi} - a e^{i\phi}))/2 \end{cases}. \tag{2.30}$$

The homodyne signal is the difference between the two intensities given by the photodetectors. With $a = (X + iP)/\sqrt{2}$ it reads

$$S = a_1^\dagger a_1 - a_2^\dagger a_2 = \beta\sqrt{2}(P\cos\phi + X\sin\phi) . \tag{2.31}$$
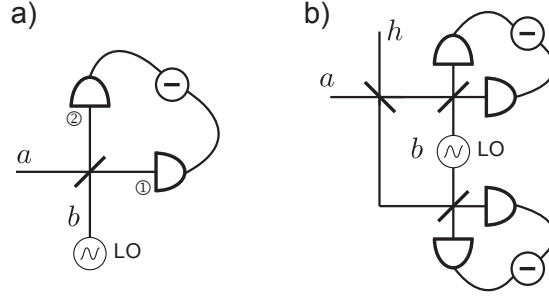
Figure 2.8: a) Homodyne detection with photodetectors: the incoming field a is added to a local oscillator b on resonance using a balanced beam splitter. The measured quadrature is obtained by subtraction of the intensities in the two arms, and its direction depends on the phase of the LO.
b) Heterodyne detection: the incoming field is split before performing two parallel homodyne measurements, and as such adds an extra-mode h.

Thus the phase ϕ of the local oscillator fixes the direction of the field quadrature measured by the homodyne signal. Importantly, the LO enables to amplify the field quadrature, with the linear gain $\beta = \sqrt{G}$.

For measuring the two orthogonal quadratures X and P at the same time, called *heterodyne* detection, one only needs to split the incoming field and perform two homodyne detections in parallel with the same local oscillator, as represented in Fig. 2.8b). Similarly to the case of losses, the first beamsplitter adds a field h on top of a and the two fields at its output are thus given by $(a + ih)/\sqrt{2}$ and $(ia + h)/\sqrt{2}$. For the sake of simplicity let us assume that the phase of the LO has been fixed $\phi = 0$ with the definition made in the case of homodyne measurement. The intensities measured by the photodetectors are easily obtained from Eq. (2.31) by substituting a by $(a + ih)/\sqrt{2}$ and $(ia + h)/\sqrt{2}$. The two homodyne signals are hence

$$\begin{cases} S_1 & = (\sqrt{G}P_a - \sqrt{G}X_h) \\ S_2 & = (-\sqrt{G}X_a + \sqrt{G}P_h) \end{cases}. \tag{2.32}$$

Therefore heterodyne detection is made at the expense of increasing the fluctuations of the two quadratures, with a lowest bound set by the vacuum fluctuations of h.

2.3.3 *Phase-preserving amplification at the quantum limit with the Josephson Parametric Converter*

We now turn towards microwave measurements. When the signals are weak it is necessary to amplify them by adding the minimum amount of noise allowed by quantum mechanics. Here we study the case of phase preserving amplification, where both quadratures are amplified by the same amount. We label a_{in} the field propagating towards the amplifier and a_{out} the field after amplification. Ideally, we would like the following relation between the input and output quadratures

$$\begin{cases} X_{\text{out}} & = \sqrt{G}X_{\text{in}} \\ P_{\text{out}} & = \sqrt{G}P_{\text{in}} \end{cases} \tag{2.33}$$

with G the power gain. On the other hand a_{out} needs to verify the commutation relation $\left[a_{\text{out}}(t), a_{\text{out}}(t')^\dagger \right] = \delta(t - t')$ with δ the Dirac distribution. The ideal expressions of

Eq. (2.33) do not fulfill the commutation relations except in the trivial case of no amplification at all $G = 1$. They are restored by adding a second mode $h_{\text{in}}^{\dagger}$ at the output amplified by a power gain $G - 1$

$$a_{\text{out}} = \sqrt{G}a_{\text{in}} + \sqrt{G - 1}h_{\text{in}}^{\dagger} \ . \tag{2.34}$$

Indeed with this extra-mode the commutation relation becomes

$$
\begin{aligned}
\left[a_{\text{out}}(t), a_{\text{out}}(t')^{\dagger}\right] &= G\left[a_{\text{in}}(t), a_{\text{in}}(t')^{\dagger}\right] \\
&\quad + (G - 1)\left[h_{\text{in}}(t)^{\dagger}, h_{\text{in}}(t')\right] \\
&= G\delta(t - t') - (G - 1)\delta(t - t') \\
&= \delta(t - t') \ ,
\end{aligned}
\tag{2.35}
$$

where we used the fact that $\left[a_{\text{in}}(t), h_{\text{in}}(t')\right] = \left[a_{\text{in}}(t)^{\dagger}, h_{\text{in}}(t')\right] = 0$. If h_{in} is in the vacuum state or more generally in a thermal state, then $\langle h_{\text{in}}^{\dagger}\rangle = 0$ and the quadrature amplification relation given by Eq. (2.33) holds on average. Therefore quantum-limited amplification is possible at the expense of adding the contribution of an extra-mode on top of the mode of interest. Even when h_{in} is in vacuum, this results in an effective increase of the fluctuations of a_{out}, a phenomenon often interpreted as extra noise added on the mode. Yet this interpretation is stricto-sensu incorrect. Phase-preserving amplification does not lose any information in the process as it would be the case with noisy amplification [85]. On the contrary, the increase of the variance of the amplified mode is the clear manifestation of the uncertainty principle, since we amplify two non-commuting quadratures that cannot both be determined simultaneously with infinite precision [86]. It is interesting to compare the result of phase-preserving amplification to the one obtained in the case of optical heterodyne measurement. With heterodyne detection the field added was given by $\sqrt{G}h$, while it reads $\sqrt{G - 1}h_{\text{in}}^{\dagger}$ for phase-preserving amplification. In the limit of large gain $G \gg 1$, the two processes can be considered equivalent. At $G = 1$ however, they become extremely different: there is still an added mode and hence greater fluctuations for optical heterodyne detection while the extra mode disappears for phase-preserving amplification. This indicates that phase-preserving amplification does not degrade the information in the process, while optical heterodyne measurements cannot spare the expense of losing some information in the environment, even when the process is ideal.

Experimentally we use a home-made JPC consisting of two modes a and b coupled by an inductively shunted Josephson Ring Modulator (JRM) [66] represented in Fig. 2.9. The JRM implements the three-wave mixing Hamiltonian

$$H_{3\text{WM}} = \hbar\chi_3(a + a^{\dagger})(b + b^{\dagger})(c + c^{\dagger}) \ , \tag{2.36}$$

where c represents the third normal mode of the JRM. When a pump p is applied on mode c at the sum of the frequencies of a and b, $\omega_p = \omega_a + \omega_b$, the Hamiltonian becomes, in the RWA

$$H_{\text{amp}} = \hbar\chi_3\text{p}(a^{\dagger}b^{\dagger} + ab) \ . \tag{2.37}$$

The first term of this Hamiltonian consists of the creation of one photon in each mode a and b through the destruction of one pump photon and performs parametric amplification. The two modes a and b are coupled to the lines with the coupling rates $\kappa_{a,b}$. In
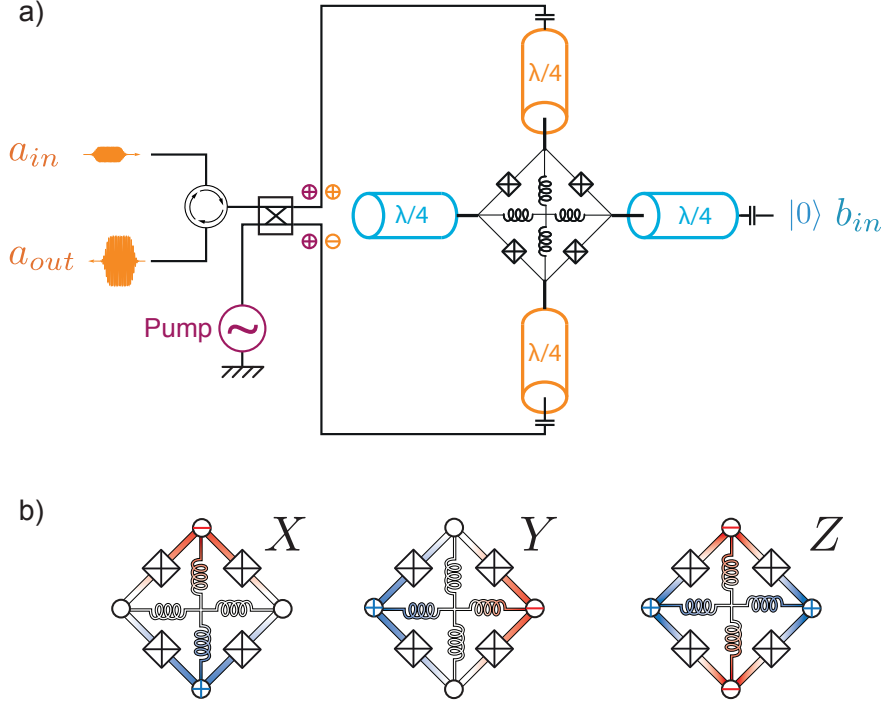
Figure 2.9: Josephson Parametric Converter with the shunted JRM. a) The two modes a (orange) and b (blue) are made of $\lambda/2$ resonators coupled together by the ring. The input signal a_{in} is sent on the corresponding resonator by antisymmetric excitation, the input on b is ideally left in the vacuum state (thanks to a 50 Ω termination at $k_B T \ll \hbar \omega_b$) and the pump is applied by symmetric excitation. When $\omega_c = \omega_a + \omega_b$ the JPC functions as a phase-preserving amplifier.
b) Normal modes of the shunted JRM, that diagonalize the impedance matrix of the quadrupole. X, Y and Z participate respectively into the modes a, b and c.

the Heisenberg picture, if we assume a_{in} and b_{in} on resonance with the resonators, the dynamics of a and b is given by the two Langevin equations

$$
\begin{cases}
\dot{a} & = \frac{i}{\hbar}[H_{\text{amp}}, a] + \sqrt{\kappa_a}a_{\text{in}} - \frac{\kappa_a}{2}a \\
\dot{b}^\dagger & = \frac{i}{\hbar}[H_{\text{amp}}, b^\dagger] + \sqrt{\kappa_b}b_{\text{in}}^\dagger - \frac{\kappa_b}{2}b^\dagger
\end{cases}
$$
$$
\Leftrightarrow \qquad\qquad\qquad\qquad\qquad\qquad\qquad\qquad\qquad\qquad (2.38)
$$
$$
\begin{cases}
\dot{a} & = -i\chi_3 \text{p} b^\dagger + \sqrt{\kappa_a}a_{\text{in}} - \frac{\kappa_a}{2}a \\
\dot{b}^\dagger & = i\chi_3 \text{p} a + \sqrt{\kappa_b}b_{\text{in}}^\dagger - \frac{\kappa_b}{2}b^\dagger
\end{cases}.
$$

The output field is given by an input-output relation similar to Eq. (2.19): $a_{\text{out}} = a_{\text{in}} - \sqrt{\kappa_a}a$. Combining it with the steady-state of Eq. (2.38) leads to

$$
a_{\text{out}} = -\frac{1+\mathcal{C}}{1-\mathcal{C}}a_{\text{in}} + i\frac{2\sqrt{\mathcal{C}}}{1-\mathcal{C}}b_{\text{in}}^\dagger \tag{2.39}
$$

where we have introduced the cooperativity $\mathcal{C} = (2\chi_3|\text{p}|)^2/(\kappa_a\kappa_b)$. When $\mathcal{C} < 1$, we indeed end up with a relation similar to Eq. (2.34) up to a global phase π, with an extra-mode $h_{\text{in}}^\dagger = -ib_{\text{in}}^\dagger$ and a power gain [12]

$$
G = \left(\frac{1+\mathcal{C}}{1-\mathcal{C}}\right)^2 = \left(\frac{\kappa_a\kappa_b + (2\chi_3|\text{p}|)^2}{(\kappa_a\kappa_b - (2\chi_3|\text{p}|)^2}\right)^2. \tag{2.40}
$$

The gain diverges when $\mathcal{C} \to 1^-$. Above this threshold, the JPC enters the self-oscillation regime analogous to lasing in optics [87]. We assumed in the previous derivation that the JPC modes a and b reached their steady-states. When a_{in} and b_{in} vary in time, this approximation still holds as long as their time evolution is larger than the correlation time induced by the amplifier. In the frequency domain this corresponds to working with signals centered at the JPC frequency and that have a frequency width smaller than the bandwidth γ of the JPC. With parametric amplifiers the gain-bandpass product is constant [66] and given by

$$\sqrt{G} \times \gamma = \frac{2}{\dfrac{1}{\kappa_a} + \dfrac{1}{\kappa_b}} \ . \tag{2.41}$$

Concretely in our experiments, we adapted the gain of the JPC so that its bandpass would be larger than the frequency width of the signals. Before acquisition, the microwave signal needs to be further amplified. These amplifications do not have to be performed at the quantum limit since the signal has already emerged from the noise.

2.3.4 *Frequency conversion of microwaves*

The fastest state of the art electronics is in theory able to digitize signals up to 100 GHz [84]. However, ultra fast Analog to Digital Converters (ADC) are still expensive and can be challenging to use as they generate a high flow of information that has to be treated and transferred to the computer at very high speeds. Moreover, the signals emitted by superconducting circuits vary over a few nanoseconds for the fastest processes, so there is no need for a numeric resolution a hundred times faster. Fortunately the microwave toolbox contains mixers that are non-linear elements allowing frequency conversion. Concretely, the signal is down-converted to a few dozens of MHz and then digitized with a typical time resolution of 1 ns. For the study of conversion and digitization, we have to keep the explicit time dependence of the operators, which means working in the laboratory frame instead of the rotating frame.
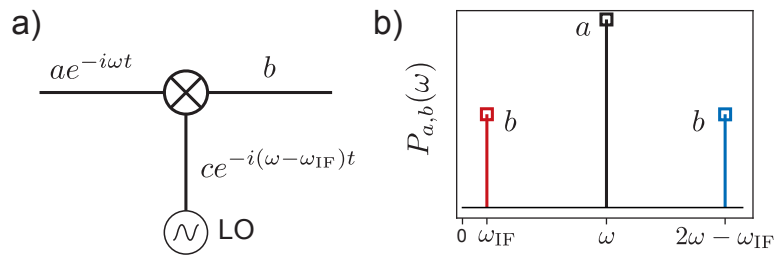
Figure 2.10: Frequency conversion using a microwave mixer: a) the incoming signal in a at frequency ω is multiplied by a LO signal, which outputs through mode b.
b) in the frequency domain, the initial wave at ω (black) is split in the upper (blue) and lower (red) sidebands.

The principle of conversion is represented in Fig. 2.10 and consists of a three port operation[5]. The signal voltage in mode a at frequency ω is multiplied by a strong signal coming from the local oscillator (LO) c at frequency $\omega - \omega_{IF}$. Here ω_{IF} denotes that this

---

[5] We describe here simple demodulation, where the two quadratures exit through the same port. It is also possible to use IQ mixers, where the two quadratures of the down-converted signal output to different ports.

frequency lies in the MHz range. The output voltage in port b consists of the product of the signal and LO voltages

$$
\begin{aligned}
V_b^{\text{out}}(t) &= \frac{1}{V_1} V_a(t) \times V_c(t) \\
&= V_0 \Big(a e^{-i\omega t} + a^\dagger e^{i\omega t} \Big) \Big(c e^{-i(\omega - \omega_{\text{IF}})t} + c^\dagger e^{i(\omega - \omega_{\text{IF}})t} \Big) \\
&= V_0 C \Big(a e^{-i(\omega_{\text{IF}} t - \phi)} + a^\dagger e^{i(\omega_{\text{IF}} t - \phi)} \Big) \\
&\quad + V_0 C \Big(a e^{-i(2\omega - \omega_{\text{IF}} t + \phi)} + a^\dagger e^{i(2\omega - \omega_{\text{IF}} t + \phi)} \Big)
\end{aligned}
\tag{2.42}
$$

where we used $c = C e^{i\phi}$ as already done in the case of optical homodyne and heterodyne detection (note that here we use c as the LO and not b) and V_0 and V_1 are constants homogeneous to a voltage. As expected we obtain two sidebands centered around ω at the output, the lower sideband lying in the MHz range and the higher one in the GHz range. The high frequency sideband is eliminated by low-pass filtering of the signal. Interestingly, digitization implements an inherent low-pass filter, so this process can be directly done in the acquisition. However, it can be useful experimentally to perform bandpass filtering of the signal at ω_{IF} before digitization to prevent $1/f$ noise (low frequencies) and aliasing (high frequencies). In any case getting rid of the high frequency sideband induces a loss of information, that can, again, be represented by the addition of an extra-mode h that increases the fluctuations of the operators.

After frequency conversion and filtering we can express the voltage operator as a function of the position and momentum operators $X_{a,h}$ and $P_{a,h}$ as

$$
\begin{aligned}
V_b(t) = V_0 C \sqrt{2} \Big((X_a + X_h) \cos(\omega_{\text{IF}} t - \phi) \\
+ (P_a + P_h) \sin(\omega_{\text{IF}} t - \phi) \Big) .
\end{aligned}
\tag{2.43}
$$

If we set the demodulation frequency ω_{IF} to zero we obtain a DC voltage $V_b = V_0 C \sqrt{2} ((X_a + X_h) \cos \phi - (P_a + P_h) \sin \phi)$. This is the same expression as the one we got for optical homodyne detection in Eq. (2.31) (up to a shift in ϕ and the exchange $\beta \leftrightarrow C$), but here the quadrature is encoded in a voltage instead of the power. If $\omega_{\text{IF}} \neq 0$, we keep the information about the two quadratures and perform heterodyne detection.

Frequency conversion is routinely performed at room temperature and can be modeled as a unitary operation acting on thermal fields. It can also be performed at the quantum limit. For a quantum treatment we can take the example of a JPC pumped in frequency conversion. We assume that high-frequency signals at ω (respectively low-frequency at ω_{IF}) propagate towards and from a (respectively b). Like in amplification, the dynamics of the JPC modes follows the three-wave-mixing Hamiltonian (2.36), but here we consider a pump at $\omega - \omega_{\text{IF}}$ applied on c. In the RWA, it comes down to [88]

$$
H_{\text{conv}} = \hbar \chi_3 \text{p} (a b^\dagger + a^\dagger b) .
\tag{2.44}
$$

This is the beamsplitter Hamiltonian, but here it contains an inherent frequency conversion. Writing explicitly the time dependence $a_{\text{in,out}}(t) = a_{\text{in,out}}^0 e^{-i\omega t}$ and $b_{\text{in,out}}(t) = b_{\text{in,out}}^0 e^{-i\omega_{\text{IF}} t}$ we can follow the same calculations as the ones made for phase-preserving amplification. They lead to

$$
\begin{aligned}
b_{\text{out}}(t) &= \left(-\frac{1-\mathcal{C}}{1+\mathcal{C}} b_{\text{in}}^0 + i \frac{2\sqrt{\mathcal{C}}}{1+\mathcal{C}} a_{\text{in}}^0 e^{i\phi} \right) e^{-i\omega_{\text{IF}} t} \\
&= \left(\sin(\theta) b_{\text{in}}^0 + i \cos(\theta) a_{\text{in}}^0 e^{i\phi} \right) e^{-i\omega_{\text{IF}} t}
\end{aligned}
\tag{2.45}
$$

with $\mathcal{C}$ the cooperativity introduced previously, $\mathrm{p} = |\mathrm{p}|e^{i\phi}$, and $\theta = \arctan(-2\sqrt{\mathcal{C}}/(1 - \mathcal{C}))$. In general the output field in b contains both the contributions of a_{in} and b_{in}, meaning that information is reflected in the process. However at the critical point $\mathcal{C} = 1$, frequency conversion is lossless as b_{out} resumes to $a_{\mathrm{in}}^0 e^{-i\omega_{\mathrm{IF}}t}$. For this reason it is fundamentally different than optical heterodyne detection and phase-preserving amplification, where one could not spare the expense of adding an extra-mode. Note that in this model, the sideband at $2\omega - \omega_{\mathrm{IF}}$ is absent. It corresponds to the terms $ab^{\dagger}c + a^{\dagger}bc^{\dagger}$ in the original Hamiltonian, that have been left out of the study since we where considering a resonance mode b at ω_{IF}. If conversion is performed with traveling waves, as it is the case with classical frequency conversion, all the frequencies are possible for b and we have to take the upper sideband into account.

2.3.5 Field digitization

Following down-conversion the voltage is digitized and generates a numerical signal. We consider here that the LO phase has been fixed to $\phi = 0$. Digitalization returns an array

$$s[n] = s_0\Big((X_a + X_h)\cos(\omega_{\mathrm{IF}}n\Delta t) + (P_a + P_h)\sin(\omega_{\mathrm{IF}}n\Delta t)\Big) \tag{2.46}$$

with Δt the sampling period (the interval between two time bins) and n the position of the bin. The two quadratures are finally extracted by numerical demodulation over the total number N_0 of bins during the acquisition

$$\begin{cases} I &= \frac{2}{N_0}\sum_{n=1}^{N_0} s[n]\cos(n\omega_{\mathrm{IF}}\Delta t) \\ Q &= \frac{2}{N_0}\sum_{n=1}^{N_0} s[n]\sin(n\omega_{\mathrm{IF}}\Delta t) \end{cases}$$
$$\Leftrightarrow \tag{2.47}$$
$$\begin{cases} I &= s_0(X_a + X_h) \\ Q &= s_0(P_a + P_h) \end{cases}.$$

We get a result very similar to optical heterodyne measurement in Eq. (2.32). Here, h represents the modes added by the chain of phase-preserving amplification and down-conversion.
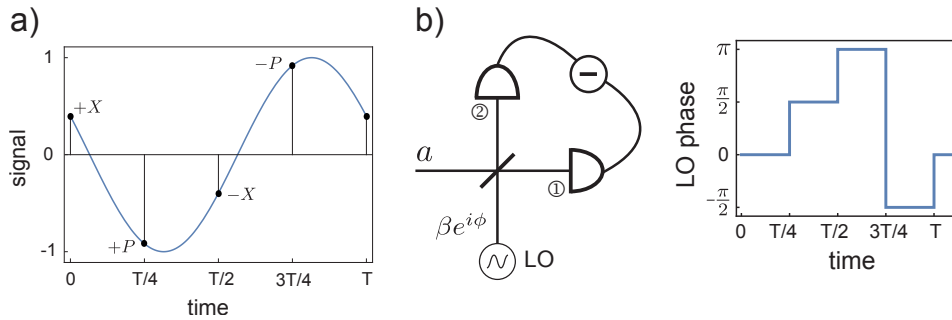
Figure 2.11: Field digitization and Heisenberg principle: a) the continuous voltage (blue) is digitized every fourth a signal period T (black dots) and results in alternative measurements of X and P. It is would be equivalent to b) optical homodyne detection with the LO phase varying in time steps.

Now, if we imagine an experimental setup where the field is digitized at low temperature and high frequency, there would be no need for amplification nor down-conversion, and it seems that digitization would allow one to measure simultaneously X and P without loss of information, in clear violation of the Heisenberg principle. This apparent paradox fades out when we take into account the generation of the numerical signal. According to the Nyquist-Shannon sampling theorem, to reconstruct the amplitude and the phase of the incoming voltage with a full precision we need to digitize it at a sampling frequency at least equal to four times the signal frequency $\Delta t = 1/(8\pi\omega_{\mathrm{IF}})$ (assuming there is no other signal at a higher frequency), as represented in Fig. 2.11. If we suppose that the first point is taken at $t = 0$, then we would get the following numerical signal during a period

$$
\begin{aligned}
s[0] &= s_0 X \\
s[1] &= s_0 P \\
s[2] &= -s_0 X \\
s[3] &= -s_0 P \; .
\end{aligned}
\tag{2.48}
$$

The results of digitization hence return an ouput alternatively proportional to X or P. Therefore we only get information about a quadrature during half of the measurement time, and recover the limit set on the measurement by the Heisenberg principle. Optically, this is equivalent to the situation showed in Fig. 2.11b), a homodyne measurement where the phase of the local oscillator is changed periodically. This is another way of performing heterodyne detection, but in this case the separation between the two quadratures is made in time instead of spatially.

2.4 PHOTON NUMBER MEASUREMENT WITH LINEAR DETECTORS

It is clear at this point of our study that field digitization naturally provides the field quadratures while optics offers both the possibilities of measuring the number of photons contained in the field and its quadratures by homodyne or heterodyne detection. We show in this section how the knowledge of the statistics of the quadratures in heterodyne detection allows to measure the photon number, and discuss the limits of this method.

2.4.1 *Measurement output distribution function*

We consider here the canonical situation of microwave heterodyne detection, where the field of interest undergoes phase-preserving amplification followed by a classical amplification chain, down-conversion and digitization at room temperature. As already done earlier, let us label a the annihilation operator of the mode that contains the quantum information that we want to measure. The joint effects of losses, noise added by the amplification chain and temperature can be represented by a single noise mode h in a thermal state. In reality, there may be many modes that couple to a but a single one coming for an unbalanced beamsplitter can be used effectively to capture the total effect of the added noise. We hence record a field corresponding to the following operator [89, 90]

$$
S = \sqrt{G}a + \sqrt{G-1}h^\dagger \underset{G\gg 1}{\approx} \sqrt{G}(a + h^\dagger)
\tag{2.49}
$$

where this time G denotes the gain of the total amplification chain. The choice to use $h^\dagger$ instead of h is a pure convention leading to recover easily the case of ideal phase-preserving amplification given by Eq. (2.34). The field S is entirely determined by one of his quasiprobability distributions in the (X_S, P_S) plane, in the sense that for one choice of distribution, there exist an isomorphism between this distribution and the ensemble of quantum states. Thus all the quasiprobability distributions are related to each other by a unique mathematical transformation. However this does not mean that all the experimental setups provide the same link to the quasiprobability distributions. For heterodyne detection the two quadratures are recorded at the same time. The same experiment is repeated $N \gg 1$ times and we label $(I^{(n)}, Q^{(n)})$ the measurement outcomes of the n-th experiment given by Eq. (2.47)[6]. The histogram of the measurement outcomes $I^{(n)} + iQ^{(n)}$ converges towards the probability to get a point $\alpha \in \mathbb{C}$ in phase space. For a linear oscillator in a state ρ this probability is directly given by the Husimi Q-function [70]

$$D^{[\rho]}(\alpha) = Q(\alpha) = \frac{1}{\pi}\langle\alpha|\rho|\alpha\rangle \ . \tag{2.50}$$

Since S is the sum of two independent contributions the Q-function of S is given by the convolution of the distributions of a and $h^\dagger$. Since here h is in a thermal state, it reads [91]

$$D_S^{[\rho]}(\alpha) = Q_S(\alpha) = \frac{1}{G}\int_{\mathbb{C}} Q_a(\alpha/\sqrt{G} - \beta^*)P_h(\beta^*)\mathrm{d}^2\beta \tag{2.51}$$

with P_h the Glauber-Sudarshan P-representation defined so that the density matrix ρ_h of h is given by $\rho_h = \int_{\mathbb{C}} P_h(\beta)|\beta\rangle\langle\beta|\mathrm{d}^2\beta$. Writing n_{th} the number of thermal photons in h, the distribution fonction of the measurement is finally

$$D_S^{[\rho]}(\alpha) = \frac{1}{\pi n_{\mathrm{th}}G}\int_{\mathbb{C}} Q_a(\alpha/\sqrt{G} - \beta^*)e^{-|\beta|^2/n_{\mathrm{th}}}\mathrm{d}^2\beta \ . \tag{2.52}$$

The interpretation of this equation is straightforward: the information contained in the field a is blurred by the (possibly large) thermal fluctuations of the added field h. Yet if one knows the number of thermal photons added in the measurement process it becomes possible to deconvolute the two distributions, and hence to reconstruct the state of the mode a. Practically, it has been proposed to perform a Maximum Likehood reconstruction of the density matrix of a in presence of noise [89]. Another option is to use a calibration measurement where a is in vacuum to deconvolute the outcome distribution and extract P_h, and then use this knowledge to extract Q_a [92].

2.4.2 Measurement records: field measurement, power measurement

If it is possible to reconstruct the whole density matrix of a from the measurement histograms, such a task is not always necessary. For instance, when we measure the fluorescence of a qubit, we might be interested only by the emitted field amplitude $\langle a \rangle$ or the emitted energy $\langle a^\dagger a \rangle$. In that case, knowing the first two cumulants of the

---

6 In microwave language we use the in-phase $I \leftrightarrow X$ and in-quadrature $Q \leftrightarrow P$ outcomes.

distribution of the outcome is enough. Taking into account the fact that $\langle h^\dagger \rangle = 0$ we obtain

$$
\boxed{
\begin{aligned}
\langle a \rangle = \frac{1}{\sqrt{G}} \langle S \rangle &= \frac{1}{\sqrt{G}} \int_{\mathbb{C}} \alpha D_S^{[\rho]}(\alpha) \mathrm{d}^2\alpha \\
&= \frac{1}{\sqrt{G}} \, \overline{I + iQ}
\end{aligned}
}
\tag{2.53}
$$

where $\overline{I + iQ} = \frac{1}{N} \sum_{n=1}^{N} I^{(n)} + iQ^{(n)}$ is the mean value of the measurement outcomes. As we would expect, the thermal fluctuations vanish when we take the average of the measurements and we recover the mean value of a up to the linear gain of the chain. The case of the measurement of the number of photons is a bit less obvious. If we compute the energy contained in S we find

$$
\langle S^\dagger S \rangle = G \left(\langle a^\dagger a \rangle + \langle hh^\dagger \rangle + \langle a^\dagger h^\dagger + ha \rangle \right) .
\tag{2.54}
$$

If the noise a and the noise h are uncorrelated then $\langle ha \rangle = \langle h \rangle \langle a \rangle = 0$ and the last term of the previous equation is zero. However there is a non-zero contribution due to the noise h, because we directly measure the number of thermal photons n_{th} added to the signal. With that, we find

$$
\boxed{
\begin{aligned}
\langle a^\dagger a \rangle = \frac{1}{G} \langle S^\dagger S \rangle - n_{\mathrm{th}} &= \frac{1}{G} \int_{\mathbb{C}} |\alpha|^2 D_S^{[\rho]}(\alpha) \mathrm{d}^2\alpha - n_{\mathrm{th}} \\
&= \frac{1}{G} \, \overline{I^2 + Q^2} - n_{\mathrm{th}} .
\end{aligned}
}
\tag{2.55}
$$

In practice it is a simple task to get rid of the offset term due to n_{th}: it only causes an offset that can be determined by a calibration experiment where a is set in vacuum. The two results provided by Eq. (2.53) and (2.55) are remarkable: with the same measurement setup and the same measurement records it is possible to measure the mean values of two different operators, just by changing the way the records are averaged. However this data treatment to get the photon number is only possible on average: even if the measurement was perfect we could not build a single-shot photodetector this way, because the Heisenberg limit on the two quadratures automatically induces an indeterminacy on the reconstructed number of photons.

2.5 PURCELL RATE MEASUREMENT

We have seen in the input-output relations that the fluorescence emitted by a qubit in a line depends on its effective coupling rate Γ_a to the line a, called the Purcell rate. Since the qubit is coupled to other loss channels such as dielectric loss, quasiparticle loss, or emission towards other ports, the Purcell rate is always smaller than the total qubit decay rate Γ_1. In most fluorescence measurement experiments it is crucial to maximize the ratio Γ_a/Γ_1, as it represents the amount of information emitted by the qubit into the line during its decay, and that can be theoretically recovered by a measurement apparatus. For instance, the ratio Γ_a/Γ_1 limits the total quantum efficiency in the reconstruction of quantum trajectories based on fluorescence [34, 59, 93]. With a given design, it should be possible to compute the Purcell rate theoretically. For a superconducting transmon dispersively coupled to a single cavity mode, it is for instance given

by $\Gamma_a = \kappa_a \frac{g^2}{\Delta^2}$ with κ_a the cavity coupling rate to the line, g the qubit-cavity coupling rate, and Δ the qubit-cavity detuning. Unfortunately this relation has been shown to be inaccurate [34, 94]. It is therefore important to be able to determine experimentally the value of this ratio, but such a task can prove itself challenging. A possibility is to rely on spectroscopy measurement, where the reflection coefficient of light on a qubit is measured as a function of frequency. The problem is that the qubit linewidth is given by the total dephasing rate $\Gamma_2 = \Gamma_1/2 + \Gamma_\varphi$ as defined in Eq. (2.13), and not by Γ_a. It gives the Purcell rate only is we can assume that it is much larger than other known dephasing and decay processes and hence write $\Gamma_2 \approx \Gamma_a/2$. We will use and study this approach more carefully in Chap. 4. In this section, we present a method to determine the Purcell rate with a good accuracy, based on the measurement of the photon rate emitted by a qubit under two resonant drives in phase. Interestingly, this approach only works when measuring the photon rate and not the field amplitude, and illustrates the fundamental difference between the two measurements.

2.5.1 *Principle*

We use the two-port measurement previously studied and represented Fig. 2.5, but this time the two drives are applied simultaneously and in phase. According to Eq. (2.23), the Rabi frequency Ω is thus simply

$$\Omega = \sqrt{\Gamma_a}\alpha_{\text{in}} + \sqrt{\Gamma_b}\beta_{\text{in}} \ . \tag{2.56}$$

We vary α_{in} from 0 to a maximal value and keep β_{in} constant so that $\Omega_{\text{min}} = \sqrt{\Gamma_b}\beta_{\text{in}} \gg \Gamma_1, \Gamma_2$. With that condition fulfilled we ensure that the qubit always undergoes Rabi oscillations described by Eq. (2.18). The rate of photons emitted into a is given by Eq. (2.26). Combining the two yields

$$\langle a_{\text{out}}^\dagger a_{\text{out}}\rangle(t) = \langle \sigma_z^0\rangle\Big(\frac{\Gamma_a}{2}\cos(\Omega t) + \sqrt{\Gamma_a}\alpha_{\text{in}}\sin(\Omega t)\Big)e^{-\Gamma_R t} + C_{\text{P}} \ . \tag{2.57}$$

We only kept the explicit time dependence of the photon rate and put all the constant terms into C_{P}. We use a strongly asymmetric cavity that is widely open towards a so that $\Gamma_a \gg \Gamma_b$ and most of the fluorescence is emitted in a. The signal is amplified using a JPC followed by a classical amplification chain, down-converted and digitized to obtain time-resolved measurement records $(I(t), Q(t))$ with a timestep $\mathrm{d}t$ between two records. According to Eq. (2.55) we get

$$\begin{aligned}
\overline{I(^2(t) + Q^2(t))} &= G_{\text{P}}\langle a_{\text{out}}^\dagger a_{\text{out}}\rangle(t) + \frac{n_{\text{th}}}{\mathrm{d}t} \\
&= G_{\text{P}}\langle \sigma_z^0\rangle\Big(\frac{\Gamma_a}{2}\cos(\Omega t) + \sqrt{\Gamma_a}\alpha_{\text{in}}\sin(\Omega t)\Big)e^{-\Gamma_R t} + \text{offset}
\end{aligned} \tag{2.58}$$

with G_{P} the total gain of the amplification chain. The photon number measurement thus exhibits oscillations of amplitude

$$\boxed{\mathcal{A}(\alpha_{\text{in}}) = G_{\text{P}}|\langle \sigma_z\rangle^0|\sqrt{\frac{\Gamma_a^2}{4} + \Gamma_a\alpha_{\text{in}}^2}} \ . \tag{2.59}$$

The measurement of Ω as a function of α_{in} gives the proportionality factor between the experimental drive amplitude (in arbitrary units) and $\sqrt{\Gamma_a}\alpha_{\text{in}}$. The determination of Γ_a, the Purcell rate of the qubit towards a is then straightforward: by varying the drive

amplitude through a, we vary the amplitude of the photon rate oscillations, allowing us to deduce the Purcell rate unambiguously. Physically, this corresponds to changing the signal from a situation where the photon number is dominated by spontaneous emission (for $\sqrt{\Gamma_a}\alpha_{\text{in}} \ll \Gamma_a$) to the one where the stimulated emission term takes over (for $\sqrt{\Gamma_a}\alpha_{\text{in}} \gg \Gamma_a$). Interestingly there is no need to know the qubit temperature to get the Purcell rate, as it only generates a scaling factor like the gain.

2.5.2   *Experimental measurement*
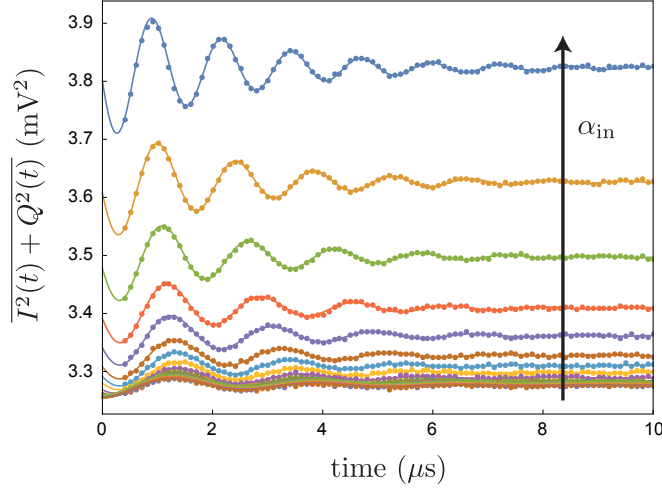
Figure 2.12: Experimental measurement of the photon rate emitted by a qubit under two drives (one in reflection and one in transmission) in phase. The points are the experimental data with a timestep of 100 ns and the plain line is the fit by a cosine of varying phase and amplitude decreasing at $\Gamma_R = (2.32\ \mu s)^{-1}$. The error bars have the same size as the data points, or smaller. The amplitude of the drive in reflection α_{in} is varied from 0 to a maximal value by the voltage x of an arbitrary waveform generator and is only known up to a scaling factor as this point of the study.

For this experiment we used a transmon qubit embedded in a far-detuned aluminum 3D-cavity. Here the cavity only effect is that it acts as a filter of the electromagnetic noise at qubit frequency, and can be left out of the study to only keep the effective coupling rates of the qubit towards lines a and b. The qubit frequency is $f_q = 7.09$ GHz, its lifetime is $T_1 = (\Gamma_1)^{-1} = 1.95\ \mu s$ and its coherence time is $T_2 = (\Gamma_2)^{-1} = 2.88\ \mu s$. To avoid any distortion of the signal by the amplification chain, we need to have the JPC bandwidth larger than the maximal Rabi frequency. We set it at 5 MHz, with a gain $G_{\text{JPC}} = 26$ dB. We down-convert the signal to $f_{\text{mod}} = 200$ MHz and demodulate it to get the measurement records $(I(t), Q(t))$ with a time resolution of 100 ns. The average of $I^2 + Q^2$ over 4×10^6 realizations is represented in Fig. 2.12 for various values of α_{in}. Even when $\alpha_{\text{in}} = 0$ the oscillations are offset from zero because of the many thermal photons in the signal. In fact if we compare the offset of the oscillations and their amplitude at $\alpha_{\text{in}} = 0$, we find than the number of thermal photons is roughly 150 times larger than the number of photons emitted by the qubit by spontaneous emission. Each experimental curve is fitted by a sine wave of various amplitude and phase and exponentially decreasing at $\Gamma_R = (2.32\ \mu s)^{-1}$, given by the independent

measurements of Γ_1 and Γ_2. The phase of the oscillations does not quite follow the theoretical prediction that we would expect from Eq. (2.58), because of a small delay between the two drives. This does not affect our conclusions for this measurement, as we are interested in the frequency and amplitude of the oscillations only.

The evolution of the Rabi frequency Ω with the drive amplitude is represented in Fig. 2.13a). We fit its evolution by a simple affine function $c\,x + d$ with x the voltage of a waveform generator used to vary the drive amplitude , so that we get simply $d = \sqrt{\Gamma_b}\beta_{\text{in}}$ and $c\,x = \sqrt{\Gamma_a}\alpha_{\text{in}}$. With that we can display the evolution of the photon rate oscillations amplitude $\mathcal{A}$ with $\sqrt{\Gamma_a}\alpha_{\text{in}} = c\,x$, represented in Fig. 2.13b). It is fitted according to Eq. (2.59) with two fit parameters: the global conversion factor $G_{\text{P}}\langle\sigma_z\rangle^0$ and the Purcell rate Γ_a. We find

$$\Gamma_a = 0.88\Gamma_1 \ , \tag{2.60}$$

meaning that for this particular experiment the decay of the qubit is indeed dominated by radiation towards the transmission line a. The good agreement between the theoretical prediction for the photon rate amplitude and the experimental data validates our use of the approximate expressions of $\langle\sigma_{x,z}\rangle(t)$ given by Eq. (2.18) for the Rabi oscillations instead of the exact solutions.
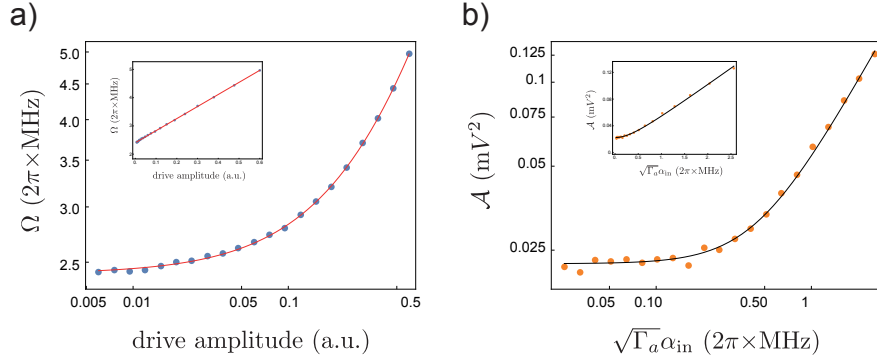
Figure 2.13: Purcell rate determination by photon rate measurement. a) Rabi frequency as a function of the drive amplitude control x (log scale, linear scale in inset). The points represent the data and the line a linear fit $\Omega = cx + d$ giving $\Gamma_b\beta_{\text{in}} = 2.4$ ($2\pi\times$MHz) and $c = 4.27$ ($2\pi\times$MHz). b) Amplitude of the oscillations of the photon rate measured in a as a function of the drive amplitude (log scale, linear scale in inset). The points represent the data and the line the theory of Eq. (2.59) where $\Gamma_a = 0.88\Gamma_1$ was fitted to match the experimental results.

2.6 TEMPERATURE AND SPURIOUS REFLECTIONS MEASUREMENT

In the previous measurement we determined the Purcell rate without ambiguity, but the gain of the amplification chain was only known up to a scaling factor given by the thermal equilibrium of the qubit. If it is in equilibrium at temperature T the excited state is occupied with a probability $P_{\text{eq}} = 1/(1 + e^{\hbar\omega_q/k_B T})$ with ω_q the qubit frequency. This reduces the contrast of Rabi oscillations by a factor $|\langle\sigma_z\rangle^0| = 1 - 2P_{\text{eq}}$. When one only has access to values averaged over many realizations and no single-shot measurements are possible, it is not trivial to determine with precision the temperature of a quantum system. The reason is that in general we capture signals that

are proportional to the population in a given state but the conversion factor between the two is unknown. In this section we present a new method to measure the temperature of a qubit using fluorescence measurements only. We base the study on the comparison between the amplitude of Rabi oscillations in reflection and the amount of reflected drive. For the study to be complete we need to suppose that there might be unwanted spurious reflections between the cavity and the measurement setup. As we will see, the original method we introduce here calibrates with certainty the amount of spurious reflections and the qubit temperature.

2.6.1 *Fluorescence field and photons in presence of parasitic reflections*

We have to be careful in the way we introduce the reflections in our model. If they happen sufficiently close to the quantum system then they coherently affect the amount of stimulated emission emitted by the qubit, because they coherently interfere with the fluorescence field emitted by the qubit. In other words we would sum the operators, compute the photon rate, and then take the expectation values in a process similar to the derivation done in 2.2. However if they happen in the classical domain, for instance at the point where the signals are demodulated, then they do not affect the radiation emitted by the qubit and we must sum the mean values of the field and of the number of photons. In our experimental setup the vast majority of spurious reflections comes for the modulation / demodulation setup at room temperature and therefore corresponds to the second situation. We model the presence of spurious reflections by an additional term $r\alpha_{\text{in}}$ in the mean value of the reflected field, with $r \in \mathbb{C}$. The fact that r is complex takes into account the dephasing due to propagation between the drive reflected on the cavity and the sum of the parasitic reflections. Under these assumptions the fluorescence field reads

$$\langle a_{\text{out}} \rangle = \alpha_{\text{in}} - \sqrt{\Gamma_a}\langle \sigma_- \rangle + r\alpha_{\text{in}} = (1+r)\alpha_{\text{in}} - \sqrt{\Gamma_a}\langle \sigma_- \rangle \ . \tag{2.61}$$

For the photon rate we need to add the number of photons due to these reflections and we obtain

$$\langle a_{\text{out}}^{\dagger} a_{\text{out}} \rangle = |1+r|^2 \alpha_{\text{in}}^2 + \Gamma_a \frac{1 + \langle \sigma_z \rangle}{2} - \sqrt{\Gamma_a}\alpha_{\text{in}}\langle \sigma_x \rangle \ . \tag{2.62}$$

The central idea of this method lies upon the fact that the contrast of the Rabi oscillations of the qubit is given by the equilibrium state $|\langle \sigma_z \rangle^0|$ for both the measurements of the field and photon rate, while the offset due to the reflected drive scales with the amplitude either with the factor $(1+r)$ in the case of field amplitude measurement or with the factor $|1+r|^2$ in the case of a photon rate measurement. The comparison of the two allows to deduce both r and $\langle \sigma_z \rangle^0$. Similarly to the Purcell rate measurement in 2.5, we drive the qubit with two drives in phase and measure simultaneously the average values $\overline{I + iQ} = \sqrt{G_{\text{lin}}}\langle a_{\text{out}} \rangle$ and $\overline{I^2 + Q^2} = G_{\text{P}}\langle a_{\text{out}}^{\dagger} a_{\text{out}} \rangle + n_{\text{th}}/\text{d}t$. We use two different factors G_{lin} and G_{P} for the effective gain when measuring the field or the power because of the presence of phase drifts between the different realizations. The qubit undergoes underdamped Rabi oscillations due to the drives that we measure in two different ways. With Eq. (2.18) we obtain the amplitude of the oscillations $\mathcal{A}_{\text{lin}}$ that we measure for the fluorescence field

$$\mathcal{A}_{\text{lin}} = \sqrt{G_{\text{lin}}}|\langle \sigma_z \rangle^0| \frac{\sqrt{\Gamma_a}}{2} \ . \tag{2.63}$$

The amplitude $\mathcal{A}_{\mathrm{P}}$ of the oscillations measured with the photon rate has already been computed and is given by Eq. (2.59). The oscillations happen on top of a constant term C_{lin} or C_{P} due to the total reflected drives and the final steady-state of the qubit. In the limit of large Rabi frequencie(s Ω we have $z_\infty \propto \Omega^{-2}$ while $x_\infty \propto \Omega^{-1}$ according to Eq. (2.14). Therefore in the regime of parameters used for this measurement we have $z_\infty \ll 1$ but x_∞ is not always negligible and needs to be kept in the expression of the constants. They read

$$
\begin{aligned}
C_{\mathrm{lin}} &= \sqrt{G_{\mathrm{lin}}}\Big((1+r)\alpha_{\mathrm{in}} - \frac{\sqrt{\Gamma_a}}{2}x_\infty\Big) \\
C_{\mathrm{P}} &= G_{\mathrm{P}}\Big(|1+r|^2\alpha_{\mathrm{in}}^2 - \sqrt{\Gamma_a}\alpha_{\mathrm{in}}x_\infty\Big) + n_{\mathrm{th}} \ .
\end{aligned}
\tag{2.64}
$$

Thanks to the previous measurement we know the value of the Purcell rate Γ_a. With it and using the evolution of the Rabi frequency with the drive amplitude we also know the factor between the drive amplitude set experimentally and α_{in}. The determination of the amplitudes and constants of the Rabi oscillations therefore gives access to $\sqrt{G_{\mathrm{lin}}}|\langle\sigma_z\rangle^0|$ and $\sqrt{G_{\mathrm{lin}}}(1+r)$ for the field measurement, and $G_{\mathrm{P}}|\langle\sigma_z\rangle^0|$ and $G_{\mathrm{P}}|1+r|^2$ for the photon rate measurement. We introduce the ratios of the constants by the amplitudes

$$
R_{\mathrm{lin}} = \frac{\sqrt{G_{\mathrm{lin}}}|1+r|}{\sqrt{G_{\mathrm{lin}}}|\langle\sigma_z\rangle^0|} = \frac{|1+r|}{|\langle\sigma_z\rangle^0|}
$$

$$
R_{\mathrm{P}} = \frac{G_{\mathrm{P}}|1+r|^2}{G_{\mathrm{P}}|\langle\sigma_z\rangle^0|} = \frac{|1+r|^2}{|\langle\sigma_z\rangle^0|} \ .
\tag{2.65}
$$

With the ratios we removed the explicit dependence with the linear and power gains, and we can easily compute the temperature and amount of reflections with

$$
\boxed{
\begin{cases}
|1+r| &= R_{\mathrm{P}}/R_{\mathrm{lin}} \\
|\langle\sigma_z\rangle^0| &= R_{\mathrm{P}}/R_{\mathrm{lin}}^2
\end{cases}
}
\ .
\tag{2.66}
$$

2.6.2 Experimental results

We use the same measurement records as for the Purcell rate determination. The data are rotated in the complex plane so that $\overline{I} \propto \mathrm{Re}(\langle a_{\mathrm{out}}\rangle)$. The time evolutions of $\overline{I}$ and $\overline{Q}$ are represented in Fig. 2.14. The comparison with the photon rate measurement displayed in Fig. 2.12 exhibits a clear difference in the amplitude of the oscillations. The amplitude of the oscillations of $\overline{I(t)}$ is constant and does not depend on α_{in}, only the frequency changes. On the other hand, $\overline{Q}$ is constant. All the oscillations are fitted with the same amplitude and decay time, giving immediately the factor $\sqrt{G_{\mathrm{lin}}}|\langle\sigma_z\rangle^0|$. The constant parts of the curves of $\overline{I}$ and $\overline{Q}$ correspond to respectively the real and imaginary parts of $\mathcal{C}_{\mathrm{lin}}$.

We represent the evolution of the offsets $\mathrm{Re}(\mathcal{C}_{\mathrm{lin}})$, $\mathrm{Im}(\mathcal{C}_{\mathrm{lin}})$ and $\mathcal{C}_{\mathrm{P}}$ as a function of respectively α_{in} and α_{in}^2 in Fig. 2.15. Each curve can be approximated by a slope and is hence fitted by an affine function to extract the coefficients $\sqrt{G_{\mathrm{lin}}}|1+r|$ and $G_{\mathrm{P}}|1+r|^2$. The presence of the steady-state value $x_\infty(\alpha_{\mathrm{in}})$ in the offset expressions of Eq. (2.64) means that the offsets do not exactly scale linearly with the drive amplitude. In practice it induces an error of no more than 2% on the determination of the slope.
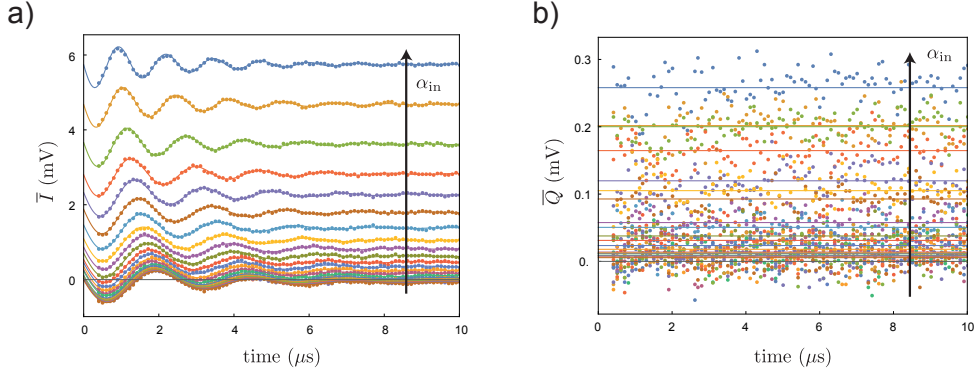
Figure 2.14: a) Real and b) imaginary parts of the fluorescence field emitted by a qubit undergoing Rabi oscillations due to two drives in phase where we sweep the amplitude of the drive in reflection α_{in}. The oscillations are fitted by an exponentially decreasing sine wave of constant amplitude and decay time (plain line) and give $\sqrt{G_{\mathrm{lin}}}|\langle\sigma_z\rangle^0| = 2.10 \ \mathrm{mV}\sqrt{2\pi \times \mathrm{MHz}}^{-1}$. The imaginary part is constant and corresponds to the imaginary part of the spurious reflections. Lines are the average of $\bar{Q}$ on time.

With the linear fit we can now deduce the ratios R_{lin} and R_{P}. We find $R_{\mathrm{lin}} = 1.48$ and $R_{\mathrm{P}} = 1.51$ and deduce the equilibrium state of the qubit and the amount of parasitic reflections

$$
\begin{aligned}
|1 + r| &= 1.02 \pm 0.02 \\
|\langle\sigma_z\rangle^0| &= 0.69 \pm 0.02 \ .
\end{aligned}
\tag{2.67}
$$

The uncertainty of this measurement comes mostly from the error made in approximating $\mathcal{C}_{\mathrm{lin}}$ and $\mathcal{C}_{\mathrm{P}}$ by a linear function of respectively α_{in} and α_{in}^2. Note that this error can be arbitrarily suppressed by using a higher amplitude for the drive used in transmission. It would strongly reduce the value of x_∞ and hence its contribution in the offsets. The probability of excited state at thermal equilibrium measured with this method is $P_e^{\mathrm{eq}} = (1 - |\langle\sigma_z\rangle^0|)/2 = 16\%$ corresponding to a temperature $T = 205$ mK. We also notice that the parasitic reflections measured by this method do not exceed 4% of the total reflected signal.
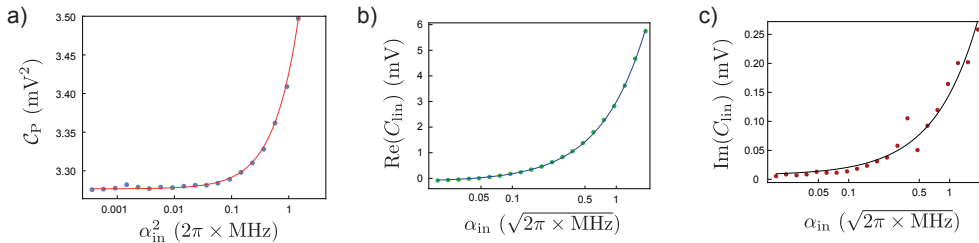
Figure 2.15: Offsets of time-resolved fluorescence measurements. a) Evolution of the offset of the photon number measurement C_P with the reflection drive α_{in}^2, (points) experimental data and (line) approximation of the theoretical amplitude of Eq. (2.64) by the affine function $C_P = G_P|1+r|^2\alpha_{\mathrm{in}}^2 + \mathrm{cst}$ with $G_P|1+r|^2 = 0.15 \ \mathrm{mV}^2(2\pi\times\mathrm{MHz})^{-1}$. b) and c) Evolution of the field amplitude offset C_{lin} with α_{in}. Similarly the data (point) are reproduced by the theory (line) coming from Eq. (2.64) with $\sqrt{G_{\mathrm{lin}}}(1+r) = 3.11 + 0.14i \ \mathrm{mV}\sqrt{2\pi\times\mathrm{MHz}}^{-1}$.

2.6.3 *Comparison with independent temperature measurements*

The result for the qubit temperature found with this fluorescence-based method is in clear contradiction with independent measurements conducted on the same system during the same experimental run, with an identical modulation and demodulation setup, and presented in Chap. 7. When comparing the contrast of Rabi oscillations of the qubit between the first and the second excited states $|e\rangle$ and $|f\rangle$, we find that P_e^{eq} should not exceed 5% (see Sec. 7.2.2), while the previous fluorescence method yields $P_e^{\mathrm{eq}} = 16\%$. This is reinforced by the spectroscopy of the qubit that does not exhibit a line at $f_c - \chi$ hence indicating that the residual qubit excitation at thermal equilibrium is small.

If we decide to take the independent temperature measurement for granted and use it to deduce the amount of spurious reflections in the system, we hit two major issues. First, the quantity of parasitic reflections would not be the same whether we base our study on the fluorescence field or on the photon rate. Second, if we use the fluorescence field, we find about 47% of extra reflections *in phase* with the drive. Such a possibility is extremely unlikely. For instance, if we imagine that most of the reflections comes from a sideband, there is no reason for it to be in phase with the signal.

The reason why we deduce a higher temperature from the fluorescence measurement is that we measure Rabi oscillations with a smaller amplitude than expected from independent temperature measurements. We hence identify two possible explanations for this discrepancy:

- there was a mistake in the determination of the Rabi oscillation amplitudes;

- the qubit was indeed warmer when we performed the fluorescence measurement.

For the first reason we could invoque that we used a detuned drive and hence got a smaller amplitude for the Rabi oscillations. The qubit frequency is measured using Ramsey oscillations and is found stable below the MHz. With the range of Rabi frequency used in the previous method, a detuning of less than a MHz cannot induce a loss of contrast of about 10%. Moreover in presence of a large detuning we should expect to see a clear dependence of the amplitude of the field oscillations with the drive amplitude while in our measurement this amplitude is constant (see Fig. 2.14a)). Another possibility would be an error in the determination of the initial time of the oscillations. Indeed, since the Rabi oscillations are damped with a rate Γ_R, it is crucial to know with precision the initial time to get the amplitude right. In practice we look at the instant where the reflected drive is detected. It is typically a step with a width of about 200 ns due to filtering of the experimental setup. If we take the step width as the error for the initial time (which is a large estimation), we find that the lowest value for P_e^{eq} is 11%, still above the independent measurements.

The second reason if of different nature. Since we find two different temperatures with no apparent mistake in the measurements, then there are indeed two temperatures. All the problem here is to understand why. One could argue that the qubit is driven for quite a long time and does not have time to fully relax between two consecutive measurements. If we indeed drive the qubit for 15 μs, we then let it relax during 30 μs, a duration more than ten times larger than the qubit lifetime. Since we use the same room temperature setup for all the measurements during the same experimental run, we must evacuate the possible leakage of the LO or of mixers sidebands that would warm up the qubit. The only difference between the experiments is that the AWG

channel corresponding to the drive sent in reflection was physically turned off during the measurements giving a low temperature. Even when supposed to output a null voltage we noted that the channel has a small residual signal at 1 GHz corresponding to its numerical time resolution. However it remains very unlikely that this small signal could, after modulation, excite the qubit enough to explain the temperature difference.

In conclusion at this point of the study and in the absence of additional measurements we cannot explain why we see this discrepancy. In the following we therefore have a choice to make, trusting one measurement or the other. We choose to set the qubit temperature at the one measured independently. It has been measured in different ways, at different moments of the experiment and stays consistent. This point of view corresponds to stating that the reconstruction of the fluorescence signal is imperfect but is enough to deduce the signal that is really emitted by the qubit in the line. Even though this choice is problematic in terms of the reflected drive in the fluorescence signals, we can easily take out this issue by manually subtracting the "excess" reflected drive.

2.7 CONCLUSION

The expression of the fluorescence field amplitude and photon rate in the input-output formalism allowed us to define the time-resolved expressions of spontaneous and stimulated emission. Based on linear detectors and amplification at the quantum limit we were able to reconstruct the evolution of both the field amplitude and the photon rate in time from the measurement records. This reconstruction is validated by driving the qubit either in transmission or in reflection. While the transmitted and reflected field amplitudes are similar up to a constant corresponding to the reflected drive, the photon rates differ strongly, as the transmitted field only contains spontaneous emission while the reflected one contains spontaneous and stimulated emission. We use these measurements to measure the Purcell rate of the qubit to the line and the temperature of the qubit. Our ability to track in time the energy exchanges between the qubit and an external drive opens the way to measuring the residual entanglement between the qubit and the drive when the latter prepares the former in a quantum superposition.

The main results of this chapter are the following

- expression of the fluorescence field amplitude and photon rate in time using the input-output formalism, Eq. (2.19) and (2.26)

- reconstruction of the field amplitude and photon rate from the measurement records of heterodyne detection, Eq. (2.53) and (2.55)

- time-resolved measurement of spontaneous and stimulated emission, Fig. 2.6

- Purcell rate measurement using fluorescence, Fig. 2.13

- Qubit temperature and spurious reflections measurement using fluorescence, Fig. 2.15

POWER TRANSFER CONTROLLED BY THE PHASE OF A QUANTUM SUPERPOSITION

The rising interest for quantum thermodynamics puts the exchanges of energy and information between quantum systems and their environment at the center of attention [95]. Most of quantum physics experiments use classical controls such as light pulses to manipulate the state of quantum objects and generate non-classical states of matter. The attempts to identify and use quantum resources reverses this point of view. In particular we can ask the question: Can we can conceive machines whose power flows are linked to non-classical properties? Recent experiments on quantum routing have shown that quantum systems like atoms can be used to efficiently direct photons in a network, either by using dark and bright states [96] or interferences generated by light scattering on the atom [97, 98]. However these experiments rely on classical controls like the initial state of the atom or a voltage dictating the artificial atom's frequency. In this chapter, we present the experimental realization of a power transfer between two spatially separated drives where the direction of the transfer is set by the phase of a quantum superposition. The qubit acts as a pump of power from one drive to the other and does so depending on the phase of the superposition. This is in contrast with heat flows depending on superconducting phase difference between electrodes of a junction [99]. We demonstrate that we can control the direction of transfer by changing the phase of the superposition, define a transfer efficiency to quantify the quality of the transfer and study its evolution with the drive amplitudes and the qubit initial state.

3.1 PHOTON ROUTING BY STIMULATED EMISSION AND INTERFERENCE

3.1.1 *Principle*

A qubit symmetrically coupled to two transmission lines a and b ($\Gamma_a = \Gamma_b = \Gamma$) spontaneously emits the same fluorescence field into each line. Yet, when driven, stimulated emission can differ because its power is proportional to the complex amplitude of the drive in the line. We can therefore imagine a situation where the stimulated emission power would be negative on one side and positive on the other thus creating a net difference of power between the two lines. The principle of the experiment is represented in Fig. 3.1. The two drives are tuned so that they have the same amplitude and opposite phase $\beta_{\mathrm{in}} = -\alpha_{\mathrm{in}}$. At the level of the qubit, the two drives cancel each other out exactly. According to Eq. (2.23), the qubit Hamiltonian simply reads

$$H = \left(\sqrt{\Gamma_a}\alpha_{\mathrm{in}} + \sqrt{\Gamma_b}\beta_{\mathrm{in}} \right)\sigma_x = \sqrt{\Gamma}(\alpha_{\mathrm{in}} - \alpha_{\mathrm{in}})\sigma_x = 0 \; . \tag{3.1}$$

The qubit evolution is thus given by the Lindbladian terms only, energy decay and dephasing. The photon rate in lines a and b is given by Eq. (2.26). Its expectation value is

$$\begin{cases} \langle a_{\mathrm{out}}^\dagger a_{\mathrm{out}} \rangle & = \alpha_{\mathrm{in}}^2 + \Gamma \frac{1+\langle\sigma_z\rangle}{2} - \sqrt{\Gamma}\alpha_{\mathrm{in}}\langle\sigma_x\rangle \\ \langle b_{\mathrm{out}}^\dagger b_{\mathrm{out}} \rangle & = \alpha_{\mathrm{in}}^2 + \Gamma \frac{1+\langle\sigma_z\rangle}{2} + \sqrt{\Gamma}\alpha_{\mathrm{in}}\langle\sigma_x\rangle \end{cases} \; . \tag{3.2}$$

The directionality is ensured by the last term, and can be controlled by the value of $\langle\sigma_x\rangle$. If $\langle\sigma_x\rangle \geq 0$, energy is taken from a and transferred to b. From the point of view of the qubit this situation corresponds to the drive a tending to excite the qubit and drive b tending to deexcite it. Thus the qubit absorbs energy from a and reemits it in b by a stimulated emission-like process.
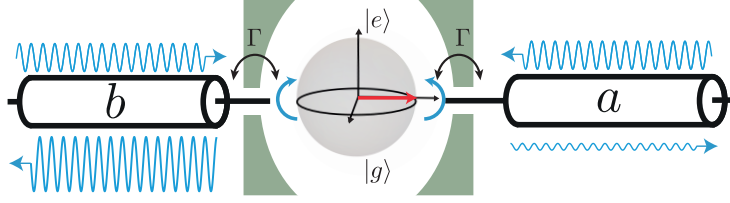
Figure 3.1: Principle of power transfer between two drives mediated by a symmetrically coupled qubit. Two drives of same amplitude and in opposition of phase interfere destructively and do not make the qubit evolve. When the qubit is in $|+_x\rangle = (|e\rangle + |g\rangle)/\sqrt{2}$ (red arrow in the Bloch sphere), the qubit continuously absorbs energy from a and emits it to b by stimulated emission.

The qubit is initialized in a superposed state $\sin(\frac{\theta}{2})|e\rangle + e^{i\phi}\cos(\frac{\theta}{2})|g\rangle$. Due to energy decay (assuming a bath at zero temperature) and dephasing, the expectation values of σ_z and σ_x evolve in the following way

$$
\begin{cases}
\langle\sigma_z\rangle(t) &= (1-\cos(\theta))e^{-t/T_1} - 1 \\
\langle\sigma_x\rangle(t) &= \cos(\phi)\sin(\theta)e^{-t/T_2}
\end{cases}
. \tag{3.3}
$$

The photon rates in the lines are thus

$$
\begin{cases}
\langle a_{\text{out}}^\dagger a_{\text{out}}\rangle(t) = \alpha_{\text{in}}^2 + \dfrac{\Gamma}{2}(1-\cos(\theta))e^{-t/T_1} \\
\qquad\qquad\qquad - \cos(\phi)\sin(\theta)\sqrt{\Gamma}\alpha_{\text{in}}e^{-t/T_2} \\
\langle b_{\text{out}}^\dagger b_{\text{out}}\rangle(t) = \alpha_{\text{in}}^2 + \dfrac{\Gamma}{2}(1-\cos(\theta))e^{-t/T_1} \\
\qquad\qquad\qquad + \cos(\phi)\sin(\theta)\sqrt{\Gamma}\alpha_{\text{in}}e^{-t/T_2}
\end{cases}
. \tag{3.4}
$$

The phase of the quantum superposition therefore controls the direction of the energy transfer. This is an external knob that we can control at will. Note that even in the perfect case of no pure dephasing $\Gamma_\varphi = 0$ and no extra energy decay, we would still get a decay of $\sigma_{z,x}$ with the rates $\Gamma_1 = 2\Gamma$ and $\Gamma_2 = \Gamma$ because of the coupling to the lines. An important consequence is that for a given number of input photons there is an optimal time duration for the input pulses to obtain the maximal transferred energy. Moreover our router needs to be reset after each pulse, since the qubit decays to the ground state.

3.1.2 *Experimental implementation*

In our experimental realization we use a 3D transmon qubit coupled to an asymmetrical cavity, with about an order of magnitude difference between the two ports, and always measure the fluorescence that outputs in the line a. Our experiment hence simulates what would happen in the case of symmetrical coupling but still exhibits an

actual transfer of power. The main reason why we use an asymmetrical cavity for this experiment is that it maximizes the quantity of fluorescence light emitted towards the quantum-limited amplifier when we place it so that $\Gamma_a \gg \Gamma_b$, and hence helps to reduce the averaging time. We use the same qubit and the same JPC as in 2.5 with the same gain and bandwidth. A sketch of the experiment containing its most important features is represented in Fig. 3.2. The phase coherence between the two drives is fundamental for this experiment. To ensure a sufficient phase coherence we use one microwave source that we split and modulate at $f^q_{\mathrm{mod}} = 200$ MHz by two channels of an Arbitrary Waveform Generator (AWG), before sending one in line a and the other one in b. The amplitude and phase of the two pulses in a and b can hence be finely controlled by changing the phase and amplitude of the modulation tone of the AWG. Since the coupling rates are asymmetrical and we want the two drives to perfectly cancel out on the qubit, we attenuate the line going to a more than the one going to a. This allow us to use the full amplitude range of the AWG. We also keep a weakly attenuated line sent on b to perform fast pulses on the qubit for preparation and tomography, with gate times typically below 50 ns. Finally we use a drive at cavity frequency in transmission to perform a spectroscopy of the qubit when needed using a High Power Readout (HPR) measurement as described in Sec. B.2. The signals coming from the fridge at qubit frequency f_q and cavity frequency f_c are eventually demodulated, filtered and digitized. For time-resolved measurements of $\langle a_{\mathrm{out}} \rangle$ and $\langle a^\dagger_{\mathrm{out}} a_{\mathrm{out}} \rangle$, the time interval between two points is $\mathrm{d}t = 100$ ns.
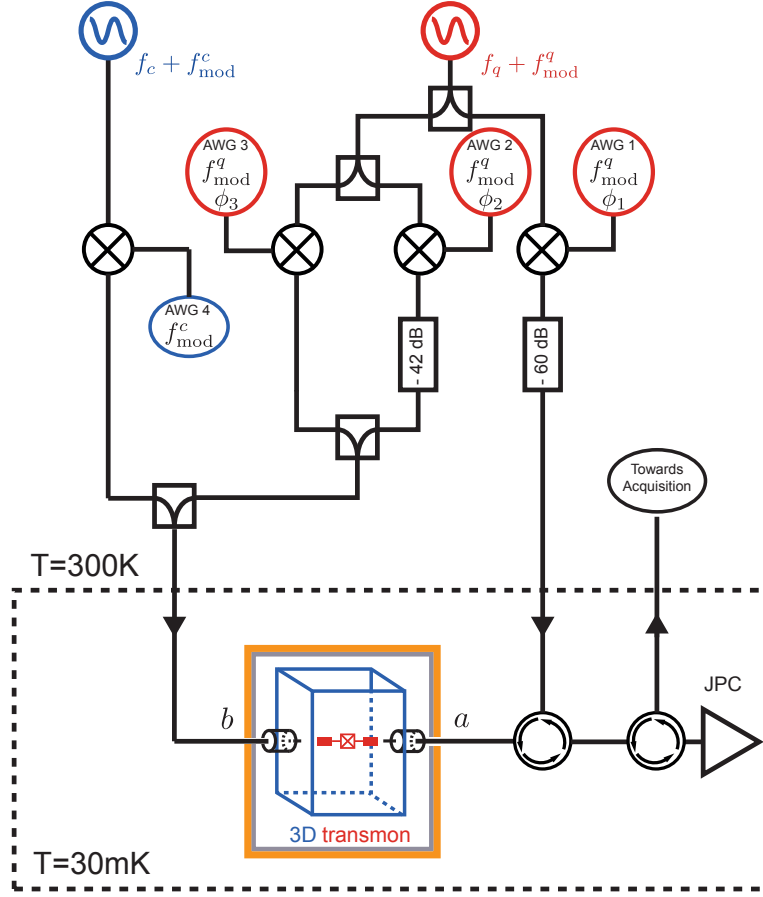
Figure 3.2: Sketch of the experimental setup for the double drive experiment. The same source at qubit frequency is split three times and sent on the qubit+cavity system at low temperature, together with a drive at cavity frequency used for qubit tomography. The phase and amplitude of each drive is controlled using AWG channels. For the sake of simplicity we did not represent the attenuation at the different stages of the cryostat nor the particular of signals amplification and acquisition. A precise picture of the cryostat wiring is shown in Fig. A.1

3.2 CALIBRATING THE DRIVES

The central condition for our experiment to work is to achieve a perfect cancellation of the drives at the level of the qubit and hence a free evolution. Since the qubit coupling and the optical length are not the same for the two lines, we need to carefully tune the amplitude and phase of the drives. One could think naively that it would be enough to measure the Rabi oscillations induced by each drive independently using a full qubit tomography in the Bloch sphere. This approach fails because we want to be able to possibly use large drive amplitudes to maximize stimulated emission, and hence need an amplitude and phase precision below the percent to efficiently cancel out the drives. However we can use this method to get a first estimation of the amplitude and phase. A more precise approach is to turn on the drives simultaneously, and to sweep the phase and amplitude of one of the two drives. In general, the conjugate action of the drives induces overdamped or underdamped Rabi oscillations on a plane given by the amplitudes and phases of the drives. By fitting the evolution of the qubit by the exact solutions of the Bloch equations, we can deduce the correct phase and amplitude with a very good accuracy.

3.2.1 *Phase calibration*
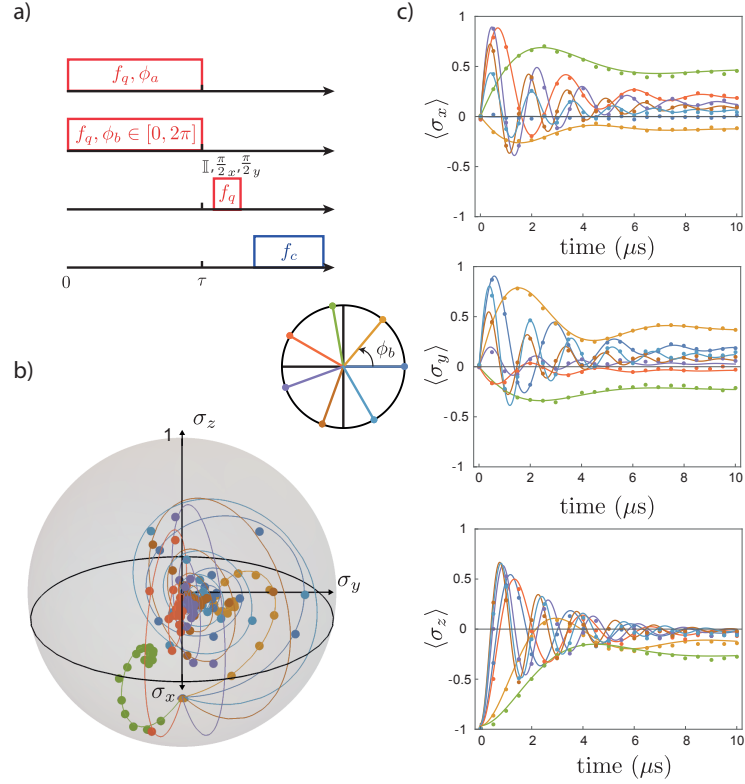
Figure 3.3: Rabi oscillations induced by two drives varying in phase. a) Pulse sequence of the experiment. The two drives are applied simultaneously on the qubit for a time τ before performing a full tomography. b) Parametric evolution of the Bloch vector with time in the Bloch sphere (unit radius). We note that the plan containing the qubit trajectory changes with the phase of the drive. c) Evolution of $\langle \sigma_{x,y,z} \rangle$ with time. The points represent the data and the lines the theoretical fit. When the qubit oscillates quickly, the two drives are close to be in phase. When the qubit does not oscillate the two drives are almost in opposition of phase.

When we perform a final tomographic measurement the orientation of the Bloch sphere is naturally fixed by the tomographic qubit drive. We hence write the two drives in a and b as $\alpha_{\text{in}} e^{i\phi_a}$ and $\beta_{\text{in}} e^{i\phi_b}$ with $\alpha_{\text{in}}, \beta_{\text{in}} \in \mathbb{R}$. When the two drives are applied simultaneously on the qubit the Hamiltonian is given by Eq. (2.23) and we get

$$\frac{H}{\hbar} = -\frac{\Omega_y(\phi_a, \phi_b)}{2}\sigma_y - \frac{\Omega_x(\phi_a, \phi_b)}{2}\sigma_x \tag{3.5}$$

with $\Omega_y(\phi_a, \phi_b) = \sqrt{\Gamma}\big(\alpha_{\text{in}}\cos(\phi_a) + \beta_{\text{in}}\cos(\phi_b)\big)$ and $\Omega_x(\phi_a, \phi_b) = \sqrt{\Gamma}\big(\alpha_{\text{in}}\sin(\phi_a) + \beta_{\text{in}}\sin(\phi_b)\big)$. This Hamiltonian describes an effective single Rabi drive and can be rewritten as

$$\frac{H}{\hbar} = -\frac{\Omega_{\text{eff}}}{2}\big(\cos(\phi_{\text{eff}})\sigma_y + \sin(\phi_{\text{eff}})\sigma_x\big) \ , \tag{3.6}$$

with

$$\Omega_{\text{eff}} = 2\sqrt{\Omega_y(\phi_a, \phi_b)^2 + \Omega_x(\phi_a, \phi_b)^2} \tag{3.7}$$

the effective Rabi frequency and

$$\tan(\phi_{\text{eff}}) = \frac{\Omega_y(\phi_a, \phi_b)}{\Omega_x(\phi_a, \phi_b)} \ . \tag{3.8}$$

We keep the phase of the drive in a ϕ_a constant and vary ϕ_b from 0 to 2π at constant amplitude. For each phase, we let the qubit evolve for a time τ varying between 0 and 10 μs before performing a full tomography, as represented in Fig. 3.3a). When the two drives are in phase, their amplitudes add up and the qubit undergoes underdamped Rabi oscillations described by Eq. (2.17). When they are in opposition of phase they partially cancel each other out, and the qubit undergoes overdamped Rabi oscillations. They are simply described by replacing ν_R by $|\nu_R|$ and sines and cosines by respectively hyperbolic sines and cosines in Eq. (2.17). With independent measurements of the qubit lifetime $T_1 = 1.95$ μs and coherence time $T_2 = 2.88$ μs, each curve gives the effective amplitude Ω_{eff} and phase ϕ_{eff} appearing in Eq. (3.6). The qubit time evolution for various phases together with the theoretical fit is represented in the Bloch sphere in Fig. 3.3b) and as a function of time in Fig. 3.3c).

With the set of Rabi oscillations we can now display the evolution of Ω_{eff} and ϕ_{eff} with the phase ϕ_b. A good way to represent this evolution is to plot $\Omega_{\text{eff}} \cos(\phi_{\text{eff}}) = \Omega_x(\phi_a, \phi_b) = \sqrt{\Gamma}\alpha_{\text{in}} \cos(\phi_a) + \sqrt{\Gamma}\beta_{\text{in}} \cos(\phi_b)$ and $\Omega_{\text{eff}} \sin(\phi_{\text{eff}}) = \Omega_y(\phi_a, \phi_b) = \sqrt{\Gamma}\alpha_{\text{in}} \sin(\phi_a) + \sqrt{\Gamma}\beta_{\text{in}} \sin(\phi_b)$ as a function of ϕ_b, as they exhibit an oscillatory behavior, see Fig. 3.4. We fit these two functions simultaneously using Eq. (3.7) and (3.8) with four fit parameters, $\alpha_{\text{in}}, \beta_{\text{in}}, \phi_a$ and ϕ_b^0 the initial unknown phase of the drive in b. We find $\phi_a - \phi_b^0 = 4.54$ rad and $\phi_a = 0.73$ rad.
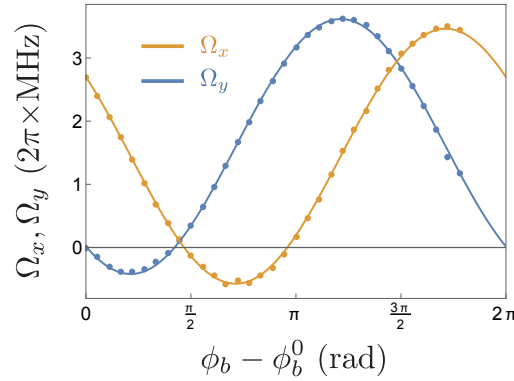
Figure 3.4: Evolution of Ω_x and Ω_y with the phase of the drive in b, the points are experimental data and the lines result from Eq. (3.7) and (3.8) with $\phi_a = 0.73$ rad, $\phi_b^0 = 2.47$rad, $\sqrt{\Gamma}\alpha_{\text{in}} = 2.15$ $2\pi\times$MHz and $\sqrt{\Gamma}\beta_{\text{in}} = 2.02$ $2\pi\times$MHz.

3.2.2 Amplitude calibration

In theory the previous measurement also gave us the ratio of the two drive amplitudes α_{in} and β_{in}. However, by construction, the previous measurement is much more accurate for determining the phases of the drives than for determining their amplitude, since we were changing the phase of the drive in b. To calibrate the amplitude correctly, we fix this time the phase of the drive in b so that the two drives are almost in opposition of phase, and vary the amplitude β_{in}. We use exactly the same sequence as in the phase calibration experiment, and similarly fit the resulting overdamped Rabi oscillations. The evolution of Ω_x and Ω_y with the drive amplitude is represented in Fig. 3.5. What we set experimentally is the amplitude of the modulation pulses generated by the AWG, α_{AWG} and β_{AWG}. The two lines do not cross at zero, meaning that the two drives are indeed

not quite in opposition of phase and hence we never get $\Omega_{\text{eff}} = 0$. The simultaneous fit gives the scaling factor in the AWG amplitudes that we need to use to obtain the same drive amplitudes at the level of the qubit $\beta_{\text{in}} = \alpha_{\text{in}} \Leftrightarrow \beta_{\text{AWG}} = 1.076 \times \alpha_{\text{AWG}}$.
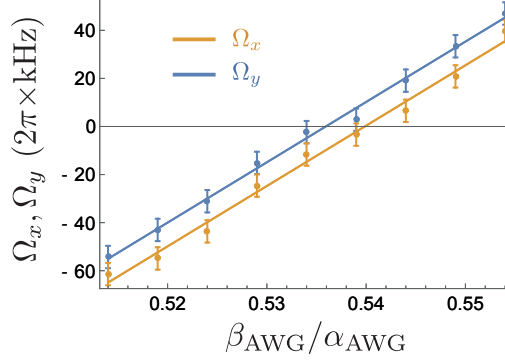
Figure 3.5: Evolution of Ω_x and Ω_y with the amplitude of the drive in b when the two drives are almost in opposition of phase, the points are experimental data and the line is theory with $\phi_a - \phi_b = 1.001\pi$ rad and $\sqrt{\Gamma}\alpha_{\text{in}} = 1.91$ $2\pi\times$MHz.

3.3 PHOTON RATE CONTROL

Now that the amplitudes and phases of the drives are known we can turn to the experiment itself. We fix the drives in opposition of phase and with a similar amplitude so that we have all the time $\beta_{\text{in}} = -\alpha_{\text{in}}$. The control of the experiment is now the phase ϕ of the quantum superposition $sin(\theta/2)|e\rangle + e^{i\phi}\cos(\theta/2)|g\rangle$. Let us start by validating the principle of the experiment given by Eq. (3.4). We measure the photon rate emitted only in the line a and see the directionality by changing the phase ϕ of the superposition and measure the time evolution of the photon rate.

3.3.1 *Photon rate time evolution*

We initialize the qubit in a superposed state $|\psi\rangle(\theta, \phi) = \sin(\theta/2)|e\rangle + \cos(\theta/2)e^{i\phi}|g\rangle$ with a variable θ and $\phi = 0$ or $\phi = \pi$ using a fast pulse on b. Then we turn on the two pulses in opposition of phase with similar amplitude, and record the photon rate $\langle a_{\text{out}}^\dagger a_{\text{out}}\rangle$ in a as a function of time. According to Eq. (2.55) the photon rate is known up to a constant offset corresponding to the noise power and a scaling factor G corresponding to the gain of the detection setup. Using the Purcell rate measurement in 2.5, we know the correspondence between the amplitude set in the AWG and α_{in} and the Purcell rate Γ. In theory this measurement should also determine the gain G if the thermal state of the qubit $\langle\sigma_z\rangle^0$ is known. With independent measurements presented in 7, we obtain $\langle\sigma_z\rangle^0 = -0.93$. Unfortunately the gain varies over time and we cannot simply take the value obtained from Sec. 2.5. However the previous measurement demonstrated the link between the measured $\overline{I^2(t) + Q^2(t)}$ and $\langle a_{\text{out}}^\dagger a_{\text{out}}\rangle$, and we can use this link to determine the gain.

The time evolution of $\langle a_{\text{out}}^\dagger a_{\text{out}}\rangle$ is represented in Fig. 3.6 for various preparation angles. It exhibits a clear directionality with a quasi-exponential decay described by Eq. (3.4), with the qubit lifetime and coherence time measured independently $T_1 =$
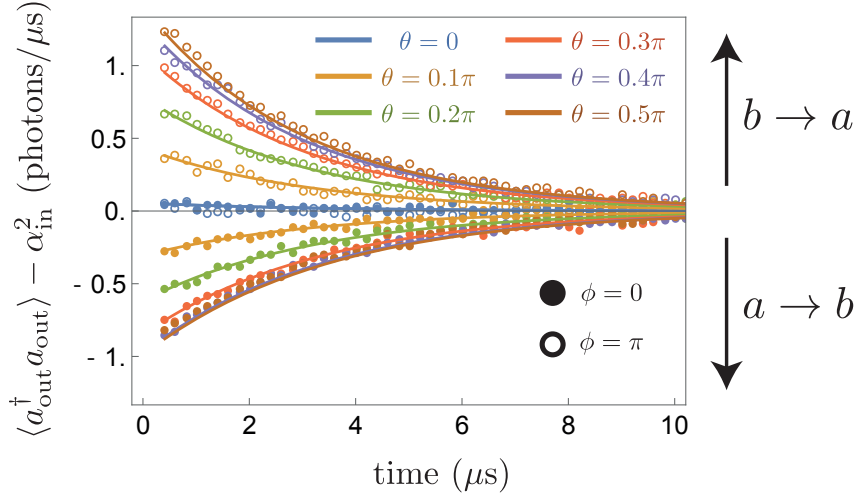
Figure 3.6: Photon rate as a function of time for a qubit decaying from $\sin(\theta/2)|e\rangle + \cos(\theta/2)e^{i\phi}|g\rangle$, (points) experimental data and (line) theory with $\sqrt{\Gamma}\alpha_{\text{in}} = 2\pi \times 0.41$ MHz. When $\phi = 0$ the pulse reflected on port a contains less energy than the input one $\langle a^{\dagger}_{\text{out}} a_{\text{out}}\rangle \leq \alpha^2_{\text{in}}$. When $\phi = \pi$ it contains more.

2.22 μs and $T_2 = 3.21$ μs. In oder to maximize the quantity of stimulated emission and increase the directionality, we set the drive amplitudes so that $\sqrt{\Gamma}\alpha_{\text{in}} = 2\pi \times 0.41$ MHz $\approx 6\Gamma$. When the qubit is initialized in its equilibrium state $\theta = 0$, we expect the photon rate to be constant, but we notice that it is not the case. This is due to a small delay τ between the times at which the two drives reach the qubit. The experimental data are hence reproduced using only the gain G and the delay τ as global fitting parameters, and the theory shows a good agreement with the experimental measurements with $\tau = 18$ ns. Note that the curves corresponding to $\phi = 0$ and $\phi = \pi$ are not symmetrical because of spontaneous emission.

3.3.2 *Control of stimulated emission*

As we saw in Eq. (3.4) the photon rate direction given by the stimulated emission term depends on $\cos(\phi)$. To test this we prepare the qubit with various values of ϕ between 0 and 2π, and measure the time evolution of $\langle a^{\dagger}_{\text{out}} a_{\text{out}}\rangle$. According to Eq. (3.4) each curves evolves as the sum of two exponentials decaying with the characteristic times T_1 and T_2. The evolution of the measured amplitude of the decay $\delta\langle a^{\dagger}_{\text{out}} a_{\text{out}}\rangle = \langle a^{\dagger}_{\text{out}} a_{\text{out}}\rangle(t = 0)$ with the phase ϕ for various preparation angles θ is represented in Fig. 3.7, together with the theory from Eq. (3.4). As expected it oscillates with ϕ with an amplitude that depends on θ. When the qubit is initialized along the y-axis of the Bloch sphere ($\phi = \pi/2$) stimulated emission is cancelled and there is no directionality in the power transfer. Because of spontaneous emission, the cosine is not centered around 0. Without the delay between the two drives it should be shifted by $+\Gamma(1 - \cos(\theta))/2$. With the delay the shift does not have a simple expression but can be easily reproduced and taken into account by the theory. In any case this offset induces a tradeoff when one wants to maximize the transferred energy. The closer the qubit to the ground state, the less spontaneously it emits. On the other hand one cannot reduce the qubit excitation too much, as the directional power transfer is given by $\langle \sigma_x\rangle$.
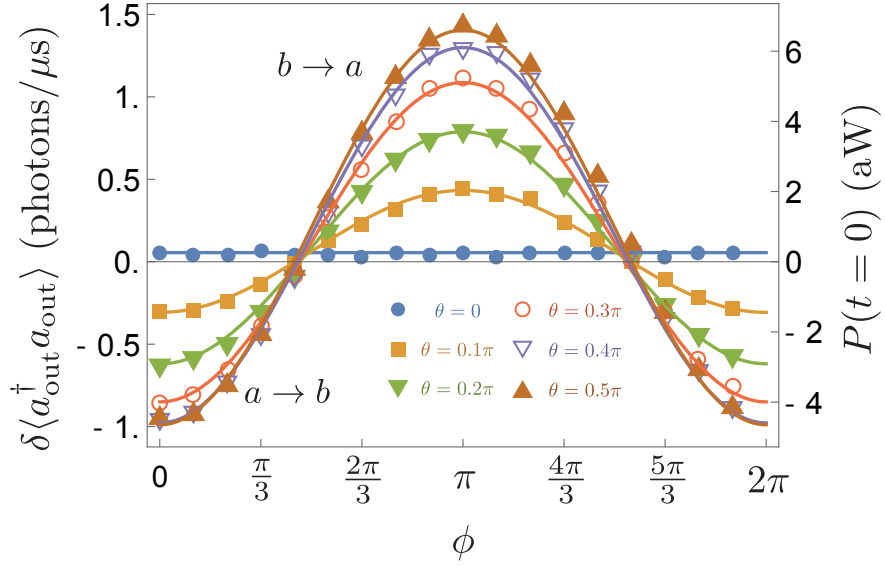
Figure 3.7: Power transfer amplitude between b and a a a function of the qubit phase ϕ for different values of θ with $\sqrt{\Gamma}\alpha_{\text{in}} = 2\pi \times 0.41$ MHz. The amplitude of the photon rate decay $\delta\langle a_{\text{out}}^{\dagger} a_{\text{out}}\rangle$ (left label), giving the initial power $P(t = 0) = \hbar\omega_q\delta\langle a_{\text{out}}^{\dagger} a_{\text{out}}\rangle$ (right label), evolves as a cosine of ϕ, (points) experimental data and (line) theory.

3.4 TRANSFER EFFICIENCY

We demonstrated in the previous section that we can control the direction of the photon transfer by changing the phase of the qubit. However the quality of the transfer has to be quantified. In other words, we need to define a transfer efficiency, that would be equal to 1 when all the photons on one side are transferred to the other, and 0 if the situation stays symmetrical. This efficiency will naturally depend on the qubit initial state that quantifies the amount of spontaneous emission, the amplitude of the drives as it quantifies the number of photons sent on the qubit, and the duration of the drives as there is a time dependence of the routing. Since the directionality is maximal when $\phi = 0$ $[\pi]$ we will consider only this situation in the following.

3.4.1 Energy transfer efficiency

One can choose several options for defining the transfer efficiency. For instance, one could define a power efficiency where we would compare the instantaneous power (the photon rate) in the two lines. For photon routing however, the natural way is to define an energy transfer efficiency. One sends a given number of photons on the qubit and compare how many photons output on the two lines. With such a definition, the shape of the impulsions is of first importance, as it would mean that α_{in} depends on time. In the following we will restrain ourselves to square impulsions of duration t_p. If we use the simple comparison between the number of photons at the output in a and b we get

$$\eta = \left| \frac{\int_0^{t_p} \langle a_{\text{out}}^{\dagger} a_{\text{out}}\rangle(t)\mathrm{d}t - \int_0^{t_p} \langle b_{\text{out}}^{\dagger} b_{\text{out}}\rangle(t)\mathrm{d}t}{\int_0^{t_p} \langle a_{\text{out}}^{\dagger} a_{\text{out}}\rangle(t)\mathrm{d}t + \int_0^{t_p} \langle b_{\text{out}}^{\dagger} b_{\text{out}}\rangle(t)\mathrm{d}t} \right| . \tag{3.9}$$

From Eq. (3.4) we straightforwardly see that the numerator contains the spontaneous emission terms and the denominator the reflected drives and the spontaneous emission

radiated by the qubit during the duration of the pulse. When the qubit is initialized in $\cos(\frac{\theta}{2})|g\rangle + \sin(\frac{\theta}{2})|e\rangle$ the efficiency reads

$$\eta = \frac{2\sqrt{\Gamma}\alpha_{\text{in}}T_2\sin(\theta)(1 - e^{-t_p/T_2})}{2\alpha_{\text{in}}^2 t_p + \Gamma\ T_1(1 - \cos(\theta))(1 - e^{-t_p/T_1})} \ . \tag{3.10}$$

This efficiency is well-defined and stays smaller than 1 except at the singularity ($\theta = 0, \alpha_{\text{in}} = 0$) where it is not defined. This singular point corresponds to the qubit in the ground state and no light sent at all, which is a trivial situation.

There are several ways to maximize this function, depending on the physical constraints that one sets. For instance one might want to keep the number of photons in the pulse $N = \alpha_{\text{in}}^2 t_p$ constant, and find the amplitude, time and qubit angle θ that maximize the transfer. On the other hand when the operation time is constrained one might keep the impulsion time t_p constant and find the best values for α_{in} and θ. In any case, it is interesting to look at the global maximum of the efficiency. It decreases with time and hence tends to a maximum when $t_p \to 0$ given by

$$\eta(t_p \to 0) = \frac{2\Gamma\alpha_{\text{in}}\sin(\theta)}{2\alpha_{\text{in}}^2 + \Gamma(1 - \cos(\theta))} \ . \tag{3.11}$$

We derive the maximum $\eta_{\text{max}}(\theta)$ for various values of $\theta \in]0, \pi]$, represented in Fig.3.8a) while Fig.3.8b) displays the value of $\alpha_{\text{in}}/\sqrt{\Gamma}$ maximizing η at a given angle θ. The efficiency tends towards 1 when $\theta \to 0$ for $\alpha_{\text{in}} \to 0$ as well. This means that the less energy we spend for photon routing, the more efficient it becomes. This is similar to thermodynamical cycles tending to the Carnot efficiency at infinitely low power. In the following we will illustrate this point by initializing the qubit either with $\theta = \pi/2$ or $\theta = \pi/6$ and maximizing the efficiency over α_{in} and t_p.
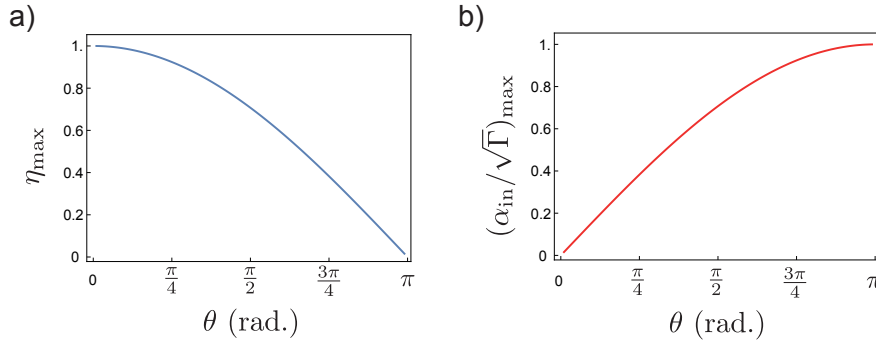
Figure 3.8: a) Maximum of the transfer efficiency as a function of the qubit preparation angle θ. The efficiency tends to 1 when the qubit gets close to the ground state ($\theta = 0$) and to zero when the qubit is in the excited state ($\theta = 0$).
b) Value of the drive amplitude maximizing the transfer efficiency as a function of the preparation angle θ.

3.4.2 *Efficiency expression for the experimental model*

In our experimental model we use a strongly asymmetric cavity with $\Gamma_b \ll \Gamma_a$ and measure the number of photons in the line a only. If we try to use the previous definition for the transfer efficiency we would encounter two issues. First, we are not able to access experimentally the number of photons propagating in b. Second, to obtain the

cancellation of the drives at the level of the qubit $\Gamma_b\beta_{\rm in} = -\Gamma_a\alpha_{\rm in}$ we need an extremely large drive in b. This strong drive obviously reduces the maximum efficiency that one can achieve to a small value. However there is an easy way to model the previous efficiency with this configuration by defining the efficiency by the on-off ratio in the line a. This ratio is defined by comparing the number of photons collected in a when the qubit is initialized with the phase of its superposition ϕ set to 0 to the number of photons collected when $\phi = \pi$

$$
\eta = \left| \frac{\int_0^{t_p}\langle a_{\rm out}^\dagger a_{\rm out}\rangle_{\phi=0}(t)\mathrm{d}t - \int_0^{t_p}\langle a_{\rm out}^\dagger a_{\rm out}\rangle_{\phi=\pi}(t)\mathrm{d}t}{\int_0^{t_p}\langle a_{\rm out}^\dagger a_{\rm out}\rangle_{\phi=0}(t)\mathrm{d}t + \int_0^{t_p}\langle a_{\rm out}^\dagger a_{\rm out}\rangle_{\phi=\pi}(t)\mathrm{d}t} \right|
$$

(3.12)

$$
= \frac{2\sqrt{\Gamma_a}\alpha_{\rm in}T_2\sin(\theta)(1 - e^{-t_p/T_2})}{2\alpha_{\rm in}^2 t_p + \Gamma_a\,T_1(1 - \cos(\theta))(1 - e^{-t_p/T_1})} \;.
$$

Formally this equation is similar to the previous one for the symmetrical case in Eq. (3.10), but their time evolutions differ. In the ideal case of no extra losses and no dephasing $\Gamma_{\rm nr} = 0$ and $\Gamma_\varphi = 0$, we would indeed obtain $T_1 = 1/(2\Gamma)$, $T_2 = 1/\Gamma$ for the symmetrical case and $T_1 = 1/\Gamma_a$, $T_2 = 2/\Gamma_a$ for the asymmetrical one. Yet we noted that the maximal value of η is reached for $t_p \to 0$ and does not depend on the particular values of T_1 and T_2 as given by Eq. (3.11). Therefore we should expect the same maximum for the asymmetrical situation as for the symmetrical one with $\Gamma_a = \Gamma$.

3.4.3 Efficiency evolution
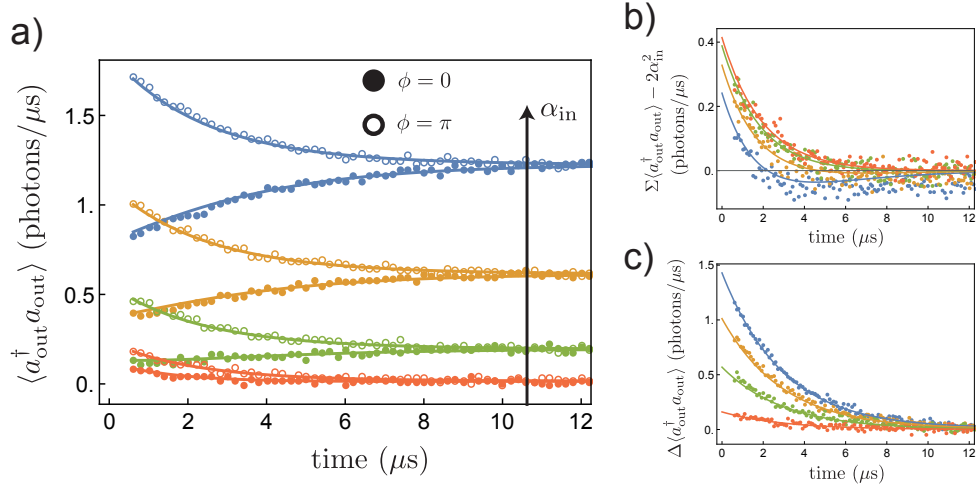
Figure 3.9: Time evolutions of a) the photon rate emitted by the qubit prepared in (plain circles) $(|e\rangle + |g\rangle)/\sqrt{2}$ and (empty circles) $(|e\rangle - |g\rangle)/\sqrt{2}$ for $\sqrt{\Gamma}\alpha_{\rm in} = 2\pi\times$ (0.026, 0.091, 0.16, 0.23) MHz, b) sum of the photon rates emitted by the qubit initialized in $(|e\rangle + |g\rangle)/\sqrt{2}$ and $(|e\rangle - |g\rangle)/\sqrt{2}$ (the reflected drive has been subtracted), and c) difference of the rates. In the ideal case, the sum of the photon rates should contain only the spontaneous emission term and therefore be independent of the drive amplitude. In practice it deviates from it due to a small residual drive. Lines are theory with 3% of residual drive.

Similarly to 3.3.1 we initialize the qubit with $\phi = 0$ or π before turning on the two drives and measure the photon rate evolution with time. We perform this measurement

for various values of the amplitude of the drives from $\sqrt{\Gamma_a}\alpha_{\rm in} \ll \Gamma_a$ to $\sqrt{\Gamma_a}\alpha_{\rm in} \gg \Gamma_a$. The time evolution of the photon rate is represented for some representative amplitudes in Fig. 3.9a) for $\theta = \frac{\pi}{2}$. The sum $\Sigma\langle a_{\rm out}^\dagger a_{\rm out}\rangle$ and the difference $\Delta\langle a_{\rm out}^\dagger a_{\rm out}\rangle$ of the photon rates emitted for $\phi = 0$ and $\phi = \pi$ are represented on respectively Fig. 3.9b) and c) (the constant term due to the reflected drives has been subtracted for clarity). In theory $\Sigma\langle a_{\rm out}^\dagger a_{\rm out}\rangle$ should contain the spontaneous emission contribution to the photon rate and $\Delta\langle a_{\rm out}^\dagger a_{\rm out}\rangle$ the stimulated emission contribution. When the drive amplitude is large (blue curve) we note is a clear difference between the time evolution of the photon rates for $\phi = 0$ and $\phi = \pi$, because stimulated emission is large. However one should expect the transfer efficiency to stay rather small because the reflected drive is bigger than the stimulated emission term. At very low driving amplitude (red curve), stimulated emission is smaller than spontaneous emission. The qubit hence emits more or less the same quantity of energy in the two lines. At intermediate amplitude (green curve), stimulated emission is of the same order of magnitude as the sum of the reflected drive and spontaneous emission. It results in a clear difference between the energy emitted in the two lines, and we expect the transfer efficiency to be large.

The photon flux measured experimentally does not exactly correspond to the one given by Eq. (3.4). Indeed, the two drives underwent a small drift between the calibration and the measurement, so that they do not perfectly interfere. As a result there exists a small residual Rabi drive on the qubit which does not decay freely. On the raw photon rate evolution this deviation is almost unnoticeable, but it appears very clearly when we display the sum $\Sigma\langle a_{\rm out}^\dagger a_{\rm out}\rangle - 2\alpha_{\rm in}^2$. In the absence of the residual drive, all the curves should superpose as they only contain the spontaneous emission term of the qubit. Here, the higher the drive amplitude, the more it deviates from an exponential decay. We fit this time evolution with as only factor the amount of residual drive and find that 3% of the drive is not destructed by interference.

Figure 3.10: a) Experimental and b) theoretical energy transfer efficiency between the two drives for a qubit initialized in $(|e\rangle \pm |g\rangle)/\sqrt{2}$ as a function of time and pulse amplitude.

We can now compute the evolution of the transfer efficiency η as defined by Eq. (3.12) by integrating the experimental photon rate. The evolution of the efficiency with time and drive amplitude is represented in Fig. 3.10. As expected from the previous theoretical study the transfer efficiency is maximal when the duration of the pulse is the smallest. In theory it is the case when the duration goes to 0, but experimentally the lowest time we can measure is 610 ns. Even in the presence of the small residual drive we find a good agreement between the experimental data and the theoretical prediction

from Eq. (3.12). We measure a maximal value for the transfer efficiency at the minimal time is 63% while the theoretical one is 69%.

The transfer efficiency should be higher when the qubit is initialized in a state closer to the ground state. To test this assumption, we prepare the qubit with $\theta = \pi/6$ in $((\sqrt{3} - 1)|e\rangle \pm (\sqrt{3} + 1)|g\rangle)/2\sqrt{2}$. The photon rate obtained with this initial state is represented in Fig. 3.11 as a function of time together with the theory. For this experimental realization the gain was calibrated independently and we noticed a small change of the lifetime and coherence time of the qubit, that we took into account in the theory plot. Since the initial expectation values of both σ_x and σ_z are smaller than for the previous case of $\theta = \pi/2$ the qubit radiates less power in the line, both from spontaneous emission (Fig. 3.11b)) and stimulated emission (Fig. 3.11c)). Spontaneous emission is more strongly reduced for $\theta = \pi/6$ than stimulated emission hence we should obtain a better transfer efficiency. For this experimental realization there was no noticeable residual drive so we can assume that the two drives interfere perfectly and that the qubit evolves freely. The only deviation from the theory comes from the small delay between the two arrival dates of the drives on the qubit, inducing a small change of the qubit initial state.
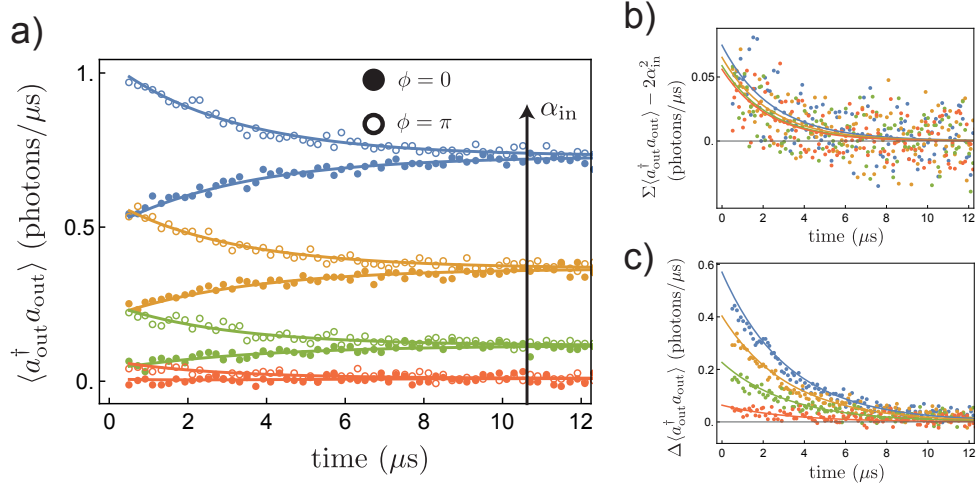
Figure 3.11: Time evolutions of a) the photon rate, b) the sum of the photon rates obtained for $\phi = 0$ and $\phi = \pi$ and c) the difference of the photon rates for a qubit initialized by a $\pi/6$-pulse and $\sqrt{\Gamma}\alpha_{\mathrm{in}} = 2\pi \times (0.020, \ 0.072, \ 0.13, \ 0.18)$ MHz.

The energy transfer efficiency for $\theta = \pi/6$ is represented in Fig. 3.12. Since stimulated emission is reduced compared to the previous case at equal drive amplitude, the optimal amplitude that maximizes the efficiency is lower than when the qubit is initialized with $\theta = \pi/2$. However it leads to a much higher transfer efficiency. In theory we should reach 94% of transfer efficiency at the smallest measurable time. Experimentally we obtain an efficiency that goes above 1, at 110%. This difference is due to the uncertainty coming from the denominator of the ratio calculated to obtain the efficiency. Here, spontaneous emission and the drive power are small and the experimental noise on the spontaneous emission rate that we see in Fig. 3.11 generates the deviation from the theoretical bound. To estimate this error we use the difference between data and theory in the photon rate measurements. This gives an estimation of the error on the maximal efficiency $\eta_{\mathrm{max}} = (110 \pm 30)\%$. It is interesting to also look at the time evolution of the efficiency, and not only at its maximum. In fact the optimal value for a zero pulse duration is fictional since any physical pulse has a precise duration. For this experiment

the global gain of the amplification chain changed with a result on the qubit coherence time and lifetime. Here, $T_1 = 2.2$ μs and $T_2 = 3.2$ μs. With these parameters the transfer efficiency stays above 80% for more than 2 μs, and above 50% for more than 10 μs.
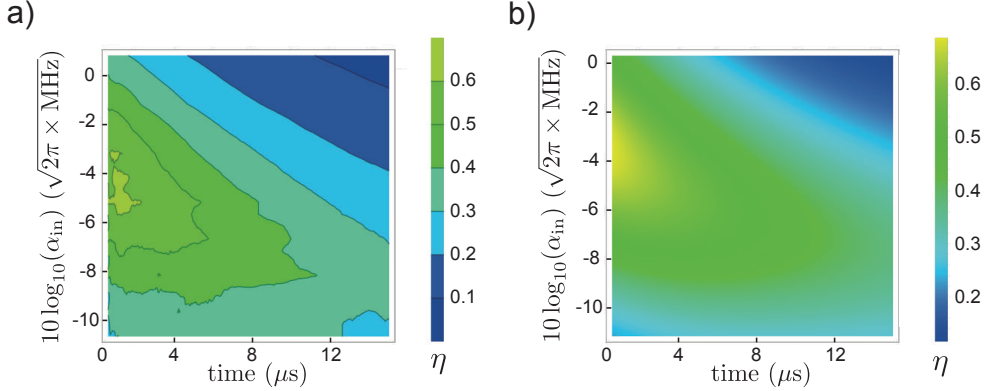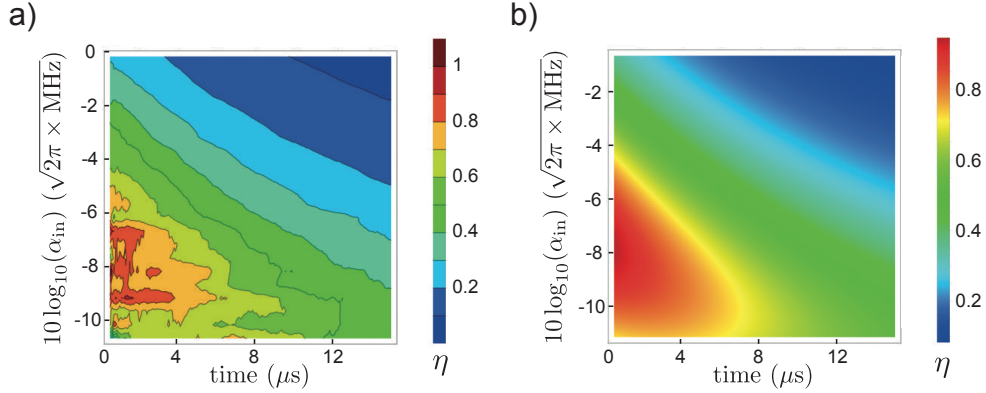

Figure 3.12: a) Experimental and b) theoretical energy transfer efficiency between the two drives for a qubit initialized with $\theta = \pi/6$ as a function of time and pulse amplitude. The estimated error bar on η for this measurement is 0.3.

3.5 CONCLUSION

Although the power transfer demonstrated in this chapter is controlled by the phase of a quantum superposition of qubit states, the principle on which our experiment is based is a classical interference effect. Indeed, one can imagine a similar experiment where the qubit has been replaced by a linear resonator hosting a coherent state $|\alpha\rangle$. The photon rates in the two lines can be easily expressed from the derivation made for the qubit leading to Eq. (3.4) by substituting σ_x by $a + a^\dagger$ and $(1 + \sigma_z)/2$ by a with a the annihilation operator of a photon in the resonator. With $\alpha = |\alpha|e^{i\phi}$ and writing κ the cavity coupling to the lines the photon rate in a is

$$\langle a_{\text{out}}^\dagger a_{\text{out}}\rangle(t) = \alpha_{\text{in}}^2 + \kappa|\alpha|^2 e^{-2\kappa t} - 2\sqrt{\kappa}|\alpha|\cos(\phi)\alpha_{\text{in}}e^{-\kappa t} \ . \tag{3.13}$$

The efficiency at $t = 0$ is thus

$$\eta(t = 0) = 2\frac{\sqrt{\kappa}\alpha_{\text{in}}\alpha}{\alpha_{\text{in}}^2 + \kappa|\alpha|^2} \ . \tag{3.14}$$

This time since there are no constraints on α we can fix the drive amplitude α_{in} and maximize the efficiency. The resolution is straightforward and gives

$$\eta(t = 0) = 1 \Leftrightarrow |\alpha| = \frac{\alpha_{\text{in}}}{\sqrt{\kappa}} \ . \tag{3.15}$$

Therefore the efficiency always reaches the maximum of 100% for a certain value of α for any drive amplitude. Moreover, if we imagine that a third weakly coupled classical drive is applied on the resonator to prevent α to decay at the rate κ, then we end up in a situation with three drives applied on a resonator, one being perfectly reflected and one perfectly transmitted by interference.

This observation does not mean that our experiment is purely classical since the control is a superposition of states, but highlights the fundamental difference between

a two-level systems and a linear oscillator. For a linear oscillator, classical states are coherent states which are superpositions of Fock states. The coherent state $|\alpha = 1\rangle$ gives an equal weight to $|0\rangle$ and $|1\rangle$. If we could truncate the Hilbert space to the subspace $\{|0\rangle, |1\rangle\}$ this state would be the same as $(|e\rangle + |g\rangle)\sqrt{2}$, which is seen for a qubit as a purely quantum state.

The main results of this chapter are the following

- realization of a power transfer controlled by the phase of a superposed state of the qubit using stimulated emission Fig. 3.7

- transient measurement of the power in a for different values of the drive amplitude, Fig. 3.11

- measured transfer efficiency of 63% for a qubit initially in $(|e\rangle \pm |g\rangle)/\sqrt{2}$, Fig. 3.10

Part II

CAVITY-FREE FLUXONIUM MEASUREMENT

In the previous part we emphasized the deep analogy between superconducting circuits and atomic physics. The evolution of a qubit under a drive is the same whether we consider real atoms or the two first states of a transmon, we recovered spontaneous and stimulated emission from the input-output formalism and we expressed the microwave measurements in terms of regular optics. However while most of quantum experiments based on atoms place them in free space, we embedded our qubit in a cavity. A cavity largely detuned from the qubit protects it by filtering out the electromagnetic environment and enhances its lifetime and coherence time, while offering an efficient readout (see Chap 1 and Appendix B). The reason why the cavity seems necessary to obtain a good qubit is that most of superconducting circuits (for instance the transmon) present transitions whose decay rates towards the 50Ω measurement port are of the same orders of magnitude. If we couple them directly to a dissipative environment we expect a very low coherence time in return. On the other hand, real atoms in free space present transitions that are strongly isolated from the environment where quantum information can be stored for very long times, and transitions strongly coupled to the environment that can be used to readout the quantum state. The question we want to address in this part is can we push the analogy with atomic physics further and directly couple a superconducting circuit to its environment while keeping a good coherence? To do so we need to design a circuit with several orders of magnitude between two types of transitions. This is the case with the fluxonium circuit which, unlike the transmon, presents a large variety of transitions with various frequencies and coupling rates.

Apart from proving that superconducting circuits can reproduce results obtained by the atomic physics community, the direct coupling of a circuit to the environment offers many advantages. It simplifies the quantum system under study, a process important for building a quantum network [43, 44]. In particular with this setup two fluxonium circuits could directly exchange excitations without having to convert a circuit excitation into a cavity one, as done recently [100, 101]. We also demonstrate how optical pumping can be implemented on this system to initialize the qubit. Finally, since our circuit is strongly coupled to the electromagnetic environment it naturally realizes a good noise spectrometer and can possibly lead to an efficient way of studying the various loss mechanisms in action in superconducting circuits.

In this part we describe the design and realization of the fluorescence readout of a fluxonium circuit. We detail how to engineer the coupling to the environment by choosing the right circuit parameters and by the use of a 3D waveguide, emphasize how to optimize the readout and present it in action. In a second time we study in detail the effect of the readout on the qubit logical subspace and the realization of optical pumping.

FLUORESCENCE READOUT OF A FLUXONIUM CIRCUIT

The principle of readout based on fluorescence is represented in Fig. 4.1. It is based on two distinct transitions with decay rates differing by orders of magnitude. The long-lived transition is chosen to be the logical qubit (represented by the $|0\rangle \rightarrow |1\rangle$ transition on the figure) where quantum information is stored. The short-lived transition is used as the readout transition as it is largely coupled to the environment (represented by $|0\rangle \rightarrow |R\rangle$ on the figure). To read the state of the qubit a drive is applied at the readout frequency ω_r. If the qubit is in the excited state $|1\rangle$ this drive is off-resonant and nothing happens. If the qubit is in $|0\rangle$, some population transits through the state $|R\rangle$ and eventually decays spontaneously towards $|0\rangle$ at a rate Γ_r while emitting fluorescence. If the fluorescence signal is collected by a detector it is thus possible to determine whether or not the qubit was initially in the ground state [42]. In the visible or near-visible range the fluorescence signal is detected by a photodiode. As we have seen in Sec. 2.3, linear detectors are more suited to microwave light. This change of the measured observable changes the expression of the optimal readout. In this chapter we present the design and characterization of two fluxonium circuits embedded in a waveguide, discuss the specificities of the fluorescence readout in the microwave domain and implement the readout scheme presented in Fig. 4.1. The main characteristics of the two fluxoniums are summarized in Table 4.1 at the end of the chapter together with the list of the related figures.
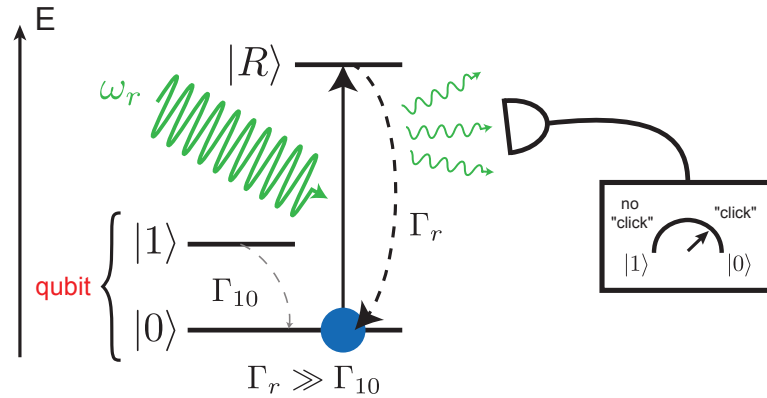
Figure 4.1: Principle of qubit state readout using fluorescence. A long-lifetime transition characterized by the decay rate Γ_{10} is chosen to be the logical qubit and is read using a readout transition strongly coupled to the environment with the rate Γ_r. Sending light at the readout frequency ω_r generates fluorescence of the system only if the qubit is initially in $|0\rangle$.

4.1 ENGINEERING THE COUPLING OF FLUXONIUM TRANSITIONS TO THE ENVIRONMENT

To implement a readout scheme similar to the one used in atomic physics we need to design a circuit with a transition strongly coupled to the electromagnetic environment

to maximize the rate of information extracted from the system, and another strongly isolated from any loss mechanism to protect quantum information. This situation is impossible in weakly anharmonic qubits, because all available transitions have similar frequencies and transition matrix elements. We describe in this section the different loss mechanisms affecting fluxonium circuits and present how we tailor the transitions as required by the proposed readout scheme.

4.1.1 *Loss mechanisms matrix elements*

Superconducting circuits suffer from losses due to various mechanisms. Indeed, they are coupled to many uncontrolled degrees of freedom, such as quasiparticles in the superconductor, impurities of the substrate, and obviously photons in the transmission lines [26, 27, 45, 47]. These degrees of freedom can be coupled to different operators of the circuit and therefore might exhibit a different evolution with the circuit parameters, for instance the frequency of the transition. The linear coupling between a decay channel represented by the operator $\hat{X}$ and the circuit can be expressed by the interaction Hamiltonian $H_{\text{int}} = A\hat{X}\hat{d}$ with $\hat{d}$ the generalized coordinate of the circuit. Using Fermi's Golden Rule, the relaxation rate from the eigenstate $|i\rangle$ to $|j\rangle$ is given by [102]

$$\Gamma_{i\to j} = \left(\frac{A}{\hbar}\right)^2 |d_{\text{ij}}|^2 S_X[\omega_{\text{ij}}] \tag{4.1}$$

with $S_X[\omega_{\text{ij}}]$ the noise spectral density of $\hat{X}$ at the transition frequency $\omega_{ij} = (E_j - E_i)/\hbar$ and $d_{ij} = \langle i|\hat{d}|j\rangle$ the matrix element of the circuit's coordinate. For an atom coupled to the electromagnetic field d_{ij} would be the dipole momentum of the $|i\rangle \to |j\rangle$ transition. For a circuit, the operator d depends on the type of loss considered.

a)   b)
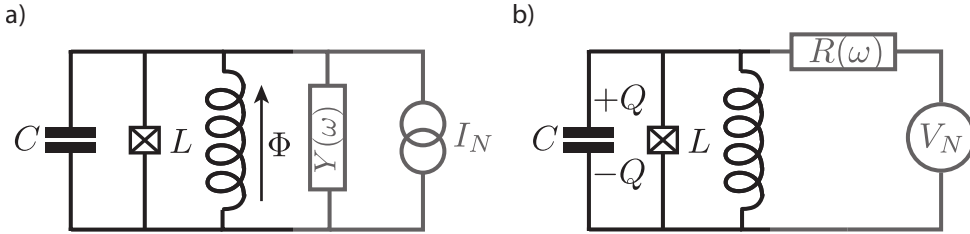
Figure 4.2: a) Norton and b) Thévenin equivalents of linear dissipation of a superconducting circuit. The circuit is either a) coupled through the flux to a noisy current source via an admittance or b) coupled through the charge to a noisy voltage source through an impedance.

Energy decay by spontaneous emission in the transmission lines and non-radiative decay due to a lossy dielectric have the common feature of being linear processes. A linear dissipation source is modeled by an admittance or an impedance coupling a fluctuating current or voltage source, respectively, to the circuit, as represented in Fig. 4.2. These two representations are the Norton and Thévenin equivalents, respectively. In the case of the admittance the coupling is made through the phase operator $\hat{\varphi}$ while it is made through the number of charge operator $\hat{n}$ for the impedance [11]. The phase and charge operators are conjugate variables of the circuit. Therefore their matrix elements are related by [25]

$$|n_{ij}| = |\varphi_{ij}|\frac{\omega_{ij}}{2\pi}R_Q C \tag{4.2}$$

with $R_Q = \frac{h}{(2e)^2}$ the resistance quantum. This relation can be demonstrated using the circuit Hamiltonian and the conjugation relation between $\hat{\varphi}$ and $\hat{n}$. The presence of the total shunting capacitance C (see Sec. 1.1) comes from the fact that it plays the role of the mass in the conjugation relation equivalent to the one of position and momentum of a particle. With this link between the phase and reduced charge operators it is possible to model any linear dissipation as affecting (for instance) the phase operator only and write $\hat{d} = \hat{\varphi}$, and to put the particular properties of the dissipation mechanism in the frequency evolution of the admittance $Y(\omega)$.

Unlike linear dissipation, quasiparticles tunneling in a Josephson junction cannot be represented electrically by coupling the circuit to a resistor because of the cosine relation between the phase and the current. For the fluxonium circuit described by the Hamiltonian of Eq. (1.15) the generalized coordinate for quasiparticle loss reads [27]

$$d_{ij} = \langle i| \sin\left(\frac{\hat{\varphi} - \varphi_{\text{ext}}}{2}\right)|j\rangle \tag{4.3}$$

with $\varphi_{\text{ext}} = 2\pi\Phi_{\text{ext}}/\Phi_0$ the phase bias due to an external magnetic field threading the loop. To design the circuits we only need the dependence of the loss rates with the matrix elements of the generalized coordinates. We give a quantitative description of the loss rates in Sec. 5.1.

4.1.2 *Purcell emission control*

With the expression of the decay rate in Eq. (4.1) we see that we can play on three knobs to control the energy decay into the environment. One can try to change the coupling constant A for a given loss mechanism by changing the design of the circuit. This is particularly the case in the recent pushes towards eliminating dielectric losses in 2D circuits, either by using trenches in coplanar waveguide architectures [103], using new materials as TiN [104], or using approaches combining the two [105]. The coupling to the measurement port can be modified by changing the electromagnetic coupling between the circuit and the transmission line, for instance by changing the size of the antennas of a 3D transmon. For our goal however, this approach cannot work as by changing the coupling constant we affect all the transitions by the same amount. The two other terms in $\Gamma_{i\to j}$ depend on the particular $|i\rangle \to |j\rangle$ transition and as such are the two parameters on which we will act. Fluxonium circuits have demonstrated the evolution of the matrix elements for linear and quasiparticle loss over three orders of magnitude for fluxon transitions by varying the external flux [26, 47]. On the other hand the presence of almost flux-independent transitions (plasmons) allowed to keep a non-zero dispersive shift with the readout cavity.

In general one does not try to play on the last term of the decay rate expression, because spectral density is usually a property of the bath and little can be done to affect it. One important exception is Purcell emission into the measurement port. The way the circuit is coupled to a transmission line directly affects the frequency variation of the noise spectral density seen by the circuit and hence its decay properties. This is the core of the Purcell effect where spontaneous emission of a qubit is strongly enhanced by embedding it in a resonant cavity of larger linewidth [21]. On the other hand, if the qubit is largely detuned from the cavity, the spectral density is strongly reduced at the qubit frequency and limits spontaneous emission. More generally, let us consider the coupling of the circuit to a transmission line through a "black box", an element described by its transmission coefficient $t(\omega) = S_{21}$ with S the scattering

matrix at frequency ω as represented in Fig. 4.3. To compute the spectral density seen by the qubit we need to consider the noise power transmitted by the box. The electromagnetic noise of the transmission line is hence filtered with the coefficient $|t|^2$. If we write explicitly the frequency dependence of the Purcell emission rate Γ^P we therefore obtain

$$\Gamma_{ij}^P \propto |\varphi_{ij}|^2 |t(\omega_{ij})|^2 S_{\text{line}}[\omega_{ij}] \tag{4.4}$$

with S_{line} the spectral density of noise in the line.
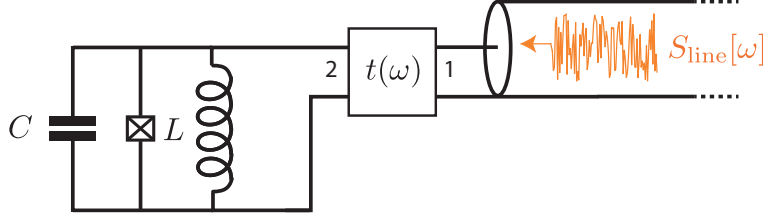
Figure 4.3: Spontaneous emission of a circuit into a transmission line controlled by a "black box" represented by the transmission coefficient $t(\omega)$. It has a filtering effect on the spectral density of noise seen by the circuit.

To reinforce the effect of the matrix elements, we therefore embed the fluxonium circuit in a homemade 3D-waveguide represented in Fig. 4.4a), and design the circuit such that the readout transition is above or close to the cutoff while the qubit transition stays below the cutoff[1]. The evolution of the waveguide's transmission coefficient with frequency is represented in Fig. 4.4b). By design the waveguide cutoff frequency is set around 7.5 GHz.
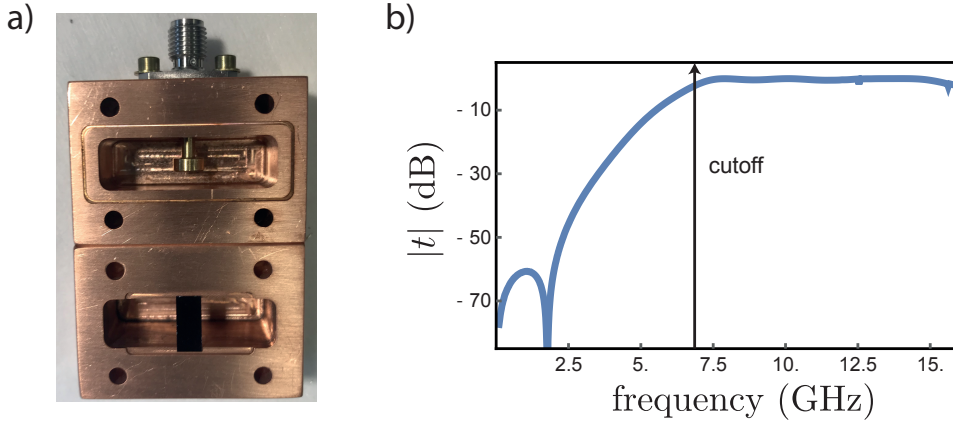
Figure 4.4: a) Picture of the homemade copper waveguide used in the experiments. b) Waveguide transmission coefficient as a function of frequency. The cutoff is represented by the black arrow.

4.1.3   *From design to circuit parameters*

In order to design a fluxonium circuit for fluorescence readout experiments we need to study two of its properties: the frequency of the transitions as they are affected by the

---

[1] As we will see in the following it is possible to use only one of the two knobs to ensure a good qubit transition. In some cases we will rely only upon the waveguide, in others only on the matrix element.

waveguide and their phase matrix element that can go to zero when selection rules apply. The first constraint we face is to design a readout transition with the right frequency. Plasmon transitions have a large matrix element because they correspond to intra-well oscillations and as such are a promising candidate for the readout. The frequency of the transition between two consecutive states of the same well is approximatively given by the plasma frequency of the Josephson junction (see Sec. 1.1)

$$\omega_p = \frac{1}{\hbar} \sqrt{8 E_C E_J} \ . \tag{4.5}$$

This is the resonance frequency of a transmon qubit. Our 3D fluxonium circuits have a design close to 3D transmons without the need to enter the transmon regime $E_J \gg E_C$ thanks to the inductive shunting of the small junction. Therefore we can play either on E_C or E_J to adapt the plasma frequency to the waveguide cutoff. We designed two different circuits to meet the frequency constraint on the readout frequency. Their parameters varied over the course of the experiment, mostly because of the aging of the junctions between different experimental runs (warm-up and cool-down cycles). Aging affected E_J and E_L by not more than 10% and almost did not change E_C, as the latter is set by geometrical properties. Nevertheless these small changes do not change the physical properties of the circuit and the scaling of frequencies and matrix elements.

The most straightforward way to increase the plasma frequency is to use a large Josephson energy E_J for the small junction. Moreover, since E_J sets the height of the energy barrier between the wells in the potential energy, the eigenstates are well localized in the wells and fluxon transitions are exponentially suppressed. We hence designed a first circuit "fluxonium A" with the parameters

- $E_C/\hbar = 2\pi \times 0.74$ GHz

- $E_J/\hbar = 2\pi \times 9.4$ GHz

- $E_L/\hbar = 2\pi \times 2.1$ GHz.

Images of the actual circuit are shown in Fig. 4.5a). Note that contrarily to the designs made in other groups [27–29], there is no resonator coupled to the fluxonium in this circuit.

The evolution of the lowest transitions $|0\rangle \rightarrow |i\rangle$ frequencies and phase matrix elements with the external flux for these parameters are represented in Fig. 4.6a) and b). We can see two transitions with very distinct behaviors. The plasmon (black dashed line) is almost constant and only varies within 1 GHz while the fluxon (red dashed line) is strongly flux dependent and almost reaches zero frequency at the half flux quantum $\Phi_{\text{ext}} = \Phi_0/2$. Fluxon and plasmon anticross at a certain value of flux quantum. The size of the anticrossing is given by the competition between E_L and E_J. The larger the ratio E_L/E_J, the larger the anticrossing. The hybridization between plasmon and fluxon at this point has a big effect on the phase matrix elements of the transitions. As expected the plasmon matrix element is large while the fluxon matrix element is ten times smaller when the two transitions are well separated. At the anticrossing however the two transitions have an equal matrix element at an intermediate value.

We represented in Fig. 4.6c) the circuit potential energy and the first eigenstates wavefunctions for the flux bias such that (c1) the fluxon has a higher frequency than the plasmon, (c2) fluxon and plasmon anticross, (c3) the fluxon has a lower frequency than the plasmon and (c4) the external flux equals half the flux quantum. It displays the clear signature of the hybridization of the states localized in the two wells at the
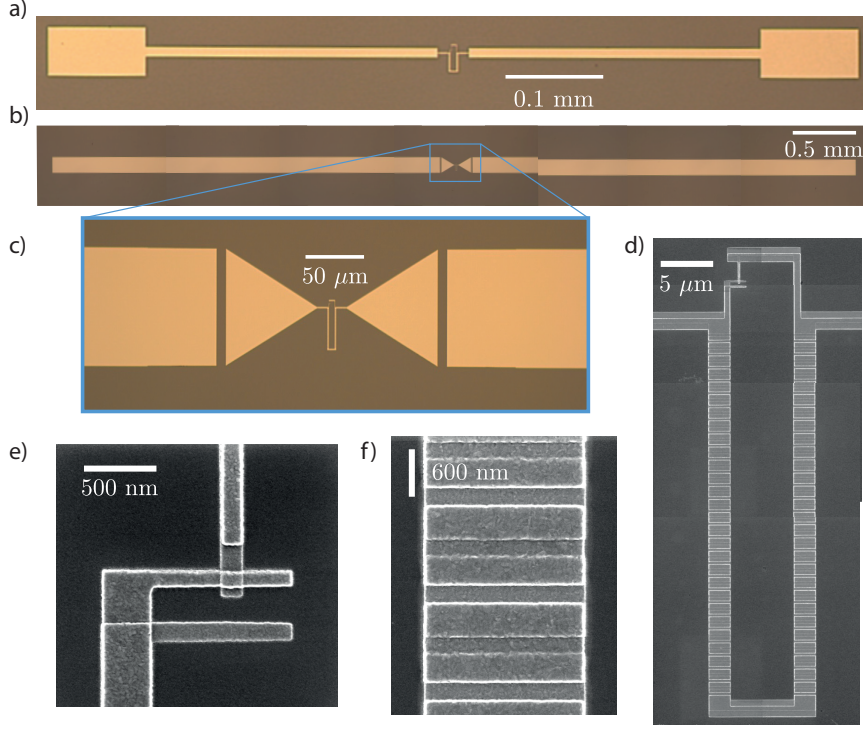
Figure 4.5: a) and b) Optical microscope pictures of the (respectively) 3D fluxonium ciruits A and B used in the experiments. Circuit B is capacitively coupled to long couplers to increase the coupling to the electromagnetic field. c) Zoom on the bow-tie-like antennas. d) Electronic microscope picture of the superconducting loop and zooms on the e) small junction and f) array of junctions realizing the superinductance.

anticrossing. At half flux quantum, the ground state and the first excited state consist of the symmetric and antisymmetric superpositions of the states localized in the left and right wells. Since the barrier between the two wells is high, the energy spacing between the two stays small. This sample is particularly suited to testing the feasibility of the readout for two reasons. First, the plasmon has a high frequency and high matrix element, and will naturally be strongly coupled to the transmission line. Second, the fluxon frequency varies over several GHz and we will be able to study the evolution of the lifetime of the fluxon with the frequency to test the influence of the waveguide. However we cannot expect this sample to show great performances in terms of coherence time. The fluxon frequency is strongly flux dependent and the coherence time will be limited by the first order flux noise in the loop. A solution would be to work at half flux quantum, where the first derivative of the frequency is zero. However for this circuit the qubit frequency is too low because of the high value of the Josephson energy. Therefore we designed a second circuit where it is possible to work at half flux quantum.

The objective for this second circuit is to lower the height of the barrier, hence E_J, and therefore to increase E_C to keep the plasma frequency around the waveguide cutoff. This means that we need to design a circuit with a small shunt capacitance. The shunt capacitance is the sum of the junction capacitance C_J fixed by the dimensions of the junction and the antenna capacitance C_a. The larger the fluxonium antennas, the smaller the charging energy. On the other hand, large antennas are necessary to increase the coupling to the electromagnetic field, hence help to maximize the rate at which information will be extracted from the system. To solve this tradeoff we design
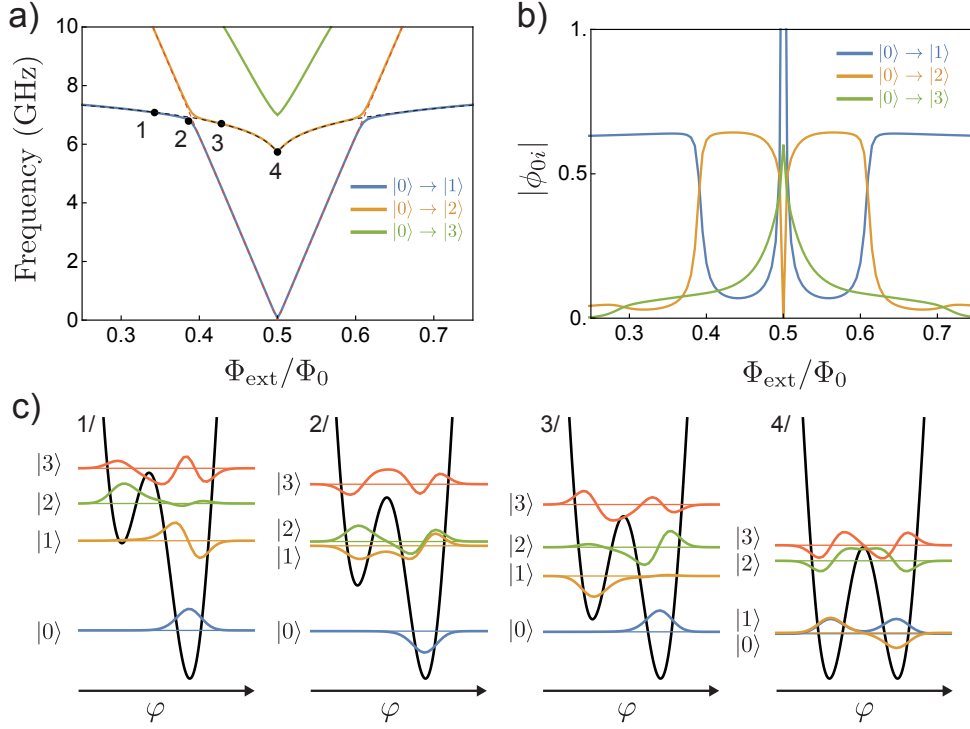
Figure 4.6: a) Frequency and b) phase matrix element of the first transitions of the fluxonium circuit A with $E_C/\hbar = 2\pi \times 0.74$ GHz, $E_J/\hbar = 2\pi \times 9.4$ GHz and $E_L/\hbar = 2\pi \times 2.1$ GHz as a function of the external flux. The plasmon and fluxon transitions are highlighted by respectively the black and red dashed lines.
c) Potential energy (black line) and first eigenstate wavefunctions at the 4 different flux points represented on a).

antennas with a bow-tie-like shape to minimize the shunting capacitance while keeping a large coupling to the field, and capacitively couple them to couplers made of a long stripline to further increase the coupling, see Fig. 4.5. Finite-element simulations of the electromagnetic field with the software "High Frequency Simulation Software" (HFSS) indicate that the couplers do not contribute to the shunting capacitance while they increase the coupling to the electromagnetic field by a factor of at least 2. With this design, the antenna capacitance C_a becomes of the same order of magnitude of the junction capacitance C_J. It allows us to design the second circuit called "fluxonium B" with the following parameters

- $E_C/\hbar = 2\pi \times 1.2$ GHz

- $E_J/\hbar = 2\pi \times 2.5$ GHz

- $E_L/\hbar = 2\pi \times 0.61$ GHz.

Since E_J is lower for this circuit than previously we also lower E_L to increase the anharmonicity of the excited states. With these parameters the plasma frequency is lower than the waveguide cutoff but this issue is resolved if we use the allowed $|0\rangle \to |3\rangle$ transition for the readout. This choice is reinforced by the fact that we want to use the circuit at half flux quantum, where a selection rule applies. Due to symmetry reasons the matrix elements of even transitions are exactly zero when $\Phi_\text{ext} = \Phi_0/2$. The selection rule appears very clearly on the evolution of the frequencies and matrix elements represented in Fig. 4.7a) and b). With the lower energy barrier between the

wells it becomes much harder to distinguish between plasmon and fluxon transitions. As displayed in Fig. 4.7c) the circuit eigenstates are largely delocalized in the two wells. A consequence is that the matrix element of the $|0\rangle \rightarrow |1\rangle$ transition is always larger than the one of other transitions. The presence of the waveguide will therefore be of first importance when we will be using this circuit.
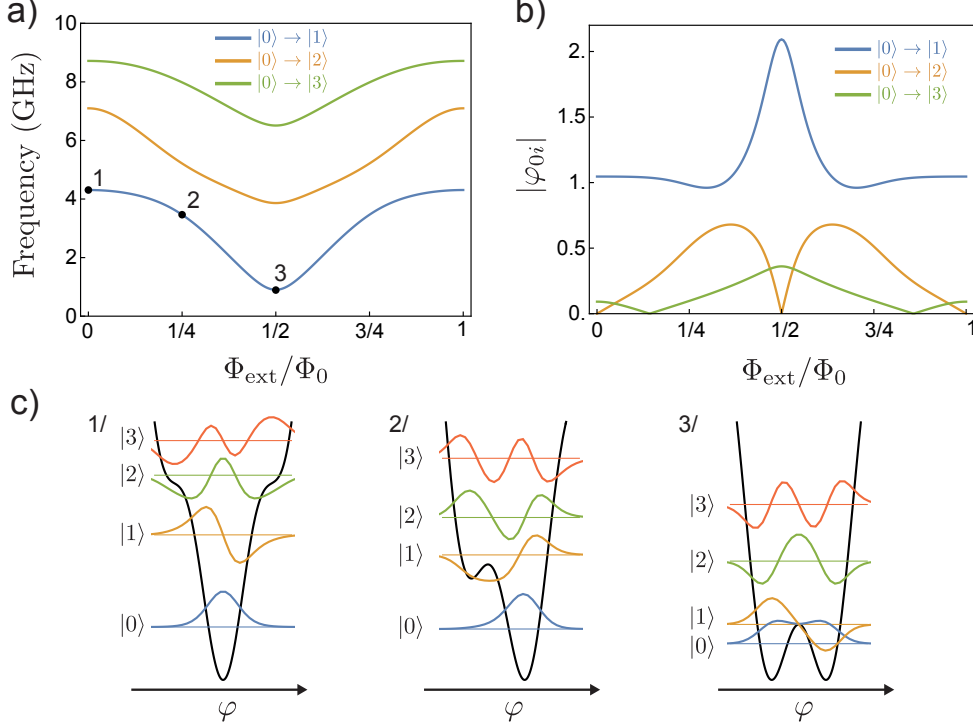
Figure 4.7: a) Frequency and b) phase matrix element of the first transitions of the fluxonium B circuit with $E_C/\hbar = 2\pi \times 1.2$ GHz, $E_J/\hbar = 2\pi \times 2.5$ GHz and $E_L/\hbar = 2\pi \times 0.61$ GHz as a function of the external flux.
c) Potential energy (black line) and first eigenstate wavefunctions at the 3 different flux points represented on a).

4.2 FLUORESCENCE READOUT

In this section we present and characterize the readout made by resonance fluorescence and the role of the waveguide on the qubit transition lifetime. In particular we highlight the difference between the realization of this readout using linear detectors of microwave instead of photodetectors as it is done in atomic physics.

4.2.1 *Optimal readout for quadrature measurements*

Atoms under a resonant drive emit light in the whole space around them. While stimulated emission stays within the driving laser, spontaneous emission is distributed as the emission of the dipole corresponding to the driven transition. To avoid being saturated by the drive the photodetector is placed outside the direction of propagation of the laser and detects the photons spontaneously emitted by the atom. According to Sec. 2.2.3 the amount of signal is hence proportional to the population in the excited state of the readout transition $|R\rangle$. Therefore the stronger the drive, the more signal is acquired

and the optimal driving amplitude is simply reached when it largely overcomes the losses. In fact, in atomic systems, the typical spontaneous emission linewidth of readout transitions is so large that the cycling Rabi frequency is always much smaller than this linewidth.

Even though we showed how it is possible to reconstruct the photon number emitted by a system from linear detectors, this operation relies on squaring the measured signal, and hence increases the effective noise. Therefore we do not have interest in copying the tools of atomic physics but better to adapt our measurement to the specificities of our detectors. As we have seen in Sec. 2.3, microwave detectors are sensitive to the amplitude of the fluorescence field emitted by the circuit hence the lowering operator of the readout transition $\sigma_-^R = |0\rangle\langle R|$. In order to maximize the amount of information collected by the detector, we remove one of the two ports of the waveguide and use a reflection measurement setup where we send a wave a_{in} and collect the reflected wave a_{out}. We write $\alpha_{\text{in}} = \langle a_{\text{in}}\rangle$. In all the following we will write Γ the Purcell rate of the readout transition towards the line. From the input-output relation in Eq. (2.19) the reflection coefficient r reads

$$r = \frac{\langle a_{\text{out}}\rangle}{\langle a_{\text{in}}\rangle} = 1 - \sqrt{\Gamma}\,\frac{\langle \sigma_-^R\rangle}{\alpha_{\text{in}}}\ . \tag{4.6}$$

From the steady-state expressions of the operators of a two-level system under a near-resonant drive in Eq. (2.14) and with $\langle\sigma_-^R\rangle = \left(\langle\sigma_x^R\rangle - i\langle\sigma_y^R\rangle\right)/2$ we obtain

$$r = 1 - \frac{\sqrt{\Gamma}\,\Omega}{2\alpha_{\text{in}}}\frac{\Gamma_1(\Gamma_2 + i\delta)}{\Gamma_1(\Gamma_2^2 + \delta^2) + \Gamma_2\Omega^2} \tag{4.7}$$

where Γ_1 and Γ_2 represent respectively the lifetime and coherence time of the readout transition, and $\Omega = 2\sqrt{\Gamma}\alpha_{\text{in}}$ is the Rabi frequency induced by the drive [32]. Since we designed the readout so that its Purcell rate is large, let us assume it dominates all the other energy decay and dephasing processes and write $\Gamma_1 = \Gamma$ and $\Gamma_2 = \Gamma/2$. Moreover the previous equation was obtained considering that all the population is initially in the ground state $|0\rangle$. If the population is initially in the qubit excited state $|1\rangle$ then the transition becomes transparent. We hence add the contrast factor corresponding to the population in the ground state p_0 and get

$$\boxed{\begin{aligned} r &= 1 - p_0\Gamma\,\frac{\Gamma/2 + i\delta}{\Gamma^2/4 + \delta^2 + \Omega^2/2} \\ &= 1 - 2p_0\frac{1 + 2i\frac{\delta}{\Gamma}}{1 + 4\left(\frac{\delta}{\Gamma}\right)^2 + 2\left(\frac{\Omega}{\Gamma}\right)^2}\ . \end{aligned}} \tag{4.8}$$

At infinitely low power $\Omega \ll \Gamma$ the reflection coefficient describes at circle of radius 2 centered around 0 in phase space when the detuning is swept between $\pm\infty$. It is then equivalent to a linear oscillator probed in reflection, which should not be surprising. At low drive power the system does not explore any other states than the ground and first excited state and it not possible to distinguish between a linear and a non-linear oscillator. At higher power we start saturating the transition and the reflection coefficient describes an oval. This is due to the steady-state of the qubit under a detuned Rabi drive as seen in Sec. 2.1.3, which describes an oval in the Bloch sphere (see Fig. 2.3).

The evolution of the reflection coefficient at thermal equilibrium with the detuning at various powers is represented for fluxonium A biased with $\Phi_{\text{ext}} = 0.32\Phi_0$ in Fig. 4.8.

We fit the experimental data with the theoretical equation (4.8) with four fitting parameters, the thermal equilibrium population in the ground state p_0^{th}, the resonance frequency of the transition f_0, the Purcell rate Γ and the scaling factor between the drive amplitude and the Rabi frequency Ω. We obtain $\Gamma = 2\pi \times 6.5$ MHz and $p_0^{\text{th}} = 96\%$. If we compare this value to other decay and dephasing processes obtained with a very similar chip in [26] this allows us to justify our previous assumption that spontaneous emission is the dominant process for the readout transition.
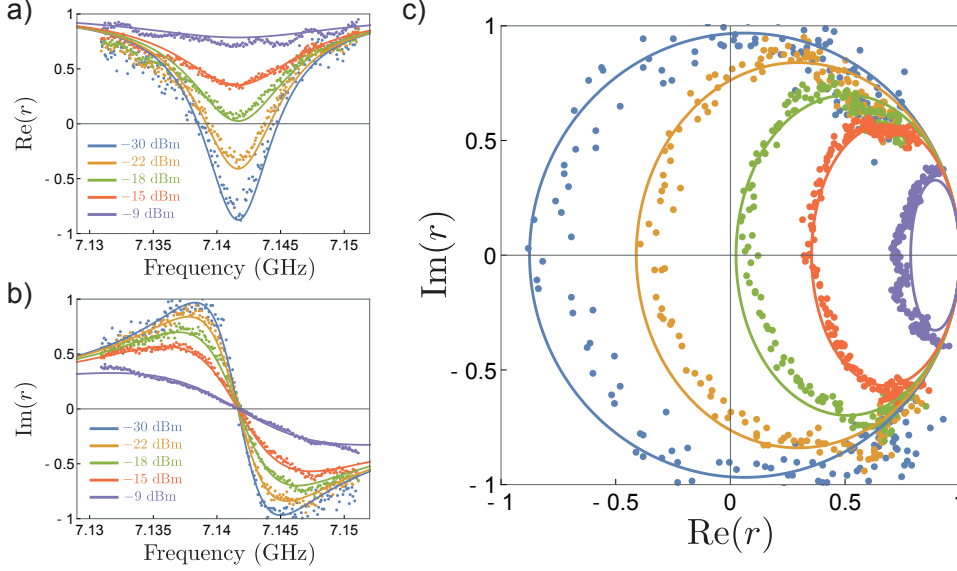
Figure 4.8: Fluorescence readout calibration. a) Real and b) imaginary parts of the reflection coefficient around readout transition and c) parametric plot for fluxonium A biased with $\Phi_{\text{ext}} = 0.32\Phi_0$. The data (points) are displayed with the theory (plain lines) with $\Gamma = 2\pi \times 6.5$ MHz and $p_0 = 96\%$.

From this measurement we can deduce the readout parameters that maximize the signal to noise ratio (SNR). What we detect is a change of the reflection coefficient with the ground state population. In particular $p_0 = 0$ always corresponds to $r = 1$. On resonance we thus have

$$
\boxed{
\begin{aligned}
p_0 &= 0 \Leftrightarrow r = 1 \\
p_0 &= 1 \Leftrightarrow r = 1 - \frac{2}{1 + 2(\Omega/\Gamma)^2}
\end{aligned}
}
\qquad (4.9)
$$

Note that one should not maximize the swing of the reflection coefficient at resonance $r(\delta = 0)$ between the two qubit states. This quantity is maximized on the limit of vanishing drive power such that the fluorescence signal is vanishing as well. To maximize the SNR we need to maximize the steady-state value of $\langle \sigma_-^R \rangle$. As we described in 2.1.3 the maximum can be reached when $\Omega \geq \Gamma/\sqrt{2}$. Even though one can adapt the detuning to get to the maximum when $\Omega > \Gamma/\sqrt{2}$, we choose to set $\delta = 0$ and work at the power so that $\Omega = \Gamma/\sqrt{2}$. This value of the drive amplitude is particularly easy to obtain from the reflection coefficient measurement. When $p_0 = 1$ it corresponds to the power reaching total extinction on resonance $r = 0$.

4.2.2 *Fluxonium spectrum*

To obtain the spectrum of the fluxonium we fix the readout power near the optimum and sweep the readout frequency and the external flux. With this technique we expect to see only the resonances that have both a high frequency and a large matrix element. When we sweep the external flux we also change the matrix element, so strictly speaking the readout power is not optimal for all fluxes. Nevertheless it is enough to get a good contrast and extract the spectrum. We display the evolution of the real part of the reflection coefficient as a function of frequency and external flux for the two fluxonium circuits in Fig. 4.9. The spectra are fitted to extract the circuit parameters. For the fluxonium A we are able to distinguish two transitions when the flux is set near the anticrossing because the plasmon and fluxon transitions hybridize strongly. The spectrum of the fluxonium B is represented near half flux quantum because it is where we expect to get the best coherence time. The readout is set on the $|0\rangle \to |3\rangle$ transition whose matrix element decays as soon as we go away from $\Phi_{\mathrm{ext}} = \Phi_0/2$. We also note that this measurement looks noisier than the previous one. It is mostly due to the thermal occupation of the first excited state $|1\rangle$ because, as we saw in Fig. 4.7, the frequency of the $|0\rangle \to |1\rangle$ transition lies around 1 GHz and the typical temperature of such circuits is between 20 and 100 mK.
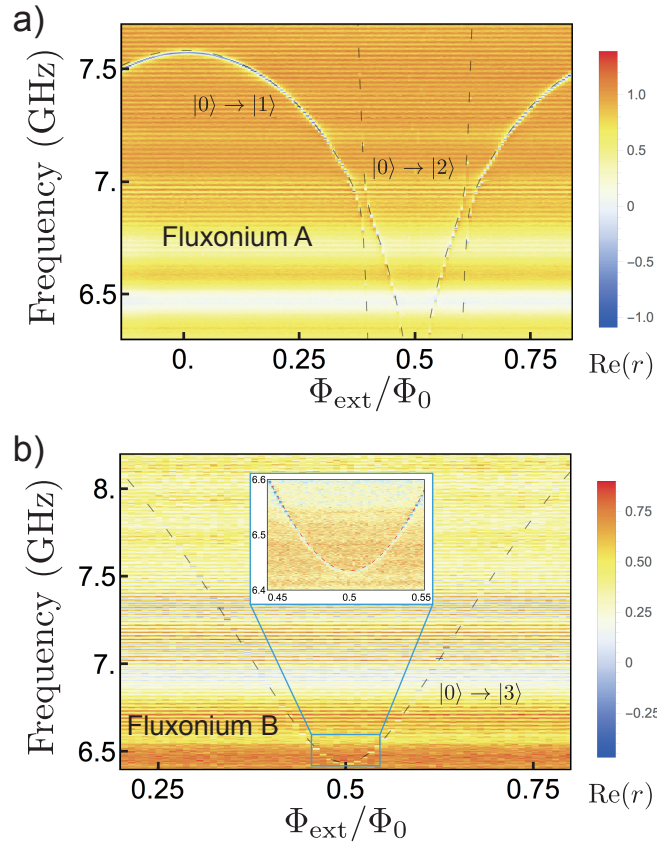
Figure 4.9: Evolution of the real part of the reflection coefficient with the frequency and the external flux for a) fluxonium A and b) fluxonium B. The theoretical fit of the resonance frequencies is represented by the dashed lines. They give parameters close to the ones in Table 4.1.

4.2.3 *Qubit transition readout*

After validating the principle of the readout by fluorescence and in particular having found the optimal readout power we now characterize the qubit transitions. We perform a simple two-tone spectroscopy consisting of a long saturation pulse around the qubit frequency followed by a readout pulse. We expect to measure a change in the reflection coefficient proportional to the change of population in the ground state when we hit the qubit transition frequency. An example of such a two-ton spectroscopy is represented in Fig. 4.10a), for the fluxonium A flux-biased before the anticrossing. At this point the plasmon transition is lower than the fluxon one and the readout frequency $f_R = 7.143$ GHz is lower than the qubit frequency $f_R = 10.943$ GHz. To highlight the difference between this readout and a dispersive readout based on a cavity we sweep the readout frequency near the resonance preceded or not by a qubit saturation pulse. With a dispersive readout we would await a shift of the resonance when we excite the qubit. It is not the case here as shown in Fig. 4.10b), where we only lose the contrast of the jump of reflection coefficient as represented by the theoretical lines where the only changed parameter is the ground state population. We can note a slight deviation of the experimental data from theory near 7.155 GHz, where the reflection coefficient exhibits an oscillatory behavior. This is due to the presence of spurious modes (see Sec. D.1).
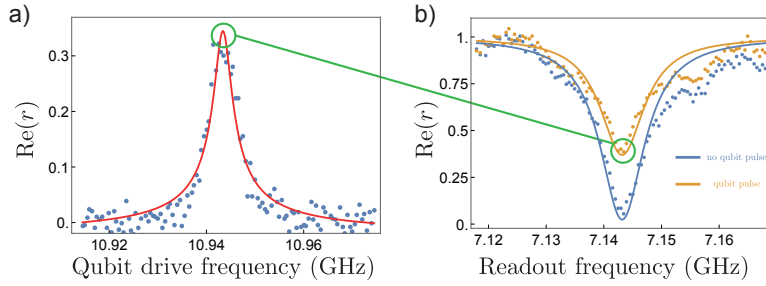
Figure 4.10: Qubit two-ton spectroscopy of fluxonium A. a) Evolution of the real part of the reflection coefficient measured at the readout frequency with the qubit drive frequency, (points) experimental data and (line) theoretical lorentzian response. b) Readout spectroscopy preceded (orange) or not (blue) by a qubit pulse, (point) experiment and (line) theory from Eq. (4.8) with $p_0 = 0.96$ (blue) and $p_0 = 0.62$ (orange).

Just like we extracted the fluxonium spectrum with a one-tone spectroscopy we can measure the evolution of the qubit frequency with the external flux. To do so we have to take into account the change of the readout frequency with the flux. Concretely we use the theoretical evolution of the readout frequencies obtained from the fitted circuit parameters to take a short readout spectroscopy in a small frequency window for each flux. The readout frequency is found automatically by taking the minimum of the real part of the reflection coefficient before performing a two-tone spectroscopy. We show an example of a flux-dependent two-tone spectroscopy in Fig. 4.11 for the fluxonium A. As we would expect from the circuit parameters and the first spectroscopy the fluxon frequency varies over several GHz when Φ_{ext} is changed by less than $0.05\Phi_0$. The fact that we can successfully track the qubit transition over a large frequency span demonstrates the robustness of our new readout.
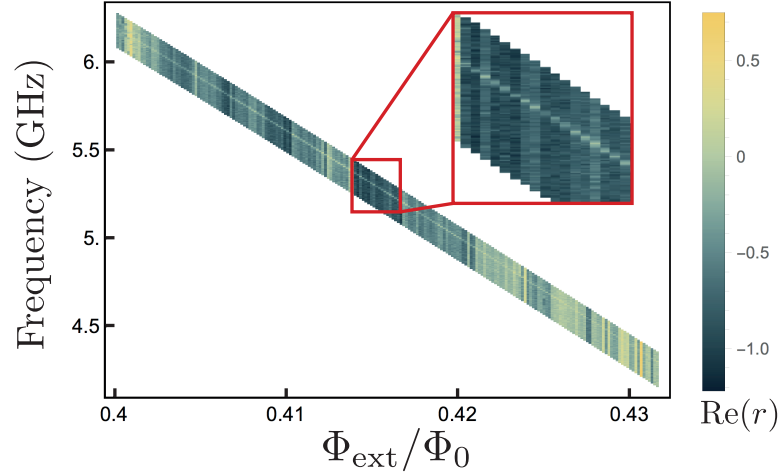
Figure 4.11: Qubit spectroscopy versus flux for fluxonium A. At each point of flux the readout frequency is measured and extracted before performing the two-tone spectroscopy.

4.3 QUBIT COHERENT MANIPULATIONS

So far we have demonstrated how to use the fluorescence readout to extract the circuit parameters and perform qubit spectroscopy. Let us now characterize the qubit in time domain and discuss the perspectives offered by our system for quantum information. In this section we present the coherent manipulation of the qubit read by the fluorescence readout scheme, highlight the role of the waveguide for the qubit lifetime and present the qubit coherence times for the two circuits at different flux points.

4.3.1 Rabi oscillations
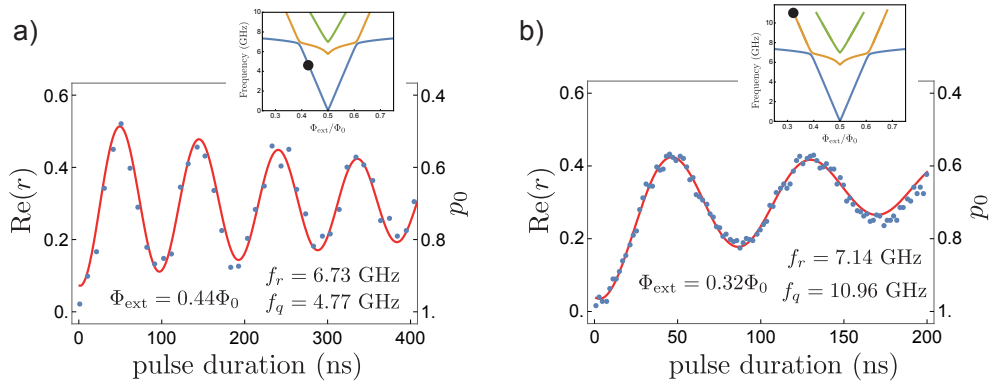
Figure 4.12: Rabi oscillations of the qubit transition of the fluxonium A measured in fluorescence at two different flux points represented in the insets (the black dots represent the frequency of the qubit transition). The reflection coefficient (left axis) is equal to $1 - 2p_0C$ where p_0 is the population in the ground state (right axis) and C a constant depending on the readout power. The experimental points are represented together with the theory (red line). In a) we use an exponentially decreasing cosine while in b) we add an exponentially decreasing constant term to take into account the decay towards other states.

We start by measuring Rabi oscillations of the qubit transitions. We drive the chosen qubit transition with a square pulse and study the evolution of the reflection coefficient at the readout frequency with the duration of the qubit pulse. For the fluxonium A we recall that the readout transition is the first plasmon while the qubit transition is the fluxon transition. Two examples of Rabi oscillations obtained for the fluxonium A are represented in Fig. 4.12. On Fig 4.12a) we set $\Phi_{\text{ext}} = 0.44\Phi_0$ and obtain a qubit frequency $f_q = 4.77$ GHz lower than the readout frequency $f_r = 6.73$ GHz. in Fig. 4.12b) we set $\Phi_{\text{ext}} = 0.32\Phi_0$ and $f_q = 10.96$ GHz is higher than $f_r = 7.14$ GHz. We convert the reflection coefficient into the ground state population using Eq. (4.8). Importantly, a reflection coefficient equal to 1 indicates that there is no population left in the ground state, no matter the readout amplitude. The reflection coefficient, and hence the ground state population, is integrated during the whole duration of the readout and because of energy decay during the readout we do not measure $p_0 = 0$ after a π-pulse. The amplitude of the two Rabi oscillations are the same at the two flux points because the effect of temperature is negligible at the readout and qubit frequencies. We obtain a π-pulse duration of about 50 ns in both cases. The fact that we can still observe coherent oscillations of the fluxon transition when the latter is near 11 GHz is remarkable. Indeed such a frequency is far above the waveguide cutoff therefore the transition is not protected by the waveguide at all. We only rely here on the weak matrix element of the transition to limit energy decay. On Fig 4.12b) we can note also that the oscillations do not decay towards the center of the oscillations as we would expect from the solutions of the Bloch equations. This is due to the fact that there is one (or more) state between the ground and the excited state used for the qubit transition. Here the readout frequency is lower than the qubit one. As a result, population can decay from the logical excited state $|2\rangle$ to the readout excited state $|1\rangle$. We will use this effect in the next chapter to reset the qubit by optical pumping. For quantum information purposes however this effect is detrimental as population exits the logical computational subspace.
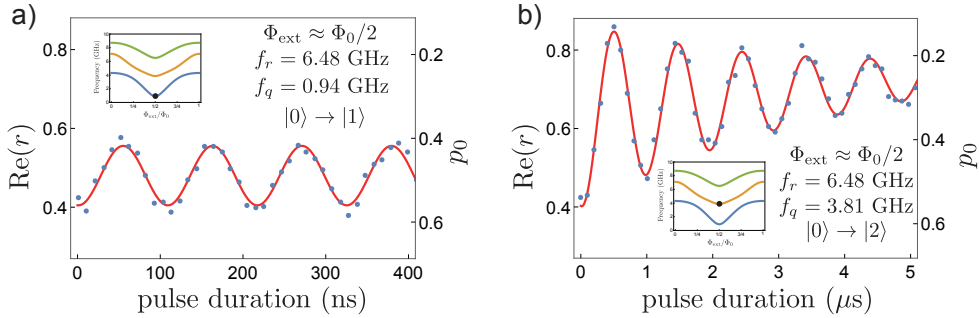
Figure 4.13: Rabi oscillations of the a) $|0\rangle \rightarrow |1\rangle$ transition and b) $|0\rangle \rightarrow |2\rangle$ transition of fluxonium B near half flux quantum, (points) data and (line) fit with exponentially decreasing sine with $p_0^{\text{th}} = 0.56$, $p_1^{\text{th}} = 0.35$ and $p_2^{\text{th}} = 0.09$. In b) we add an exponentially decreasing constant to take into account pumping to excited states.

For the fluxonium B we only present Rabi oscillations near half flux quantum since it is the flux point at which we get the lowest flux noise, thus the smallest dephasing rate. The readout transition is then $|0\rangle \rightarrow |3\rangle$ and we can think of two possible qubit transitions, either $|0\rangle \rightarrow |1\rangle$ or $|0\rangle \rightarrow |2\rangle$. At exactly half flux quantum the matrix element of the latter is exactly 0 because of the appearance of a selection rule. This selection rule is quickly lifted if we move a little bit away from half flux quantum

since the evolution of the matrix element is similar to an absolute value near half flux quantum as we saw in Fig. 4.7b). On the other hand the frequencies are quadratic near $\Phi_{\text{ext}} = \Phi_0/2$ and the coherence should stay near its maximum. Therefore we set the flux to $\Phi_{\text{ext}} = (1/2 + 2.6 \times 10^{-3})\Phi_0$ which allows us to drive the $|0\rangle \rightarrow |2\rangle$ transition. The Rabi oscillations of the two transitions are represented in Fig. 4.13. The $|0\rangle \rightarrow |1\rangle$ transition frequency is 0.94 GHz and the $|0\rangle \rightarrow |2\rangle$ one is 3.81 GHz.

When the qubit frequency is less than 1 GHz the thermal occupation of the first excited state becomes large and the amplitude of the oscillations is largely reduced as shown in Fig. 4.13a). For the second transition the amplitude is larger because state $|2\rangle$ is barely occupied, therefore we almost entirely empty the ground state when performing a π-pulse. More precisely we measure the thermal equilibrium population in the ground state $p_0^{\text{th}} = 0.56$, corresponding to a temperature $T = 98$ mK. This gives the estimate populations in the first and second excited state $p_1^{\text{th}} = 0.35$ and $p_2^{\text{th}} = 0.09$, in good agreement with the amplitudes of the Rabi oscillations. When we drive the second transition we note again the presence of decay towards the first excited state. Because of the small matrix element of the transition we cannot get a faster π-pulse duration than 500 ns. In the following we will focus ourselves on the first transition to be the logical qubit, and use the second one either to perform optical pumping or to study the various decay mechanisms.

4.3.2 *Qubit lifetime and role of the waveguide*
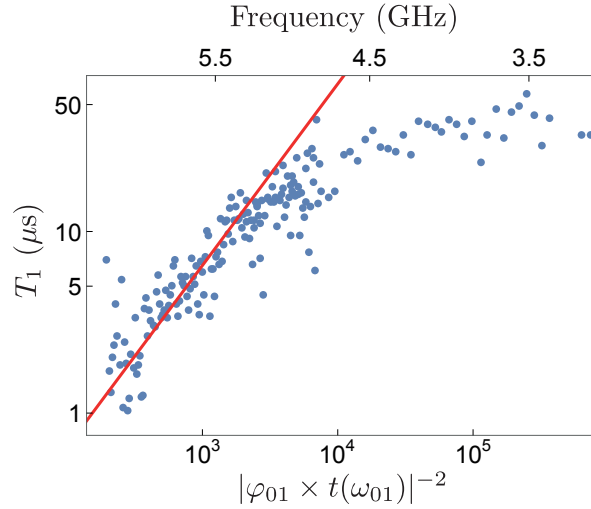
Figure 4.14: Evolution of the qubit transition lifetime of fluxonium A with the phase matrix element φ_{01} and the waveguide transmission coefficient at qubit frequency $t(\omega_{01})$. The points are experimental data and the red line represents a linear relation.

The qubit lifetime is affected by the several loss mechanisms described in Sec. 4.1.1. We use the waveguide to filter the electromagnetic environment associated with the readout port and therefore diminish the Purcell emission rate of the qubit transition. On the fluxonium A we saw that we can tune the qubit frequency over several GHz. Since the waveguide transmission coefficient has been measured independently, it is possible to test the relation linking the Purcell rate to the waveguide transmission and the qubit matrix element in Eq. (4.4). Concretely, we tune the external flux from

0.8π to 0.93π, and at each point we automatically measure the readout frequency, qubit frequency, and qubit transition lifetime. For each qubit frequency we extract the waveguide transmission coefficient using the measurement presented in Fig. 4.4b) and compute the phase matrix element (see Fig. 4.6b). The evolution of the qubit lifetime as a function of $|\varphi_{01} \times t(\omega_{01})|^{-2}$ is represented in Fig. 4.14. The lifetime is increased by a factor 40 when the qubit transition goes from 6 GHz to 3 GHz because the waveguide filters more strongly towards lower frequency. The evolution exhibits a linear part represented by the red line, which indicates that in this region T_1 is directly limited by Purcell emission and is hence proportional to the inverse square of the matrix element and waveguide transmission coefficient. After this linear evolution the lifetime saturates because other decay processes such as dielectric loss take over.

When we work with fluxonium B at half flux quantum the matrix element of the $|0\rangle \to |1\rangle$ transition is at its maximum as represented in Fig. 4.7b). It is balanced by the very low frequency that will strongly suppress Purcell emission. Moreover having a low-frequency qubit generally improves the lifetime because is reduces the spectral density of noise associated with dielectric noise (see Sec. 5.1). We will provide a more precise description of the decay processes in action in the circuit in the next chapter. The lifetime measurement of $|1\rangle$ is show in Fig. 4.15a) and gives $T_1 = 40$ μs[2]. Measuring the lifetime of $|2\rangle$ is less straightforward as our readout is sensitive to the population in the ground state only while $|2\rangle$ can decay to both $|0\rangle$ and $|1\rangle$. However doing a lifetime-like measurement for this transition is not meaningless as it provides a global relaxation time to thermal equilibrium. The evolution of the ground state population with the delay time when the qubit is initialized in the second excited state is represented in Fig. 4.15b). It presents a double-exponential behavior with the short and long times $T_1^s = 4.2$ μs and $T_1^l = 44$ μs, possibly indicating the presence of quasiparticles (see Sec. 5.1 for a more precise treatment).
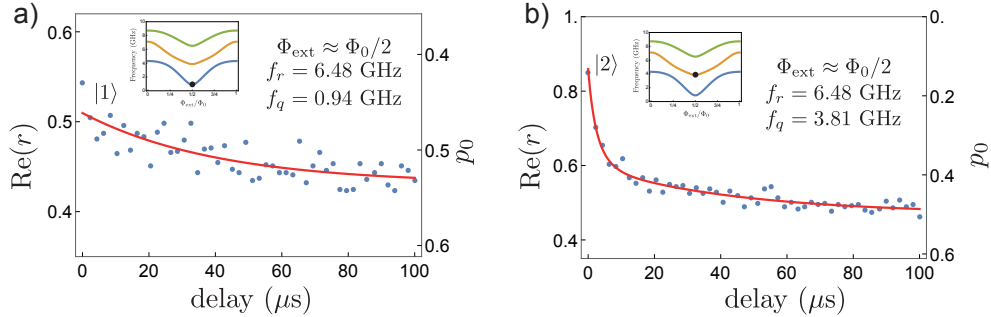
Figure 4.15: Evolution of the ground state population as a function of the waiting time between initialization and measurement when the system is initialized in a) $|1\rangle$ and b) $|2\rangle$ for the fluxonium B at half flux quantum, (points) data and (red line) theory with a single exponential decay with the lifetime $T_1 = 40$ μs for a) and a double exponential decay with $T_1^s = 4.2$ μs and $T_1^l = 44$ μs.

---

2 Because of the noise in the measurement it is not possible to discriminate between simple and double exponential decays. Double-exponential decays have been measured for this transition and are discussed in details in Sec. 5.1.

4.3.3 Coherence time

The downside of circuits whose frequencies are flux-tunable is dephasing due to magnetic flux noise. Indeed, flux fluctuations generate small frequency variations around a mean value and therefore generate dephasing of superpositions of states. If we consider the transition $|i\rangle \rightarrow |j\rangle$ only we can approximate it at first order by a two-level system and write its Hamiltonian as $H \approx \hbar\omega_{ij}(\Phi_{\text{ext}})\sigma_z^{ij}/2$ where we kept the explicit dependence of the frequency with the external flux[3]. We decompose the external flux into $\Phi_{\text{ext}} = \Phi_{\text{ext}}^0 + \delta\Phi$ where Φ_{ext}^0 is the constant term and $\delta\Phi$ is a random variable centered around 0 representing the fluctuations. The Hamiltonian can hence be decomposed as $H = H^0 + \delta H$ with

$$
\begin{aligned}
H^0 &\approx \hbar\omega_{ij}(\Phi_{\text{ext}}^0)\frac{\sigma_z^{ij}}{2} \\
\delta H &\approx \hbar\delta\Phi\frac{\partial\omega_{ij}}{\partial\Phi_{\text{ext}}}\bigg|_{\Phi_{\text{ext}}^0}\frac{\sigma_z^{ij}}{2} \ .
\end{aligned}
\tag{4.10}
$$

The time decay of the coherences due to flux noise depends on the time properties of the random variable $\delta\Phi$. If the noise can be considered uncorrelated then we can apply the Bloch-Redfield theory and obtain an exponential decay with the rate

$$
\Gamma_\varphi^{ij} = \frac{1}{2}\left(\frac{\partial\omega_{ij}}{\partial\Phi_{\text{ext}}}\right)^2\bigg|_{\Phi_{\text{ext}}^0} S_{\delta\Phi}[\omega = 0]
\tag{4.11}
$$

where $S_{\delta\Phi}$ denotes the spectral density of noise of the fluctuations [106]. The derivation assumes that the noise is constant in a frequency window contained between 0 and frequencies of the order of Γ_φ^{ij}. At low frequencies this assumption breaks down as $1/f$ noise becomes larger than white noise (the spectral density is even singular at $\omega = 0$). If we follow the derivation with a $1/f$ noise instead, then the decoherence should follow a gaussian shape $\exp(-(\Gamma_\varphi^{ij}t)^2)$ with [106–108].

$$
\Gamma_\varphi^{ij} = \frac{\partial\omega_{ij}}{\partial\Phi_{\text{ext}}}\bigg|_{\Phi_{\text{ext}}^0} A\sqrt{\ln 2}
\tag{4.12}
$$

where A is a parameter representing the flux noise expressed in units of Φ_0. Note that the fact that the spectral density varies as $1/f$ is by itself an approximation, as it has been shown that a more general variation in $1/f^\alpha$ with $0.61 \leq \alpha \leq 0.95$ seems to represent better the experimental observations [109, 110].

In any case the coherence time of the qubit transition of the fluxonium A biased away from the sweet spot is strongly reduced because of the factor $\frac{\partial\omega_{ij}}{\partial\Phi_{\text{ext}}}$ and we expect the coherence time to be much better for the fluxonium B at half flux quantum as $\frac{\partial\omega_{ij}}{\partial\Phi_{\text{ext}}}\big|_{\Phi_0/2} = 0$. We measure the coherence time by a Ramsey experiment constituted of two $\pi/2$-pulses separated by a delay. We present the result of two Ramsey experiments for the fluxon of the fluxonium A in Fig. 4.16a) and for the qubit transition of the fluxonium B at half flux quantum in Fig. 4.16b). On the experimental data it can be hard to distinguish between simple exponential and gaussian decay. To illustrate this point we displayed the two possible theory lines in Fig. 4.16a), in the red dashed line for exponential decay and green plain line for gaussian decay, with the respective decay times $T_2 = 220$ ns and $T_2 = 280$ ns. At this flux point the qubit lifetime has been

---

3 This assumption is true as long as there are no other transitions resonant with ω_{ij}.

measured around 20 μs, hence we can write $T_2 = \Gamma_\phi^{-1}$. Applied to the $1/f$ noise scenario this value gives $A \approx 10^{-5}\Phi_0$. For well-controlled magnetic environments in presence of filtered DC sources and magnetic shields, the origin of flux noise is to be found in the substrate itself [111–113] and the value $A \approx 10^{-6}\Phi_0$ has been consistently reported in many independent experiments [106–109, 112]. Moreover an experiment ran in our group with the same experimental setup, coil, wiring, current source and magnetic shield but with a 3D fluxonium embedded in a cavity also reported $A \approx 10^{-6}\Phi_0$. We do not have an explanation for this difference yet and it might require a more careful analysis. One can assume that high frequency electromagnetic noise plays a role in this faster dephasing, since high frequencies are not cut by the waveguide.
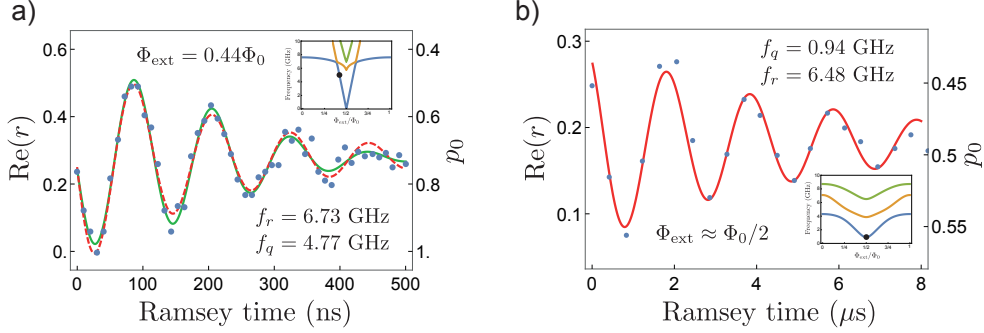
Figure 4.16: Qubit Ramsey oscillations measurement. a) The fluxonium A is sensitive to flux noise. The Ramsey decay is fitted either by a simple exponential decay with $T_2 = $ 220 ns (red dashed line) or by a gaussian decay with $T_2 = 280$ ns (green plain line). b) The qubit transition of the fluxonium B at the half flux quantum is protected from first order flux noise. The decay of Ramsey oscillations is well reproduced with $T_2 = 5.3$ μs.

When the qubit is at the sweet spot the first order equations of the decay rates are not valid anymore and the coherence time is be limited by other effects. Therefore we chose to describe the decay of Ramsey oscillations by a simple exponential with a time $T_2 = 5.3$ μs. Note that in Fig. 4.16b), the power of the readout has been changed compared to the previous Rabi measurement, therefore the absolute value of the reflection coefficient has shifted. Since we have measured $T_1 = 40$ μs at this point, we are far from having a coherence time T_1-limited. It means that other decoherence processes are acting in this circuit. Again we can invoke high frequency noise to explain these results, at it can generate measurement-induced dephasing due to high-frequency transitions.

4.4 CONCLUSION

The fluorescence readout scheme implemented on a fluxonium circuit open to a transmission line demonstrates the versatility of superconducting circuits and their ability to reproduce and adapt atomic physics experiments. In particular we discussed the design of strongly and weakly coupled transitions necessary to the realization of the readout and the specificities of performing the readout in the microwave domain. By embedding the circuit in a waveguide we consistently measure degraded coherence times compared to almost similar circuits in a cavity. The role of high-frequency transitions, as well as

quasiparticles possibly excited by high frequency noise has yet to be specified. The next chapter studies in more details this point.

The main unpublished results of this chapter are the following

- determination of the readout expression and optimum, Eq. (4.8) and Fig. 4.8

- qubit two-time spectroscopy with fluorescence readout, Fig. 4.10

- qubit coherent excitation and readout without a cavity, Fig. 4.12 and 4.13

- role of the waveguide on qubit transition lifetime, Fig. 4.14.

We summarize in the table below the experimental results obtained for the two fluxonium circuits A and B.

	Fluxonium A	FluxoniumB
E_C	$h \times 0.75$ GHz	$h \times 1.2$ GHz
E_J	$h \times 9.4$ GHz	$h \times 2.5$ GHz
E_L	$h \times 2.1$ GHz	$h \times 0.61$ GHz
readout transition	plasmon	$|0\rangle \leftrightarrow |3\rangle$
calculated spectrum	Fig. 4.6	Fig. 4.7
experimental spectrum	Fig. 4.9a)	Fig. 4.9b)
Rabi oscillations	Fig. 4.12	Fig. 4.13
Lifetime measurement	Fig. 4.14	Fig. 4.15
Ramsey measurement	Fig. 4.16a)	Fig. 4.16b)

Table 4.1: Fluxonium circuits used in the experiments.

INCOHERENT PROCESSES IN FLUXONIUM

Energy decay and decoherence induce errors for the storage and manipulation of quantum information but can also be used practically. For instance autonomous stabilization of quantum superpositions of states have been demonstrated in superconducting circuits by carefully engineering the system-environment interaction [48–51], and qubit initialization with a good fidelity was obtained by transferring thermal excitations to a dissipative resonator using a pump [114, 115]. This chapter is devoted to the determination of the detrimental and useful effects due to incoherent processes in action in the fluxonium circuit embedded in a waveguide and measured using the fluorescence readout presented in Chap. 4. We show examples and discuss quantitatively the role of the various loss mechanisms in the circuit and study two important effects. First, when quantum states are present between the two states used for the readout, population can decay out of the readout subspace. To reach a Quantum Non Demolition (QND) readout it is hence necessary to maximize the branching ratio of the readout transition. We quantify it experimentally and propose an interpretation in terms of dielectric loss. Second, it is possible to reset the state of the qubit using optical pumping schemes similar to atomic physics. This reset is of first importance when working at frequencies below 1 GHz because thermal occupation is then large. We present and characterize different schemes and study the effect of the pump on the circuit coherence. All the experiments presented in this chapter are done on the fluxonium B biased at half flux quantum (see its spectrum in Fig. 4.7) and measured using the transition $|0\rangle \rightarrow |3\rangle$.

5.1 DISCRIMINATING BETWEEN LOSS MECHANISMS

In this section we give a more complete description of the fluxonium relaxation mechanisms presented in Sec. 4.3.2. We highlight the role of quasiparticles in decoherence and discuss their role in the time fluctuations of the relaxation rate. In order to distinguish between the possible processes we estimate the order of magnitude of these processes with the goal of further explaining the results obtained about the branching ratio and optical pumping.

5.1.1 *Effects of quasiparticles on relaxation*

The double exponential decay from state $|2\rangle$ in Fig. 4.15b) is typical of energy relaxation due to quasiparticles [27, 47, 116]. The fluctuations of the quasiparticle population are time-averaged by the energy decay measurement, resulting in the double exponential behavior. When the fluxonium was decaying from $|1\rangle$ we found a simple exponential (see Fig. 4.15a). With a more careful study a double exponential decay appears for some realizations of the experiment as represented in Fig. 5.1. in Fig. 5.1a) we performed a π-pulse to exchange the populations of $|0\rangle$ and $|1\rangle$. Since the frequency of the first transition is 0.94 GHz, the difference between the thermal equilibrium populations in the ground $p_0^{\text{th}} = 0.56$ and excited states $p_1^{\text{th}} = 0.35$ is small (see Sec. 4.3). Therefore the amplitude of the decay is reduced. Experimentally, a larger averaging to resolve the

double exponential from the noise is required. Figure 5.1b) presents the energy decay from $|1\rangle$ prepared by pumping a higher frequency transition (see Sec. 5.3). It has the advantage of presenting a higher amplitude and therefore a better resolution, but it is at the price of possibly exciting quasiparticles while pumping. This possibility will be explored further in the following. In both cases energy decay is well represented by the theory (red lines) given by

$$p_0(t) = p_0^{\text{th}} + \left(p_0(0) - p_0^{\text{th}}\right) \exp\left(-\frac{t}{T_l} + \beta(\exp(-\frac{t}{\beta T_s}) - 1)\right), \ \beta > 0 \qquad (5.1)$$

with $T_l \gg T_s$. At short times $t \ll T_s$ the time population is

$$
\begin{aligned}
p_0(t \ll T_s) &\simeq p_0^{\text{th}} + \left(p_0(0) - p_0^{\text{th}}\right)e^{-t/T_l - \beta t/\beta T_s} \\
&\simeq p_0^{\text{th}} + \left(p_0(0) - p_0^{\text{th}}\right)e^{-t/T_s} \ .
\end{aligned}
\qquad (5.2)
$$

At long times the population is given by

$$p_0(t \gg T_l) \simeq p_0^{\text{th}} + \left(p_0(0) - p_0^{\text{th}}\right)e^{-t/T_l - \beta} \ . \qquad (5.3)$$

Thus T_l and T_s are respectively the long and short lifetimes characterizing the decay at large and small times. The factor β represents how separated the two time scales are in time. Indeed $\beta^{-1}T_s$ is the typical duration after which the decay becomes dominated by T_l. For the first measurement we find $T_s = 5.7 \ \mu$s and $T_l = 172 \ \mu$s. For the second $T_s = 14 \ \mu$s and $T_l = 92 \ \mu$s.
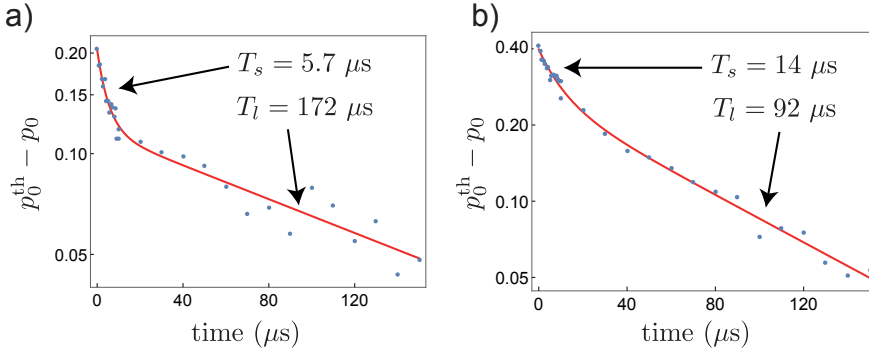
Figure 5.1: Relaxation of the fluxonium circuit after a) a π-pulse on $|0\rangle \rightarrow |1\rangle$ or b) preparation of $|1\rangle$ by optical pumping (log scale). The data (points) are well reproduced by the theory of a double exponential (red line) with the parameters indicated on the figure.

We note that the values of the decay constants do not agree between the two measurements. There could be two reasons for this, either the lifetime fluctuates or pumping changes the decay dynamics. The latter possibility will be studied in Sec. 5.3. It has been showed that quasiparticles population variations are responsible for the lifetime fluctuations of superconducting qubits [117]. To test this possibility we measure the decay several times over an hour. Since at long times the qubit is close to thermal equilibrium we expect to have a large uncertainty over T_l. Moreover the quasiparticles are supposedly responsible for the short decay time of the double exponential. We thus characterize the evolution of T_s with time. To make the characterization complete we also fit the data at small time with a simple exponential. The results are displayed in Fig. 5.2. The error bars are estimated from the deviation between the experimental measurement and the result of the fit. It is larger in the case of the double exponential

because the fit involves more parameters. In particular the errors on β, T_l and T_s are related. Nevertheless the two results agree for most experiments because the simple exponential fit is more sensitive to the evolution at small times. We hence measure fluctuations of the lifetime of about a factor 2 around the mean values 9.8 μs and 8.35 μs for respectively the simple and double exponential.
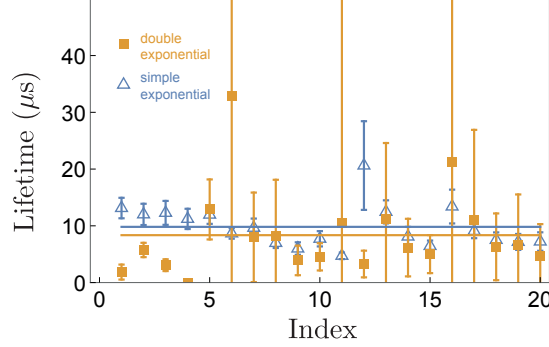
Figure 5.2: Lifetime fluctuations. Evolution of (orange squares) the short decay time T_s for a double exponential fit and (blue triangles) the decay time T_1 for a single exponential fit of the energy decay measurements of the qubit transition with the index of the experiment (related to the time). The duration of the total measurement is about an hour. The mean values of T_s and T_1 are represented by respectively the orange and blue lines.

The presence of quasiparticles is thus attested by both the double exponential decay and the lifetime fluctuations. Recent works have attested the central role of quasiparticles in the thermal excitation of superconducting circuits [118, 119]. The measured circuit thermal occupation corresponds to an effective equilibrium temperature $T = 98$ mK which is much warmer than the dilution cryostat base temperature $T_{\mathrm{cryo}} \approx 12$ mK where our system is placed. It is thus possible that dissipation into the environment is made at various temperatures depending on the considered loss mechanism.

5.1.2 *Quantitative predictions*

Depending on the transitions the important loss mechanisms to consider might differ because their evolutions with frequency or external flux are different. For instance phase and charge matrix elements at half flux quantum are zero for even transitions due to a selection rule. This selection rule does not apply to quasiparticle loss, therefore the only direct decay between two states separated by an even number of transitions is through quasiparticle tunneling. However cascade processes are obviously possible and have also to be quantified. In a previous section (Sec. 4.1.1) we distinguished between the matrix elements of linear and quasiparticle loss and showed how Purcell emission could be controlled by the waveguide. Here we give quantitative predictions for the decay of all transitions involving the fluxonium states up to $|3\rangle$. It is important to note that the decay rates given in Sec. 4.1.1 are the jump rates from a state $|i\rangle$ to another state $|j\rangle$. Experimentally we measure an equilibration time T_{ij} corresponding to $T_{ij}^{-1} = \Gamma_{i \to j} + \Gamma_{j \to i}$. Since we are interested into finding out what processes are important for a given transition the calculations below are made at zero temperature.

Besides Purcell emission the main source of linear dissipation in superconducting circuits is dielectric loss [45, 120], possibly due to microscopic two-level systems (TLS)

present at the interface between the circuit and the substrate. In that case the circuit-environment interaction corresponds directly to the electric circuit of Fig. 4.2a) where the admittance represents the dissipative dielectric filling up the capacitance C shunting the junction. Therefore we have obtain coupling between the noisy external current I_N and the phase operator φ of the circuit given by the Hamiltonian $H_{\text{int}} = -(\Phi_0/2\pi)\varphi I$. The current spectral density is expressed by [45] $S_{I_N}[\omega] + S_{I_N}[-\omega] = 2\hbar\omega \times C\omega Q_{\text{diel}}^{-1}$ where the inverse quality factor $Q_{\text{diel}}^{-1} = \tan\delta$ is the loss tangent characterizing the dielectric. Combining with Eq. (4.1) yields

$$\frac{1}{T_{ij}^{\text{diel}}} = \omega_{ij}^2 \frac{R_Q C}{\pi Q_{\text{diel}}} |\varphi_{ij}|^2 \tag{5.4}$$

where we introduced the resistance quantum $R_Q = h/(2e)^2$ to express the decay rate in terms of the time constant $\tau = R_Q C$. The value of Q_{diel} has been measured in various superconducting circuits and for aluminum circuits has been found consistently within the interval [26, 45, 47] $10^5 \leq Q_{\text{diel}} \leq 10^6$. The capacitance is obtained from $E_C = e^2/2C = h \times 1.2$ GHz.

The decay rate due to quasiparticle tunneling in the small junction is computed directly from the junction Hamiltonian $-E_J \cos(\varphi - \varphi_{\text{ext}})$ under noisy variations of $\varphi(t)$. The quasiparticle spectral density is computed in [27] and the decay rate reads

$$\frac{1}{T_{ij}^{\text{junction}}} = x_{\text{qp}} \frac{8E_J}{\hbar\pi} \sqrt{\frac{2\Delta}{\omega_{ij}}} |\langle i| \sin\left(\frac{\varphi - \varphi_{\text{ext}}}{2}\right)|j\rangle|^2 \tag{5.5}$$

where x_{qp} is the quasiparticles population and Δ is the superconducting gap (normalized by $\hbar$). Quasiparticles are also supposed to generate losses by tunneling through the large junctions composing the chain. In this case by linearization of the matrix element the decay time due to quasiparticles in the chain is given by

$$\frac{1}{T_{ij}^{\text{chain}}} = x_{\text{qp}} \frac{8E_L}{\hbar\pi} \sqrt{\frac{2\Delta}{\omega_{ij}}} |\varphi_{ij}|^2 \; . \tag{5.6}$$

For aluminum $\Delta = 2\pi \times 82$ GHz [13]. The quasiparticle populations has been estimated experimentally to be contained in [26, 47, 121–125] $10^{-7} \leq x_{\text{qp}} \leq 10^{-5}$. Note that the quasiparticle population is not necessarily the same around the small junction and in the chain. Moreover we have $E_J = h \times 2.0$ GHz and $E_L = h \times 0.61$ GHz (the value of E_J is smaller than the one used for the generalized spectrum of Fig. 4.7 because of aging of the junction over the course of the experiment).

The 3D fluxonium is capacitively coupled to the electromagnetic modes of the waveguide through its antennas. This picture therefore corresponds to the electrical circuit of Fig. 4.2b). The waveguide can be represented by a frequency-dependent capacitance proportional to the power transmission coefficient $|t(\omega)|^2$ coupling a noisy voltage source V_N and a resistor R to the circuit operator. The voltage spectral density is thus $S_{V_N}[\omega] + S_{V_N}[-\omega] = 2\hbar\omega R$. We obtain

$$\frac{1}{T_{ij}^{\text{Purcell}}} \propto 2\hbar\omega_{ij}|t(\omega_{ij})n_{ij}|^2 \propto 2\hbar\omega_{ij}^3 |t(\omega_{ij})\varphi_{ij}|^2 \tag{5.7}$$

where we used the link between n_{ij} and φ_{ij} given in Eq. (4.2). The Purcell decay time is known up to a scaling factor taking into account the unknown dissipative resistance R

and the factor between the waveguide transmission and the coupling capacitance. We determine this constant experimentally when we characterize the fluorescence readout. Indeed ,we measure $1/(T_{03}^{\text{Purcell}}) = 2\pi \times 2.68$ MHz and use it to compute the Purcell decay rates for other transitions since the waveguide transmission is known.

The calculated decay times for Purcell, dielectric and quasiparticle loss for transitions between $|0\rangle$ and $|3\rangle$ at half flux quantum are represented on Table. 5.1 (in μs). We obtained them by computing the matrix elements and the transition frequencies from the fitted spectrum and using the values of Q_{diel} and x_{qp} from the literature. It shows that the double exponential decay of $|1\rangle \to |0\rangle$ is due to quasiparticle tunneling in the chain. The values are in good agreement with the measured lifetimes. The measured decay rates from $|2\rangle$ (Fig. 4.15b) giving $T_s = 4.2$ μs) and $|1\rangle$ (Fig. 5.2 giving $T_s \simeq 9$ μs) seem to indicate that the quasiparticle population in the chain is at most 10 times smaller than the one near the junction. Indeed, in the case of a dominant direct decay from $|2\rangle$ to $|0\rangle$, the measured energy relaxation from $|2\rangle$ would impose the quasiparticle population in the junction to verify

$$x_{\text{qp}}^{\text{junction}} \leq 10^{-5} \tag{5.8}$$

while decay from $|1\rangle$ imposes

$$x_{\text{qp}}^{\text{chain}} \leq 10^{-6} . \tag{5.9}$$

Such a variation of x_{qp} along the device seems unlikely, as no physical effects identified up to date can explain it. Another interpretation is that the quasiparticle population is the same in all the device and that the main relaxation effect from $|2\rangle$ to $|0\rangle$ is via a cascade decay induced by quasiparticle tunneling $|2\rangle \to |1\rangle \to |0\rangle$. Such a process would still exhibit a double exponential decay since the quasiparticle population remains constant while the system relaxes and only fluctuates from one experiment to the other. On the other hand we see that the Purcell emission rate of the readout transition $|0\rangle \to |3\rangle$ is the most dominant effect as it is more than one order of magnitude larger than other decays. This validate our design and our choice of readout transition.

Transition	Purcell	Dielectric	Junction quasiparticles	Chain quasiparticles
$|0\rangle \leftrightarrow |1\rangle$	1.4×10^5	$16 \leq T_{01}^{\text{diel}} \leq 160$	∞	$0.2 \leq T_{01}^{\text{chain}} \leq 20$
$|0\rangle \leftrightarrow |2\rangle$	∞	∞	$3 \leq T_{02}^{\text{junction}} \leq 300$	∞
$|0\rangle \leftrightarrow |3\rangle$	0.06	$23 \leq T_{03}^{\text{diel}} \leq 230$	∞	$26 \leq T_{03}^{\text{chain}} \leq 2.6 \times 10^3$
$|1\rangle \leftrightarrow |2\rangle$	125	$3 \leq T_{12}^{\text{diel}} \leq 30$	∞	$0.4 \leq T_{12}^{\text{chain}} \leq 40$
$|1\rangle \leftrightarrow |3\rangle$	∞	∞	$3 \leq T_{13}^{\text{junction}} \leq 300$	∞
$|2\rangle \leftrightarrow |3\rangle$	126	$2 \leq T_{23}^{\text{diel}} \leq 20$	∞	$0.3 \leq T_{23}^{\text{chain}} \leq 30$

Table 5.1: Calculated transition decay times in μs for Purcell emission, dielectric loss and quasiparticle tunneling in the junction and in the chain, for $10^5 \leq Q_{\text{diel}} \leq 10^6$ and $10^{-7} \leq x_{\text{qp}} \leq 10^{-5}$.

5.2 BRANCHING RATIO

When working at half flux quantum we use the $|0\rangle \to |3\rangle$ transition for readout. It has the advantage of presenting a large Purcell rate and therefore allows to perform a quick

readout. On the downside, population can decay from $|3\rangle$ to other states than $|0\rangle$. In particular $|3\rangle$ can decay to $|1\rangle$ either directly through quasiparticle tunneling in the junction, or in a cascade decay through $|2\rangle$ under the joint effect of dielectric loss and quasiparticle tunneling in the chain. This results into qubit population originally in $|0\rangle$ leaving the logical computational subspace $\{|0\rangle, |1\rangle\}$ or being pumped to the exited state $|1\rangle$ by the readout drive. In either cases it directly sets a limit on the Quantum Non-Demolition (QND) status of the readout. For the readout this unwanted processes can be represented by the general escape rate Γ_{out} from the readout transition (Fig. 5.3) to the ensemble of other states than $|0\rangle$. The limit on the readout QNDness is thus quantified by the

$$\boxed{\text{branching ratio} = \frac{\Gamma_{03}}{\Gamma_{\text{out}}}} \quad . \tag{5.10}$$

It represents the average number of photons fluoresced by the readout transition before the bright readout transition becomes dark. For an ideal fluorescence measurement $\Gamma_{\text{out}} = 0$ and one can measure for as long as needed. In practice a branching ratio around 10 allows to perform measurements with a good fidelity and above 100 we can start using the readout transition for the realization of useful quantum information treatment with low errors. For instance using the readout transition for state transfer would result in an error rate of less than 99% necessary for building quantum networks such as the quantum internet [43]. In this section we propose and achieve a measurement of the branching ratio based on the time evolution of the ground state population under the readout drive at various powers.

5.2.1 *Pumping rate theory*

The principle of a fluorescence readout with a finite branching ratio is represented in Fig. 5.3. Once in the readout state $|R\rangle$ (in our case $|3\rangle$) population can decay towards an ensemble of intermediate states represented by the gray rectangle (in our case $|2\rangle$ and $|1\rangle$). This decay can be represented by only one effective rate Γ_{out}. After an inner dynamics in the ensemble of intermediate states population goes back to $|0\rangle$ with the effective rate Γ_{in}. Importantly in the absence of coherent drives there is no need to resolve the inner dynamics in action when population is outside the readout transition states. It can be modeled by a single effective escape state $|E\rangle$, so that this situation is formally equivalent to a three level system where the readout drive effectively pumps population from the ground state $|0\rangle$ to the excited state $|E\rangle$. The decay rate of the readout transition is by design the largest rate of all processes thus $\Gamma_r \gg \Gamma_{\text{out}}, \ \Gamma_{\text{in}}$. This is confirmed by the calculations of Table. 5.1.

A direct measurement of Γ_{out} is challenging as it involves multiple levels and our fluorescence readout is sensitive to the population in $|0\rangle$ only. In theory we could resolve the population transfer in time by applying π-pulses to map the populations in $|R\rangle$ and $|E\rangle$ back to $|0\rangle$. However this measurement is limited by the fidelities of the pulses. Yet it is possible to directly deduce Γ_{out} from transients measurements of the evolution of the population in $|0\rangle$ under a continuous drive at ω_r with various amplitudes Ω. To do so let us separate the time scales of the experiment. The drive generates damped Rabi oscillations between $|0\rangle$ and $|3\rangle$ which reach the steady-state in a typical fast time $T_{\text{fast}} \approx \Gamma_r^{-1}$. On the other hand decay to and from $|E\rangle$ happens at the typical slow times $T_{\text{slow}} \approx (\Gamma_{\text{in}}, \Gamma_{\text{out}})^{-1} \ll T_{\text{fast}}$. The populations $p_i, \ i \in \{0, R, E\}$ observe
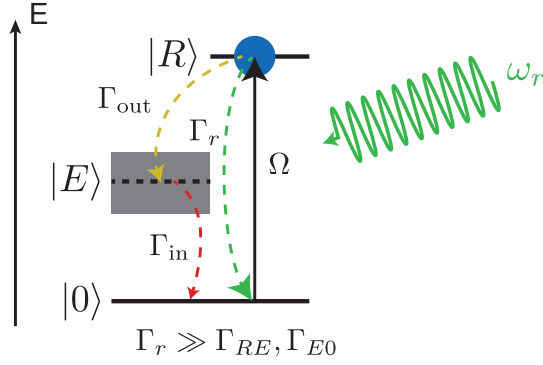
Figure 5.3: Branching ratio in fluorescence readout. The readout drive at ω_r generates a Rabi frequency Ω between $|0\rangle$ and $|R\rangle$. Population transiting through $|R\rangle$ can decays either towards $|0\rangle$ at the rate Γ_r or towards the effective escape state $|E\rangle$ at the rate $\Gamma_{\rm out}$ representing all the states outside the readout transition. Population eventually goes back to $|0\rangle$ with the rate $\Gamma_{\rm in}$.

the conservation law $p_0 + p_R + p_E = 1 \Leftrightarrow p_0 + p_R = 1 - p_E$. The steady-state of Rabi oscillations is given by Eq. (2.14) with zero detuning $\delta = 0$ and the rates $\Gamma_1 = 2$, $\Gamma_2 = \Gamma_r$. Equation (2.14) was obtained assuming that the sum of the populations in the ground and excited states was conserved $p_0 + p_R = 1$. Here, population leaves the subspace but it does it slowly so that we can consider that at all times the population ratio p_R/p_0 is constant with

$$\frac{p_R}{p_0} = \frac{1 + z_\infty(\Omega, \delta = 0)}{1 - z_\infty(\Omega, \delta = 0)} \tag{5.11}$$

where $z_\infty(\Omega, \delta = 0)$ is computed using Eq. (2.14). We can thus express the population $p_R(t)$ varying slowly in terms of $p_E(t)$ as

$$p_R(t) = \frac{1 + z_\infty(\Omega, \delta = 0)}{2}\left(1 - p_E(t)\right) = \frac{\Omega^2}{\Gamma_r^2 + 2\Omega^2}\left(1 - p_E(t)\right). \tag{5.12}$$

The slow evolution of p_E is given by the rate equation

$$\begin{aligned} \dot{p_E} &= \Gamma_{\rm out}p_R - \Gamma_{\rm in}p_E \\ &= \Gamma_{\rm out}\frac{\Omega^2}{\Gamma_r^2 + 2\Omega^2}(1 - p_E) - \Gamma_{\rm in}p_E \\ &= -\left(\Gamma_{\rm in} + \frac{\Omega^2\Gamma_{\rm out}}{\Gamma_r^2 + 2\Omega^2}\right)p_E + \frac{\Omega^2\Gamma_{\rm out}}{\Gamma_r^2 + 2\Omega^2}. \end{aligned} \tag{5.13}$$

The escape state $|E\rangle$ is therefore pumped at the effective pumping rate

$$\boxed{\Gamma_{\rm pump} = \Gamma_{\rm in} + \frac{\Omega^2\Gamma_{\rm out}}{\Gamma_r^2 + 2\Omega^2}}. \tag{5.14}$$

It is interesting to note that in the limit $\Omega \to 0$ the pumping rate is non-zero. This is due to the fact that we assumed in our derivation that some population was transiting through $|R\rangle$. In fact, when $\Omega = 0$, no population goes to neither $|R\rangle$ nor $|E\rangle$ and the equation of evolution of p_E becomes the tautology $0 = 0$. When $\Omega \gg \Gamma_r$ we have $\Gamma_{\rm pump} \approx \Gamma_{\rm in} + \Gamma_{\rm out}/2$. The steady state population in $|E\rangle$ is given by

$$\boxed{p_E^{\rm ss} = \frac{\Omega^2\Gamma_{\rm out}}{\Gamma_{\rm in}\Gamma_r^2 + (2\Gamma_{\rm in} + \Gamma_{\rm out})\Omega^2}}. \tag{5.15}$$

Here we indeed recover the fact that at low pump amplitude no population is found in $|E\rangle$.

When measuring p_0 we hence expect to find an exponential decay with the rate Γ_{pump}. The readout rate Γ_r is measured using the fluorescence readout characterization presented in Sec. 4.2.1. It also gives the scaling factor between the drive amplitude set experimentally and the Rabi frequency Ω. On the other hand Γ_{in} can be estimated using the measured energy relaxation from $|2\rangle$ and $|1\rangle$. Therefore we can fit the evolution of $\Gamma_{\text{pump}}(\Omega)$ with only one fit parameter: Γ_{out}, and compute the branching ratio.

5.2.2 *Branching ratio measurement*

In order to measure the pumping effect due to the readout we implement the sequence represented in Fig. 5.4a). First we apply a pulse at $\omega_r = \omega_{03} = 2\pi \times 6.54$ GHz with various amplitudes. After a duration τ we stop the drive and measure the population p_0 using another pulse at ω_r but this time with constant duration and amplitude, during which we measure the reflection coefficient. The readout rate is $\Gamma_r = 2\pi \times 2.68$ MHz. Such a pump-probe experiment where the pump and probe have the same frequency allows us to use only one scaling factor between the measured reflection coefficient and p_0 for all measurements (see Sec. 4.2). We leave a 500 ns delay between the pump drive and the readout during which the population in $|3\rangle$ decays quickly to mostly $|0\rangle$. When the readout starts the populations are thus $p_3 = 0$ and $p_0 \approx 1 - p_E$. The time evolution of p_0 is represented in Fig. 5.4b) for various values of Ω. Turning up the pump amplitude decreases the final population in $|0\rangle$ and increases the pumping rate. At large pump amplitude (turquoise and braun curves in the figure) we start to see a small deviation from the exponential fit used to extract Γ_{pump} (plain lines), possibly due to quasiparticles. From these transients it is clear that the pumping time $T_{\text{pump}} = \Gamma_{\text{pump}}^{-1}$ due to driving at the readout frequency is not less than a couple μs, to be compared to the decay time from $|3\rangle$ to $|0\rangle$ $T_r = \Gamma_r^{-1} = 60$ ns due to the readout rate.

The evolution of the pumping time with Ω is represented in Fig. 5.5. To quantify the fluctuations of the branching ratio we repeated the same measurements over a total duration of three days. The points are the averaged values of T_{pump} and the error bars represent their standard deviations. According to Eq. (5.14), the pumping time at small values of Ω is given by Γ_{in}^{-1}. At the lowest experimental value $\Omega = 2\pi \times 0.37$ MHz the measured pumping time is about 50 μs. It is larger than the fast times of the double exponential decays measured from both $|2\rangle$ and $|1\rangle$, which were measured around 10 μs (see Figs. 5.2 and 4.15). We can interpret this effect by noticing that the optical pumping rate is only sensitive to slow processes. If some population decays quickly to the ground state, it is immediately pumped back to the readout state with almost no influence on the pumping rate. On the other hand if some population stays in the effective escape state for a long time the population in the ground state will be reduced. However the presence of a fast decay time has obviously an influence on the steady-state populations and can limit the preparation of a given state by optical pumping. The evolution of the branching ratio is well reproduced by the theoretical expression of Eq. (5.14) (red line). We obtained it by fitting Γ_{out} as the only fitting parameter, Γ_{in} being fixed at $\Gamma_{\text{in}} = (65 \ \mu\text{s})^{-1}$. This value was inferred from the long lifetimes of the energy decay measurements from $|1\rangle$ and $|2\rangle$. To determine the uncertainty on Γ_{out} we fit the decay rate measurements in the two limit cases $\Gamma_{\text{in}} = (50 \ \mu\text{s})^{-1}$ and $\Gamma_{\text{in}} = (80 \ \mu\text{s})^{-1}$. These
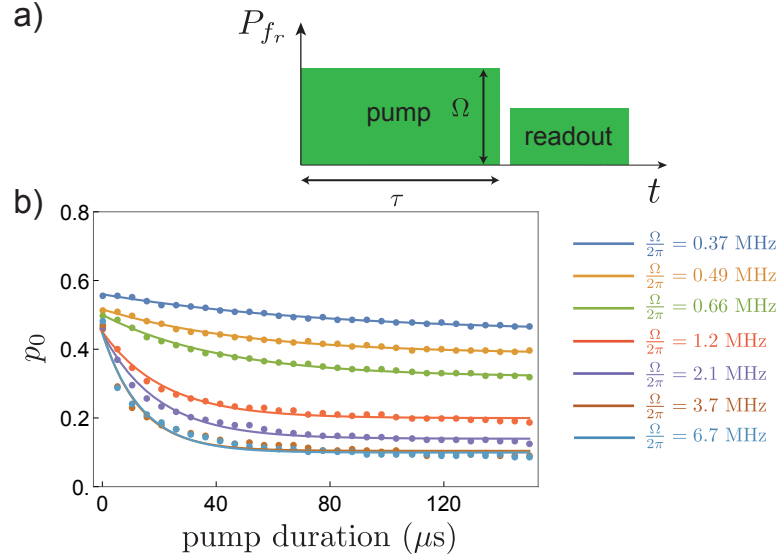
Figure 5.4: Transient measurement of excited states pumping due to finite branching ratio. a) Experimental pulse sequence. It uses two drives at readout frequency ω_r, the first one acting as a pump and the second one being used to measure the population in $|0\rangle$. b) Time evolution of the ground state population p_0 under the pump at ω_r at various amplitudes (see inset). The experimental data (points) are fitted by a simple exponential decrease (lines).

values correspond to theoretical lines that would go through the top and bottom of the measurement error bars, respectively. With this we obtain

$$\Gamma_{\text{out}} = \left(7.7\mu s \pm 0.6\mu s\right)^{-1} . \tag{5.16}$$

We deduce the experimental branching ratio

$$\boxed{\frac{\Gamma_r}{\Gamma_{\text{out}}} = 128 \pm 10 .} \tag{5.17}$$

We have thus demonstrated that the branching ratio in our experiment is above 100. This validates our circuit design for the readout and paves the way towards a finer determination of the readout QNDness.

5.2.3 *Possible explanation*

The measured branching ratio is in good agreement with the estimated decay times of Table 5.1. It is possible to give an interpretation of the branching ratio in terms of dielectric loss while neglecting the decay due to quasiparticles. This assumption means that quasiparticles would be responsible for lifetime fluctuations, double exponential decay and possible circuit equilibrium temperature, but that longer lifetimes are dominated by dielectric loss. To demonstrate this point we simulate numerically the whole dynamics of the fluxonium at half flux quantum under the drive at ω_r, and consider the decay rates due to Purcell emission and dielectric loss only (see Sec. D.2). For simplicity we run the simulation at zero temperature with the only consequence that the amplitude of the simulated transients of p_0 do not agree with the experimental one displayed in Fig. 5.4. The dielectric quality factor depends on frequency and temperature [46]

$$Q_{\text{diel}} = Q_0 \coth\left(\frac{\hbar\omega}{2k_B T}\right) \tag{5.18}$$
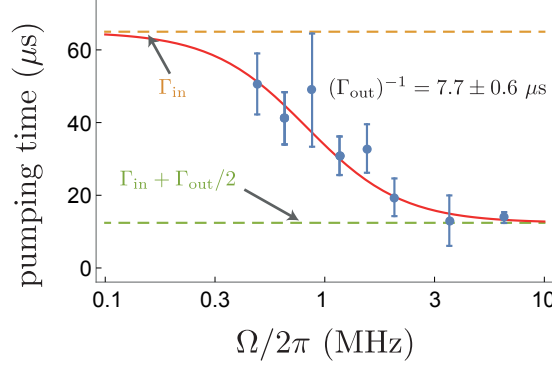
Figure 5.5: Branching ratio measurement. The measured pumping times $T_{\text{pump}} = (\Gamma_{\text{pump}})^{-1}$ at various Rabi frequencies (points and error bars) are fitted with the theoretical expression of Eq. (5.14) with Γ_{out} as the only fit parameter with $\Gamma_r = (60 \text{ ns})^{-1}$ and $\Gamma_{\text{in}} = (65 \ \mu s)^{-1}$. Red line is obtained for $\Gamma_{\text{out}} = (7.7 \mu s)^{-1}$. Error bars come from the repetition of the measurements over three days. The value of the pumping rate in the limits $\Omega \gg \Gamma_r$ and $\Omega \ll \Gamma_r$ are represented by respectively the green and orange dashed lines.

where Q_0 is the quality factor at zero temperature. Here, the only effect of temperature is to generates an effective quality factor.

The result of the simulation is presented with the experimental measurement in Fig. 5.6. For each simulated Rabi frequency (green squares) we computed the time-evolution of the population in the ground state right after stopping the pump and fitted the transient to extract the simulated Γ_{pump} (see Sec. D.2). The numerical calculations reproduce very well the experimental data with

$$\boxed{Q_{\text{diel}} = 4.2 \times 10^{-5}} \ . \tag{5.19}$$

With the simulations we obtain $\Gamma_{\text{in}}^{\text{diel}} = (70 \ \mu s)^{-1}$ in good agreement with the experimental value and $\Gamma_{\text{out}}^{\text{diel}} = (6.67 \ \mu s)^{-1}$, resulting in the slightly smaller simulated branching ratio

$$\left(\frac{\Gamma_r}{\Gamma_{\text{out}}} \right)^{\text{sim}} = 112 \ . \tag{5.20}$$

This good agreement between numerical simulations and experimental measurements is an indication that dielectric loss might be the dominant effect limiting the branching ratio of the readout. However it is not a full proof since quasiparticle tunneling can generate decay rates with the same amplitude. In particular quasiparticle tunneling in the chain have the same matrix element as dielectric loss, though not the same frequency dependence.

5.3   QUBIT RESET BY OPTICAL PUMPING

The pumping effect due to the finite branching ratio is an inconvenient for the readout since it limits the QNDness but can be used practically to prepare the circuit in a state with a better purity than thermal equilibrium. In superconducting circuits, qubit reset based on the strong measurement of the qubit state followed by a fast feedback loop [126] and pumping schemes involving the transfer of qubit excitations to a lossy resonator [114, 115] (in a continuous version of the Maxwell's demon experiment presented in Chap. 7) have been achieved. Our fluxonium circuit embedded in a waveguide
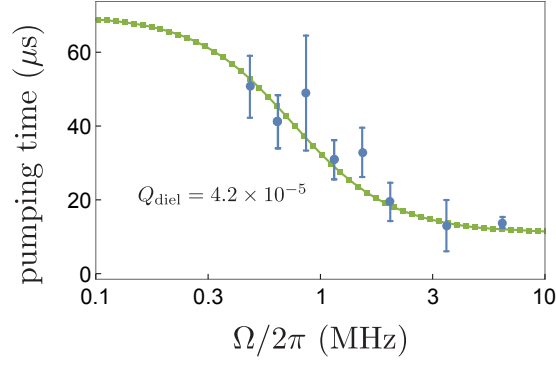
Figure 5.6: Branching ratio simulation based on dielectric loss with $Q_{\text{diel}} = 4.2 \times 10^5$ (green squares) and experimental results (points and error bars). Each simulation point (green squares) corresponds to a simulation of the time evolution of p_0 followed by an exponential fit giving the pumping rate.

naturally presents high-frequency, lossy transitions that can be used for realizing optical pumping. In this section we discuss the feasibility of pumping schemes and study the effect of the pump on the circuit.

5.3.1 *Pumping transitions*

The picture for optical pumping is similar to the one of the branching ratio (Fig. 5.3) but with different conditions over the rates. In order to maximize the pumped population in the target state it is necessary to have $\Gamma_{\text{out}} \gg \Gamma_{\text{in}}$. This condition appears clearly in the case considered theoretically when $\Gamma_r \gg \Gamma_{\text{out}}, \Gamma_{\text{in}}$. The steady-state population in the excited state $|E\rangle$ is given by Eq. (5.15) and becomes close to 1 when $\Gamma_{\text{out}} \gg \Gamma_{\text{in}}$ and $\Omega \gg \Gamma_r$. Physically it means that the population stays in the target state for most of the time. This limit case also maximizes the pumping rate and thus the qubit initialization time. Interestingly enough the steady-state population and pumping rate at large pump amplitude does not depend on Γ_r. Practically this means that we can drive a weakly-coupled transition to pump a state preventing that we can compensate the small coupling by a large pump amplitude realizing $\Omega \gg \Gamma_{\text{out}}, \Gamma_{\text{in}}, \Gamma_r$.
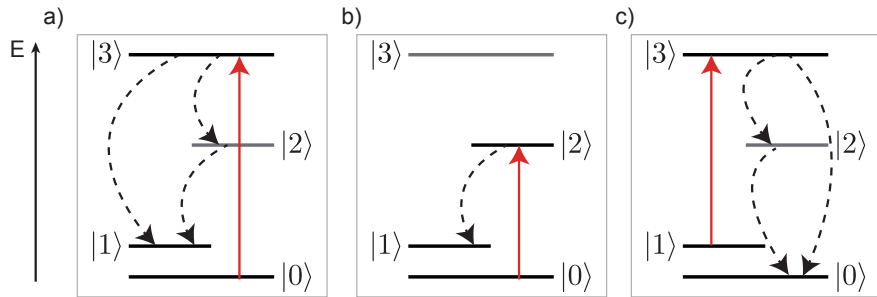
Figure 5.7: Possible pumping schemes targeting (a and b) the first excited state $|1\rangle$ or (c) the ground state $|0\rangle$. The pump drive is represented by the red arrow and the decay processes realizing the pumping by the dashed arrows. Other decays whose effect is to limit the pumped population in the target state are not represented.

We consider the three pumping schemes represented in Fig. 5.7. The first (Fig. 5.7a) uses the readout transition to pump the excited state $|1\rangle$. Population can decay from

$|3\rangle$ to $|1\rangle$ either directly due to quasiparticle tunneling in the junction or in a cascade decay passing through $|2\rangle$ (see Table 5.1 for the estimated decay times). As a result this pump prepares a mix of $|1\rangle$ and $|2\rangle$ and hence limits the final amount of population in $|1\rangle$. The second and third readout schemes (Fig. 5.7b and c) are based on pumping the forbidden even transitions, respectively $|0\rangle \to |2\rangle$ and $|1\rangle \to |3\rangle$, to prepare respectively $|1\rangle$ and $|0\rangle$. At exactly half flux quantum $\Phi_{ext} = \Phi_0/2$ it is impossible to drive these transitions because of the selection rule $\varphi_{i,i+2} = 0 \ \forall i \in \mathbb{N}$. To overcome this issue we set the external flux at $\Phi_{ext} = (1/2 + 2.6 \times 10^{-3})\Phi_0$, which is enough to obtain $\varphi_{02}, \varphi_{13} \neq 0$ and increase the pump power (see Fig. 4.13b where we obtained Rabi oscillations of $|0\rangle \to |2\rangle$). However the slow matrix element of the pumping transition might set a practical limit on the pump amplitude. For $|1\rangle \to |3\rangle$ some population can decay from $|3\rangle$ to $|2\rangle$ instead of $|0\rangle$. Thanks to the branching ratio measurement we know that this effect is about 100 times smaller than the decay to $|0\rangle$.

5.3.2 *State preparation*
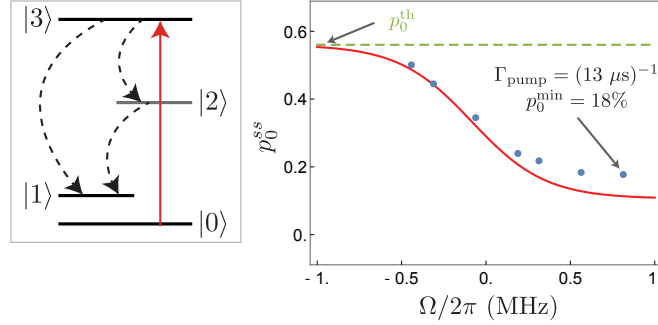
Figure 5.8: Pumping with $|0\rangle \to |3\rangle$. Evolution of the steady-state population in the ground state after optical pumping at ω_{03} with the induced Rabi frequency Ω. The measured values (points) follow the theoretical curve (red) calculated from Eq. (5.15) with $p_0^{ss} = p_0^{th}(1 - p_E^{ss})$. All the parameters entering the theory line have been measured independently in the branching ratio measurement and $p_0^{th} = 0.56$.

We characterize the various pumping schemes using the transient measurement technique presented in the study of the branching ratio. A good pumping scheme is fast and prepares the target state with a good fidelity. Therefore in this part we are not only interested by the pumping rates but also by the final populations right after the pump has been stopped. The experimental transients for $|0\rangle \to |3\rangle$ pumping were already presented in Fig. 5.4, and the evolution of the population in $|0\rangle$ coming from the steady-state p_0^{ss} is represented in Fig. 5.8. We show the experimental measurements (points) together with the theoretical prediction (red line) coming from Eq. (5.15) and using the branching ratio determined previously. More precisely we consider that the population in $|3\rangle$ relaxes quickly towards $|0\rangle$ as soon as the pump has been turned off. Moreover the theory resulting in the steady-state equation (5.15) was done at zero temperature. We take into account the non-zero temperature by rescaling the theoretical prediction by the thermal equilibrium population $p_0^{th} = 0.56$ and obtain

$$p_0^{ss} = p_0^{th}(1 - p_E^{ss}) \ . \tag{5.21}$$

At low pump amplitude the data is in good agreement with the theoretical prediction but is smaller than predicted at higher power. This might originate in the fast decay towards the ground state due to quasiparticles that was hidden in the sole pumping rate measurement. At optimal power we measure a final population $p_0^{\min} = 18\%$ and pumping rate $\Gamma_{\text{pump}} = (13\ \mu\text{s})^{-1}$. It is important to precise that this value means that $p_1^{\text{ss}} + p_2^{\text{ss}} = 82\%$ and further measurements are needed to obtain p_1^{ss}, for instance by studying the contrast of Rabi oscillations. The measurement of p_0^{ss} is still a useful characterization of how efficient the pumping is, since a perfect pumping scheme would totally empty the ground state.

Figure 5.9: Pumping with $|0\rangle \to |2\rangle$. a) Evolution of the ground state population p_0 with the duration of the pump at various powers $P_{\omega_{02}}$, (points) data and (lines) exponential fit. b) Steady-state ground state population as a function of the pump power. When the power is increased p_0^{ss} goes from p_0^{th} to $p_0^{\min}$ before going up. The data at low and intermediate power are well represented by the semi-quantitative theory of Eq. (5.22) (red dashed line).

We now turn to the second scheme using $|0\rangle \to |2\rangle$. The population time evolutions when the pump is applied are represented in Fig. 5.9a) for various pump powers. The data (points) are fitted by a simple exponential to extract the pumping rate and the final ground state population p_0^{ss}. The latter is represented as a function of the pump power $P_{\omega_{02}}$ in Fig. 5.9b). Near half flux quantum the phase matrix element of the $|0\rangle \to |2\rangle$ transition is small $\varphi_{02} \ll 1$ therefore the derivation made in Sec. 5.2.1 is not valid. However it is possible to represent the evolution of the population by a semi-quantitative formula inspired from Eq. (5.15)

$$1 - p_0^{\text{ss}} = \frac{\alpha P_{\omega_{02}}}{\Gamma_{\text{eff}}^2 + \alpha P_{\omega_{02}}} \tag{5.22}$$

with α and Γ_{eff} two constants adapted to recover the data. This calculated trend is represented by the red dashed line on the figure. It gives a good representation of the experimental data at low and intermediate power. We would expect that a high power would lead to a lower residual population in $|0\rangle$. In practice the final population goes up after having reached a minimum. At the minimum we measure a residual population $p_0^{\min} = 9\%$ for a pumping rate $\Gamma_{\text{pump}} = (4\ \mu\text{s})^{-1}$.

We make the same analysis with pumping the $|1\rangle \to |3\rangle$ transition, represented in Fig. 5.10. Even though the characterization is not as clear as for the two other processes we obtain a similar behavior. Contrarily to the two other studied schemes the pump aims at preparing the ground state. We prepare at most $p_0^{\max} = 78\%$ in an inverse time $\Gamma_{\text{pump}} = (7\ \mu\text{s})^{-1}$.
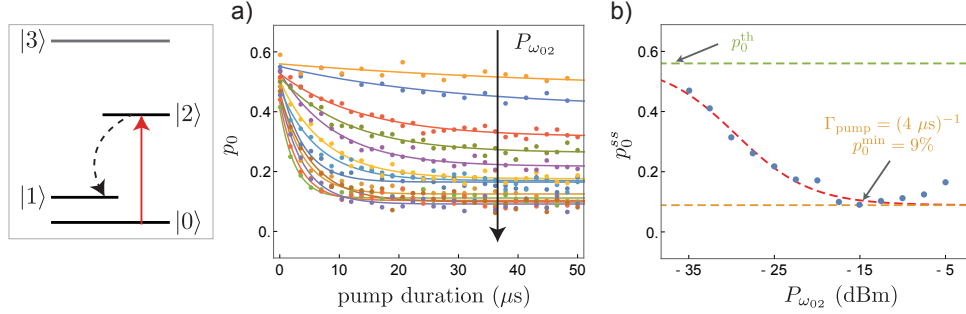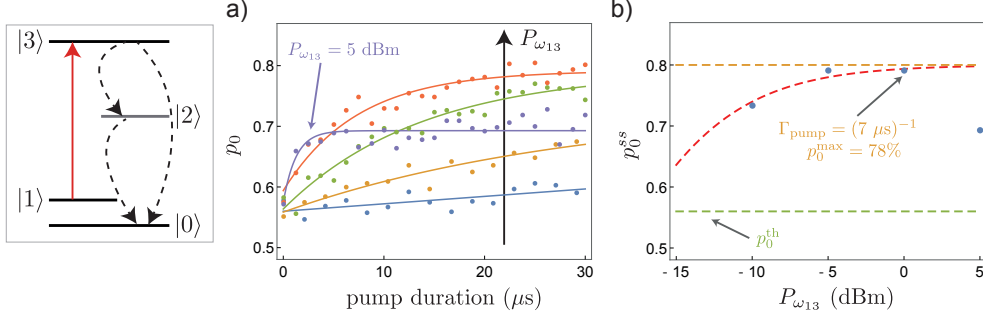
Figure 5.10: Pumping with $|1\rangle \rightarrow |3\rangle$. a) Evolution of the ground state population p_0 with the duration of the pump at various powers $P_{\omega_{13}}$, (points) data and (lines) exponential fit.
b) Steady-state population in the ground state as a function of the pump power. In a similar manner to the other pumping schemes the pumping becomes less effective when the power becomes too high.

The two pumping schemes using the even transitions $|0\rangle \rightarrow |2\rangle$ and $|1\rangle \rightarrow |3\rangle$ exhibit a deviation from the optimal preparation at high pump power, where optical pumping becomes less effective. We interpret this deviation as coming from an effective detuning of the pump at high power due to AC-Stark shift. Indeed, these two schemes require large pump amplitudes to compensate the small matrix element of the transitions. At large power the many fluxonium levels are renormalized so that the pump becomes off-resonant with the pumping transition. A way to overcome this effect would be to adapt the pump frequency to a given power. However there will still be a limitation on the pump amplitude set by the breakdown of the fluxonium circuit at high driving energy, in an effect close to the recently measured ionization of a superconducting transmon [127]. The experimental results obtained for the three pumping schemes are summarized in Table. 5.2. The pumping times are one order of magnitude longer and the preparation fidelity at least ten times smaller than the state-of-the-art of superconducting circuit reset based on pumps where a qubit residual excitation of 0.2% was achieved in 500 ns [115]. Yet these measurements are promising and better values could be obtained with the proper circuit design.

Scheme	Target state	p_0^{ss}	$(\Gamma_{pump})^{-1}$
$|0\rangle \rightarrow |3\rangle$	$|1\rangle$	18%	13 μs
$|0\rangle \rightarrow |2\rangle$	$|1\rangle$	9%	4 μ s
$|1\rangle \rightarrow |3\rangle$	$|0\rangle$	78%	7 μ s

Table 5.2: Summary on the three pumping schemes presented in Fig. 5.7.

5.3.3 *Effect of pumping on coherence*

The previous study gave a good indication on how good our pumping schemes are but is incomplete. Indeed it is important to check that the pump did not perturb the system even at the highest power we used and that it is still possible to coherently manipulate the quantum states of the fluxonium. Moreover, when we pump the excited state $|1\rangle$
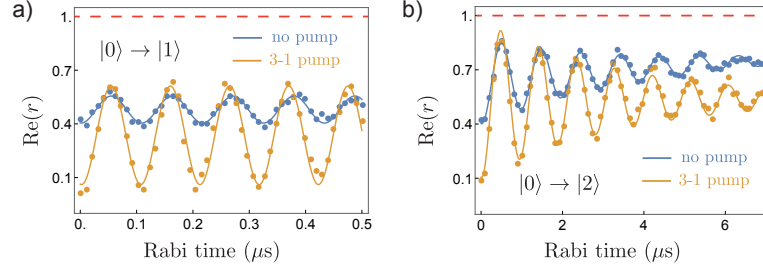
Figure 5.11: Rabi oscillations after qubit initialization by a pump on $|1\rangle \to |3\rangle$. a) Oscillations between $|0\rangle$ and $|1\rangle$ and b) $|0\rangle$ and $|2\rangle$ in the presence (orange) or absence (blue) of the pump at $P_{\omega_{31}} = 0$ dBm. We show the raw measurement of the reflection coefficient and not the deduced populations to highlight the global unexplained shift of the oscillations when the qubit is initialized by the pump.

we need to be sure that the pump did not put population in higher-energy states by multi-photon transitions.

Let us start with a quick characterization of the pumping scheme preparing $|0\rangle$ with a pump on the $|1\rangle \to |3\rangle$ transition (Fig. 5.7c). Unlike the schemes preparing $|1\rangle$, we directly measured the final amount of population in the target state $|0\rangle$. Fig. 5.11 shows time Rabi oscillations of $|0\rangle \to |1\rangle$ and $|0\rangle \to |2\rangle$ with or without initialization using a pump at ω_{31} applied with $P_{\omega_{31}} = 0$ dBm during 50 μs (see Fig. 5.10). As expected the oscillation contrast is increased by the use of the pump, but it is done with a general shift of the oscillations in the measurement of the reflection coefficient r. This result is surprising because we do not expect the relation between r and the ground state population p_0 to change, nor the reflection coefficient to depend on the population in other states than $|0\rangle$. Therefore one should expect the reflection coefficient to get much closer to 1 (red dashed line), which corresponds to an empty ground state $p_0 = 0$, when a π-pulse has been applied. The reason for this global shift is not explained at this date. Interpretations such as a saturation of the amplifiers due to the reflected drive and an effective detuning of the fluxonium transitions due to the large pump have been studied and refuted. As we will see, this effect is absent for the two other pumping schemes.
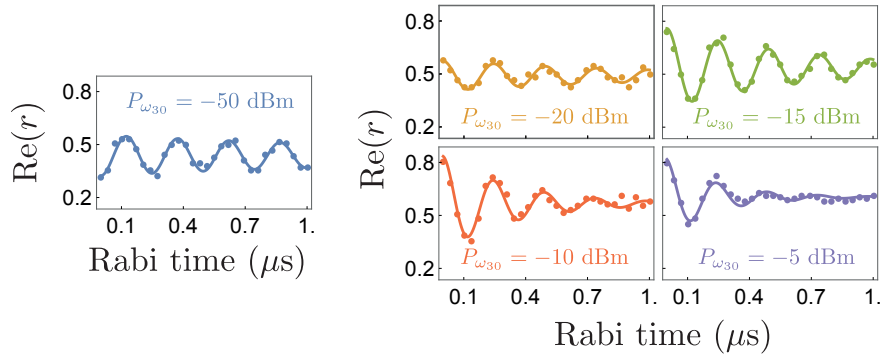
Figure 5.12: Rabi oscillations between $|0\rangle$ and $|1\rangle$ after qubit initialization using a pump on $|0\rangle \to |3\rangle$ for various values of the pump power (see insets).

To characterize the schemes preparing $|1\rangle$ we measure Rabi oscillations of $|0\rangle \to |1\rangle$ with the qubit initialized by a pump of different powers. The results are presented in Fig. 5.12 for the qubit prepared by pumping the $|0\rangle \to |3\rangle$ transition and in Fig. 5.13
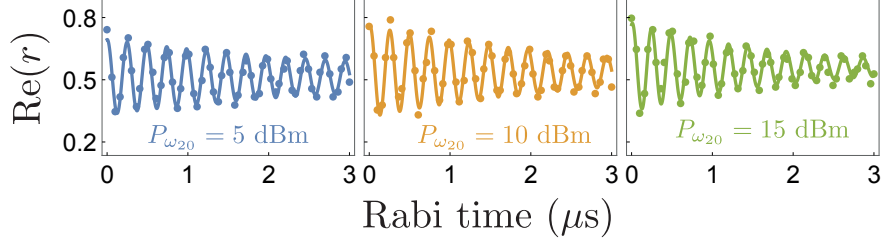
Figure 5.13: Rabi oscillations between $|0\rangle$ and $|1\rangle$ after qubit initialization using a pump on $|0\rangle \to |2\rangle$ for various values of the pump power (see insets).

for the qubit prepared by pumping the $|0\rangle \to |2\rangle$ transition. In both cases if the pump indeed performs population inversion and increases the amplitude of the oscillations (without the shift measured for the other pumping scheme), the large pump power strongly reduces the decay time of the oscillations. This effect sets a very important and strong limitation on the pump power used for preparation.
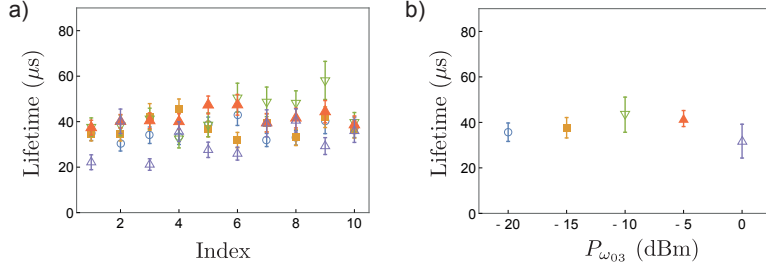
Figure 5.14: Lifetime of $|1\rangle$ after qubit preparation using the pump on $|0\rangle \to |3\rangle$ as a function of a) time (represented by the index of a several hour-long experiment) at various powers and b) power, obtained by integrating over the time variations. The markers on a) correspond to the powers of b).
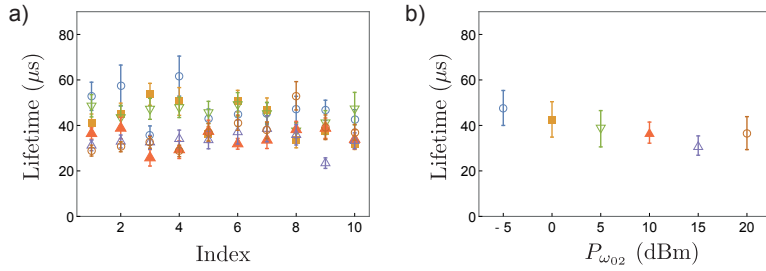
Figure 5.15: Lifetime of $|1\rangle$ after qubit preparation using the pump on $|0\rangle \to |2\rangle$ as a function of a) time (represented by the index of a several hour-long experiment) at various powers and b) power, obtained by integrating over the time variations. The markers on a) correspond to the powers of b).

An immediate lead to explain this effect is that the strong pump generates losses in the circuit, for instance by exciting quasiparticles of the superconductor. To test it we measured the lifetime of $|1\rangle$ prepared by optical pumping at different drive amplitudes, and repeated this measurements over five hours to take into account the lifetime fluctuations. The evolution of the lifetimes with the index of the experiment (related to the time of the day when the experiment has been conducted) is represented in Fig. 5.14a)

for the pumping scheme using the $|0\rangle \rightarrow |3\rangle$ transition. As we already observed the lifetimes fluctuate by about a factor 2 for all pump powers[1]. Averaging these times gives the evolution of the lifetime with the power in Fig. 5.14b), which exhibits no noticeable evolution in the range of power where we measured the strong reduction of the Rabi decay time. We perform the same measurements for a pump on $|0\rangle \rightarrow |2\rangle$, see Fig. 5.15, with the same conclusions. We have thus demonstrated that the decay of the Rabi oscillations is *not* due to a reduction of the qubit lifetime because of the large pump amplitude. This means that the pump generates pure dephasing of the fluxonium. We can for instance imagine that the pump would generate extra measurement-induced dephasing due to photons reemitted by higher-energy levels, but such an assumption would have to be tested further. In particular it would be enlightening to study the evolution of the coherence time T_2 and dephasing time T_φ with the pump power.

5.4 CONCLUSION

In this chapter we have characterized two important effects coming from incoherent processes. First, dissipation induces a finite branching ratio of the readout that we have described theoretically and measured experimentally. This branching ratio is well explained by a model of dissipation based on dielectric loss only. Second we investigated the feasibility of optical pumping in our circuit and studied three different pumping schemes. At large amplitude the pump generates pure dephasing affecting the coherent evolution of the qubit. Future experiments could try to reach better branching ratios by fine tuning the waveguide cutoff frequency. In particular the use of the transition $|1\rangle \rightarrow |2\rangle$ as a readout transition would result in a branching ratio limited by quasiparticles only.

The main unpublished results of this chapter are the following

- analytical determination of the pumping rate and steady-state populations, Eqs. (5.14) and (5.14)

- demonstration of a branching ratio of 128 for the readout transition, Fig. 5.5

- interpretation of the branching ratio with $Q_{\mathrm{diel}} = 4.2 \times 10^5$, Fig. 5.6

- optical pumping schemes characterization, Table 5.2, Figs. 5.12, 5.12, 5.14 and 5.14.

---

[1] These measured lifetimes are longer than the one presented in Fig. 5.2. They were taken during a different experimental run and possibly some parameters changed.

Part III

QUANTUM THERMODYNAMICS

Quantum physics is fundamentally a science of information. Our theoretical description of quantum objects aims at predicting successfully the outcome of experiments given the *knowledge* an observer has on the system, a prediction being a set of probabilities. In a quantum measurement, information is transferred from a quantum system to a classical one and disturbs the system. This change of the system's state can be seen as being driven by the update made by the observer based on the newly acquired information. Beyond the question of quantum measurement the recent push towards quantum computation proved that information can also be exchanged between and processed by quantum systems. Since they are never fully isolated the role of thermal baths surrounding the systems is of first importance. In thermodynamics the role of information is central as it appears under the form of entropy in the laws of thermodynamics. The blooming field of quantum thermodynamics investigates the interactions between thermal baths and quantum systems. In particular the topic of thermal machines operating in the quantum regime addresses questions such as: Are there so-called quantum ressources? Can the efficiency of quantum thermal machines beat classical ones? How can we define properly heat and work while the result of measurements is stochastic?

This part is devoted to the experimental study of a Maxwell's demon operating both in the classical and quantum regimes. In the second half of the 19th century, following the early discoveries of the link between thermodynamics and statistical physics, Maxwell proposed a thought experiment where a "demon" extracts works from a thermodynamic system beyond the limits set by the second law by basing its action upon the information it obtains about the system [52, 53]. The contradiction with the second law arises when this process is repeated cyclically to realize a thermal engine. This apparent paradox triggered a large amount of theoretical works on the role of information and was eventually solved a century later. The development of computers shed light on the fact that information is physical in the sense that it is always carried by a physical support and as such does not escape from the laws of Nature. Consequently, Landauer argued that information processing has an entropic cost [128, 129] while Bennett clarified the role of the demon's memory in the thermodynamic cycle [130]. The first experiments on classical demons have only been carried out recently as they require a fine control of all parts of the system [131–134]. The quantum version was similarly long investigated [54–58] and experiments on the subject are recent [135–138]. Here we present our experimental realization of the quantum demon based on superconducting circuits. By measuring the qubit fluorescence with the tools described in the first part, we directly probe the work extracted by the demon. Moreover we make the characterization complete by measuring the entropy and energy of both the system and demon.

MAXWELL'S DEMON IN CLASSICAL AND QUANTUM PHYSICS

Before turning to our particular implementation of the quantum Maxwell's demon let us investigate more generally its core concepts and results. This chapter is devoted to developing some ideas that will be central in the next chapter instead of trying to cover all the aspects of the topic of information and thermodynamics.

6.1 CLASSICAL MAXWELL'S DEMON

The modern description of the classical demon is actually far from the original thought experiment described by Maxwell. We give here the modern schematic description, name the central constituents and give the fundamental limit to the amount of energy one can extract from a single heat bath known as the Landauer bound.

6.1.1 *Qualitative description of the classical demon*

The principle of the Maxwell's demon is represented in Fig. 6.1. The system (S), a gas at thermal equilibrium at temperature T, is divided into two parts A and B with a gate in between. The demon (D) is a being able to measure the celerity of each particle of the gas trying to pass through the gate from one side to the other. Based upon this information the demon sorts the fast particles from the slow ones by deciding whether or not it opens the gate. Importantly the demon's actions can be achieved without the expenditure of work as the opening/closing operations can be made reversible. Eventually the sorting results in the two containers having different temperatures, a situation from which one can extract work (represented by a piston lifting a mass on the figure). This is an apparent violation of the second law of thermodynamics that prevents from extracting work cyclically from a single heat bath. This paradox is resolved if we finely model the information processing in action during the cycle, for instance by modeling the demon's memory as a series of bits. Initially it only contains "0"'s. When the demon measures the celerity of a particle it writes a "1" if the particle belongs to B and "0" otherwise. At the end the entropy of the system has been decreased by the sorting while the entropy of the demon's memory has increased. To close the thermodynamical cycle the demon's memory has to be reset. This operation can be either done using a hidden cold bath in which the demon dissipates the information or at thermal equilibrium at T with a net work cost. In the first case the demon appears as nothing else but a regular thermal machine. In the second case the work cost of information erasure is at least equal to the extracted work, hence restoring the validity of the second law.

With this description we can refine what we call the "demon" in the experiment. In the initial description one might think that the demon is the being opening and closing the door to sort the particles. In the literature the demon is often presented as the whole ensemble acquiring information and acting on the system all the way to work extraction. Even though this description is valid, we saw that the gate opening and closing has no effect in the thermodynamical balance since it can be done reversibly.
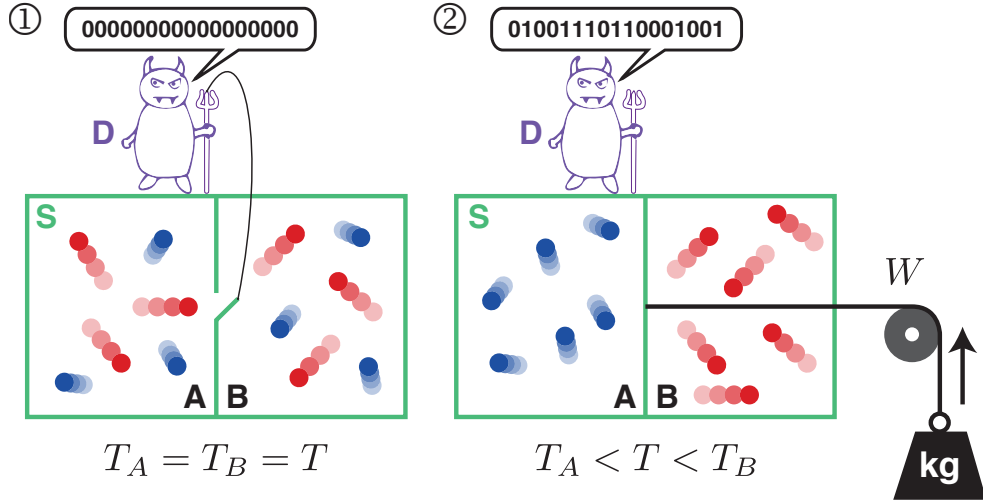
Figure 6.1: Principle of the Maxwell's demon. ① A demon (D) measures the celerities of the particles of the system (S) and sorts them by opening/closing the gate. ② This generates a temperature difference from which one can extract a work W. The process induces a transfer of entropy from the gas to the demon's memory.

On the other hand the final work extraction can be done by an independent operator. What is specific to the demon is actually the acquisition of information. Therefore the "demon" can be reduced to its memory, the object in which the information about the system is stored and eventually erased. This is the denomination we will use in the following.

6.1.2 *Szilard engine and Landauer bound*

The previous qualitative description is voluntarily vague to be as general as possible. In particular we did not describe the particular of the information transfer nor work extraction, and obviously the working fluid is not necessarily a gas. However it is possible to compute a fundamental bound on the amount of work one can extract from a single heat bath by acquiring 1 bit of information on the system. To do so let us study a simplified version of the Maxwell's demon, the Szilard engine [139]. The gas is simplified to a single particle at temperature T. The box is divided into two equal parts so that the particle is either on one side or the other. If the particle is found by the demon to be on the left (respectively right) side the demon attaches the mass on the left side of the piston (resp. right). In doing so, the mass is always lifted when the particle pushes the piston due to thermal expansion. In the final state the particle occupies the whole box. If the process is isothermal we can write $\Delta U = Q - W = 0$ with ΔU the variation of internal energy between the initial and final states, Q the heat received by the system and W the work extracted and used to lift the mass. With the second principle the variation of the system's entropy is $\Delta S \geq Q/T$ with the equality reached at reversibility. The entropy variation can be directly computed from the probabilities of presence in the initial and final states. The initial state is known because the demon acquired information on the particle thus the initial entropy is $S_i = 0$. In the final state

the particle occupies the whole box, therefore it has an equal probability to be on the left or on the right side $p_L = p_R = 1/2$. We get

$$\Delta S = S_f - S_i = S_f = -k_B \sum_{j=L,R} p_i \ln p_j = k_B \ln 2 . \tag{6.1}$$

We therefore obtain $W = Q \leq T\Delta S$ leading to the following limit on the extracted work [128]

$$\boxed{W \leq k_B T \ln 2} . \tag{6.2}$$

This is the Landauer bound for the work extracted from one bit of information. Initially this bound was found as the fundamental minimum for the energy cost of the erasure of 1 bit of information. This proves that the total amount of work extracted from a single heat bath during a cycle is at best zero if the demon erases its information at the same temperature than the system.

6.2 QUANTUM-MECHANICAL MAXWELL'S DEMON

The question of the quantum version of the demon has been investigated for the past thirty years [54, 55] and comes from a simple question. The particles of the gas in the classical description are actually quantum objects, so it is legitimate to ask if we could see any deviations from the classical description when quantum properties such as superposition, discord[1] or entanglement appear. We give here a minimal description of possible demons in quantum mechanics, and discuss the question of the saturation of the Landauer bound in the case of fixed and variable energy levels.

6.2.1 *A demon measuring a quantum bit*

Let us simplify a system exhibiting quantum properties to a qubit with the ground and excited states $|g\rangle$ and $|e\rangle$ and coupled to a heat bath at temperature T. The demon acquires information on the state of the qubit and acts on the system to extract work. For instance the system is measured in the energy basis and a π-pulse is applied whenever the system is found in the excited state to extract one quantum of energy. Initially the qubit can be either in a thermal state or in a quantum superposition of states. When the system is quantum the nature of the demon is fundamental. One possibility is that the demon is a classical measurement apparatus applying a feedback based on the measurement outcome. For such a "quantum to classical demon", the measurement projects (entirely or not) the state of the qubit when the latter starts from a superposition of states. But if the demon itself is a quantum object we can map the qubit state onto the demon state and information never leaves the quantum world, hence preserving quantum coherences. A consequence is that one cannot use a classical feedback loop to extract work but has to rely on autonomous operations to perform work extraction.

A simple example of an "autonomous demon" is the early proposal by Lloyd [55] where both the system and demon are qubits. The demon's ground and excited states are denoted by $|0,1\rangle$, and it is initialized in $|0\rangle$. The transfer of information and work extraction are represented in Fig. 6.2 and consist of the following two steps

---

1 Quantum discords quantifies the amount of quantum correlations in a state that is not necessarily entangled.

1. information transfer: conditional π-pulse on the demon conditioned on the system being in $|e\rangle$

2. work extraction: conditional π-pulse on the system conditioned on the demon being in $|1\rangle$.
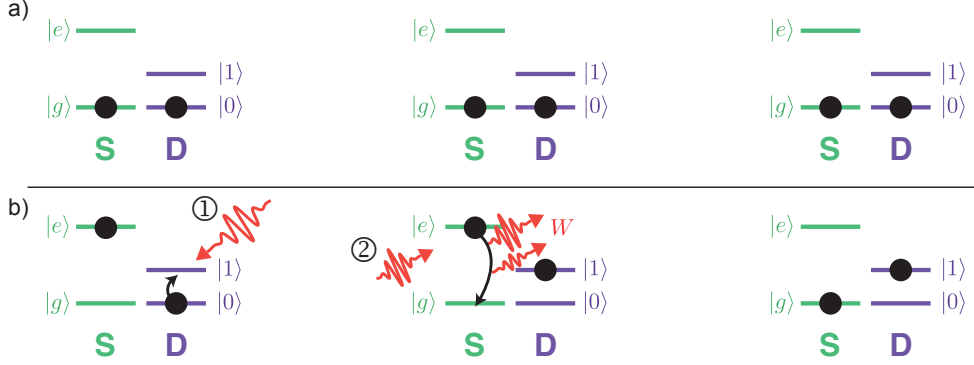
Figure 6.2: Two-qubits autonomous Maxwell's demon when the system is initially in a) the ground state and b) the excited state. The demon is initialized in the ground state and information is transferred by ① exciting the demon only if the system is in $|e\rangle$. It is followed by work extraction ② where the system is flipped only if the demon is in $|1\rangle$.

In the end the system is always in the ground state while the demon's state mimics the initial state of the qubit. Importantly, the two conditional operations can be operated without measuring the quantum states in the presence of an interaction Hamiltonian between the system and the demon. We will investigate a particular implementation in Chap. 7. Therefore if the qubit is initially in a superposed state the experiment will exhibit quantum coherences. More precisely if the system is initially in $(|g\rangle + |e\rangle)/\sqrt{2}$ the first conditional pulse generates the entangled state $(|g0\rangle + |e1\rangle)/\sqrt{2}$ and the work extraction pulse leaves the demon in the state $(|0\rangle + |1\rangle)/\sqrt{2}$. The work extraction pulse extracts an energy E corresponding to the level spacing if the system is excited and none otherwise. On average the total work extracted is $W = p_e E$ with p_e the probability to have the system initially excited[2].

6.2.2 *Limit on the extracted work with fixed energy levels*

In many quantum systems the energy levels of qubits are fixed. This fixes a limit on the net amount of work that can be extracted from a single heat bath. We start with the system thermalized at temperature T. The probability to find it in the excited state is

$$p_e = \frac{e^{-E/k_B T}}{1 + e^{-E/k_B T}} \ .$$
(6.3)

Hence the extracted work reads

$$W = p_e E = E \frac{e^{-E/k_B T}}{1 + e^{-E/k_B T}} \ .$$
(6.4)

---

2 One could argue that there is a negative net work due to the first conditional pulse on the demon. This energy cost becomes zero if the demon's states $|0\rangle$ and $|1\rangle$ have the same energy. Of course the cost associated to information erasure is still present and was not represented here.

This quantity is naturally maximized when the temperature is large compared to the energy spacing of the qubit $k_B T \gg E$, giving $p_e \approx 1/2$. However in this limit the amount of work is small compared to the characteristic thermal energy contained of the bath. More precisely the extracted work is much lower than the Landauer bound fixing the maximal amount of work one can extract with one bit of information since $W \approx E/2 \ll k_B T \ln 2$. A better figure of merit than the raw amount of extracted work is hence the ratio

$$\frac{W}{k_B T \ln 2} = \frac{1}{\ln 2} \frac{(E/k_B T)e^{-E/k_B T}}{1 + e^{-E/k_B T}} \ . \tag{6.5}$$

The goal is thus to maximize the function $f(x) = \frac{xe^{-x}}{1+e^{-x}}$. It can be done numerically and gives the optimal parameters and maximal work-to-bound ratio

$$\boxed{\begin{aligned} E &= 1.28 \times k_B T \\ W &= 0.4 \times k_B T \ln 2 \ . \end{aligned}} \tag{6.6}$$

Therefore with fixed energy levels one cannot hope to get an extracted work better than 40% of the Landauer bound.

6.2.3 Landauer bound saturation with variable energy levels
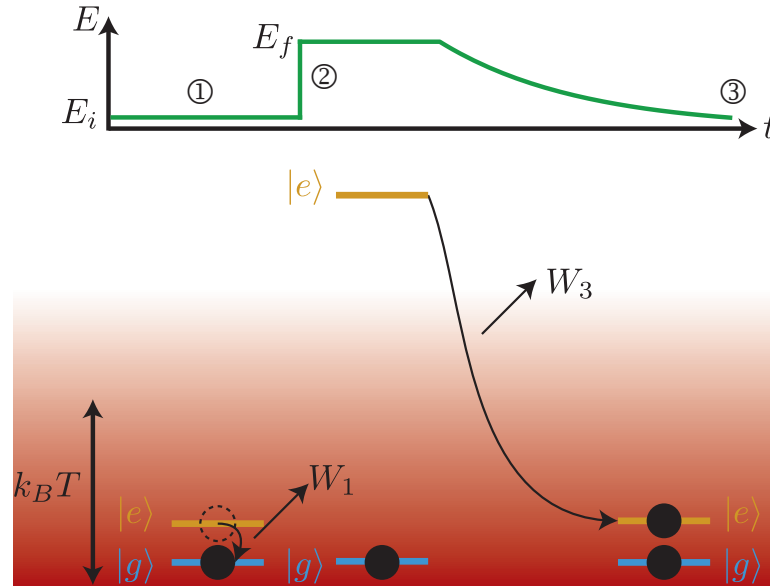
Figure 6.3: Principle of work extraction at the Landauer limit with a qubit with variable energy levels. The bath is represented in red with $E_i \ll k_B T \ll E_f$.

It is possible to reach the Landauer bound if one can tune the energy levels from an initial energy $E_i \ll k_B T$ to a final energy $E_f \gg k_B T$. An example on how this process can be done is represented in Fig. 6.3, and is similar to a proposal based on Landau-Zener transitions [140]. Note that this is not the only way to proceed as the only necessary step in the process is to know at one point with certainty the state of the system. Our principle is based on three steps where we will denote the variation of the system's internal energy, of the system's entropy and the extracted work and received heat at the j-th step by respectively ΔU_j, ΔS_j, W_j and Q_j. The system is initially

at thermal equilibrium at T with the energy E_i. In a way similar to the previously described demons, the demon first measures the state of the system and applies a pulse if necessary to bring it to the ground state, extracting a work W_1. Second, the energy levels are brought *adiabatically* to the energy spacing E_f. Since the energy change is done out-of-equilibrium the system stays in the ground state and there is no work cost to this operation $W_2 = 0$. Third, the energy levels are brought back to E_i in a *quasistatic* way, extracting a work W_3 from the heat bath.

We assume that the time corresponding to the measurement and feedback is much smaller than the thermalization time of the system with the bath. Consequently there is no heat associated to this process $Q_1 = 0$ and the extracted work is simply $W_1 = \Delta U_1 = p_e E_i$. When the energy level is slowly decreased we go from a situation where the system is in the ground state at thermal equilibrium since $E_f \gg k_B T$ to a situation where it has a probability p_e to be excited. During the third step the two thermodynamical principles hence give the following relations

$$
\begin{aligned}
&\Delta U_3 = p_e E_i \Leftrightarrow W_3 = Q_3 - p_e E_i \\
&\Delta S_3 = -k_B\big(p_e \ln p_e + (1 - p_e)\ln(1 - p_e)\big) = \frac{Q_3}{T}
\end{aligned}
\tag{6.7}
$$

from which we obtain

$$
W_3 = -k_B T\big(p_e \ln p_e + (1 - p_e)\ln(1 - p_e)\big) - p_e E_i \ .
\tag{6.8}
$$

With $p_e = \frac{e^{-E_i/k_B T}}{1 + e^{-E_i/k_B T}}$ we have

$$
\begin{aligned}
p_e \ln p_e &+ (1 - p_e)\ln(1 - p_e) \\
&= -\Big(e^{-E_i/k_B T}\big(\frac{E_i}{k_B T} + \ln(1 + e^{-E_i/k_B T})\big) \\
&\qquad + \ln(1 + e^{-E_i/k_B T})\Big)\frac{1}{1 + e^{-E_i/k_B T}} \\
&= -\frac{p_e E_i}{k_B T} - \ln(1 + e^{-E_i/k_B T}) \ .
\end{aligned}
\tag{6.9}
$$

The total work extracted is then $W = W_1 + W_3 = p_e E_i + p_e E_i + k_B T \ln(1 + e^{-E_i/k_B T}) - p_e E_i$ from which we get

$$
\begin{aligned}
W &= E_i\frac{e^{-E_i/k_B T}}{1 + e^{-E_i/k_B T}} + k_B T \ln(1 + e^{-E_i/k_B T}) \\
W &\underset{E_i \ll k_B T}{\approx} k_B T \ln 2 \ .
\end{aligned}
\tag{6.10}
$$

It is important to note that for any value of E_i the extracted work verifies $W \leq k_B T \ln 2$ as we should expect since there was only one bit of information acquired in the process. The question of the quantumness of this thermal machine can be asked since the system is always in a thermal state and never exhibits quantum coherences, only its energy levels are quantized. It is possible to complicate the previous principle to use quantum coherence as a resource. Recent works have investigated more profoundly the question of work extraction from quantum coherence [141, 142]. However the question whether or not quantum coherence can be considered as a thermodynamical resource remains open [143].

6.3 EXPERIMENTAL PLATFORMS FOR THE QUANTUM MAXWELL'S DEMON

The increased level of control on quantum systems and the raising interest for quantum thermodynamics have triggered the recent realizations of quantum thermodynamics experiments using several physical systems. We briefly present these various platforms before focusing on superconducting circuits.

6.3.1 *Experiments on quantum systems*

The general principles of the quantum to classical and autonomous demons can be implemented on many different quantum systems. They require quantum systems with a good coherence, projective measurements with a good fidelity, a fast feedback loop when the demon is classical, and a large interaction Hamiltonian between two quantum objects for the autonomous version. A photonic demon where the system is a thermal state of light has been performed using strong projective measurements and a feedfoward loop [135]. In this experiment work is extracted from thermal fluctuations using photodiodes charging a capacitance and hence is directly measured. The information gained by the demon is reconstructed from the large measurement signal. Thermal machines studying work fluctuations using projective measurements are also investigated experimentally using trapped ions [144, 145] although they do not realize completely a demon experiment as the demon requires a feedback based on the acquired information.

An autonomous demon close to the one described in Fig. 6.2 has been performed experimentally using two spins 1/2 on NMR systems [136], where the natural interaction term between the two spins allows to perform conditional operations. The extracted work is hence contained in the pulse that flips the system to the ground state, and is not directly measured here. Instead, it is inferred from the tomography of the ensemble system+demon in the initial and final states. This tomography gives direct access to the information transfer in the experiment. Single electron devices consist another very promising approach as an autonomous demon has been done using a single electron box playing the role of the demon coupled to a single electron transistor playing the system [146]. The demon is here used to cool-down a bath and the flows of heat and information are measured in situ. However this experiment does not prepare the system in a state exhibiting quantum coherences even though it is operated at the single electron level.

6.3.2 *Paper on Maxwell's demons in circuit-QED*

Superconducting circuits offer a promising platform for investigating the physics of the quantum demon. We reproduce here the review on the state-of-the art of experimental realizations of Maxwell's demon in superconducting circuits. The paper can be found under this reference [147] and will appear in the book *Thermodynamics in the Quantum Regime - Recent Progress and Outlook* to be published in November-December 2018 [95]. It presents and compares the three experimental realizations done so far, including our experiment presented in far more details in the next chapter.

Maxwell's demon in superconducting circuits

Nathanaël Cottet, Benjamin Huard

May 4, 2018

Abstract

This chapter provides an overview of the first experimental realizations of quantum-mechanical Maxwell's demons based on superconducting circuits. The principal results of these experiments are recalled and put into context. We highlight the versatility offered by superconducting circuits for studying quantum thermodynamics.

INTRODUCTION

The past decades have seen the development of superconducting circuits based on Josephson junctions as one of the most promising platforms for quantum information processing [9]. Owing to their high level of control in both their design and their manipulation, they naturally constitute a convenient testbed of fundamental properties of quantum mechanics. Superconducting circuits reach strong coupling with microwave light, allowing quantum-limited amplification [148], strong Quantum Non Demolition measurement [149], weak measurement [93, 150], quantum feedback [151], and the observation of quantum trajectories [152]. From a quantum thermodynamics point of view, this high level of control gives full access to the dynamics of energy and entropy flows between the different parts of the experimental system. Up to now, three experimental realizations of a Maxwell's demon have been achieved using superconducting circuits in the quantum regime [137, 138, 153]. They all consist of a 3D-transmon qubit dispersively coupled to a 3D cavity waveguide measured at cryogenic temperatures around 20 mK [17]. The characteristic frequencies of such systems are in the microwave range.

Szilard reformulated the original Maxwell's demon gedanken experiment in the case of a single molecule in a two sided box [154]. In general, one can cast the experiment in terms of five components with different roles: system, demon, two thermal baths and battery. At the beginning of each thermodynamic cycle, the system is thermalized to its thermal bath. The demon then acquires information on the system to extract work, which can then charge a battery. The apparent possibility to extract work out of a single heat bath vanishes when considering the need to reset the demon state in order to close the thermodynamic cycle [128, 130]. One way to reset the demon state consists in thermalizing it with a hidden thermal bath at the end of the cycle, or by actively resetting its state at the expense of external work. There are plenty of ways to transfer information, extract work and thermalize the system. From an experimental perspective, the manner work and entropy flows are measured or inferred is also crucial since the measurement of a quantum system is inherently invasive. This

chapter will therefore focus on the existing experimental realizations that illustrate what superconducting circuits can bring to quantum thermodynamics. The chapter is organized as follows. We first introduce the reader to the field of circuit Quantum Electro-Dynamics. Then we present the spirit of the three existing experiments before describing the particular experimental realizations in details.

Introduction to circuit-QED

In this section, we provide a brief introduction to circuit-QED. The interested reader is advised to look into a recent review on the subject [155].

A superconducting qubit that is coupled to a cavity can reach two main regimes of interest. First, close to resonance, they can swap excitations, which results in vacuum Rabi splitting. In this chapter, we focus on the opposite regime, where the cavity-qubit detuning is much larger than their coupling rate. This so called dispersive regime can be described by the Hamiltonian [40]

$$H_{\mathrm{disp}} = \frac{\hbar\omega_q}{2}\sigma_z + \hbar\omega_c a^\dagger a - \hbar\frac{\chi}{2}a^\dagger a \sigma_z \,, \tag{6.11}$$

where a is the annihilation operator of a photon in the cavity, ω_q (respectively ω_c) the frequency of the qubit (resp. cavity), and σ_z the Pauli matrix of the qubit along z. The two first terms represent the Hamiltonians of the qubit and cavity, while the last term describes the coupling between them. Compared to the case of the ground state of both qubit and cavity, the interaction induces a frequency shift $-\chi$ of the cavity when the qubit is excited while the qubit frequency is shifted by $-N\chi$ when the cavity hosts N photons. Thanks to this coupling term it is possible to entangle the qubit and the cavity and hence to transfer information between the two. Moreover, when the cavity is coupled to a transmission line, this information can be either dissipated in the environment or collected into a measurement apparatus.

The state of the qubit and cavity is controlled using microwave drives on or near resonance with either the qubit or the cavity. Let us consider first a drive near qubit frequency at $\omega_q - \delta$. Without loss of generality one can set the phase of the drive so that it is along the y-axis of the Bloch sphere. In the rotating frame of the drive and only keeping the slowly rotating terms (rotating wave approximation) the Hamiltonian becomes

$$H_{\mathrm{driven}}^{\mathrm{q}} = \frac{\hbar}{2}(\delta - \chi a^\dagger a)\sigma_z + \Omega_q \sigma_y \,, \tag{6.12}$$

where Ω_q is proportional to the amplitude of the drive. This Hamiltonian induces Rabi oscillations of the qubit around an axis, which depends on the number of photons in the cavity. Energetically the qubit undergoes cycles of absorption where work is absorbed from the drive and stimulated emission where work is emitted in the drive. Similarly a drive near cavity frequency at $\omega_c - \Delta$ gives the following Hamiltonian

$$H_{\mathrm{driven}}^{\mathrm{c}} = \hbar(\Delta - \frac{\chi}{2}\sigma_z)a^\dagger a + \Omega_c(a + a^\dagger) \,, \tag{6.13}$$

where the complex drive amplitude, proportional to Ω_c, is here chosen to be positive. The result is a displacement of the cavity field that depends on the state of the qubit. Assuming the cavity is initially in vacuum it results in the preparation of a coherent

state $|\alpha_g\rangle$ (respectively $|\alpha_e\rangle$) in the cavity when the qubit is in the ground (respectively excited) state. Note that two coherent states are never fully orthogonal ($\langle\alpha_e|\alpha_g\rangle \neq 0$) so that they cannot perfectly encode the qubit state.

All the processes described so far are unitary. In the Zurek description of a quantum measurement [156], driving the cavity corresponds to a *premeasurement* of the qubit state. The information stored in the cavity eventually escapes towards the transmission line, and can therefore be amplified and detected by classical detectors hence terminating the measurement process of the qubit's state. In the dispersive regime, the observable σ_z commutes with the qubit-cavity Hamiltonian (6.11), ensuring that the measurement is Quantum Non Demolition.

Description of the existing experiments

All three experimental realizations presented in this chapter share the common feature of using the qubit as the system. Its state is measured by the demon (of different nature depending on the experiments) thanks to the coupling term of the dispersive Hamiltonian (6.11). Work is extracted through a pulse on resonance with the qubit that induces a rotation of the qubit. The pulse acts as the battery [3] and is powered-up when the qubit is flipped from a high-energy state to a lower-energy one.

Masuyama *et al.* [137] base their Maxwell's demon on a measurement-based feedback scheme. After initialization, the qubit is measured and feedback control is used conditionally on the result of the measurement in the following way: whenever the qubit is measured in $|e\rangle$, a π-pulse flips it back to the ground state and transfers one quantum of work to the battery. In contrast when the qubit is measured in $|g\rangle$ no pulse is applied. The operation time of the sequence is much faster than the thermalization time of the qubit with the rest of the environment so that the whole process can be considered adiabatic. In this experiment the demon is therefore the classical measurement apparatus and information is acquired and stored into a classical memory (Fig. 6.4). An interesting twist is added by the possibility to use a weak measurement for the feedback control input. Masuyama *et al.* are then able to demonstrate the role of mutual information in the second law for quantum systems.

Naghiloo *et al.* [138] also present a Maxwell's demon based on a classical detector. In their case the demon tracks the quantum trajectory of the qubit thanks to time-resolved measurement records. In this case, after initialization, the qubit is driven on resonance while a weak measurement tone is applied at cavity frequency. The qubit state is then reconstructed using the measurement records based on the stochastic master equation (see Appendix). This classical detector acts as a demon that uses its knowledge on both the qubit excitation and coherences to apply an optimal feedback pulse that flips the qubit to the ground state hence extracting work out of the qubit (Fig. 6.5). Importantly in this experiment, the qubit exchanges work with the qubit

---

3 Strictly speaking, the battery is the propagating electromagnetic mode that contains the pulse. It can both store and use the energy it contains, hence qualifying as a battery. Indeed, it can store the excitation of a qubit or of a classical cavity field as described in the text. Moreover, if it interacts with an other distant ancillary qubit or cavity in its ground state, it can provide work to excite it. In the text, the qubit extracted work is used to amplify the pulse in the battery.
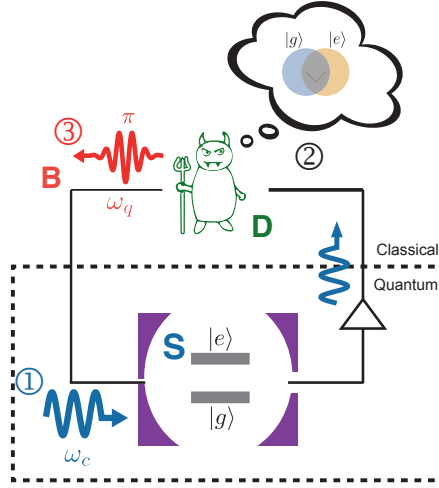
Figure 6.4: Demon whose action is based on a single measurement. ① After qubit initialization, a pulse at cavity frequency is transmitted through the cavity so that its phase encodes the state of the qubit. ② This information is recorded by a classical measurement apparatus acting as the demon. ③ A feedback π-pulse is applied conditioned on the measurement outcome in order to extract work.

drive during the measurement process. Using the quantum trajectory, one can determine how much work is exchanged at each time step. Interestingly, this amount of work cannot be controlled and present a stochastic behavior (see chapter 14 in [95]). This experiment confirms the crucial role of mutual information in the second law for quantum systems.
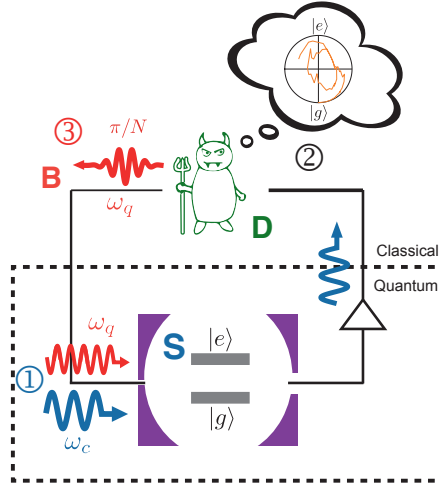
Figure 6.5: Trajectory based demon. ① After initialization, the qubit is driven at ω_q while a weak tone at ω_c measures its state. ② The information is recorded in a time-resolved way, allowing the demon to reconstruct the quantum trajectory of the qubit in the XZ plane of the Bloch sphere. ③ Based on this information, an optimized feedback pulse is applied to flip down the qubit to the ground state and extract work.

In the previous experiments, the demon is a classical black box. The resolution of the paradox of the Maxwell demon involves the acknowledgment of the demon's information as a physical object. In order to analyze the inner dynamics of the demon and even probe its quantum coherence, Cottet, Jezouin *et al.* [153] demonstrated an

autonomous Maxwell's demon in the quantum regime (classical autonomous demons using single electron transistors are discussed in chapter 37 in [95]). After initialization in a thermal or a superposed state, a pulse at ω_c is applied on the cavity and displaces it conditioned on the qubit being in the ground state. It is followed by a π-pulse at ω_q that flips the qubit conditioned to the cavity hosting 0 photon. This sequence is realized in a time smaller than the lifetimes of both the qubit and cavity so that the information stored in the cavity does not have the time to escape into the transmission line. Therefore the demon is here the cavity whose quantum state could be measured in a quantum state that exhibits quantum coherences (Fig. 6.6). Another particularity of this experiment is the direct measurement of the work extracted into the battery. The other experiments use a Two Point Measurement protocol, which is described below.
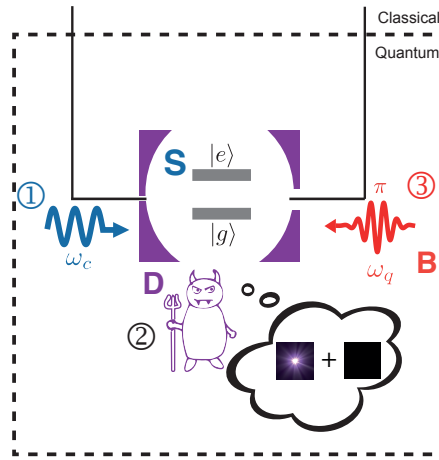
Figure 6.6: Autonomous quantum demon. ① After initialization the cavity is populated conditioned to the qubit being in $|g\rangle$ using a drive at ω_c. ② The cavity state reflects the qubit state, hence acting as the demon and possibly exhibiting quantum coherences. ③ A π-pulse at ω_q extracts work conditioned to the cavity being in the vacuum state. Importantly, the information never leaves the quantum world during the whole process.

QUANTUM-CLASSICAL DEMON

Inferring work and tuning the measurement strength

Before detailing how fluctuation relations can be investigated using superconducting circuit based quantum-classical demons, we discuss two key tools for the realization of these experiments.

Inferring work from Two Point Measurement

Acquiring information on a quantum system is known to be invasive: if the quantum system is not in an eigenstate of the measured observable, the outcome of the measurement is non deterministic and the system state changes following measurement. Work is not an observable [157]. Therefore quantifying the work done on a quantum system is subject to interpretation. However, there is one case that does not suffer

from these inconsistencies. It is the work done on a system that starts from an eigen-state of the Hamiltonian, evolves adiabatically and ends up in an eigenstate of the Hamiltonian. In the Two-Point Measurement (TPM) scheme [158, 159], the adiabatic evolution takes place between two projective measurements of the Hamiltonian at times t_i and t_f leading to measurement outcomes indicating the energies $E(t_i)$ and $E(t_f)$ so that the extracted work (positive when the system provides work) is defined by the change of energy $W = E(t_i) - E(t_f)$. Note that lifting the adiabatic assumption leads to an additional contribution in the change of energy coming from the exchange heat. This TPM scheme allows to recover thermodynamics fluctuation relations such as the Jarzynski equality in the case of classical information acquired on a quantum system.

The two experiments of Masuyama *et al.* [137] and Naghiloo *et al.* [138] both use a TPM scheme to infer the work exchanged between the qubit and the battery. Note that a strong assumption of this TPM scheme is the adiabatic nature of the evolution between projective measurements. For the above experiments, it requires that the operation time (about 0.01 to 1 μs) is much smaller than the thermalization time of the qubit, which is given by the qubit lifetime T_1 (about 10-100 μs).

Weak and strong measurements

We have discussed in the introduction on circuit-QED the way dispersive measure-ment operates. A big asset of circuit-QED for implementing a Maxwell demon is the possibility to arbitrarily tune the amount of information that the demon extracts from the qubit. This skill arises from the fact that the two cavity coherent states $|\alpha_{g,e}\rangle$ cor-responding to the qubit in $|g\rangle$ or $|e\rangle$ are not orthogonal. More precisely, their overlap is $|\langle \alpha_e | \alpha_g \rangle| = e^{-|\alpha_e - \alpha_g|^2/2}$. When the cavity is coupled to a transmission line at a rate κ, the measurement rate [160] , i.e. the rate at which information about the qubit state leaks towards the transmission line, is given by $\Gamma_m = \kappa |\alpha_e - \alpha_g|^2/2 \propto \Omega_c^2$ where Ω_c is a drive strength that appears in equation (6.13) and is proportional to the drive am-plitude. The measurement rate does not necessarily quantifies how much information is effectively acquired by the measurement apparatus at the other end of the trans-mission line. It just sets an upper bound by describing the case of a perfect measure-ment, and thus corresponds to the measurement induced dephasing rate. Taking into account the finite efficiency $0 \le \eta \le 1$ with which information is transmitted between the transmission line input and the final detector, one can more generally write the ef-fective rate at which information about the qubit is acquired by the detector $\Gamma_m^{\text{eff}} = \eta \Gamma_m$. For a given measurement duration t_m, the measurement is said to be weak (respec-tively projective) when $\Gamma_m t_m < 1$ (resp. $\Gamma_m t_m \gg 1$). The strength of the measurement can be experimentally tuned by choosing the drive strength Ω_c (see Fig. 6.7).

Probing quantum fluctuation theorems with weak measurements

Jarzynski for a discrete weak quantum measurement

One of the main interest of the experiment of Masuyama *et al.* is that it puts to the test [137] the Sagawa-Ueda quantum generalization of the Jarzynski equality where a so-called Quantum-to-Classical mutual information plays a key role (see Ref. [161] and chapter 9 in [95]). Varying the measurement strength at which the demon ex-
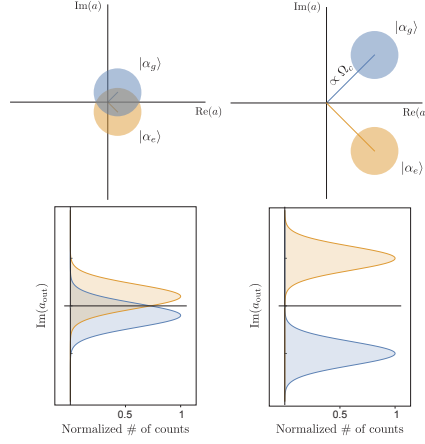
Figure 6.7: Weak to strong measurement of a qubit. (top) When driven at resonance, the cavity hosts a coherent state $|\alpha_{g,e}\rangle$ that depends on the qubit state. Each disk represents the Gaussian distribution of the Wigner function of states $|\alpha_{g,e}\rangle$ in the phase space of the cavity mode quadratures. The disk radius corresponds to the vacuum fluctuations. (bottom) Histograms of the measurement outcomes for a detector that is sensitive to the quadrature encoding the qubit state in the cavity output field. When the drive amplitude Ω_c is small enough (left) the two states strongly overlap and the histograms are not well separated leading to a weak measurement. At larger Ω_c (right) the states and histograms are well separated and the measurement is strong.

tracts information about the system allows them to tune this mutual information and provides a relevant test of the equality. The demon first performs a weak or strong measurement that leads to a measurement outcome k. A projective measurement is then performed, leading to some outcome y, right afterwards so that the system gets either to the ground or to the excited state. Based on the outcome k alone, the demon then sends a feedback pulse to the qubit in order to try to extract a quantum of work out of it. Following the work of Funo, Watanabe and Ueda (see Ref. [161] and chapter 9 in [95]) the quantity of information acquired by the demon during the measurement of outcome k is given by the stochastic Quantum-to-Classical mutual information

$$I_{\mathrm{QC}}(i,k,y) = \ln p(y|k) - \ln p(i), \tag{6.14}$$

where $p(i)$ is the probability to get the outcome i during the first projective measurement of the TPM that surrounds the whole pulse sequence, $p(y|k)$ is the probability to measure the outcome y during the projective measurement conditioned on k. $I_{\mathrm{Sh}}(i) = -\ln p(i)$ is the stochastic Shannon entropy of the initially thermalized qubit. In the limit where the first measurement is strong and in the absence of decay of the qubit the two outcomes k and y match, therefore $p(y|k) = \delta_{y,k}$ and the stochastic mutual information $I_{\mathrm{QC}}(i,k,y)$ is simply given by the stochastic Shannon entropy corresponding to the first measurement of the TPM.

In presence of feedback and when the initial and final Hamiltonian are identical, the work W and the information I_{QC} extracted from the system by the demon verify the following generalized Jarzynski equality (see chapter 9 in [95])

$$\langle e^{\beta W - I_{\mathrm{QC}}} \rangle = 1 - \lambda_{\mathrm{fb}} \tag{6.15}$$

with $\beta = 1/k_B T$ the inverse temperature. This equality takes into account the absolute irreversibility induced by the measurement operation of the demon. It is done via the probability λ_{fb} of irreversible events owing to the measurement. In the case of weak measurements irreversible events disappear because any forward events become possible, as unlikely as they can be. As a result $\lambda_{\mathrm{fb}} = 0$ for weak measurements. The usual Jarzynski equality $\langle e^{\beta W} \rangle = 1$ can thus be simply generalized to the case of non zero stochastic mutual information by replacing W by $W - k_B T I_{\mathrm{QC}}$ in the equality.
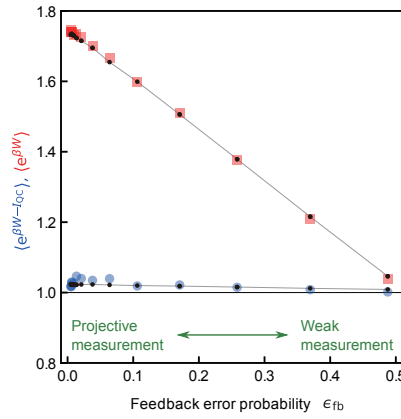
Figure 6.8: (Adapted from Ref. [137]) Jarzynski equality is verified for any measurement strength only when the mutual information I_{QC} is taken into account. Here the blue dots correspond to the measured $\langle e^{\beta W - I_{\mathrm{QC}}} \rangle$ as a function of feedback error probability while red squares correspond to $\langle e^{\beta W} \rangle$.

Fig. 6.8 shows experimental data of $\langle e^{\beta W - I_{\mathrm{QC}}} \rangle$ and $\langle e^{\beta W} \rangle$ as a function of the feedback error probability ϵ_{fb} for a qubit initialized with approximatively 10% of excited state (from [137]). It is defined as the probability that the projective measurement outcome y does not match the weak measurement outcome k: $\epsilon_{\mathrm{fb}} = p(y = e|k = g) + p(y = g|k = e)$. For strong measurement, the feedback process is almost error free ($\epsilon_{\mathrm{fb}} \ll 1$), while when the measurement gets weaker and weaker, the error goes towards $\epsilon_{\mathrm{fb}} = 50\ \%$. The latter value corresponds to the limit where the demon acts completely erratically because of its lack of information. The experiment shows that $\langle e^{\beta W - I_{\mathrm{QC}}} \rangle$ (blue dots) is almost equal to 1 no matter the strength of the measurement, while the uncorrected Jarzynski expression $\langle e^{\beta W} \rangle$ (red squares) only reaches 1 when the feedback reaches its highest error probability. This effect can be simply understood by the fact that a $50\ \%$ error probability means that no information is acquired by the demon and therefore $I_{\mathrm{QC}} = 0$. In contrast, the situation when the measurement is so strong that it can be considered as projective might look surprising. According to equation 6.15, when the feedback measurement is projective, one should expect irreversible events to appear, yielding $\lambda_{\mathrm{fb}} > 0$ and implying $\langle e^{\beta W - I_{\mathrm{QC}}} \rangle < 1$. Yet experimental data suggest otherwise, showing an average above one. The reason is to be found in qubit decay.

First, as highlighted previously, the work has been assimilated to the energy change of the qubit in the TPM, resulting in a small overestimation of the work extracted from the qubit when it decays. Second, the qubit decay between the first TPM measurement and the two measurements k and y does not restrict forward processes and λ_{fb} stays null even in the strong measurement limit. Equivalently the qubit decay means that $p(y|k)$ is never strictly equal to $\delta_{y,k}$, and hence I_{QC} does not equal I_{Sh} even in the strong measurement limit.

Jarzynski for continuous quantum measurements

In the previous part, the weak measurement provides a single measurement outcome k on which the feedback is conditioned. In all generality, the measurement record can be a continuous signal $\{V(t)\}_{0<t<t_m}$ that lasts for some total duration t_m. Then how can the demon optimally extract work from the system and how to quantify the knowledge of the demon about the system? This is what the experiment of Naghiloo *et al.* [138] addresses. It is in fact possible to infer the qubit state ρ_t at any time conditioned on the continuous measurement record (see Appendix and Ref. [34]). This is called a quantum trajectory. Importantly, the conditional density matrix ρ_{t_m} at the end of the measurement encodes everything one needs to know to predict the statistics of any following measurement on the qubit. In their experiment, Naghiloo *et al.* chose to drive the qubit during the measurement so that σ_X is non zero during the quantum trajectory. The information acquired by the demon then takes into account the fact that the demon not only has knowledge on the qubit energy expectation in σ_Z as in the previous experiment but also in the qubit coherence in σ_X. The density matrix can always be written as $\rho_{t_m} = p_1|\psi_{t_m}\rangle\langle\psi_{t_m}| + p_0|\psi_{t_m}^\perp\rangle\langle\psi_{t_m}^\perp|$ for one particular pure qubit state $|\psi_{t_m}\rangle$ and its orthogonal one $|\psi_{t_m}^\perp\rangle$. Note that due to the limited efficiency of the detector (here $\eta = 30$ %), the quantum states are mixed and $p_1, p_0 < 1$. In order to optimally extract work out of the qubit, the demon needs to perform a pulse at the qubit frequency that brings ρ_{t_m} to $\max(p_0, p_1)|g\rangle\langle g| + \min(p_0, p_1)|e\rangle\langle e|$. In their experiment, Naghiloo *et al.* [138] avoid the complexity of calculating the proper pulse to send in real time by performing rotations around the y axis of the Bloch sphere with a random angle and then postselecting the right ones by postprocessing.

As we have seen above, in the case of a quantum system and a classical demon such as here, the fluctuation relation needs to take into account the stochastic mutual information I_{QC}. This quantity is determined in a slightly different manner from for a discrete weak measurement. If one were to perform an ideal projective measurement at time t_m of the observable $|\psi_{t_m}\rangle\langle\psi_{t_m}|$, one would get an outcome $z' = 1$ with probability $p_{t_m}(z' = 1) = p_1$ and $z' = 0$ with probability $p_{t_m}(z' = 0) = p_0$. With similar notations, a projective measurement of the observable $|e\rangle\langle e|$ after the qubit is thermalized at the beginning of the experiment (time 0) leads to an outcome $z = 1$ with probability $p_0(z = 1) = (1 + e^{\beta\hbar\omega_q})^{-1}$ and $z = 0$ with probability $p_0(z = 0) = (1 + e^{-\beta\hbar\omega_q})^{-1}$. The stochastic mutual information [161] can then be written as

$$I_{QC}(z, z') = \ln p_{t_m}(z') - \ln p_0(z). \tag{6.16}$$

The above expression is very similar to Eq. (6.14). This illustrates that the main difference between the experiments of Masuyama *et al.* and Naghiloo *et al.* is not so much in the discrete versus continuous measurement approach since in the end only the last quantum state ρ_{t_m} matters. It is in the fact that the first focuses on states that do

not have any quantum coherence while the second extends the experiment to finite coherences by adding a drive during the measurement.

Concretely, after initialization in a thermal state, Naghiloo *et al.* perform the first TPM projective measurement and measure continuously and dispersively the qubit state while a drive resonating at the qubit frequency induces a rotation of the qubit in the Bloch sphere. A feedback pulse is then applied by a postselection based on the reconstructed quantum trajectory. The sequence is terminated by the second TPM measurement. While the strength of the measurement allowed to tune the stochastic mutual information in the work of Masuyama *et al.*, here the authors decided to keep a constant measurement rate and vary the duration t_m of the measurement. Noting that the free energy difference between the initial and final states is zero because the Hamiltonian is the same, the extracted work W and demon information verify:

$$\sum_{z,z'\in\{0;1\}} p_0(z)p_{t_m}(z')e^{\beta\hbar\omega_q(z-z')-I_{QC}(z,z')}$$

$$= \langle e^{\beta W - I_{QC}} \rangle = 1 \ . \tag{6.17}$$

Experimentally, the work W that is extracted both during the measurement under a drive and during the feedback pulse is determined using the TPM protocol. The inferred evolution of $\langle e^{\beta W - I} \rangle$ and $\langle e^{\beta W} \rangle$ are represented in Fig. 6.9 as a function of the measurement duration t_m for a qubit initially at equilibrium at a temperature $\hbar\omega_q/4k_B$. As in the experiment by Masuayama *et al.*, the generalized Jarzynski equality is indeed verified. This demonstrates that the feedback pulse is indeed applied the right way and validates the definition of information.
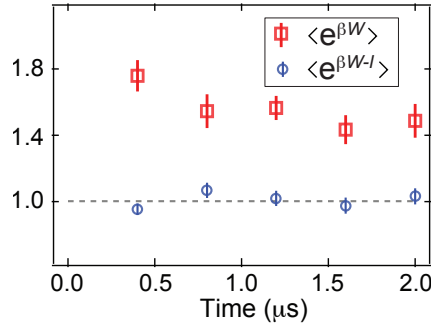
Figure 6.9: (Adapted from Ref. [138])Jarzynski equality is verified for any measurement time only when the mutual information I_{QC} is taken into account. Here the blue dots correspond to the experimentally inferred $\langle e^{\beta W - I_{QC}} \rangle$ as a function of measurement time t_m while red squares correspond to $\langle e^{\beta W} \rangle$.

Information loss during weak measurements

Beyond Jarzynski equalities, the information acquired by the demon exposes the differences between a weak measurement in the Z direction with or without a drive at the qubit frequency.

Masuyama *et al.* show the evolution of $\langle I_{QC} \rangle$ as a function of the feedback error probability ϵ_{fb}. When the collected information is maximal (or equivalently the feedback error probability is zero) the mutual information does not quite reach $\langle I_{Sh} \rangle$ due

to the finite decay of the qubit. As expected the average of the demon information decays to zero as the feedback error probability goes up.

Similarly Naghiloo *et al.* compute the information acquired by the demon in the case of a continuous measurement when the qubit starts in a thermal state ρ_0. Since the qubit is not actually projectively measured after time t_m, one needs to sum over the different possible outcomes z and z' and gets for a single measurement record $\{V(t)\}_t$

$$
\begin{aligned}
\langle I_{QC}\rangle_{\{V(t)\}_t} &= \sum_{z,z'\in\{0;1\}} p_0(z)p_{t_m}(z')I_{QC}(z,z') \\
&= S(\rho_0) - S(\rho_{t_m}).
\end{aligned}
\tag{6.18}
$$

where $S(\rho) = -\mathrm{Tr}(\rho\ln\rho)$ denotes the Von Neumann entropy. The information acquired by the demon over a trajectory is hence simply the difference between the initial and final entropies of the qubit. When the quantum efficiency η is 1, no information about the system is lost during the continuous measurement. The qubit state that is reconstructed from the measurement records using the stochastic master equation (6.21) conserves its initial purity. Since experimentally $\eta \approx 30\%$, information is lost in the environment. If the lost information is larger than the gained information during the measurement one gets $\langle I_{QC}\rangle_{\{V(t)\}_t} < 0$. This is the case when the initial state is close to a pure state: during the trajectory the state loses its coherence and hence purity because of the imperfection of the measurement, increasing its entropy. On the other hand when the initial state is close to the most entropic state, the measurement purifies the state of the qubit and the final entropy becomes smaller than the initial one. This transition has been experimentally observed and can be seen in Ref. [138] where the mutual information goes from positive to negative values.

AUTONOMOUS DEMON

Coherent information transfer and work extraction

In the two experiments presented previously the information has to leave the quantum world to be recorded and used in the feedback process of the demon. Yet, it is possible to realize a fully quantum experiment where the demon itself is a quantum system. This is a case where the control is deterministic and unconditional hence without any feedback based on measurement. Instead built-in conditional operations need to be designed for the demon to operate by autonomous feedback. In the dispersive Hamiltonian (6.11), when χ is larger than the linewidths of both the qubit and cavity, a regime known as *photon-resolved* [162], it becomes possible for a pulse at a given frequency to excite the cavity (respectively qubit) conditionally on the number of excitations in the qubit (respectively cavity). More precisely a drive at ω_c displaces the cavity only if the qubit is in its ground state, while a drive at $\omega_q - N\chi$ flips the qubit only when the cavity hosts exactly N photons.

This autonomous quantum Maxwell demon was realized in Ref. [153]. Initially we assume the cavity to be in the vacuum state $|0\rangle$ as thermal excitations can be neglected. After initialization of the qubit in a thermal or in a superposition of energy eigenstates, a pulse at ω_c is applied with a duration chosen to be larger than χ^{-1} to

ensure selectivity. The cavity thus ends up either in $|\alpha_e\rangle = |0\rangle$ if the qubit is excited, or ideally in a coherent state $|\alpha_g\rangle = |\alpha\rangle$ if the qubit is in the ground state. Since the process follows a unitary evolution, an initial superposed state like $(|e\rangle + |g\rangle)/\sqrt{2}$ results in an entangled state $(|e\rangle|0\rangle + |g\rangle|\alpha\rangle)/\sqrt{2}$. Consecutively, a π-pulse at ω_q flips the qubit only if the cavity hosts 0 photon. It is always the case when the qubit is excited, and it happens with a probability $|\langle 0|\alpha\rangle|^2 = \exp(-|\alpha|^2)$ when the qubit is in the ground state. If $\alpha \gg 1$, the demon distinguishes well between ground and excited states and the qubit always ends up in the ground state. Consequently, the information about the qubit state makes the energy exchange of 1 quantum of work between the drive pulse and the qubit unidirectional: the drive is either reflected without loss of energy (if the qubit has no energy to offer) or contains one extra stimulated-emitted photon (if the qubit is in $|e\rangle$). A positive net extraction of work is thus ensured at $\alpha \gg 1$. In the case of an initially superposed qubit, the conditional π-pulse disentangles the qubit and the cavity so that the cavity ends up a state $(|0\rangle + |\alpha\rangle)/\sqrt{\mathcal{N}}$. Therefore the conjugation of conditional displacement and π-pulse swaps the qubit and cavity states and performs a coherent information transfer from the qubit to the cavity. On the other hand if α is not large enough, the conditional π-pulse does not fully disentangle the qubit and the cavity, the information transfer is imperfect and as a result the work extracted is smaller. Similarly to what has been done in Ref. [137], the quantity of information transferred to the demon can be tuned by varying the amplitude of the displacement Ω_c or, equivalently, the mean number of photons in the cavity $\bar{n}$.

Information transfer

In our work [153], the whole sequence is terminated by a full tomography of the final qubit (system) state ρ_S using a set of projective measurements. The evolution of the final Von Neumann entropy of the qubit $S_S = -\text{Tr}(\rho_S \ln \rho_S)$ with $\sqrt{\bar{n}}$ is represented in Fig. 6.10 for various initial states of the qubit, either in a thermal or superposed state. Its evolution exhibits a clear quantum feature that highlights the quantumness of the demon. The entropy of the qubit first goes to a maximum before eventually decreasing. This increase of entropy manifests the residual presence of entanglement between the qubit and the cavity after the work extraction pulse: when measuring the state of the qubit only, one discards the information encoded in the cavity and gets a more entropic qubit. Within the interpretation of the experiment in terms of Maxwell's demon, this large qubit entropy means that the demon operates erratically due to the partial quantum information it gets on the qubit. It is not the case when $\bar{n} \ll 1$, because then the conditional π-pulse at ω_q is always on resonance. The behavior of the demon becomes perfectly predictable and does not affect the entropy of the qubit. In the limit of large $\bar{n}$ however, the information transfer is large enough so that the demon lowers the entropy of the qubit. The residual entropy is mostly due to the parasitic thermalization of the qubit with the environment during the sequence.

When the demon's memory is a quantum system, such as the cavity here, it becomes possible to realize a full quantum tomography of its state and to uncover its quantum coherences. In our experiment [153], we used the qubit to perform a tomography of the cavity at the end of the sequence based on generalized Husimi Q-functions measurement and state reconstruction [163]. Because we used a single qubit as the system and as a tomographic tool, it is necessary to be certain that the qubit is in
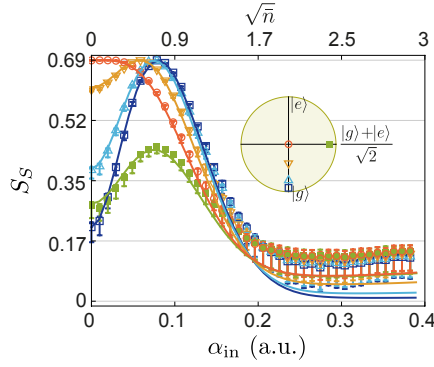
Figure 6.10: (Figure from Ref. [153]) Final measured Von Neumann entropy of the system as a function of the amplitude of the cavity displacement drive amplitude (labeled $\alpha_{\rm in}$), which tunes the information quantity that the demon extracts from the qubit.

the ground state before starting the tomography. For that reason, the range of cavity displacement amplitudes where one can reconstruct the state of the cavity is limited to the cases where the demon cools efficiently the qubit close to its ground state. In particular, the technique does not allow us to measure the variations of the demon's information with the displacement drive amplitude. Such a measurement would be possible if one would use another ancillary qubit just to perform the cavity tomography (for instance with an architecture as in Ref. [164]). The magnitude of the elements of the reconstructed density matrix of the cavity ρ_D is represented in Fig. 6.11 in the Fock state basis for 4 different initial qubit states: (a) ground, (b) excited, (c) superposed and (d) thermal at infinite temperature. As expected, the cavity contains a large number of photons when the qubit is initially in the ground state ($\bar{n} \approx 4.6$) and stays in vacuum when the qubit is initialized in the excited state. The coherence of the process arises when comparing the superposed case and the thermal one. When the qubit is initially superposed, the cavity ends up with non-zero off-diagonal terms of the form $\langle 0|\rho_D|m\rangle$, $m \in \mathbb{N}^*$, showing coherences between the vacuum and the displaced state. These off-diagonal terms are zero in the thermal case.

From the reconstructed density matrix of the demon ρ_D one can infer its Von Neumann entropy in an attempt to quantify the amount of information stored in the cavity. It is indicated on Fig. 6.11. Surprisingly its state is very entropic except when it is in vacuum. This is due to the conjugated effect of the unwanted qubit induced non-linearity in the cavity and of dissipation. As a result the displacement produces an entropic state instead of a coherent state. Yet, the comparison of the superposed and thermal cases shows that the cavity entropy in this case indeed reflects the initial entropy of the qubit, with the superposed state resulting in a less-entropic cavity than the thermal one. However, besides highlighting quantum effects in the transfer of information, it is not possible to perform an information balance between the qubit and the cavity. This is only due to the fact that the information on the two-dimensional qubit is encoded in a multi-level system, the cavity, which does not remains pure due to the aforementioned parasitic nonlinearities. With this type of encoding, the only relevant information for the demon to operate efficiently is whether or not the cavity is in $|0\rangle$. Therefore, one could think of a better definition for the stored information in such a way that it would eliminate the irrelevant contribution of entropy in the excited states of the cavity.
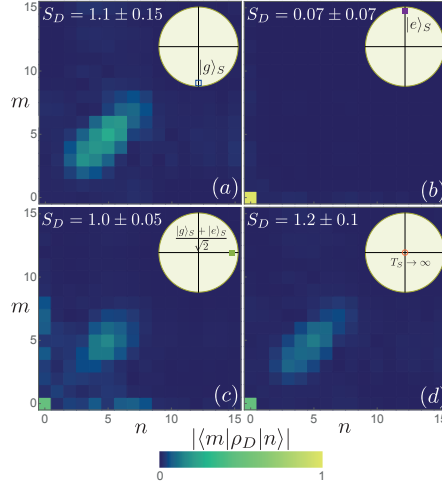
Figure 6.11: (Figure from Ref. [153]) Amplitude of the elements of the reconstructed density matrix of the cavity (demon's memory) in the Fock states basis after the sequence for a qubit initialized in the (a) ground state, (b) excited state, (c) superposed state and (d) thermal state at infinite temperature.

Direct work measurement

Interestingly, it is possible to perform a direct measurement of the work extracted by the demon without resorting to the TPM process. It is done by directly recording the power contained in the reflected π-pulse. Given the small energy of a single microwave photon, the use of quantum limited Jopsephson amplifiers was instrumental [148]. To do so in Ref. [153], we amplify the reflected pulse by a Josephson Parametric Converter (JPC) [165]. It amplifies the two field quadratures by the same amount and as a result acts as a *phase-preserving* amplifier. After amplification the field is digitized and the average instantaneous power at ω_q is extracted. Denoting as $a_{\rm in,out}$ the annihilation operator of a photon propagating in the transmission line towards (respectively from) the cavity, one can simply express the power extracted from the qubit $P_{\rm ext}$ by the difference between the photon rate that is sent and the one that is reflected $P_{\rm ext} = \hbar\omega_q(\langle a_{\rm out}^\dagger a_{\rm out}\rangle - \langle a_{\rm in}^\dagger a_{\rm in}\rangle)$. Besides one can write the propagating number of photons in the transmission line in terms of qubit operators [1]

$$\frac{P_{\rm ext}}{\hbar\omega_q} = \gamma_a \frac{1 + \langle\sigma_z\rangle}{2} + \frac{\Omega_q}{2}\langle\sigma_x\rangle, \tag{6.19}$$

where γ_a is the emission rate of the qubit towards the transmission line and Ω_q is the Rabi frequency as defined in equation 6.12. The first term is proportional to the probability to find the qubit in the excited state and thus corresponds to spontaneous emission of the qubit. To understand the second one, let us integrate it over half a Rabi oscillation. In the absence of losses ($\Omega_q \gg \gamma_a$), if the qubit goes from $|g\rangle$ to $|e\rangle$, one would find -1, and $+1$ for a qubit going from $|e\rangle$ to $|g\rangle$. Therefore, in case of negligible loss during the pulse, this term quantifies the coherent energy exchanges between the drive and the qubit through absorption/stimulated emission cycles.

Experimentally the reflected signal is decomposed into short time bins and integrated to get the extracted work $W = \int_0^{\pi/\Omega_q} P_{\rm ext}\mathrm{d}t$. The evolution of the extracted work with the number of photons contained in the demon is represented in Fig. 6.12
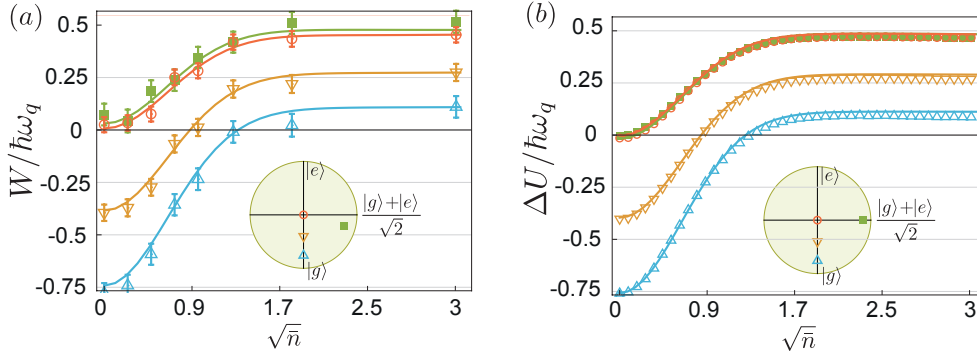
Figure 6.12: (Adapted from [153])(a) Directly measured extracted work from the qubit by the autonomous demon for various initial thermal or superposed states. The direct measurement perfectly agrees with the (b) independent measurement of the variation of energy of the qubit between two projective measurements (TPM).

as well as the variation of the qubit internal energy $\Delta U = E(t_i) - E(t_f)$ obtained from the qubit tomography, which is equivalent to a TPM in the case of projective measurement along σ_Z. As expected the extracted work is negative when the demon does not distinguish the ground from the excited state, and becomes positive as the number of photons in the cavity increases. The direct work measurement and the qubit energy change measurement are not obtained for the exact same pulse sequences due to technical issues in the work measurement (see supplementary material of [153]). A consequence is that the superposed state prepared in the two cases is not exactly the same, as represented in the Bloch sphere projections in the XZ-plane in insets. Nevertheless the agreement between the two independent measurements is remarkable.

CONCLUSION

Summary on already realized experiments

The three experimental realizations of a quantum Maxwell's demon presented in this chapter demonstrate that superconducting circuits constitute a useful and versatile testbed for quantum thermodynamics. They make possible the experimental validation of thermodynamical equalities in the context of various measurements: strong, weak, quantum trajectories or coherent transfer to an ancillary quantum system. The main features of these three experiments are shown in table 6.1. On the basis of this table, we can foresee directions towards which future experimental realizations with superconducting circuits could go. A direct work measurement (using direct microwave measurement of the released energy [153], calorimeters [166] or other techniques) coupled to a demon using classical information would give access to the influence of irreversible events and how they arise when the measurement becomes strong. Coupled to quantum trajectory measurements, a direct work measurement through fluorescence would allow one to precisely quantify and separate the flows of heat and work during the trajectory and the feedback pulse. Finally in the case of quantum demon memories, the use of an ancillary qubit would allow one to perform joint measurements of the states of the qubit and cavity, and hence to quantify the mutual information between them at any measurement strength. This would lead to

the experimental measurement of a fully quantum Jarzynski equality in the presence of quantum coherence.

Theoretical proposals

Over the past ten years few theoretical proposals have designed experiments based on superconducting circuits to probe further the physics of Maxwell's demon in quantum mechanics. First, it has been suggested to use superconducting circuits to realize a quantum Otto engine [167], by using the tunability of the coupling between two charge qubits. A second important use of superconducting circuits is the possibility to quickly tune their frequency, allowing a demon to extract work from the system up to the Landauer bound $k_B T \ln 2$. Such as scheme was proposed by Pekola *et al.* [140] for a single qubit using Landau-Zener transitions and measurement based feedback. In the three existing experiments, the energy levels of the qubit were fixed and it was thus impossible to saturate the bound. More precisely the maximal work extracted by the demon from a fixed-frequency qubit is equal to the initial mean energy of the qubit: $W_{\max} = \hbar \omega_q p_e$ where p_e denotes the initial probability to find the qubit in the excited state. At thermal equilibrium at temperature T it reads $p_e = 1/(1 + \exp(\hbar \omega_q / k_B T))$ and the ratio of work over Landauer bound reads at best

$$\frac{W_{\max}}{k_B T \ln 2} = \frac{\hbar \omega_q / k_B T}{\ln 2 (1 + e^{\hbar \omega_q / k_B T})} \tag{6.20}$$

and reaches a maximum determined numerically around 40%. However allowing to tune the energy levels of the qubit during the sequence leads to saturating the bound. First, the initial sequence is left unchanged: the qubit is thermalized at fixed frequency ω_1, then measured and flipped to the ground state (whether or not the demon is classical does not change the energy balance here). As already stated, this technique extracts at best a work $W_1 = \hbar \omega_1 p_e$. Second, the energy levels are shifted adiabatically to a frequency ω_2 so that $\hbar \omega_2 \gg k_B T$. Since the qubit is in the ground state, this process can be done without any expense of external work. Third, the energy levels are brought back quasi-statically to the initial frequency ω_1. This has to be done slowly enough so that the qubit is always at equilibrium with the heat bath at temperature T. This process extracts a work $k_B T \ln 2 - W_1$ and hence the total work extracted from the qubit reaches the bound. More generally, using tunable qubits leads to designing thermal machines able to operate at the Carnot efficiency. Josephson junction circuits offer such a tunability by the application of an external magnetic flux through a loop of two junctions [155]. Various theoretical proposals suggest to use this tunability to perform Otto thermal machines operating either as engines or refrigerators [168, 169]. Owing to the possibility to perform single-shot measurements, superconducting circuits could exhibit the role of information transfers in such systems.

In most of proposed realizations of Maxwell's demon, the information about the system is used to extract work from a single heat bath. This process is not the only apparent violation of the second principle: an information-powered refrigerator would apparently violate the second principle as well. Campisi *et al.* [170] proposed to use superconducting circuits coupled to calorimetric measurements to generate an inverse heat flow from a cold bath to a hot one. Each bath is modeled as an RLC resonator with a frequency that can be tuned by an external flux and at temperatures

	Masuyama et al. [137]	Naghiloo et al. [138]	Cottet, Jezouin et al. [153]
Nature of the demon	Classical	Classical	Quantum
Mutual information knob	Cavity drive amplitude	Measurement duration	Cavity drive amplitude
Work determination	Inferred from TPM	Inferred from TPM	Direct power measurement
Fluctuation relation	Sagawa-Ueda equality for weak to strong measurement	Jarzynski equality with quantum trajectories	No measure of mutual information
Information evolution	Classical information	Information loss causing $\langle I \rangle \leq 0$	Differing demon entropies for thermal and quantum cases

Table 6.1: Status of the three existing experiments on quantum Maxwell's demon using superconducting circuits at the time of this writing.

$T_{h,c}$, with $T_c < T_h$. Both resonators are inductively coupled to the same superconducting qubit. Recently developed calorimeters [80, 82, 171] allow to detect when an excitation leaves or enters each resistor, and provide the information acquired by the demon. Initially the cold bath and the qubit in its ground state are on resonance and the hot bath is far from resonance, inhibiting the effective coupling between the bath and the qubit. A calorimeter can detect the transfer of an excitation from the cold bath to the qubit. Such an event triggers, by measurement based feedback, pulses on two control fluxes that bring the hot bath in resonance with the qubit and put the cold bath out of resonance. The qubit eventually releases its excitation into the hot bath. This event is detected by the heating of the hot resistor through a second calorimeter and a second feedback control is applied to bring the system back to its initial state, hence closing the thermodynamic cycle.

When measuring the state of the qubit, it is interesting to consider cases where the demon does not measure its state in the energy basis, i.e. along the z-axis of the Bloch sphere. A measurement that would project the qubit in a coherent superposition [172, 173] would instead allow for more work extraction than classically allowed, by using the quantum coherence as a resource. Elouard *et al.* [174] studied the case of a demon measuring the state of a superconducting circuit in the x-direction. The qubit is initialized in $(|g\rangle + |e\rangle)/\sqrt{2}$ then measured strongly along the x-axis in a stroboscopic way, and as a result is projected each time onto $(|g\rangle \pm |e\rangle)/\sqrt{2}$. Between the measurements the qubit is driven on resonance during a time τ with a Rabi frequency Ω_q and extracts positive work from the qubit if it was initially in $(|g\rangle + |e\rangle)/\sqrt{2}$. In the limit where $\Omega_q \tau \ll 1$, the qubit has almost not evolved between two consecutive measurements and is re-projected with a very high probability on $(|g\rangle + |e\rangle)/\sqrt{2}$ by Zeno effect. Therefore the external pulse is continuously powered-up by the projective measurement of the qubit along x. Importantly, such a heat engine can be done in the absence of an external cold bath: the energy is here provided by the back-action of the measurement apparatus.

Perspectives

The first experimental realizations of quantum Maxwell's demons in this platform illustrate the many possibilities offered by superconducting circuits. They pave the way to various more experiments that will explore the intimate link between information and thermodynamics in the quantum regime. With this goal in mind, one could think of using other kinds of systems than transmon qubits as working agents. Among them, fluxonium qubits [24] appear as an extremely promising platform because they offer a whole zoology of transitions. Their transition frequency can be tuned from hundreds of MHz to about 20 GHz using an external magnetic flux, offering the possibility to study regimes where the system dynamically goes from $\hbar\omega \gg k_B T$ to $\hbar\omega \ll k_B T$. Moreover the coupling rates of fluxonium qubits with their environment can vary over 5 orders of magnitude, allowing one to finely engineer the heat exchanges with the baths. Superconducting circuits can also provide components of more sophisticated experiments that would use heat switches [175]. In a broader picture, the use of hybrid systems formed by superconducting circuits coupled to mechanical resonators appears as extremely promising. It would allow one to proceed to a work extraction that would indeed be used to lift a small mass, as in the first early descriptions

of Maxwell's gedanken experiment. This could be interesting to solve controversies about the nature of heat and work in quantum systems. Superconducting circuits are also a promising platform for realizing entanglement between two qubits by the use of thermal baths only and in the absence of any coherent drive [176]. With the steady improvement of superconducting qubits, there is no doubt that these systems offer a growing number of possibilities to test quantum thermodynamic properties and implement potential applications.

APPENDIX

Quantum trajectories

We describe here how one can determine the quantum state ρ_t in the experiment of Naghiloo *et al.* [138]. The signal $V(t)$ carrying the information being continuous, one can decompose the information into time bins and get a time-resolved measurement. In order to observe non negligible effects of measurement backaction, it is crucial to minimize the amount of information that is lost between the cavity and the measurement apparatus, i.e. to maximize the quantum efficiency η. This process is done using quantum-limited amplification right after the cavity, a process that adds the minimal amount of noise allowed by quantum mechanics [177]. In their quantum trajectories experiment, Naghiloo *et al.* use a Josephson Parametric Amplifier (JPA) [178] that amplifies one of the two quadratures of the field (equivalent to the position and momentum operators of a mechanical linear oscillator) and as such operates as a *phase-sensitive* amplifier allowing to reach a state of the art quantum efficiency of about $\eta = 30\%$. Denoting as $\mathrm{d}t$ the time interval between two successive records, the measurement record at time t is given by $\mathrm{d}V(t) = \sqrt{2\eta\Gamma_m}\langle\sigma_z\rangle_{\rho_t}\mathrm{d}t + \mathrm{d}\mathcal{W}_t$ where $\mathrm{d}\mathcal{W}_t$ a zero-mean Wiener process whose variance is $\mathrm{d}t$ and which represents the quantum and technical noise. Note that here the expectation value $\langle\sigma_z\rangle_{\rho_t} = \mathrm{Tr}(\rho_t\sigma_z)$ depends on the particular realization of the trajectory and thus on the measurement record $\{V(\tau)\}_\tau$ at all times $\tau < t$. The density matrix of the qubit is then reconstructed using the Stochastic Master Equation (SME) [179]

$$\mathrm{d}\rho_{\mathrm{t}} = -\mathrm{d}t\frac{i}{\hbar}[H,\rho_t] + \mathrm{d}t\frac{\Gamma_m}{2}\mathcal{D}[\sigma_z]\rho_t + \mathrm{d}\mathcal{W}_t\sqrt{2\eta\Gamma_m}\mathcal{M}[\sigma_z]\rho_t, \tag{6.21}$$

where $\mathcal{D}$ is the Lindblad super operator and $\mathcal{M}$ the measurement super operator $\mathcal{M}[c]\rho = \frac{1}{2}\big((c)-\langle c\rangle)\rho + \rho(c^\dagger - \langle c^\dagger\rangle)\big)$. The two first terms correspond to a Lindbladian evolution of the qubit dephased by the measurement drive (for the seek of simplicity other decoherence channels as spontaneous decay of the qubit have been omitted). The last one represents the measurement backaction: at each $\mathrm{d}t$ the state is kicked depending on the measurement record, possibly changing the mean energy of the qubit. The inherent stochasticity of the SME highlights the profound link between information and energy in quantum mechanics and has triggered recent works on the subject, including in the field of superconducting circuits. The reader can refer to the chapters 14, 28 and 33 in [95] for a more precise treatment of the subject.

<div style="text-align: right; font-size: 3em;">

7

</div>

AUTONOMOUS QUANTUM MAXWELL'S DEMON

In this chapter we describe, implement and characterize fully an autonomous Maxwell's demon experiment where the system is a superconducting qubit and the demon the first resonance mode of a cavity. We show how we can use the different constituents of the experiment to quantify the flows of energy and information and use the photon rate measurement based on time-resolved fluorescence presented in Sec 2.4 to directly measure the extracted work [147].

7.1 QUBIT-CAVITY AS AN AUTONOMOUS DEMON

It is enlightening to start our analysis with an ideal description of the experiment where the cavity is a perfectly linear oscillator, dispersively coupled to a qubit, and where the total time of the experiment is much shorter than the thermalization time of both the cavity and qubit. With this simple model we are able to derive the energy and entropy variations and define the demon's blindness. We describe how we will use the qubit and cavity to characterize the states of the system and demon and derive the experimental constraints coming from this setup. Finally we present how we will model the heat bath in the experiment.

7.1.1 *Central notions and predictions*

The principle of the experiment is represented in Fig. 7.1. The system (S) is a transmon superconducting qubit at frequency f_S dispersively coupled to the demon (D), an aluminum microwave cavity at frequency f_D. The demon is coupled to a bath at zero temperature so that it is initially in vacuum $|0\rangle$. According to Chap. 1, the dispersive Hamiltonian reads $H = h f_S |e\rangle\langle e| + h f_D d^\dagger d - h\chi d^\dagger d |e\rangle\langle e|$, where d is the annihilation operator of a photon in the cavity and $|e\rangle$ is the system's excited state. The last term induces a frequency shift of the cavity by $-\chi$ when the qubit is excited. Reciprocally the qubit frequency is shifted by $-N\chi$ when the cavity hosts N photons. This coupling enables to correlate the cavity with the qubit by driving it through one of the two microwave ports a and b and is used to perform the two conditional operations described for the autonomous demon in Sec. 6.2, with the only difference that here the demon is not a qubit but a linear oscillator.

Work extraction is performed as follows. First the system is initialized in a thermal or a superposed state using a pulse at f_S. The precise description of heating will be done later. Second the state of the system is encoded into the demon using a pulse at f_D on port a with the amplitude α_{in}. It is resonant with the cavity and generates a coherent state $|\alpha\rangle$ only if the system is in its ground state $|g\rangle$, otherwise the demon stays in vacuum. Third work is extracted using a π-pulse at f_S playing the role of the battery B and sent through port b. Without the demon, the qubit would deterministically absorb (emit) a quantum of energy $h f_S$ from (into) the battery, if it is initially in $|g\rangle$ ($|e\rangle$). Crucially the demon prevents this transfer when its memory has $N \geq 1$ photons, because then the pulse is off resonance by $-N\chi$. When the correlation between
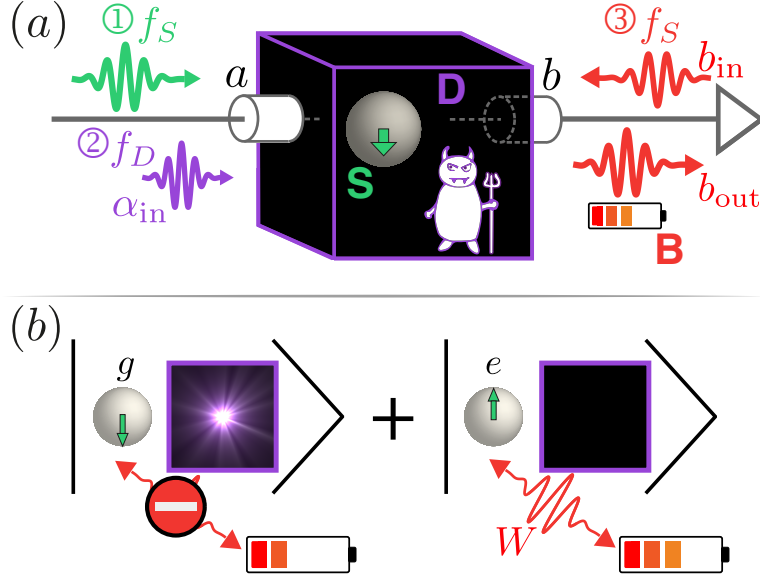
Figure 7.1: Sketch of the quantum Maxwell demon experiment. a) After preparation ① in a thermal or quantum state by a pulse at frequency f_S, the system S (superconducting qubit) state is recorded ② into the demon's quantum memory D (microwave cavity). In practice, a pulse incoming towards port a at f_D populates the cavity mode with a state $|\alpha\rangle$ only if the qubit is in the ground state $|g\rangle$. This information is used to extract work W ③, which charges a battery B (a microwave pulse at frequency f_S on port b) with one extra photon. Importantly the system emits this photon only when the demon's cavity is empty. The work is determined by amplifying and measuring the average output power at f_S on b_{out}. The memory reset step ④ is performed by cavity relaxation.
b) When the system starts in a quantum superposition of $|g\rangle$ and $|e\rangle$, the demon and system are entangled after step ②.

the demon's memory having no photons and the system being in $|e\rangle$ is perfect only stimulated emission is allowed and work is extracted from system to battery. However, when the correlation is not perfect, in particular when $|\alpha| < 1$ the demon sometimes erroneously lets the qubit absorb a quantum of energy from the battery. The demon thus ends in a state with an entropy S_D of at least the decrease of system entropy, and has to be reset to close the thermodynamic cycle. In the final step of this experiment we let the demon's memory thermalize with the bath at zero temperature. So this demon can extract work in a cyclic manner but it does so using a second bath, thus behaving as a regular heat engine.

The fact that the demon is not a qubit but a linear oscillator hosting a coherent state $|\alpha\rangle$ when the system is in the ground state has a large influence on the amount of extracted work and on the system's and demon's final entropies. In fact, $|0\rangle$ and $|\alpha\rangle$ are not orthogonal as their overlap is given by

$$\langle 0|\alpha\rangle = e^{-|\alpha|^2/2} \ . \tag{7.1}$$

Let us decompose the contribution of vacuum in the coherent state by writing $|\alpha\rangle = e^{-|\alpha|^2/2}|0\rangle + \sqrt{1 - e^{-|\alpha|^2}}|\tilde{\alpha}\rangle$. The constants in front of $|0\rangle$ and $|\tilde{\alpha}\rangle$ ensure the normalization of $|\tilde{\alpha}\rangle \propto (\mathbb{1} - |0\rangle\langle 0|)|\alpha\rangle$. The states $|0\rangle$ and $|\tilde{\alpha}\rangle$ are thus orthonormal and realize an orthonormal basis of the demon's states for a fixed value of α. After preparation the demon is in vacuum $|0\rangle$ and the system-demon state is represented by the initial

density matrix $\rho_1 = (\rho_{gg}|g\rangle\langle g| + \rho_{ee}|e\rangle\langle e| + \rho_{eg}|e\rangle\langle g| + \rho_{ge}|g\rangle\langle e|) \otimes |0\rangle\langle 0|$. After conditional displacement the system-demon state ρ_2 reads $\rho_2 = \rho_{gg}|g\alpha\rangle\langle g\alpha| + \rho_{ee}|e0\rangle\langle e0| + \rho_{eg}|e0\rangle\langle g\alpha| + \rho_{ge}|g\alpha\rangle\langle e0|$ and can be rewritten as

$$
\begin{aligned}
\rho_2 = \Big(& \rho_{gg}e^{-|\alpha|^2}|g\rangle\langle g| + \rho_{ee}|e\rangle\langle e| + \rho_{eg}e^{-|\alpha|^2/2}|e\rangle\langle g| \\
& + \rho_{ge}e^{-|\alpha|^2/2}|g\rangle\langle e| \Big) \otimes |0\rangle\langle 0| + \rho_{gg}(1 - e^{-|\alpha|^2})|g\tilde{\alpha}\rangle\langle g\tilde{\alpha}| \\
& + \rho_{eg}\sqrt{1 - e^{-|\alpha|^2}}|e0\rangle\langle g\tilde{\alpha}| + \rho_{ge}\sqrt{1 - e^{-|\alpha|^2}}|g\tilde{\alpha}\rangle\langle e0| \; .
\end{aligned}
\tag{7.2}
$$

The state ρ_3 resulting from the conditional π-pulse at f_S can be easily deduced by substituting $|g0\rangle$ and $|e0\rangle$ by respectively $|e0\rangle$ and $-|g0\rangle$. It yields

$$
\begin{aligned}
\rho_3 = \Big(& \rho_{gg}e^{-|\alpha|^2}|e\rangle\langle e| + \rho_{ee}|g\rangle\langle g| - \rho_{eg}e^{-|\alpha|^2/2}|g\rangle\langle e| \\
& - \rho_{ge}e^{-|\alpha|^2/2}|e\rangle\langle g| \Big) \otimes |0\rangle\langle 0| + \rho_{gg}(1 - e^{-|\alpha|^2})|g\tilde{\alpha}\rangle\langle g\tilde{\alpha}| \\
& - \rho_{eg}\sqrt{1 - e^{-|\alpha|^2}}|g0\rangle\langle g\tilde{\alpha}| - \rho_{ge}\sqrt{1 - e^{-|\alpha|^2}}|g\tilde{\alpha}\rangle\langle g0| \; .
\end{aligned}
\tag{7.3}
$$

The system's and demon's final states ρ_S and ρ_D are obtained by taking the partial trace over respectively the demon and system. In the respective orthonormal bases $\{|g\rangle, |e\rangle\}$ and $\{|0\rangle, |\tilde{\alpha}\rangle\}$ we get

$$
\rho_S = \begin{pmatrix} \rho_{ee} + \rho_{gg}(1 - e^{-|\alpha|^2}) & -\rho_{eg}e^{-|\alpha|^2/2} \\ -\rho_{ge}e^{-|\alpha|^2/2} & \rho_{gg}e^{-|\alpha|^2} \end{pmatrix}
\tag{7.4}
$$

$$
\rho_D = \begin{pmatrix} \rho_{ee} + \rho_{gg}e^{-|\alpha|^2} & -\rho_{eg}\sqrt{1 - e^{-|\alpha|^2}} \\ -\rho_{ge}\sqrt{1 - e^{-|\alpha|^2}} & \rho_{gg}(1 - e^{-|\alpha|^2}) \; . \end{pmatrix}
\tag{7.5}
$$

Note the symmetry between the two expressions where there is simply an exchange between $e^{-|\alpha|^2}$ and $1 - e^{-|\alpha|^2}$.

The two limiting cases $\alpha = 0$ and $\alpha \gg 1$ illustrate well the role of α. When $\alpha = 0$ the system is simply flipped by a π-pulse while the demon stays in vacuum. When $\alpha \gg 1$ the system is in the ground state and the demon's state corresponds exactly to the initial system's state mapped onto the demon's basis using the correspondence $|e\rangle \to -|0\rangle$ and $|g\rangle \to |\tilde{\alpha}\rangle$. The parameter $e^{-|\alpha|^2}$ quantifies the probability for the demon to erroneously excite the qubit instead of leaving it in the ground state and can therefore be seen as a quantum error probability. We call this quantity the *demon's blindness*, as it is related to the demon not distinguishing correctly between $|g\rangle$ and $|e\rangle$. The final internal energy of the system is given by $U_S = \langle e|\rho_S|e\rangle$ and is simply expressed in terms of the demon's blindness

$$
U_S = \rho_{gg}e^{-|\alpha|^2} \; .
\tag{7.6}
$$

The final entropies of the system and demon can be computed by the von Neumann entropies $S_{S,D} = -\mathrm{Tr}(\rho_{S,D}\ln\rho_{S,D})$. Even though they do not have a simple expression in general (though an analytical solution always exists) a simple example can help us capture the evolution of the system entropy. When it is initialized in $|g\rangle$ the final state is $\rho_S = (1 - e^{-|\alpha|^2})|g\rangle\langle g| + e^{-|\alpha|^2}|e\rangle\langle e|$. Its entropy is directly given by the Shannon entropy $H(p) = p\ln p + (1 - p)\ln(1 - p)$ with $p = e^{-|\alpha|^2}$. When α is varied from 0 to values much greater than 1, p continuously goes from 1 to 0. Therefore the final entropy first goes up from 0 until it reaches $\ln 2$ for $p = 1/2 \Leftrightarrow |\alpha|^2 = \ln 2$ corresponding to the

maximally entropic state, before decreasing towards 0. This increase of entropy between the initial non-entropic state and the final state is due to the unpredictability of the demon's action, coming from its quantum nature and quantified by the blindness, the demon being perfectly predictable when $\alpha = 0$ or $\alpha \gg 1$. This is therefore a strong signature of quantumness. For more general states we thus expect the evolution of the final system's entropy to always reach a maximum before decreasing.

7.1.2 *Following energy and entropy flows*

The use of a transmon qubit coupled to a cavity has the advantage of allowing the experimentalist to measure and characterize the initial and final states of both the system, demon and battery and therefore to quantify the transfers of energy and entropy. System tomography is made possible by using the cavity to measure the state of the qubit. In the experiment we use a High Power Readout measurement described in Sec. B.2 to measure the qubit in the energy basis. Owing to rotations of the system in the Bloch sphere we can achieve its complete tomography and deduce its energy and entropy. To avoid errors due to remaining photons in the cavity after the whole demon process we need to make sure that the cavity is in vacuum before we perform the system tomography.

The energy contained in the battery is represented by the photon rate $\langle b_{\mathrm{out}}^{\dagger} b_{\mathrm{out}} \rangle$ which is measured using the fluorescence power detection described in Sec. 2.4. Using phase-preserving amplification at the quantum limit of the field at f_S outgoing from the cavity in line b, we obtain a time-resolved measurement of the photon rate contained in the battery and integrate it to deduce the extracted work with a good accuracy.

Demon tomography is performed using the qubit as a measurement apparatus. The qubit, initially in the ground state, can be used to measure cavity operators such as the photon number parity or the projectors on Fock states $|n\rangle\langle n|$, $n \in \mathbb{N}$. This allows to measure the cavity's Wigner function or its generalized Husimi functions, which are both related to the cavity state by a bijective function [30].

7.1.3 *Experimental constraints*

The practical implementation of the experimental scheme described in Fig. 7.1 requires the fulfillment of precise experimental constraints. The main one is to ensure selectivity of conditional operations. Since it relies on frequency changes, selectivity is only possible if the dispersive shift χ is much larger than the linewidths of the qubit and cavity, respectively Γ and κ

$$\chi \gg \Gamma, \kappa . \tag{7.7}$$

The conditional displacement pulse and π-pulse are selective if their bandwidth is small enough. For a pulse duration T_{pulse}, the typical width in the frequency domain is proportional to $(T_{\mathrm{pulse}})^{-1}$. On the other hand we want the total duration of the sequence to be smaller than the thermalization time of the system and demon Γ^{-1} and κ^{-1}. We hence get the following constraint

$$\chi \gg (T_{\mathrm{pulse}})^{-1} \gg \Gamma, \kappa . \tag{7.8}$$

In order to optimize the measurement of the work contained in the battery we want to maximize the emission of qubit fluorescence towards the transmission line b. It means

that we need to maximize the Purcell rate Γ_b. Ideally to the limit where it overcomes all the losses $\Gamma \approx \Gamma_b$. For a transmon qubit the Purcell rate is theoretically given by $\Gamma_b = \kappa_b \frac{g^2}{\Delta^2}$ with κ_b the cavity coupling to b, g the qubit-cavity coupling and $\Delta = f_D - f_S$ (see Sec. 1.1.2). We thus largely open the cavity towards b. On the other hand we can reduce κ_a to limit the amount of information leaking towards line a where there is no detectors, preventing that we compensate by driving stronger. We are thus left with the condition

$$\kappa_b \gg \kappa_a, \text{hence } \kappa \approx \kappa_b . \tag{7.9}$$

The dispersive regime is based on the assumption $\Delta \gg g$. The dispersive shift for a transmon qubit is $\chi = 2\frac{E_C}{h}\frac{g^2}{\Delta^2}$ with E_C the charging energy (see Chap. 1). Both g and E_C are fixed by design and the constraint to stay in the transmon regime. We hence reduce Δ as much as possible while staying in the dispersive limit. Typically 3D-transmons yield $g \sim 200 - 300$ MHz so we design the qubit and cavity frequencies so that $\Delta \approx 1$ GHz.

An important consequence of the previous constraints is that the decay rate of the cavity is much larger than the one of the qubit $\kappa \gg \Gamma \approx \Gamma_b$. In general a realization of the demon experiment leaves the system and demon partially excited. With $\kappa \gg \Gamma$ there exists a waiting time for which the cavity has fully relaxed to vacuum while the qubit's state has almost not changed. We can thus make a full tomography of the system for all values of α. However the tomography of the demon relies on the qubit being initially in the ground state to correctly measure the cavity's Wigner or Husimi functions. We are therefore limited to the values of α ensuring that the system ends up in the ground state after the demon experiment, hence $\alpha \gg 1$. We will thus not be able to characterize the evolution of the demon's entropy with α.

This constraints would be different and some of them could have been lifted with a different design. For instance a design based on a qubit coupled to a long-lifetime cavity playing the demon and a low-quality readout resonator [50] for spectroscopy makes possible a demon spectroscopy for all values of α using a quick reset of the qubit to the ground state by converting its excitations into readout resonator excitations. Moreover a single qubit coupled to a single cavity does not allow to measure the joint entropy characterizing the information shared between the system and the demon. For performing joint tomography we could add a second pair qubit-readout resonator coupled to a long-lifetime cavity [51].

7.1.4 *Heat bath generation*

We discuss now the generation of a thermal bath for the system's initialization. When a qubit density matrix ρ is diagonal its temperature T_S can be defined by the Boltzmann weight $\langle e|\rho|e\rangle = (1 + e^{hf_S/k_B T_S})^{-1}$. T_S is indeed a properly defined temperature in the sense that the qubit will be in a state ρ such as above when in thermal equilibrium with a bath at temperature T_S. The qubit unitary interaction with other quantum objects is the same whether it was initially at thermal equilibrium or initialized in a diagonal density matrix since only the probabilities of occupation of $|g\rangle$ and $|e\rangle$ matter. Therefore we can imagine various ways to initialize the qubit in a thermal state, where the choice of the thermal environment is guided by a tradeoff between proximity to an actual heat bath coupled to the qubit and controllability of the bath. By actual bath we mean an environment in which the experimentalist has no control on and information about the

internal degrees of freedom. Therefore at a given bath temperature no post-selection can lower the bath entropy. At the other end of the spectrum the user has a full control on the effective bath and the entropy comes from an intentional loss of information.

- Warming up the whole dilution refrigerator [67]

- Johnson-Nyquist noise of a heated resistive load [34]

- Shot noise of a voltage biased normal metal tunnel junction [165]

- Modulating a tone at f_S with a noisy envelope generated by an arbitrary waveform generator

- Realizing a π-pulse on the qubit with a probability $p(T_S)$ by drawing a random number

- Realizing a π-pulse on the qubit for a subset of $p(T_S)N_{\text{tot}}$ sequences out of the N_{tot} sequences

Physically closer to an actual heat bath

Better control and fewer side effects
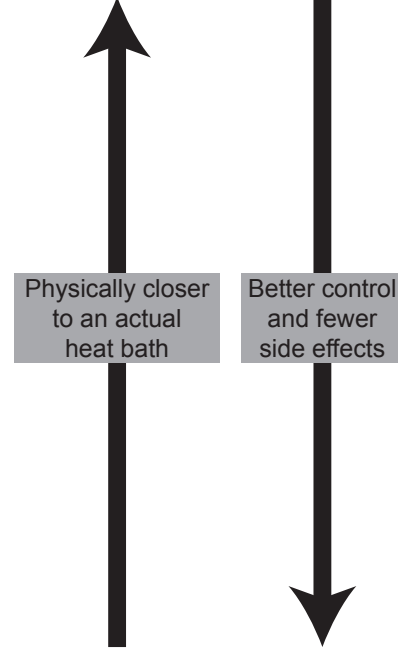
Since all these heat baths prepare the same density matrix, we chose to use the most practical one, which consists in driving the qubit with a π-pulse during the preparation stage for only a fraction $p(T_S)$ of the experimental sequences and leave it in the initial equilibrium state for a fraction $1 - p(T_S)$. The probability $p(T_S)$ has to be chosen such that for an initial qubit temperature T_S^0 the correct Boltzmann weight at T_S is reproduced. In fact even though ideally the qubit is coupled to a bath at zero temperature this is not the case practically and our thermal bath simulation needs to take it into account. Moreover the calculation has to include the imperfection of the preparation pulse quantified by the fidelity F_π of the π-pulse. It yields

$$
\begin{aligned}
\frac{1}{1 + e^{hf_S/k_B T_S}} = p(T_S)\Big(F_\pi\big(1 - \frac{1}{1 + e^{hf_S/k_B T_S^0}}\big) \\
+ \frac{1 - F_\pi}{1 + e^{hf_S/k_B T_S^0}}\Big) + \frac{1 - p(T_S)}{1 + e^{hf_S/k_B T_S^0}} \;.
\end{aligned}
\tag{7.10}
$$

This determines the form of $p(T_S)$

$$
p(T_S) = \frac{1}{F_\pi} \frac{\big(1 + e^{hf_S/k_B T_S^0}\big)\big(1 + e^{hf_S/k_B T_S}\big)^{-1} - 1}{e^{hf_S/k_B T_S^0} - 1} \;.
\tag{7.11}
$$

7.2 CONCRETE REALIZATION: SYSTEM CHARACTERIZATION AND TECHNICAL ASPECTS

The physical implementation of the experiment is studied in this section. In particular we characterize the deviations from the dispersive Hamiltonian model of the qubit and cavity, describe their effects on thermodynamical quantities and measure the equilibrium temperatures of the qubit and cavity. We precise the particularities of photon

number measurement and how it differs from the previous discussion of Sec. 2.2. As a result we use two different sequences of pulses to implement the demon. Finally we explain how to reconstruct the demon state ρ_D from experimental Husimi functions measured in presence of decoherence.

7.2.1 *Beyond the dispersive Hamiltonian approximation*

The dispersive Hamiltonian is a first approximation of the qubit-cavity Hamiltonian in the large detuning limit. Experimentally the condition $\Delta \gg g$ is barely met in order to optimize the dispersive shift χ and the Purcell emission rate Γ_b. We indeed designed the experiment so that the cavity frequency is $f_D = 7.913$ GHz and the qubit frequency $f_S = 7.088$ GHz. This gives $\Delta = 825$ MHz $\approx 5 \times g$. As a result the qubit induces a non-linearity of the cavity mode resulting in a Kerr term in the Hamiltonian with the constant K, and a linear change of the dispersive shift with the number of photons in the cavity with the constant χ_2. These corrections are small compared to the dispersive shift, about one order of magnitude smaller than χ, but their effect is of practical importance. The total Hamiltonian therefore reads

$$\boxed{\frac{H}{h} = f_S|e\rangle\langle e| + f_D d^\dagger d - \chi d^\dagger d|e\rangle\langle e| - K(d^\dagger d)^2 + \chi_2(d^\dagger d)^2|e\rangle\langle e|} \ . \tag{7.12}$$

The bare qubit frequency f_S is measured with high accuracy by standard Ramsey experiment. The joint measurement of the qubit lifetime gives $\Gamma = (2.2\ \mu s)^{-1} = 454$ kHz and the pure qubit dephasing rate $\Gamma_\varphi = 85$ kHz.
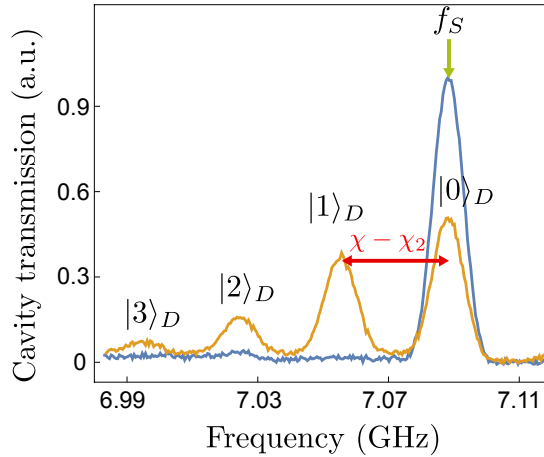
Figure 7.2: Qubit two-tone spectroscopy with cavity (blue) at thermal equilibrium and (orange) after displacement with $\alpha < 1$. Each peak corresponds to one cavity Fock state. The frequency coordinate indicates the frequency of a π-pulse performed just before measuring the cavity transmission.

The photon-number-dependent qubit frequency is then measured with two-tone spectroscopy, as represented in Fig. 7.2. An initial displacement of the cavity leads to several peaks at frequencies f_S^n in the qubit spectrum corresponding to different Fock states of the cavity according to $f_S^n = f_n - n(\chi - n\chi_2)$. Fitting the peaks center frequencies up to 6 photons, we obtain the dispersive shift $\chi = 33.8$ MHz and its non-linearity $\chi_2 = 0.9$ MHz. The two small peaks in the spectroscopy at $f_S \pm 65$ MHz correspond to a small leakage of the modulation pulse on the cavity line happening in the microwave setup at room temperature.

The cavity frequency and loss rate are accessed through measuring the AC-Stark shift and measurement-induced dephasing of the system when the cavity is weakly driven around its resonance frequency, as presented in Sec. B.1.2. We drive the cavity at frequency $f_D + \delta$ and amplitude ϵ weak enough to build a coherent state $|\alpha_{g,e}\rangle$ in the cavity when the cavity is in $|g\rangle$ (resp. $|e\rangle$). Due to the photons stored in the cavity the qubit frequency is detuned by an amount f_{Stark} given by Eq. (B.3) and the qubit acquires an extra dephasing rate Γ_d given by Eq. (B.4), where χ has to be replaced by $\chi - \chi_2$. The derivation of the AC-Stark shift and measurement-induced dephasing was obtained for a qubit coupled to a linear cavity. In our experiment the cavity non-linearity cannot be neglected at high drive amplitude. To avoid this problem we drive the cavity such that $\alpha_{g,e} \approx 0.5$ at resonance ($\delta = 0$ and $\delta = -\chi + \chi_2$). The AC-Stark shift f_{Stark} and measurement-induced dephasing Γ_d are determined by Ramsey fringes experiments. Fig. 7.3 shows their dependence in δ. Fitting the data with the theoretical expressions gives $\kappa/2\pi = 0.77$ MHz and $\chi - \chi_2 = 33.1$ MHz (in agreement with the qubit spectroscopy). The good agreement between the experimental points and the theoretical curves ensures that the corrections due to the cavity Kerr term could be neglected in this case.
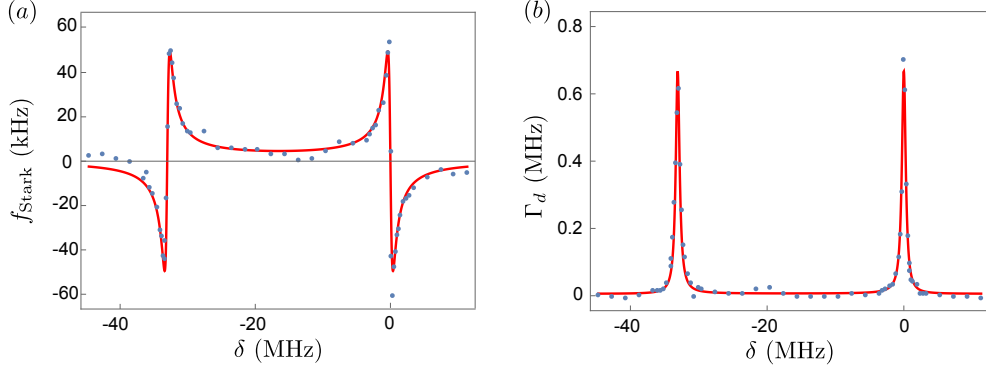
Figure 7.3: a) AC-Stark shift and (b) measurement-induced dephasing of the qubit when the cavity is weakly driven at $f_D + \delta$ so that $\alpha_{e,g} \approx 0.5$ on resonance (see text). Points are experimental data and solid lines are theoretical evolutions given by Eq. (B.3) and Eq. (B.4) respectively, with $\chi - \chi_2 = 33.1$ MHz and $\kappa/2\pi = 0.77$ MHz.

When the cavity non-linearity is not negligible compared to losses a coherent drive α_{in} generates in general a state represented by the density matrix $\rho_{\alpha_{\text{in}}}$ that is far from being a coherent state. In particular it is possible to observe an oscillatory behavior of the probability to find 0 photons in the cavity $\langle 0|\rho_{\alpha_{\text{in}}}|0\rangle$ with the driving amplitude. These oscillations are a generalization of Rabi oscillations to weakly non-linear oscillators [163] implying several Fock states. The value of the Kerr coefficient is thus determined by coherently exciting the cavity and then measuring the probability to find it in vacuum. We drive the cavity with a 100 ns-long drive of variable amplitude α_{in} followed by a π-pulse on the qubit conditioned on the cavity being in the vacuum. The evolution of $\langle 0|\rho_{\alpha_{\text{in}}}|0\rangle$ with the drive amplitude is represented in Fig. 7.4a). To extract the value of K we solve numerically the full master equation using the Python package QuTiP [180] and adapt the non-linearity so that it matches the experimental measurements, since it is at this time of the study the only unknown experimental parameter. We find a very good agreement between the theoretical line and the data for $K = 0.7$ MHz (see Sec. E.1). This large Kerr term compared to usual transmon-cavity experiments is due to the relatively small qubit-cavity detuning. In particular, we have $K \sim \kappa$, possibly

leading to strong deformations of the cavity spectroscopy from a Lorentzian shape. This comes from the deformation of coherent states under the joint effect of both the Kerr non-linearity and dissipation, as illustrated in Fig. 7.4b) where we displayed the simulated Wigner functions of the cavity state for various values of α_{in}.

Figure 7.4: Rabi-like oscillations of the cavity and Kerr estimation. a) Points show the measured probability to find the qubit in $|e\rangle$ after a 100ns-long drive of the cavity with amplitude α_{in} followed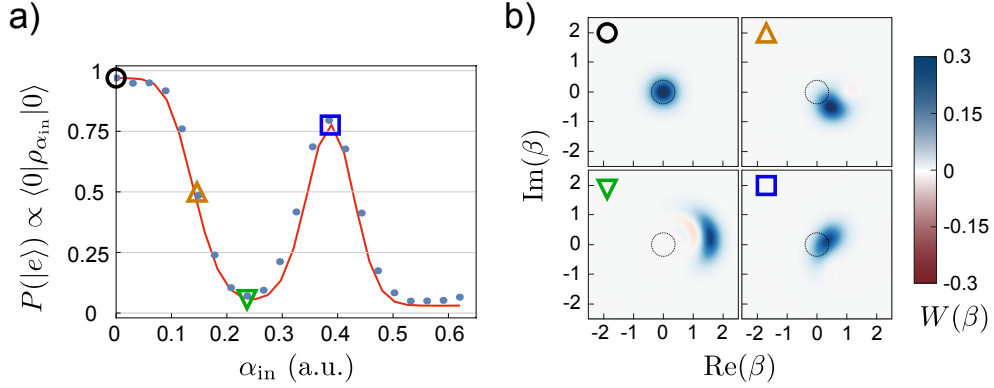 by a π-pulse on the qubit at f_S conditioned on the cavity being in the vacuum. Solid line is obtained by solving numerically the full master equation with $K = 0.7$ MHz (see Sec. E.1).
b) Simulated Wigner functions of the cavity state showing the distortion from a coherent state due to non-linearity for (black circle) $\alpha_{in} = 0$, (orange up triangle) $\alpha_{in} = 0.15$, (green down triangle) $\alpha_{in} = 0.24$ and (blue square) $\alpha_{in} = 0.39$. The variance of vacuum is represented by the black dashed line and highlights the overlap between $\rho_{\alpha_{\text{in}}}$ and vacuum.

The non-linearity of the dispersive shift has no effect on the thermodynamical analysis in the ideal case made in Sec. 7.1.1 because its only role is to ensure the selectivity of conditional pulses. On the other hand the large value of the cavity non-linearity changes dramatically the conclusions made about the final states of the system (qubit) and demon (cavity). First, as we have seen in Fig. 7.4a), the overlap between the cavity state and vacuum is not a monotonous function of the drive amplitude α_{in}. Therefore we can legitimately fear that the demon might not work well at large displacement amplitude where it is supposed to be the most efficient. This issue can be overcome by using the fact that χ is more than one order of magnitude greater than K. Therefore we set the displacement duration so that its frequency spread is much larger than K while remaining smaller than χ and hence still being selective. Second, since the cavity state is not in a coherent state $|\alpha\rangle$ we cannot use $|\alpha|$ as a parameter fixing the demon's blindness anymore. Instead we use the mean number of photons contained by the cavity $\bar{n} = \text{Tr}(d^\dagger d \rho_{\alpha_{\text{in}}})$ as the new measure, based on the analogy with $|\alpha|^2 = \langle\alpha|d^\dagger d|\alpha\rangle$. We concretely compute $\bar{n}$ by numerically solving the complete master equation of the qubit and cavity. Third, with the joint effect of non-linearity and cavity losses, the cavity state is in general entropic[1]. In particular since it cannot be written in the effective two-level system basis $\{|0\rangle, |\tilde{\alpha}\rangle\}$ its von Neumann entropy can possibly go far above 1 bit.

---

[1] It is interesting to note that it is the *joint* effect of these two parameters that leads to a high entropy of the cavity state. Indeed losses only result in a pure coherent state while non-linearity only results in a pure state since the evolution is Hamiltonian. The reason for this is quite profound. We can indeed see it as the competition between the representation of the cavity state in the energy basis, favored by the non-linearity making a difference in frequency between every Fock state, versus the phase space representation attached to the coherent state.

7.2.2 *Qubit and cavity thermal equilibrium*

In the absence of the artificial heat bath the qubit and cavity are at thermal equilibrium with their environment. In reality the system and demon are not coupled to the same bath at zero temperature but to two baths with the respective temperatures T_S^0 and T_D^0. The demon temperature is estimated with the qubit spectroscopy at thermal equilibrium (blue curve in Fig. 7.2). The relative heights of peaks corresponding to different Fock states $|n\rangle$ are given by the relative probabilities for the demon to contain $|n\rangle$ photons. Writing ρ_D^0 the density matrix of the demon when it is at thermal equilibrium with its bath, those probabilities are given by the Maxwell-Boltzmann distribution

$$P(n) = \langle n|\rho_D^0|n\rangle = \frac{e^{-nhf_D/k_B T_D^0}}{Z} \tag{7.13}$$

with $Z = \sum_{n=0}^{+\infty} e^{-nhf_D/k_B T_D^0}$ the partition function. Comparing the peaks at $n = 0$ and $n = 1$ gives $P(1) = 0.7 \pm 0.5\%$ at thermal equilibrium, which corresponds to a temperature

$$\boxed{T_D^0 = 72 \pm 13 \text{ mK}} \ . \tag{7.14}$$

The large Kerr term makes difficult to measure the system's temperature by standard cavity spectroscopy means with a sufficiently good accuracy. Instead we measured the contrast difference between two sets of Rabi oscillations of the system with different initial states. To do so we used the transmon second excited state $|f\rangle$. The resonance frequency between states $|e\rangle$ and $|f\rangle$ is equal to $f_S - E_C/h = 6.962$ GHz. We drive the transmon at $f_S - E_C/h$ to obtain Rabi oscillations between $|e\rangle$ and $|f\rangle$ and measure the transmission of the cavity at $f_D - 2(\chi - \chi_2)$, the resonance frequency of the cavity when the transmon is in $|f\rangle$. The first set of oscillations is obtained by driving the transmon at thermal equilibrium and the second one is obtained by applying a π-pulse between $|g\rangle$ and $|e\rangle$ before driving. The two sets of Rabi oscillations are represented in Fig. 7.5. At thermal equilibrium with its bath at temperature T_S^0 the system is represented by the density matrix ρ_S^0 and the contrast of the oscillations is given by $C^{\text{eq}} = \langle e|\rho_S^0|e\rangle - \langle f|\rho_S^0|f\rangle$, assuming that the oscillations are fast enough and on resonance so that we can neglect decoherence. When $k_B T_S^0 \ll hf_S$ the population in $|f\rangle$ is negligible and we simply get

$$C^{\text{eq}} \approx \langle e|\rho_S^0|e\rangle = \frac{1}{1 + e^{hf_S/k_B T_S^0}} \ . \tag{7.15}$$

The initialization π-pulse on the second set exchanges the populations in $|g\rangle$ and $|e\rangle$ with a fidelity F_π and the contrast of the oscillations is thus given by

$$C^\pi = F_\pi\left(1 - \frac{1}{1 + e^{hf_S/k_B T_S^0}}\right) + \frac{1 - F_\pi}{1 + e^{hf_S/k_B T_S^0}}$$
$$C^\pi = \frac{1 + F_\pi\left(e^{hf_S/k_B T_S^0} - 1\right)}{1 + e^{hf_S/k_B T_S^0}} \ . \tag{7.16}$$

The ratio C^π/C^{eq} hence gives a direct measurement of the quantity $F_\pi(e^{hf_S/k_B T_S^0} - 1)$. The fidelity is estimated to be $F_\pi = 92\%$ from the known system decoherence rate and pulse durations. This yields

$$\boxed{T_S^0 = 103 \pm 9 \text{ mK}} \tag{7.17}$$

which corresponds to an equilibrium population in $|e\rangle$ of $p_e^0 = 3.6 \pm 1$ %. This 1 % uncertainty on the system residual excitation takes into account the temperature fluctuations measured during the time of the experiment. Note that this qubit is the same as the one used in Sec. 2.6. It is clear here that the uncertainty on temperature measurement is not sufficient to explain the inconsistency with the results coming from fluorescence measurements presented in Sec. 2.6.
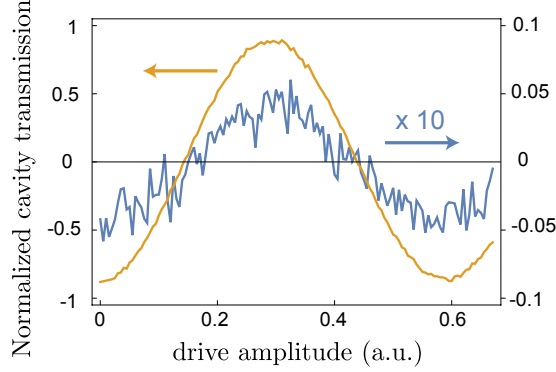

Figure 7.5: System temperature measurement by Rabi oscillations. Two Rabi oscillations between $|e\rangle$ and $|f\rangle$ are measured using the cavity transmission at $f_D - 2(\chi - \chi_2)$, (blue) at thermal equilibrium and (orange) after a π-pulse between the states $|e\rangle$ and $|g\rangle$. The blue curve is magnified 10 times. The y-axis represents the real part of the transmission of the cavity, which is normalized so that 1 indicates a state in $|f\rangle$, while -1 indicates that there is zero probability to find the system in $|f\rangle$.

7.2.3 Time-resolved photon number measurement

The energy contained in the battery after it has interacted with the qubit is measured using the quadrature measurement of the fluorescence field amplitude b_{out} followed by the reconstruction of the mean photon rate $\langle b_{\text{out}}^\dagger b_{\text{out}} \rangle$ as described in Sec. 2.4. Concretely we amplify the signal at f_S using a JPC followed by a classical low-noise amplification chain, down-conversion to 62.5 MHz digitization and demodulation to get the time-resolved field quadratures $\big(I(t), Q(t)\big)$ with a sampling time $\mathrm{d}t = (62.5 \text{ MHz})^{-1} = 16$ ns. The experimental results are averaged over 10^7 measurement records to reconstruct $\langle b_{\text{out}}^\dagger b_{\text{out}} \rangle$ using Eq. (2.55). To avoid filtering of the signal by the amplifier we need the bandwidth of the JPC BW_{JPC} to be larger than the frequency spread of the fluorescence signal around f_S. During the conditional π-pulse it oscillates in time at the Rabi frequency $\Omega = (2T_\pi)^{-1}$ with T_π the duration a square π-pulse. In the frequency domain this means that the JPC gain has to be almost constant on a range of frequency corresponding to the Mollow triplet, and in the time domain this means that the JPC correlation time has to be much smaller than the Rabi period. For a JPC the gain-bandwidth product $\sqrt{G_{\text{JPC}}} \times \text{BW}_{\text{JPC}}$ is constant and given by Eq. (2.41). Using a vector network analyzer we determine $G_{\text{JPC}} \approx 14$ dB and $\text{BW}_{\text{JPC}} = 29$ MHz.

The scaling factor G between $\overline{I^2 + Q^2}$ and $\langle b_{\text{out}}^\dagger b_{\text{out}} \rangle$ is determined in a similar manner than in Sec. 2.5. The only difference is that we exchanged here the roles of a and b. We continuously drive the qubit on resonance through port b for various drive amplitudes β_{in} resulting in various Rabi frequencies $\Omega = 2\sqrt{\Gamma_b}\beta_{\text{in}}$. The qubit undergoes damped Rabi oscillations inducing an oscillation of the photon rate in time. We measure

oscillations of $\overline{I^2 + Q^2}$ with the β_{in}-dependent amplitude $\mathcal{A}^{I^2+Q^2}$ given by Eq. (2.59). In the limit of large Rabi frequencies $\Omega \gg \Gamma_b$ we can express it simply in terms of Ω

$$\mathcal{A}^{I^2+Q^2}(\Omega) = G \times |\langle \sigma_z \rangle^0| \frac{\Omega}{2} \tag{7.18}$$

with $\langle \sigma_z \rangle^0 = \mathrm{Tr}(\sigma_z \rho_S^0)$. On the other hand the quadrature $\overline{I}$ oscillates with an amplitude independent of Ω

$$\mathcal{A}^I = \sqrt{G} \times |\langle \sigma_z \rangle^0| \sqrt{\Gamma_b} \ . \tag{7.19}$$

Since we already know the qubit temperature, we can extract the global gain G by measuring the slope $\mathrm{d}\mathcal{A}^{I^2+Q^2}/\mathrm{d}\Omega$. Fig. 7.6a) shows $\overline{I^2 + Q^2}$ for three different Rabi frequencies[2]. The oscillations can be strongly deformed at small times due to the transient response of the JPC to the rise of β_{in}. This deformation is of practical importance for the measurement of the energy contained in the battery during the demon experiment. In fact the signal is distorted during about 1 μs, a time much longer than the duration of the work extraction π-pulse. To correct for this deformation during the work measurement, we do the following. First, we measure $\overline{I^2 + Q^2}$ during a long drive of the qubit whose amplitude is such that the Rabi frequency precisely equals that of the π-pulse used for work extraction. We obtain the red curve represented in Fig. 7.6b). Second, we fit these oscillations at long enough time so that the JPC has reached its stationary regime. Finally, we extrapolate the fitted function down to $t = 0$ μs and remove it from the measured $\overline{I^2 + Q^2}$. The obtained curve is shown in blue in Fig. 7.6b). It represents the JPC transient response that will be removed from the raw data in the demon experiment.

Fig. 7.6c) and d) show in blue points the fitted values of $\mathcal{A}^I$ and $\mathcal{A}^{I^2+Q^2}$ as a function of the Rabi frequency. While a constant $\mathcal{A}^I$ is expected, a linear reduction is observed with increasing Ω. This reduction is considerably smaller when the qubit is driven in transmission through the a port instead of the b port (green points). The reduction can have two origins: saturation of the JPC due to the large $|\beta_{\mathrm{in}}|$ and filtering of the signal due to the finite bandwidth $\mathrm{BW_{JPC}}$. Since the transmission measurement is only sensitive to filtering effects, we deduce that filtering is negligible, as expected for the measured large bandwidth. We therefore model the reduction of $\mathcal{A}^I(\Omega)$ when the qubit is driven trough the b port by using a $|\beta_{\mathrm{in}}|$-dependent (or equivalently Ω-dependent) amplitude gain (black line) [68] $\sqrt{G(\Omega)} = \sqrt{G_0}(1 - \Omega/\Omega_\infty)$, where G_0 is the gain at zero input power and Ω_∞ is some constant. This $G(\Omega)$ also explains very well the saturation of $\mathcal{A}^{I^2+Q^2}$ at high Ω (black line, Fig. 7.6d) and therefore directly gives the correspondence between the measured power $\overline{I^2 + Q^2}$ and the output photon rate $\langle b_{\mathrm{out}}^\dagger b_{\mathrm{out}} \rangle$. During the experiment the gain of the amplification setup underwent a small drift between the photon rate calibration and the realization of the Maxwell's demon (separated by about a week). It is represented by the red dots in Fig. 7.6c) and d) that give the amplitude and Rabi frequency of oscillations measured during the demon experiment. This drift is taken into account and corrected to extract the energy transferred from the system to the battery.

---

2 We expressed here $\overline{I^2 + Q^2}$ in μW at the digitizer stage, converted from $m\mathrm{V}^2$ by assuming that the signal is dissipated in a 50 Ω resistor to highlight the fact that we are doing a power measurement.
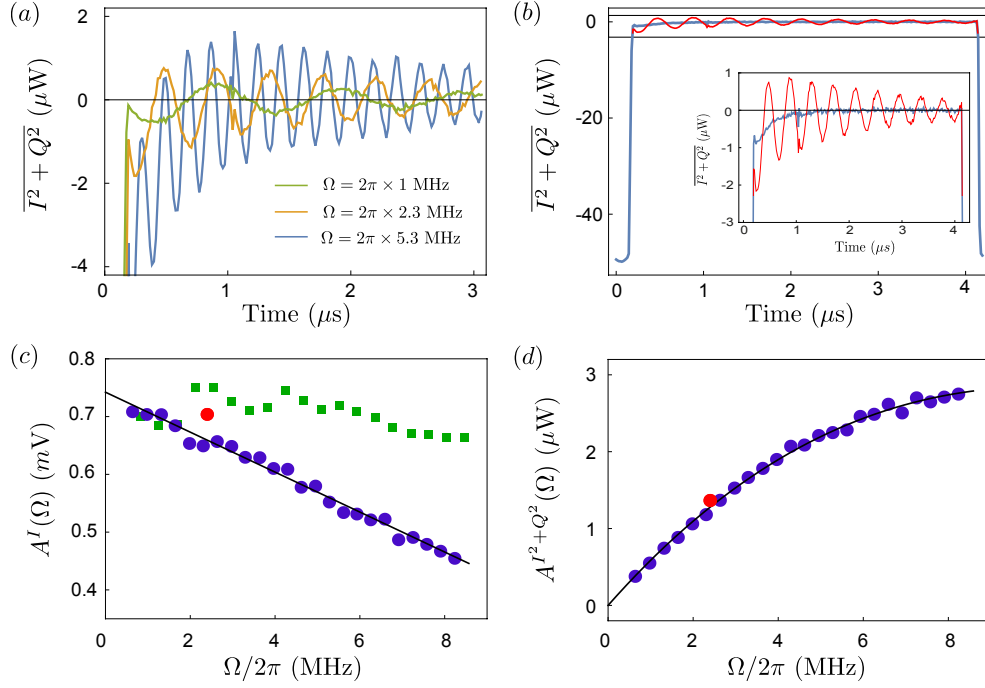
Figure 7.6: Photon number calibration. (a) Photon rate measurement of the qubit under a continuous Rabi drive for three driving amplitudes. (b) Transient response of the JPC to the rise of β_{in}. (c) Ω-dependence of the amplitude of the Rabi oscillations measured on I (blue points). The black curve is a fit with a linear gain model coming from the amplifier saturation $A^I(\Omega) = A_0(1-\Omega/\Omega_\infty)$ with $A_0 = 0.74$ mV and $\Omega_\infty = 2\pi \times 21.4$ MHz. The red dot corresponds to the Rabi oscillations used in the demon experiment and the green squares to Rabi oscillations measured in transmission. (d) Same for $I^2 + Q^2$, represented by the theoretical expression $A^{I^2+Q^2}(\Omega) = G_{\text{eff}}\Omega(1-\Omega/\Omega_\infty)^2$ with $G_{\text{eff}} = G \times |\langle\sigma_z\rangle^0|/2 = 0.63$ μW(MHz)$^{-1}$ and $\Omega_\infty = 2\pi \times 30.6$ MHz (black line).

7.2.4 Pulse sequences

The signal distortion induced by the JPC generates a strong experimental constraint if one aims at measuring the work extracted by the demon. Indeed we are only able to extract the transient response of the JPC in the case of a long drive at f_S because our method relies upon the JPC reaching the stationary regime. Therefore if we were to use a short π-pulse we would not be able to deconvolute the useful signal from the response of the JPC. We are thus facing a trade-off. On the one hand the JPC sets a minimum duration for the work extraction pulse. On the other hand the sequence should be performed as fast as possible in order to minimize the effect of decoherence and relaxation of the qubit and cavity. The purpose of the latter is to improve the demon efficiency and allows to keep trace of quantum signatures of the experiment such as negativities in the demon Wigner function. To overcome this issue we use two distinct sequences represented in Fig. 7.7.

The first sequence is made fast enough so that we can perform the system and demon's tomographies at the end of the experiment. It is represented in Fig. 7.7a) and will be called "sequential" in the following. It consists of the three steps described in Sec. 7.1.1 and represented in Fig. 7.1. The system preparation (step ①) is made using, if needed, a Gaussian-shaped π- or $\pi/2$-pulse at f_S with a standard deviation

of 12.5 ns and truncated at ± 25 ns. Step ② is done by displacing the demon by a Gaussian-shaped pulse at f_D with a standard deviation of 12.5 ns and truncated at ± 25 ns. Work extraction (step ③) is finally performed using a π-pulse with the same parameters as in step ①.

The second demon sequence, in Fig. 7.7b), called "continuous", allows to measure the work extracted by the demon to the battery by avoiding transients in the measurement of the photon rate. In this version a single long continuous square pulse at f_S realizes steps ① and ③. Its Rabi frequency is $\Omega = (416 \text{ ns})^{-1} \ll \text{BW}_{\text{JPC}}$. The demon displacement (step ②) is performed on top of this long pulse and defines the passage from step ① to ③. It is Gaussian-shaped with a shortened standard deviation of 10 ns (truncated at ± 20 ns) which is much smaller than the Rabi period. The starting time of the displacement determines the initial state of the qubit. We use 200, 300 and 400 ns starting times, which realize approximately π-, $3\pi/2$- and 2π-pulses during step ①, respectively. Not stopping the pulse at f_S during step ② and performing a 2π- (resp. $3\pi/2$-) pulse instead of nothing (resp. a $\pi/2$-pulse) to prepare the low temperature state (resp. an equal superposition of ground and excited states) is crucial as it minimizes the impact of the transient response of the JPC on the work measurement. All this results in a slightly smaller purity of the system when the continuous sequence is used, as compared to the sequential one.
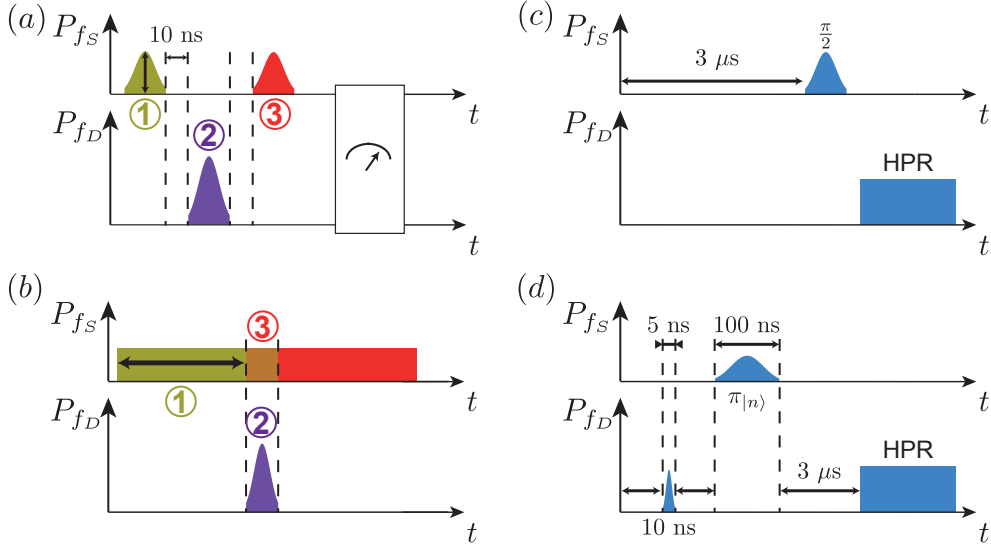
Figure 7.7: Pulse sequences. a) "Sequential" and b) "continuous" sequences realizing the Maxwell's demon experiment. c) Qubit and d) cavity tomography pulse sequences.

The sequential sequence is followed by various tomographic sequences depending on the quantity that we want to measure. The system tomography represented in Fig. 7.7c) is performed by first letting the demon relax towards thermal equilibrium during 3 μs, then performing if needed a $\pi/2$ rotation around x or y in the Bloch sphere, and finally measuring the population in $|e\rangle$ using a HPR measurement (see Sec. B.2).

The large value of the dispersive shift measured in Sec. 7.2.1 determine the type of cavity tomography that we can perform experimentally. Indeed they make impossible to measure the cavity's Wigner function since this measurement requires to perform rotations of the qubit unconditioned by the number of photons in the cavity. With $\chi = 33.8$ MHz we would need a pulse with a linewidth of several hundred MHz to meet

this requirement as soon as the mean number of cavity photons $\bar{n}$ grows over 1. Instead, we characterize the demon's state ρ_D by the set of the generalized Husimi Q-functions

$$Q_n(\beta) = \frac{1}{\pi} \langle n | D(\beta) \rho_D D(\beta)^\dagger | n \rangle, \ n \in \mathbb{N} \ . \tag{7.20}$$

The Husimi function measurement sequence is represented in Fig. 7.7d). The cavity is first displaced by a 5 ns-long pulse at f_D with tunable complex amplitude generating the unitary displacement by β. Its duration is chosen so that it performs a displacement of the cavity despite the large value of the Kerr-term K. It is followed by a π-pulse at $f_S - n(\chi - n\chi_2)$ exciting the qubit, initially in the ground state, only if the cavity hosts n photons. The consequent HPR measurement gives the probability to find the qubit in the excited state $p^e_{n,\beta}$, thus the probability to have n photons in the cavity after displacement, which is $Q_n(\beta)$. Experimentally we measure the Q_n functions with $0 \leq n \leq 5$ and reconstruct ρ_D with a procedure described in the next section.

7.2.5 Cavity state reconstruction

In theory the demon state ρ_D at the end of the demon sequence is entirely represented by the set of its generalized Husimi function $\{Q_n\}$ defined in Eq. (7.20) in the sense that there exists a bijection between the two. In reality the density matrix has to be reconstructed from the raw experimental measurements $p^e_{n,\beta}$ because the information obtained from them is limited. Indeed we obviously cannot measure the Q_n for all values of n and have to stop at a maximum. Experimentally we have to stop at $n = 5$ after which the general Hamiltonian of Eq. (7.12) breaks down[3]. Similarly, where β is supposed to be a continuous variable we measure $p^e_{n,\beta}$ for $-5.95 \leq \text{Re}(\beta), \text{Im}(\beta) \leq 5.95$ discretized on a 31×31 square array. In practice the range of β has to cover the whole phase space expansion of ρ_D in order to have a reasonably good representation of the state. Moreover, relaxation during the measurement sequence disturbs the results and has to be fully taken into account to reconstruct ρ_D from the $p^e_{n,\beta}$.

Our experimental HPR measurement is not single-shot. What we acquire is simply a voltage proportional to the qubit population in the excited state. On the other hand the cavity displacement by β is set by the AWG amplitude and phase and also has to be calibrated. We define the coefficients k_0, k_e and k_β relating the voltages V_{board} (measured by the acquisition board during the HPR measurement) and V_{AWG} (generating the displacement pulse) to the in situ quantities $p^e_{n,\beta} = k_0 + k_e V_{\text{board}}$ and $|\beta| = k_\beta V_{\text{AWG}}$. To determine them we perform a tomography of the equilibrium state $\rho^0 = \rho^0_S \otimes \rho^0_D$ represented in Fig. 7.8. Since a thermal state is rotation invariant in phase space we only take the tomography for $\beta \in \mathbb{R}^+$. The coefficients are found by simply matching the experimental data (points) with the theoretical calculations (lines).

The calculated $p^e_{n,\beta}$ are obtained using the effect matrix $E_{n,\beta}(T)$, a positive operator valued measure (POVM) [30] describing the time-reversed system-demon evolution during the tomographic pulse sequence represented in Fig. 7.7d). More precisely let us fix $t = 0$ at the beginning of the tomographic sequence with the total duration T_{tomo}. The state of the system-demon $\rho(t)$ evolves during the tomography due to Hamiltonian evolutions (containing the contributions of the drives) and decoherence and is so that $\rho(t = 0) = \rho^0$. Therefore $p^e_{n,\beta} = \text{Tr}(\rho(T_{\text{tomo}}) E_{n,\beta}(T_{\text{tomo}}))$ with $E_{n,\beta}(T_{\text{tomo}}) = \mathbb{I}_D \otimes |e\rangle\langle e|$. It can be seen as the probability to draw quantum trajectories so that the system finishes in $|e\rangle$ after the time T_{tomo}. Moving backwards, we can propagate this probability

---

3 At large number of photons, higher order terms in $d^\dagger d$ are not negligible anymore.

to draw *the same trajectories* at past times $t \leq T_{\text{tomo}}$ if we adapt $E_{n,\beta}(t)$ accordingly. The evolution of $E_{n,\beta}$ is thus given by [181]

$$\frac{\mathrm{d}E_{n,\beta}}{\mathrm{d}t} = -\frac{i}{\hbar}[H_{n,\beta}(t), E_{n,\beta}(t)] - \sum_i \gamma_i \bar{\mathcal{D}}[O_i]\big(E_{n,\beta}(t)\big) \tag{7.21}$$

with $H_{n,\beta}(t)$ the time-dependent Hamiltonian used for the tomography. For an operator O we have $\bar{\mathcal{D}}[O](E) = O^\dagger E O - \frac{1}{2}(EO^\dagger O + O^\dagger O E)$. This equation is the pendant of the Lindblad equation Eq. (2.7) when moving backwards in time [182]. Here, we include the decoherence due to cavity photon loss with a rate κ and qubit energy loss and pure dephasing with the respective rates Γ and Γ_φ. As a result $p_{n,\beta}^e$ can easily be computed from the system-demon density matrix ρ^0 since at $t = 0$

$$p_{n,\beta}^e = \mathrm{Tr}\big(\rho^0 E_{n,\beta}(0)\big) \ . \tag{7.22}$$

As we can see in Fig. 7.8 there is a very good agreement between data and theory giving the values k_β, k_e, k_0 with a good accuracy. The main effect of relaxation here is to widen and shift the peaks to higher β.

$$k_\beta = 9.918, k_e = 495.65, k_0 = 0.3626$$
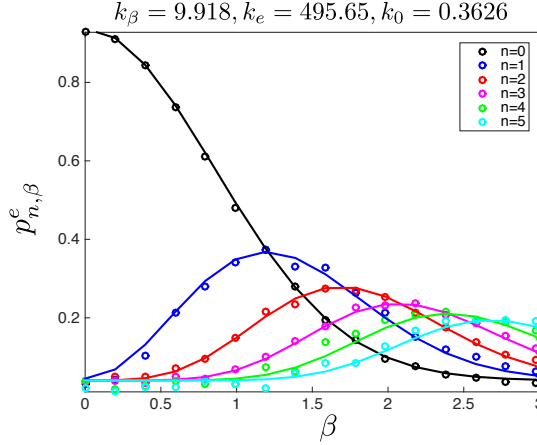
Figure 7.8: Tomography of the thermal state ρ^0. Points are measurements rescaled with the values of k_β, k_e, k_0 indicated on top of the figure. Lines are calculations.

Once this calibration measurement has been done we can now reconstruct the unknown demon state ρ_D after step ③ from the experimental Husimi functions. To do so we use a MaxLike method [183]. In theory the demon tomography is performed only in the case of an efficient demon so that the qubit is in $|g\rangle$ in the beginning of the tomography. In reality there is some residual excitation of the qubit and the qubit-cavity density matrix at the beginning of the tomography reads $\rho_S \otimes \rho_D$ with $\rho_S = p_g|g\rangle\langle g| + (1 - p_g)|e\rangle\langle e|$. Assuming Gaussian noise of the measurement records $p_{n,\beta}^e$, the reconstructed ρ_D is expected to maximize the likelihood function

$$f(\rho_D) \propto -\sum_{n,\beta} \Big(p_{n,\beta}^e - \mathrm{Tr}\big(\rho_S \otimes \rho_D E_{n,\beta}(0)\big)\Big)^2 \ . \tag{7.23}$$

Maximization of $f(\rho_D)$ is achieved by a gradient algorithm with orthogonal projection on the (convex) subspace of matrices that are positive, hermitian and with unit trace. All the physical parameters entering the MaxLike algorithm are measured independently. Two technical parameters are however also needed. First the infinite Hilbert

space of the cavity is necessarily truncated so that only Fock states $|N\rangle$ such as $N \leq N_{\mathrm{trunc}}$ are taken into account. Second we do not use all the displacements for the reconstruction but only those lower than a bound $|\beta| < \beta_{\mathrm{max}}$. Clearly, one should have $N_{\mathrm{trunc}} \gg \beta_{\mathrm{max}} > \bar{n}$. But on the other hand, N_{trunc} and β_{max} should not be too big since the Hamiltonian of Eq. (7.12) is only valid for low photon number. In practice a variation of these parameters has a direct influence on the reconstructed ρ_D, thus on the calculated entropy S_D. Therefore we will have to include the effect of reconstruction in the thermodynamical discussion of the demon experiment.

7.3 THERMODYNAMICAL RESULTS

We now present the experimental measurements of the thermodynamical quantities involved in the experiment, when the system is initialized in a thermal or a superposed state. We first validate the principle of the experiment by verifying that the demon indeed extracts work. To do so it is necessary to properly define the work from the measured battery energy changes. Then we turn to the evolution of the system induced by the demon, and verify than the energy variation of the system is mostly transformed into work and that its entropy follows the behavior determined in Sec. 7.1.1. Finally we characterize the demon's final state, show the transfer of information from the system to the demon, and discuss the specificities coming from encoding a binary information into a continuum of states. Some of the results showed in this section were already presented in Sec. 6.3.2. They are here discussed with far more precision.

7.3.1 *Coherent and incoherent photon emission*

Work is extracted during the conditional π-pulse at f_S applied through port b. It takes the form of energy powering up the pulse which thus acts as the battery. The power contained in the reflected drive is $P = h f_S \langle b_{\mathrm{out}}^\dagger b_{\mathrm{out}} \rangle$. As we have seen we are able to directly measure and quantify this additional power, but what about its thermodynamical status? What assures us that this energy could be use later for a useful task? In other words, is this energy made of work or heat, and how can we distinguish between the two?

The distinction made between spontaneous and stimulated emission in Sec. 2.2.3 appears at first as a promising lead. In fact the stimulated emission term in the photon rate equation Eq. (2.26) is associated to coherent exchanges of energy between the qubit and the drive during Rabi oscillations because its integral during a fast π-pulse between $|e\rangle$ (resp. $|g\rangle$) and $|g\rangle$ (resp. $|e\rangle$) is $+1$ (resp. -1) and corresponds to the quantum of energy emitted (resp. absorbed) by the qubit during work extraction. Therefore the entirety of stimulated emission contributes to the work extracted by the demon. On the other hand spontaneous emission, associated to qubit decoherence, might appear as being related to stochastic, uncontrolled processes and hence to the residual heat transferred from the qubit to the battery. This assumption is only partially correct, as spontaneous emission contributes to both work and heat. Before turning to the analytical and experimental results illustrating this point let us consider a simple example showing qualitatively that spontaneous emission participates to the work. Many single photon sources are based on transferring a single excitation from a long-lifetime quantum system to a system strongly coupled the environment, a transmission line (for instance for superconducting circuits [31, 89]) or free space. In this case the emit-

ted single photon is emitted by a spontaneous emission process. The stochasticity of spontaneous emission is here exceeded by the large coupling rate to the environment, making the emission time of the photon almost perfectly deterministic compared to the duration of the experiment. We might also cite effects such as superradiance of a collection of atoms where spontaneous emission is the source of a coherent effect[4] [184].

Our quantitative analysis is based on the distinction made by Cohen-Tannoudji and coworkers in [1] between coherent and incoherent emission. We re-express their calculation within the input-output formalism and give it a thermodynamical interpretation. In the total photon rate radiated by the qubit $\langle b_{\text{out}}^\dagger b_{\text{out}} \rangle$ the coherent emission is the energy emitted *in phase* with the incoming drive. It can be easily expressed in terms of the mean value of the complex field amplitude $\langle b_{\text{out}} \rangle$. To do so we define in the Heisenberg picture the quantum fluctuations of the field amplitude δb_{out} by $b_{\text{out}} = \langle b_{\text{out}} \rangle + \delta b_{\text{out}}$. By definition $\langle \delta b_{\text{out}} \rangle = 0$. The photon rate thus reads

$$
\begin{aligned}
\langle b_{\text{out}}^\dagger b_{\text{out}} \rangle &= \langle \left(\langle b_{\text{out}} \rangle + \delta b_{\text{out}} \right)^\dagger \left(\langle b_{\text{out}} \rangle + \delta b_{\text{out}} \right) \rangle \\
&= |\langle b_{\text{out}} \rangle|^2 + \langle \delta b_{\text{out}}^\dagger \delta b_{\text{out}} \rangle
\end{aligned}
\tag{7.24}
$$

where the crossed terms are equal to zero. The first term of the equation is the deterministic emission of light while the second one represents the contribution of quantum fluctuations to the photon rate, hence stochastic. We can therefore write the coherent I_{coh} and incoherent emission terms as

$$
\begin{cases}
I_{\text{coh}} &= |\langle b_{\text{out}} \rangle|^2 \\
I_{\text{incoh}} &= \langle \delta b_{\text{out}}^\dagger \delta b_{\text{out}} \rangle
\end{cases}
\tag{7.25}
$$

Using the input-output relation of Eq. (2.19) we can directly express coherent emission in terms of the drive amplitude $\beta_{\text{in}} = \langle b_{\text{in}} \rangle$ and qubit averaged operators. During the pulse the qubit oscillates around the y-axis in the Bloch sphere hence $\langle \sigma_- \rangle = \langle \sigma_x \rangle / 2$. It yields

$$
\begin{aligned}
I_{\text{coh}} &= \left| \beta_{\text{in}} - \frac{\sqrt{\Gamma_b}}{2} \langle \sigma_x \rangle \right|^2 \\
I_{\text{coh}} &= \beta_{\text{in}}^2 - \sqrt{\Gamma_b} \beta_{\text{in}} \langle \sigma_x \rangle + \frac{\Gamma_b}{4} \langle \sigma_x \rangle^2 .
\end{aligned}
\tag{7.26}
$$

Comparing this expression with the photon rate of Eq. (2.26) we see that the two first terms are the reflected drive and the stimulated emission term $I_{\text{stim}} = -\sqrt{\Gamma_b} \beta_{\text{in}} \langle \sigma_x \rangle$. This proves that stimulated emission contributes entirely to work exchanges. The last term is precisely the contribution of spontaneous emission $I_{\text{spont}} = \Gamma_b (1 + \langle \sigma_z \rangle)/2$ to work. On the other hand incoherent emission is due to the remaining part of spontaneous emission only. With $I_{\text{incoh}} = \langle b_{\text{out}}^\dagger b_{\text{out}} \rangle - I_{\text{coh}}$ and Eq. (2.26) we obtain

$$
I_{\text{incoh}} = \frac{\Gamma_b}{2} \left(1 + \langle \sigma_z \rangle - \frac{\langle \sigma_x \rangle^2}{2} \right) .
\tag{7.27}
$$

Note that incoherent emission is independent on the drive characteristics hence is purely due to the qubit. It is due to quantum fluctuations of σ_-. Indeed if we write $\sigma_{-,+} = \langle \sigma_{-,+} \rangle + \delta \sigma_{-,+}$ it is possible to show that $I_{\text{coh}} = \Gamma_b \langle \delta \sigma_+ \delta \sigma_- \rangle$.

It is possible to separate experimentally between coherent and incoherent contributions to the photon rate if one is able to measure at the same time the field complex

---

4 The seminal article by R.H. Dicke is even called *Coherence in Spontaneous Radiation Processes...*

amplitude $\langle b_{\mathrm{out}} \rangle$ and the photon rate $\langle b_{\mathrm{out}}^{\dagger} b_{\mathrm{out}} \rangle$. This is precisely the case of the photon number reconstruction from the field quadratures presented in Sec. 2.4. In a similar manner than in Sec. 2.5 we continuously drive the qubit through both ports a and b while changing the pulse amplitude β_{in} and measure $\langle b_{\mathrm{out}} \rangle$ and $\langle b_{\mathrm{out}}^{\dagger} b_{\mathrm{out}} \rangle$. The qubit undergoes underdamped Rabi oscillations at the frequency $\Omega = \sqrt{\Gamma_a} \alpha_{\mathrm{in}} + \sqrt{\Gamma_b} \beta_{\mathrm{in}}$ described by the solutions of Bloch equations Eq. (2.17) and decaying at the rate $\Gamma_R = (\Gamma + \Gamma_2)/2$. The experimental results on which we based our analysis were already presented in Sec. 2.6. Here we switched the labelling of ports a and b to adopt the same notations as in the demon experiment [147].
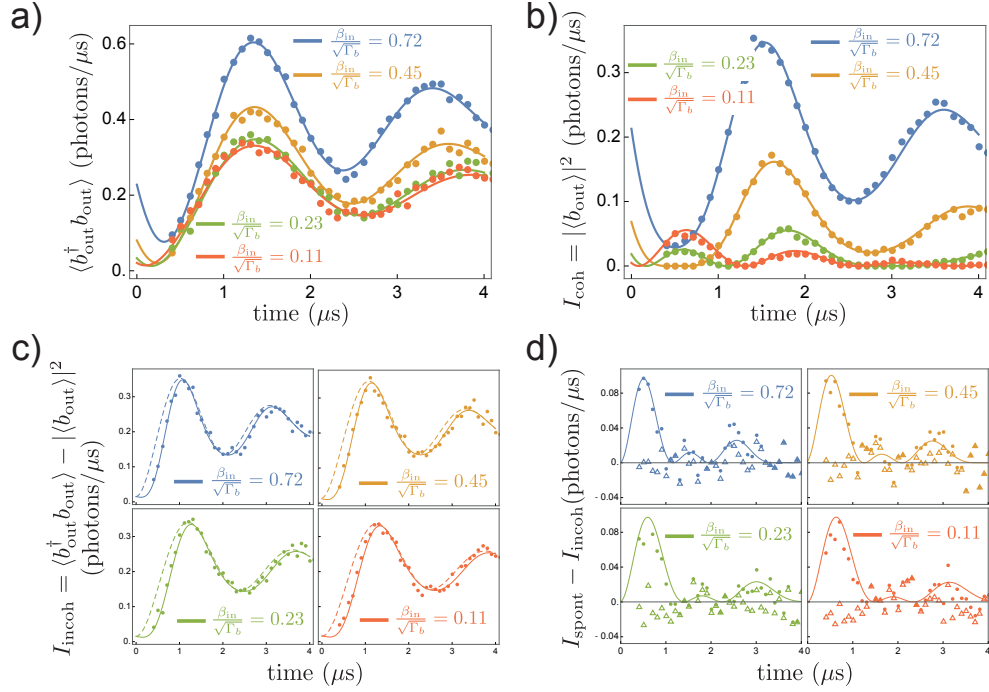

Figure 7.9: Coherent and incoherent emission of a Rabi-oscillating qubit. a) Total photon rate at various values of β_{in} (points) experimental data and (line) theory of Eq. (2.26) where $\langle \sigma_x \rangle$ and $\langle \sigma_z \rangle$ are given by the solutions of the Bloch equations Eq. (2.17) with $T_1 = 1.95~\mu s$, $T_2 = 2.88~\mu s$, $\Gamma_b = 0.88/T_1$ and $\Omega_0 = 2\pi \times 0.38$ MHz the Rabi frequency when $\beta_{\mathrm{in}} = 0$ due to the drive in a. b) Coherent emission. c) Incoherent emission. d) Coherent emission part of spontaneous emission (points and line) and error between experimental and theoretical incoherent emission (triangles).

The measured total photon rate is represented in Fig. 7.9a) (points) together with the theoretical expression of Eq. (2.26) for four different values of β_{in}. Raising β_{in} increases stimulated emission in b and therefore the amplitude of the measured oscillations. The experimental coherent emission is represented in Fig. 7.9b). Its time evolution contains two frequencies, Ω and 2Ω because of the term proportional to $\langle \sigma_x \rangle^2$ in Eq. (7.26). By subtracting the coherent emission from the total photon rate we find the incoherent emission represented in Fig. 7.9c). Its time evolution is in good agreement with the theoretical expression Eq. (7.27) (plain line). The dashed line represents the theoretical evolution of spontaneous emission I_{spont}. There is a clear discrepancy between I_{incoh} and I_{spont} at small time validated by the experimental measurement. Figure 7.9d) represents the coherent part of spontaneous emission $I_{\mathrm{spont}} - I_{\mathrm{incoh}}$, experimental (points) and theory (plain line). Even though the contribution of I_{spont} to coherent emission is small compared to the one of stimulated emission, we are able to resolve it. In particular

it is clearly above the error between the experimental and theoretical values of I_{incoh} represented by the triangles.

We can now use this distinction to separate between work and heat contributions to the energy extracted from the qubit. Labelling W and Q the work and heat extracted from the qubit, the total extracted power is given by $P = h f_S (\langle b_{\text{out}}^\dagger b_{\text{out}} \rangle - \langle b_{\text{in}}^\dagger b_{\text{in}} \rangle) = \dot{W} + \dot{Q}$, where

$$\boxed{\begin{aligned} \dot{W} &= h f_S (I_{\text{coh}} - \beta_{\text{in}}^2) \\ \dot{Q} &= h f_S I_{\text{incoh}} \ . \end{aligned}} \tag{7.28}$$

Further study is required to prove that these definitions indeed obey a second law. In the demon experiment the conditional π-pulse used for work extraction is set so that $\Omega \gg \Gamma, \Gamma_2$ to avoid decoherence. A direct interpretation from the coherent and incoherent emission Eqs. (7.26) and (7.27) is that in this limit incoherent emission is negligible compared to coherent emission and stimulated emission is then much larger than spontaneous emission. Therefore for the experimental implementation of the demon we have

$$P = \dot{W} + \dot{Q} \approx \dot{W} \approx h f_S I_{\text{stim}} \ . \tag{7.29}$$

Therefore we will only have to measure the photon number contained in the pulse and this will correspond to the work extracted by the demon from the system.

7.3.2   *Work extraction*

In order to measure the work extracted during the demon sequence we use the continuous sequence described in Sec. 7.2.4. The amplitude of the preparation and extraction pulse at f_S is set at $\Omega = 2\pi \times 2.4$ MHz. As already stated earlier displacing the demon when the system is in $|g\rangle$ does not result in a coherent state because of its non-linearity but in a more complex state represented by the density matrix $\rho_{\alpha_{\text{in}}}$. The amount of information acquired by the demon is related to the mean number of photons $\bar{n}$ contained in the demon, as it is related to the state overlap with vacuum.

The additional power contained in the battery is shown in Fig. 7.10 as a function of time during the pulse in step ③ in units of photons per microsecond for various initial system states (see inset) and for two values of $\bar{n}$. In Fig. 7.10a) the average photon number $\bar{n} = 9$ is large enough for the demon to distinguish the system states well. As expected from the demon's action, the measured power is positive for all initial states and greater for higher initial system temperature. In contrast, when the demon is unable to distinguish $|g\rangle$ and $|e\rangle$, which happens for $\alpha_{\text{in}} = \bar{n} = 0$, the extracted power is measured to be negative for the system starting in any thermal state (Fig. 7.10b). This arises because the demon is ignorant and lets the system drain energy from the battery. This failure uncovers the role of information in the work extraction by the demon.

At $\bar{n} = 0$, a distinctive feature appears when the system starts in a quantum superposition of $|g\rangle$ and $|e\rangle$ (green). Even though the total work is zero, just like for the equally mixed state (red), the instantaneous power now oscillates illustrating the work potential of coherences. In contrast, for an efficient demon ($\bar{n} = 9$ in Fig. 7.10a), there is no quantum signature in the extracted work. Note that the peak in the green curve arises due to overlapping of steps ② and ③ to avoid transients (see Sec. 7.2.4). We

directly see in time the effect of entanglement described in the ideal case of a linear oscillator in Sec. 7.1.1. Indeed when we turn on the displacement drive at f_D we increase over time the amount of entanglement between the demon and system when the latter is initialized in a superposed state. The power measurement discards the information stored in the demon therefore one has to trace over its state to recover the system's density matrix, with the effect of killing the coherences.
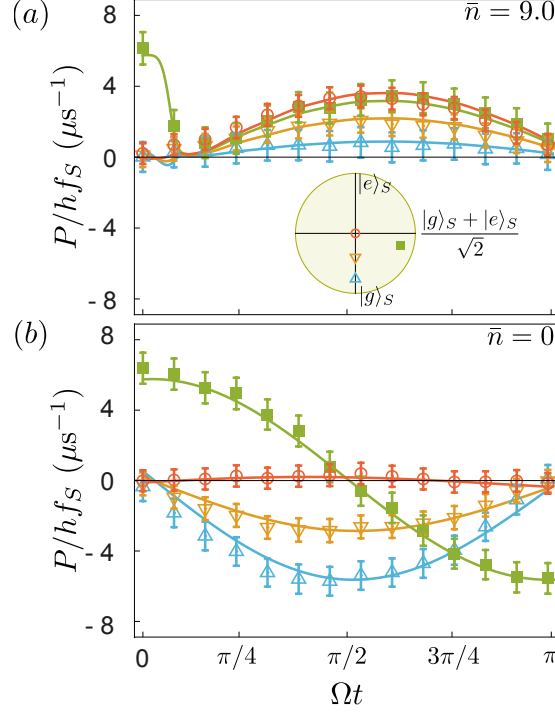
Figure 7.10: Measured extracted power. Measured extracted power (normalized by a quantum of energy hf_S) for step ③ as a function of time during the pulse at f_S. Blue, orange and red symbols and error bars correspond to an initial thermalized system at temperatures $T = 0.17$, 0.40 K and above 8K (see inset for initial Bloch vectors). Green symbols correspond to an initial quantum superposition obtained by a $3\pi/2$-pulse acting on the system at 0.10 K. Solid lines result from a numerical simulation with no fit parameters and match the measurements well. a) The demon memory state $\rho_{\alpha_{\text{in}}}$ contains $\bar{n} = 9$ photons when encoding a system in $|g\rangle$. b) Same figure for an ignorant demon ($\bar{n} = 0$ in step ②).

Integrating the extracted power over the duration of step ③ gives the total work $W = \int_0^{\pi/\Omega} P \mathrm{d}t$, whose magnitude is at most hf_S. It is represented in Fig. 7.11a) as a function of the displacement amplitude α_{in} and $\bar{n}$. Note that due to the cavity non-linearity, $\bar{n}$ does not scale linearly with $|\alpha_{\text{in}}|^2$, but it grows monotonously with it. As α_{in} increases, the demon's encoding improves and work increases from negative to positive values. The increase of W as a function of α_{in} is well reproduced numerically (solid lines in the figure). As demonstrated in Sec. 6.2.2 the work extracted with this protocol cannot not exceed 40% of the Landauer bound $k_B T \ln 2$ at fixed temperature. The temperature that maximizes $W/k_B T \ln 2$ corresponds to the orange curve in Figs. 7.10 and 7.11.
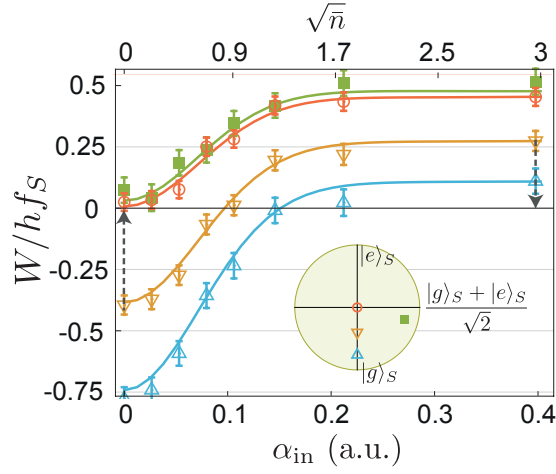
Figure 7.11: Total extracted work during step ③ as a function of α_{in} and $\sqrt{\bar{n}}$ with $\bar{n}$ the number of photons in the demon memory measuring $|g\rangle$. Symbols correspond to measurement of the battery and solid lines result from simulations. Colors correspond to the same initial states of the system as in Fig. 7.10.

7.3.3 Qubit evolution under the demon
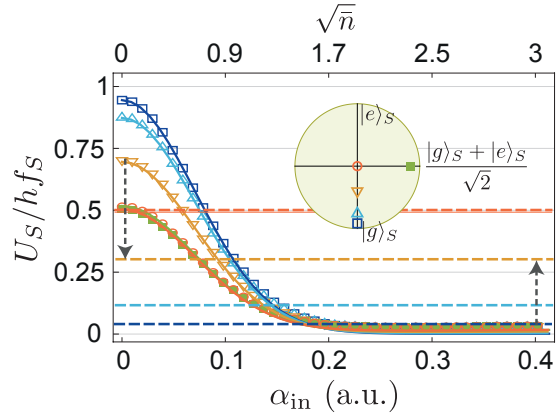
Figure 7.12: Measured final internal energy U_S of the system as a function of the amplitude α_{in} of the pulse at f_D used in step ② to encode information in the demon's memory. Error bars are smaller than symbol size. Dashed lines indicate U_S after preparation step ①. Solid lines result from the full master equation and establish the conversion between α_{in} and $\sqrt{\bar{n}}$.

We characterize the state of the qubit after the demon operations using the sequential sequence (see Sec. 7.2.4). Fig. 7.12 shows the evolution of the system's final internal energy U_S as a function of α_{in} and $\bar{n}$ for various initial states. Thanks to the sequential sequence we are able to measure U_S for $T_S = T_S^0$ by simply not driving the system in step ① and to initialize the system in a superposed state with a better purity. As α_{in} increases, the demon extracts more energy from the system making it end up close to the ground state. In the absence of relaxation during the experiment, corresponding to heat exchanged with the environment, the system would end up perfectly in $|g\rangle$. In practice we measure a residual excitation of $2.7 \pm 1\%$ whatever the initial state. This result is well reproduced by the numerical simulations of the demon (solid lines). Such a thermodynamic cycle can be used to cool down superconducting qubits in

practice, as previously demonstrated in its continuous version [114]. Again, due to the cavity non-linearity the system's final state is expected to behave in a more complex manner than Eq. (7.4). Yet the evolution of the internal energy can be well reproduced by $U_S \approx \rho_{gg} e^{-\bar{n}}$ with ρ_{gg} the probability to have the system initialized in $|g\rangle$ (not represented on the figure).

Figure 7.13: Test of the first law. Difference between the system's internal energy variation $-\Delta U_S$ and the measured extracted work W. The error bars come from the work measurement.

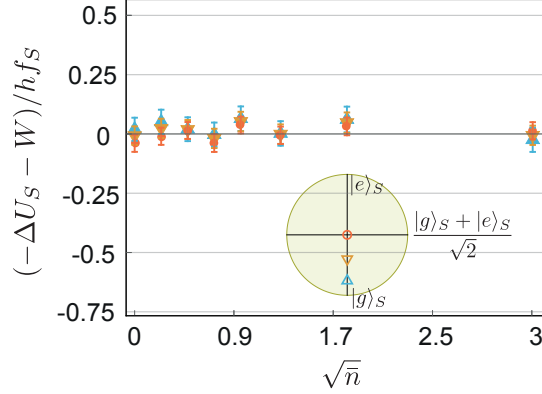It is natural to try to compare the extracted work W with the independently measured system's internal energy variation $\Delta U_S = U_S - U_S^i$ where U_S^i is the internal energy after step ① to see if our measurements agree with the first law. These results however come from different experiments in the sense that the sequences used are different. In particular the duration of the work extraction pulse in step ② is not the same whether we measure the work with the continuous sequence or the system's energy with the sequential sequence. Moreover preparation differs, in particular for the superposed states which does not have the same purity. For thermal states the difference in the preparation is taken into account to initialize the system in identical states no matter the pulse used in step ①. Since the extraction pulse is longer in the case of the continuous sequence we expect the measured extracted work W to be smaller than the measured variation of internal energy $-\Delta U_S$. In Fig. 7.13 we show the evolution of the error coming from the use of two different sequences $-\Delta U_S - W$ with $\sqrt{\bar{n}}$. This remaining error is much smaller than the total extracted work represented in Fig. 7.11 and is mostly contained within the error bars coming from the battery energy measurement. This proves that heat exchanges are negligible for both sequences and therefore that we showed $\Delta U_S \approx -W$.

The transfer of information between the system and the demon occurring during the experiment has a signature in the final system's entropy S_S. Figure 7.14 shows the evolution of S_S with α_{in} and $\bar{n}$. When the demon is blind $\alpha_{\text{in}} = \bar{n} = 0$ the system's final state corresponds to the initial state flipped by a π-pulse. In practice there was some decoherence during the process and the system ends up in a slightly more entropic state. As expected from the theoretical discussion of the ideal case in Sec. 7.1.1 the system's entropy reaches a maximum due to the unpredictability of the demon at intermediate values of $\bar{n}$. For a linear oscillator and a system initially in $|g\rangle$ it would reach the maximum for $\bar{n} = \ln 2$. Experimentally the maximum is reached before for the system initially at T_S^0 because it contains some excitations. When the system's initial temperature is increased the maximum of entropy appears earlier (orange curve in
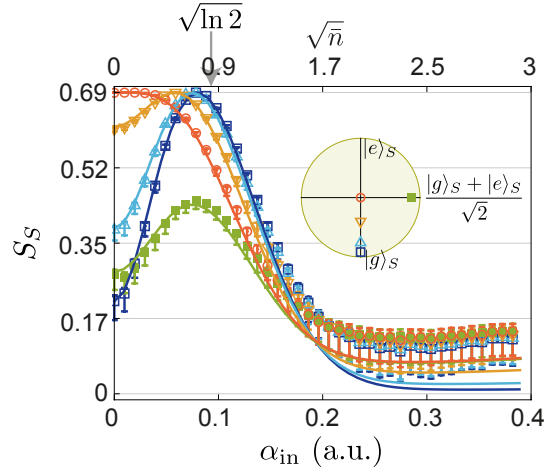
Figure 7.14: System entropy. Symbols and error bars: measured system entropy S_S after step ④ as a function of α_{in} for various initial states (inset, see also the main text). Solid lines: simulations.

Fig. 7.14) because the demon's unpredictability appears only when the system is in $|g\rangle$. At infinite temperature $k_B T_S \gg h f_S$ (red curve) the maximum of entropy corresponds to the blind demon $\alpha_{\text{in}} = 0$. From Fig. 7.12 it is clear that although there is no difference between the final internal energy of a system initially at large temperature (red) or in an equal quantum superposition of $|e\rangle$ and $|g\rangle$ (green), the entropy of these classical and quantum cases strongly differ. In particular, they do not reach their maxima at the same point because when $\alpha_{\text{in}} = 0$ the π-pulse on the system conserves its initial purity. Again, the simulation of the full master equation (solid lines) matches well the measured entropy in all cases except at the largest values of $\bar{n}$, where the entropy is the smallest and even just the slight measurement error of a couple of % on U_S (see Fig. 7.12) leads to a large error in the entropy. Indeed the derivative of the Shannon entropy $H(p)$ diverges as p gets close to 0 or 1 so that the measured entropy is imprecise when the system state gets closer to a pure state. The simulation predicts that the system reaches less than 1% excitation while, experimentally, we get between 1.5% and 4% on $U_S/h f_S$. This may indicate a small imprecision in the calibration of the bath temperature T_S^0.

7.3.4   *Demon information*

A key signature of Maxwell's demon is the transfer of entropy from the system to the memory [130]. Thanks to the previously described quantum tomography based on the measurement of generalized Husimi function we have full access to the density matrix ρ_D of the demon's memory, including its von Neumann entropy $S_D = -\text{Tr}(\rho_D \ln \rho_D)$.

The experimentally measured Husimi functions $Q_n(\beta)$, $0 \leq n \leq 5$ (see Eq. (7.20)) of the demon with $\alpha_{\text{in}} = 0.25$ are represented in Fig. 7.15 (top lines) for the system close to the ground state at T_S^0, close to the excited state and in a superposition of $|g\rangle$ and $|e\rangle$. They are in qualitative agreement with the simulations (bottom line, see Sec. E.2). When the qubit is close to $|g\rangle$ the non-linearity of the demon appears clearly. If the cavity were linear the Husimi functions would correspond to the ones of vacuum measured for the system close to $|e\rangle$ shifted by an amount α. Instead the state has diffused in phase space due to the Kerr non-linearity (Fig. 7.15a).
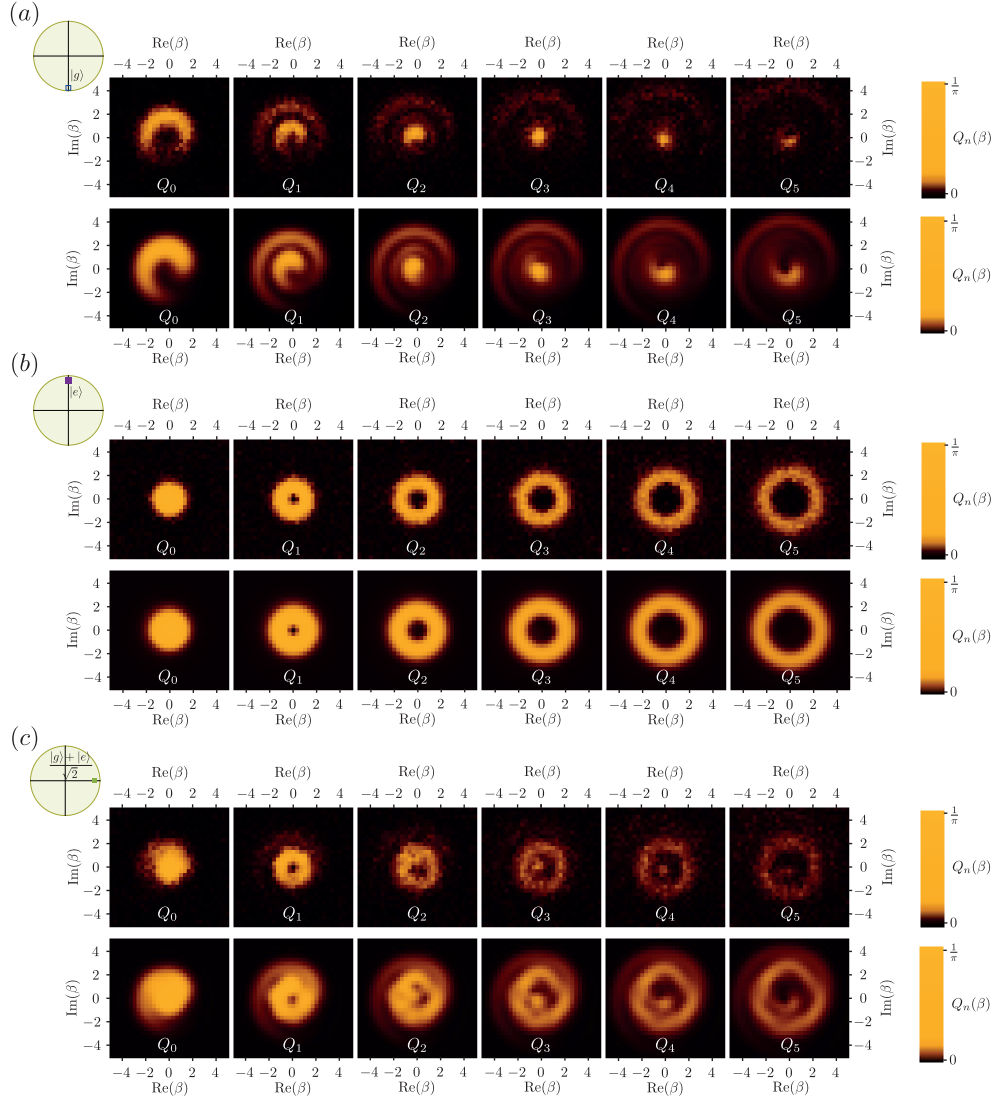
Figure 7.15: Generalized Husimi Q-functions of the demon. Experimental (top line) and calculated (bottom line, see Sec. E.2) Husimi Q-functions of the demon's memory after step ③ for $\alpha_{\mathrm{in}} = 0.25$ and the system initially close to a) $|g\rangle$, b) $|e\rangle$ and (c) a quantum superposition of $|g\rangle$ and $|e\rangle$. From left to right, $n = 0, 1, 2, 3, 4, 5$.

We deduce the demon's von Neumann entropy S_D using the MaxLike method described in Sec. 7.2.5 to reconstruct the demon's density matrix ρ_D from the experimental measurements. We implement this procedure for four various initial states of the system: thermal equilibrium at T_S^0, initialized by a π-pulse, in a superposed state and in a thermal state at $T_S \gg h f_S$. We represent the demon's state by the magnitude of the density matrix coefficients in the Fock states basis $|\langle m|\rho_D|n\rangle|$, see Fig. 7.16. When the system is initially close to $|g\rangle$ the reconstruction of the demon's state gives $\rho_{\alpha_{in}}$, which is entropic and far from a coherent state when $\alpha_{in} = 0.25$ as expected. In contrast, when the system starts in $|e\rangle$, the demon stays close to $|0\rangle$ with a small residual entropy. Most interesting is the comparison of the effect on the demon when the system starts in a quantum superposition or in a thermal state at large temperature. In the first case $S_D = 1.0 \pm 0.05$ and ρ_D exhibits coherences between $|0\rangle$ and higher Fock states, while coherences are missing in the second case leading to a larger entropy $S_D = 1.2 \pm 0.1$ (the error on the entropy is explained below). This transfer of
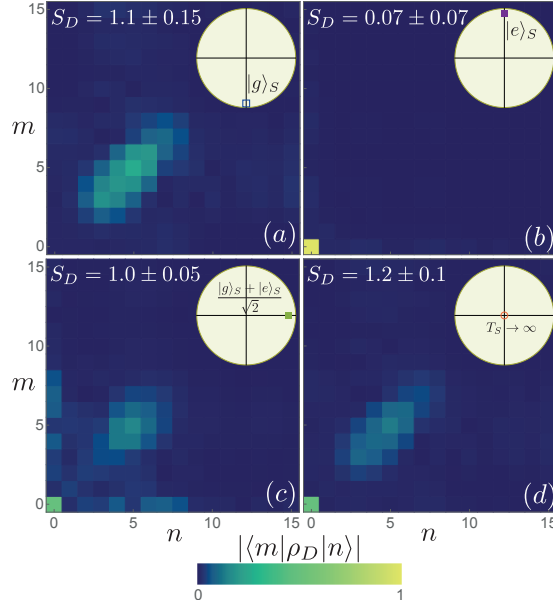
Figure 7.16: Tomography of the demon state. Reconstructed density matrix ρ_D by Maximum Likelihood at the end of the work extraction step ③ for $\alpha_{in} = 0.25$ and when the system is initially a) at temperature 0.10 K, b) close to the excited state, c) a superposition of ground and excited states, d) a maximally mixed state (see Bloch vector in insets). Each pixel represents the amplitude of a density matrix element in the Fock basis and the von Neumann entropies S_D are given.

non-classicality from the system to the memory is a signature of the quantum Maxwell demon. While the entropies of these two states are ordered as expected, their values are much larger than a bit of entropy, $\ln 2 \approx 0.7$, as predicted from the joint effect of dissipation and non-linearity of the demon. It is well reproduced by the simulations presented in Fig. 7.15, predicting $S_D = 1.06$ for the initial superposed system and $S_D = 1.17$ for the maximally entropic system. Comparing the demon's final entropy with the one of the system's (Fig. 7.14) allows us to check that the memory entropy S_D is always higher than the system entropy decrease $S_S(①) - S_S(③)$.

Numerically, the Hilbert space size N_{trunc} and displacement bound $\beta_{\max}$ affect the reconstructed ρ_D and thus the final entropy S_D. Moreover we have seen with the system tomography (Fig. 7.12) that the qubit has a residual excitation of $1 - p_g = 2.7\% \pm 1\%$ after the demon experiment. This error also affects the demon's reconstructed entropy as the qubit's impurity is transferred to the Husimi functions measurement. Fig. 7.17 shows the dependence of the reconstructed demon's entropy on N_{trunc}, $\beta_{\max}$ and p_g for the four considered initial states. Fig. 7.17a) and b) show that the truncation should be taken on the plateau $13 \leq N_{\mathrm{trunc}} \leq 21$, while there is a negligible dependence on p_g. The uncertainty on the entropy comes mostly from the choice of $\beta_{\max}$ as shown Fig. 7.17c).
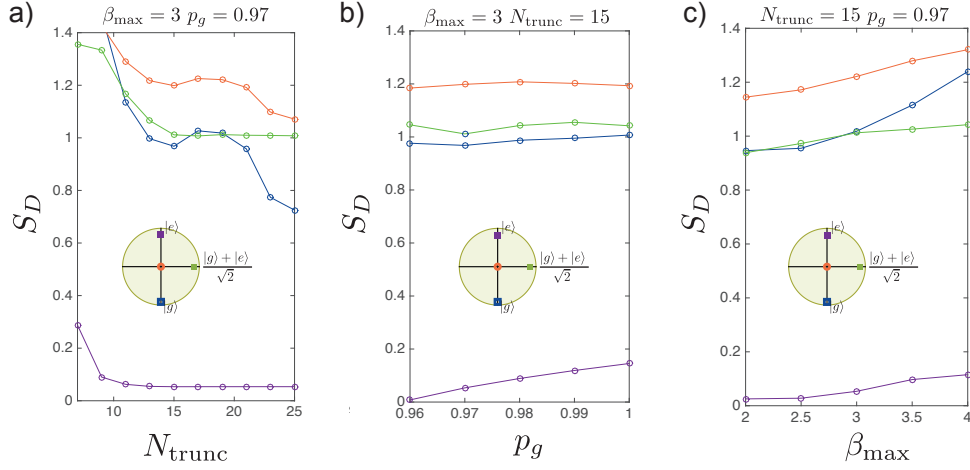
Figure 7.17: Uncertainty on the demon entropy due to the MaxLike reconstruction. The demon entropy $S_D = -\text{Tr}(\rho_D \ln \rho_D)$, calculated from the reconstructed demon density matrix ρ_D, is plotted for various values of the parameters a) N_{trunc}, b) β_{max} and c) p_g entering the MaxLike algorithm. The qubit was initially prepared in a temperature 0.1K, a superposition of ground and excited states, close to the excited state and a maximally mixed state (see inset).

7.3.5 Encoding binary information into an oscillator

The demon's non-linearity coupled to its losses results in a final state whose von Neumann entropy largely overcomes the entropy variations of the system between the initial and final states. In particular when the system is initially in $|g\rangle$, the demon's measured final entropy for $\alpha_{\text{in}} = 0.25$ is $S_D = 1.1 \pm 0.15$. This randomness does not prevent the demon to act coherently as manifested by the non-zero coherences $\langle 0|\rho_D|n\rangle, n \geq 0$ when the system is initially in a superposed state. The problem comes directly from the fact that our procedure encodes binary information about the system in a much larger Hilbert space, one state, $|e\rangle$ being encoded into a pure state while $|g\rangle$ is mapped onto a mixed, entropic state. The von Neumann entropy does not distinguish between the different Fock states since each one of them contributes equally to the entropy. Therefore we can legitimately ask if the von Neumann entropy is the right measure of the information *about the system's initial state* contained in the demon.

To illustrate this point let us consider a "mischievous" demon encoding the system's state in three different states. When the system is in $|e\rangle$ the demon encodes it in its state $|0\rangle$. When it is in $|g\rangle$, the demon flips a coin and based on the result encodes the state in $|1\rangle$ or in $|2\rangle$. Finally, just like the previous demon, it applies a π-pulse on the system conditioned on $|0\rangle$. We can represent the states transfer by the truth table

$$
\begin{array}{ccc}
\text{System} & & \text{Demon} \\
|e\rangle & \rightarrow & |0\rangle \\
|g\rangle & \rightarrow & \frac{1}{2}(|1\rangle\langle 1| + |2\rangle\langle 2|) \ .
\end{array}
$$

The demon's von Neumann entropy is thus 0 for the system initially in $|e\rangle$ and $\ln 2$

for the system initially in $|g\rangle$. The initial thermal $(|e\rangle\langle e| + |g\rangle\langle g|)/2$ and superposed $(|e\rangle + |g\rangle)\sqrt{2}$ states result in the respective demon's states ρ_D^{th} and ρ_D^{sup}

$$
\begin{aligned}
\rho_D^{\text{th}} &= \frac{1}{2}|0\rangle\langle 0| + \frac{1}{4}|1\rangle\langle 1| + \frac{1}{4}|2\rangle\langle 2| \\
\rho_D^{\text{sup}} &= \rho_D^{\text{th}} + \frac{1}{4}\big(|1\rangle\langle 0| + |0\rangle\langle 1| + |2\rangle\langle 0| + |0\rangle\langle 2|\big) \;.
\end{aligned}
\tag{7.30}
$$

The von Neuman entropy of the demon in the case of the initial thermal state is $S_D^{\text{th}} = 1.04 > \ln 2$ and $S_D^{\text{sup}} = 0.562$ for the superposed initial state. It is true that the demon's random choice during state encoding blurs the information about the qubit but the von Neumann entropy fails at representing the information acquired about the state of the system only. Indeed the demon is able to distinguish perfectly between the ground and the excited states since it deterministically puts the qubit in $|g\rangle$. Therefore if we want to quantify the amount of information acquired by the demon about the system we should adopt a measure that would give 0 when the system is initially in a pure state, $\ln 2$ for the initial thermal state and an intermediate entropy for the initial superposed state.

When binary information is mapped onto such a multi-level memory (M) we suggest to adopt what we call the *binary entropy*. Its definition is based on a procedure transferring the information contained in the large memory onto a qubit ancilla (A) initialy in a pure state $|\psi\rangle_A$. More precisely the binary entropy S_{bin} is defined as the minimum of the ancilla von Neumann entropy over all the possible memory-ancilla unitary operations $U_{\text{M}\otimes\text{A}}$

$$
S_{\text{bin}}(\rho^{\text{M}}) = \min_{U_{\text{M}\otimes\text{A}}} \big\{ - \text{Tr}(\rho^{\text{A}} \ln \rho^{\text{A}}) \big\}
\tag{7.31}
$$

where ρ^{A} is the reduced density matrix of the ancilla obtained by taking the partial trace of $U_{\text{M}\otimes\text{A}}(\rho_M \otimes |\psi\rangle\langle\psi|_A)U_{\text{M}\otimes\text{A}}^{\dagger}$. The interpretation of the binary entropy is straightforward, as it quantifies the total amount of information one can recover by encoding the memory state onto a two-level system. It is well defined since its definition is based on the von Neumann entropy and it takes values between 0 and $\ln 2$.

It is possible to compute exactly the value of ρ^{A} realizing the minimum. We demonstrated it for situations where one state is encoded deterministically onto a unique memory state (like $|e\rangle$ on $|0\rangle$) and the orthogonal one randomly encoded within an ensemble of states orthogonal to the first one (like $|g\rangle$ on $|1\rangle$ or $|2\rangle$). The full generalization is still pending at this date. When one state is encoded deterministically in $|0\rangle$ we construct the optimal ρ^{A} from the memory state ρ^{M} by

$$
\rho^{\text{A}} = \begin{pmatrix} \rho_{00}^{\text{M}} & \sqrt{\sum_{i=1}^{n_M} |\rho_{0i}^{\text{M}}|^2} \\ \sqrt{\sum_{i=1}^{n_M} |\rho_{i0}^{\text{M}}|^2} & \sum_{i=1}^{n_M} \rho_{ii}^{\text{M}} \end{pmatrix}
\tag{7.32}
$$

where n_M is the dimensions of the memory's Hilbert space. Therefore we only need to sum over the populations and over the squares of the coherences to compute the binary entropy. With this definition the binary entropy of the previous mischievous demon becomes 0 when the system is initialized in $|g\rangle$. In the initial thermal and superposed states it reads

$$
\begin{aligned}
S_{\text{bin}}(\rho_D^{\text{th}}) &= \ln 2 \\
S_{\text{bin}}(\rho_D^{\text{sup}}) &= 0.42 < \ln 2 \;.
\end{aligned}
\tag{7.33}
$$

We see with this new measure that the demon randomized acquisition indeed troubled the amount of information about the coherences of the system. But it did so in a smaller amount than indicated by the von Neumann entropy. The binary entropy is therefore an encouraging lead towards quantifying the information transfers in action in our demon experiment.

7.4 CONCLUSION

The autonomous Maxwell's demon experiment presented in this chapter related the independent measurements of the extracted work to the internal energy variation of the system while varying the amount of information acquired by the demon. In doing so we distinguished between coherent and incoherent emission of energy by the qubit and related these quantities to respectively work and heat. By preparing the system in a superposed state we attested the presence of coherences in the demon's memory which demonstrate the coherent transfer of information between the system and demon. This transfer of information is not well represented by the cavity's von Neumann entropy and we proposed a new measure for information called binary entropy. This experiment demonstrates the use of superconducting circuits for studying the roles of work, heat and information in the quantum domain.

The main unpublished results of this chapter are given here. Other results can be found in Ref. [147].

- Experimental measurement of time-resolved coherent and incoherent emission of a qubit, Fig. 7.9

- New definition for quantifying the information about a qubit encoded into a multilevel system, Eq. (7.31).

Part IV

APPENDIX

TECHNICAL ASPECTS OF SUPERCONDUCTING CIRCUITS

The experiments presented in this thesis were based on two circuits. A transmon embedded in an aluminum cavity was used to measure time-resolved fluorescence with the help of a JPC, perform phase-controlled power transfer between two drives, and realize the quantum Maxwell's demon experiment. It was fabricated and measured at the École Normale Supérieure. On the other hand the fluorescence readout was based on two fluxonium circuits made and measured in a copper waveguide at the Joint Quantum Institute, University of Maryland. The samples were measured using the Python acquisition software ExoPy [185].

We give here some information about the experimental setups and fabrication procedures used for these circuits.

A.1 CRYOSTAT WIRING

The experiments conducted at ENS and JQI were realized in BlueFors dilution cryostats, reaching base temperatures of 10-20 mK. The precise wiring at cryogenic temperatures is shown in Fig. A.1 for the experiments done at ENS. The microwave signals propagating from the room-temperature setup are thermalized at each stage of the cryostat by microwave attenuators. In the measurement line, high frequency noise above 12 GHz is filtered and the thermal noise coming from the amplification chain at higher temperature is dissipated in resistors thermalized at base temperature thanks to circulators. The JPC is pumped and flux-biased so that it amplifies in the quantum limit at qubit frequency. The signals at qubit and cavity frequency coming from the system are amplified at 4K using a High Electron Mobility (HEMT) transistor. The coil used to apply flux on the JPC consists of superconducting wire winded around a metal (brass or copper) cylinder.

The experiment at JQI used only one measurement line used to probe the waveguide in reflection and no JPC. The wiring for the driving and measurement lines is sensibly the same as the ENS setup. The flux bias used for the fluxonium is similarly applied through a superconducting coil surrounding the copper waveguide.

The room-temperature setup for the ENS experiments is represented in the main text in Fig. 3.2. For the Maxwell's demon we use the weakly attenuated line in transmission to realize the π-pulses conditioned by the cavity hosting n photons needed to measure the Husimi Q-functions of the cavity. The cavity displacement and HPR measurement (see Sec. B.2) are applied through the same line by playing with the modulation frequency of the AWG. The JQI experiment was based on a simple modulation/demodulation setup as discussed in Sec. 2.3.5 and 2.3.4.
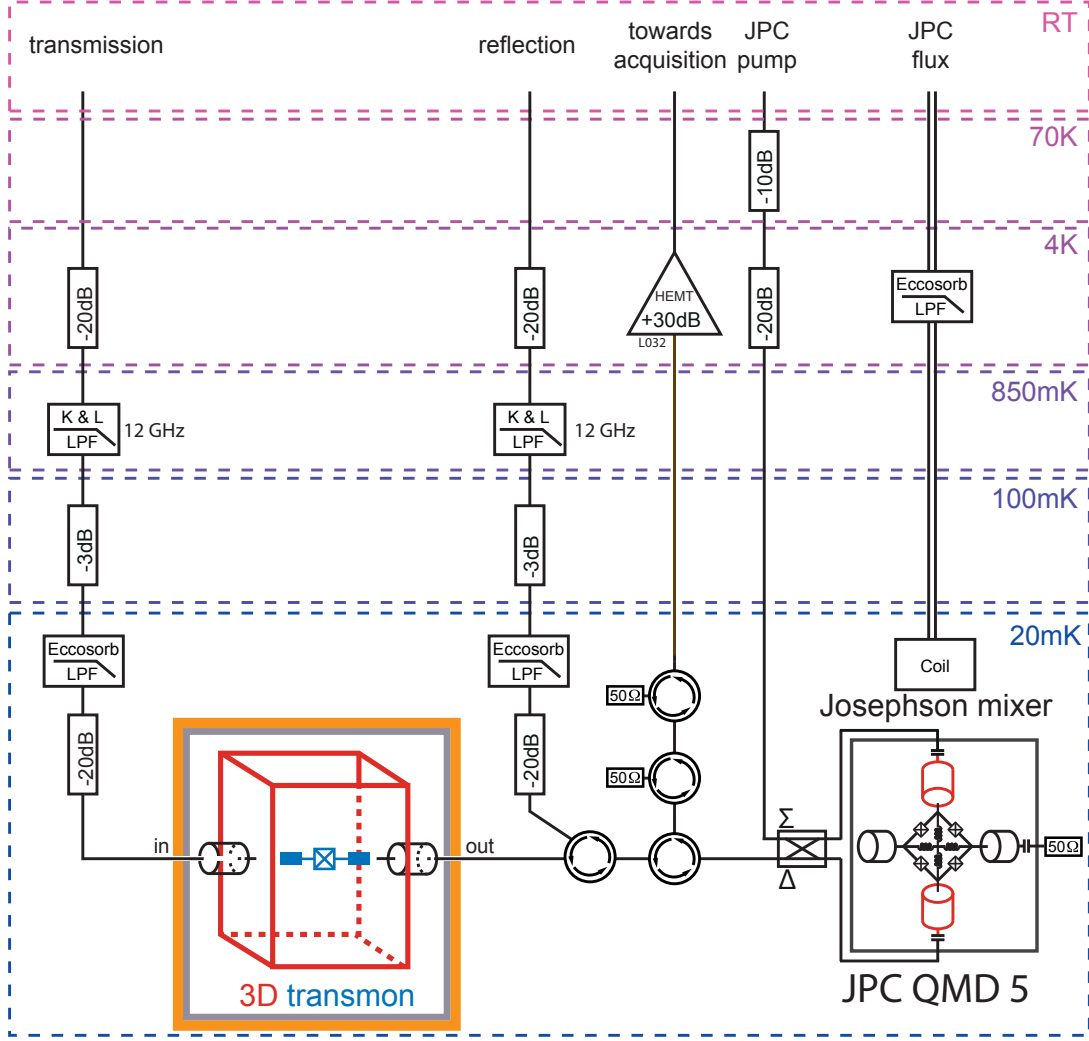
Figure A.1: Cryostat wiring used at ENS.

A.2 SAMPLE FABRICATION

A.2.1 *Josephson junctions*

Both the small junctions giving the non-linearity of the transmon, JPC and fluxonium and large junctions composing the fluxonium's superinductance are fabricated using the Dolan bridge and shadow evaporation technique represented in Fig. A.2. The substrate is silicon for the JPC and fluxonium and sapphire for the transmon. On top of the substrate we deposit a bilayer of two electron-sensitive resists, MAA and PMMA. The latter, placed on top, is less sensitive than the former. By electron lithography we shine a precise amount of electrons on different parts of the resist according to the wanted design (Fig. A.2a). With the right doses it is possible that after development all the MMA resist has been removed while a suspended bridge of PMMA remains. Using angle evaporation, we deposit aluminum on the substrate everywhere MMA has been removed but where the PMMA bridge casts its shadow (Fig. A.2b). After oxidation, a second aluminum evaporation is made at a different angle, resulting in an $Al/AlO_x/Al$ junction (Fig. A.2c). The final result after resist removal can be depicted by the top view in Fig. A.2d) (the electrodes and junctions sizes are not to scale). Even though

the electrodes contain a superposition Al/AlO$_x$/Al, there dimensions are so big that the tunnel effect is suppressed and each electrode behave as a large superconducting bulk.
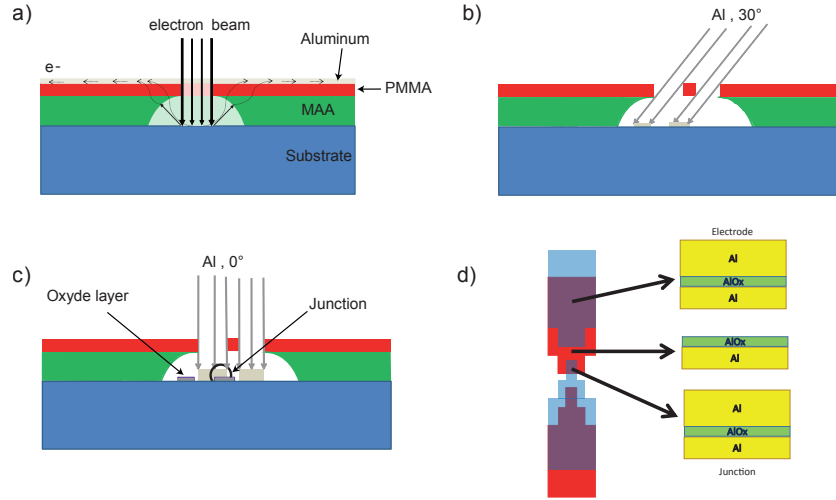
Figure A.2: Junction fabrication by shadow evaporation with Dolan bridge. a) The MAA-PMMA bilayer is shined with electrons using and electron microscope. After evaporation and depending on the electron doses, a bridge of PMMA remains on top of an empty space left by the MAA. b) The angle evaporation of aluminum does not deposit metal on certain parts of the substrate due to the PMMA bridge. c) A controlled oxidation creates an thin film of aluminum oxide and is followed by a second evaporation at a different angle to create the junction. d) Schematics of the final result after resist removal. The dimensions of the electrodes and junction are not to scale.

A.2.2 *Nanofabrication*

We provide here the full fabrication recipe used to make the transmon of the power transfer and Maxwell's demon experiments.

CLEANING

- rough cleaning in Acetone with clean-room cotton bud;

- 10 min ultrasound in Acetone;

- 2 min ultrasound in Methanol;

- 2 min ultrasound in IPA;

- N_2 blow dry;

- observation of the surface using a microscope;

- O_2 plasma, 10 min with reactive ion etching (RIE).

SPIN COATING

- 1 drop of MAA;

- spinning at 4000 rpm for 60s;

- bake at 185°C for 4 min;

- cooling for 1 min at room temperature;

- 1 drop of PMMA;

- spinning at 4000 rpm for 60s;

- bake at 185°C for 4 min.

ALUMINUM DEPOSITION FOR E-BEAM LITHOGRAPHY

- place ∼100 g of Aluminum (purity 99.99%) in a Joule crucible;

- pump for 1 hour until $P < 10^{-5}$ mBar;

- evaporation of 18 nm Al at 1 nms^{-1}.

MIBK DEVELOPMENT

- Aluminum removal ∼ 30 s in KOH;

- Rince in water for 30 s and N_2 blow dry;

- 42 s in MIBK:IPA (1:3);

- Rince in IPA for 20 s;

- N_2 blow dry.

ANGLE EVAPORATION

- pump for 45 min until $P < 3 \times 10^{-6}$ mBar;

- titanium sweep to improve the vacuum to 3×10^{-7} mBar;

- 5 s of ion milling at $-35°$ and $+35°$

- evaporation of the first Al layer at $-30°$: 35 nm at 1 nm/s ;

- static oxidation: 7 min at 20 mBar;

- titanium sweep to remove any trace of water adsorbed on the surfaces;

- evaporation of the first Al layer at $+30°$: 100 nm at 1 nm/s ;

- capping oxidation: 5 min at 40 mBar

QUBIT MEASUREMENT WITH A CAVITY

In this appendix we recall some aspects of the dispersive interaction of a qubit with a cavity. The state of the qubit can be measured in the energy basis by measuring the resonance frequency of the cavity using a near-resonant drive. The measurement backaction shifts the qubit frequency by AC-Stark shift, and dephases the qubit as measurement takes information out of the system. In the thesis we used this effect to measure Rabi oscillations of the transmon qubit between the first $|e\rangle$ and the second $|f\rangle$ excited states to determine the qubit temperature in the Maxwell's demon experiment (Sec. 7.2.2). The qubit tomographies presented in Chap. 7 are obtained using a High Power Readout (HPR) that we discuss in a second time.

B.1   DISPERSIVE MEASUREMENT

The dispersive Hamiltonian in Eq. (1.12) shows that the cavity angular frequency is ω_c is the qubit is in the ground state $|g\rangle$ and $\omega_c - \chi$ is the qubit is in $|e\rangle$. Thus probing the cavity frequency allows to deduce the state of the qubit.

B.1.1   *Cavity internal states*

We consider a drive on the cavity at $\omega_c + \delta$ and amplitude ϵ. It generates two coherent states $|\alpha_{g,e}\rangle$ depending on the state of the qubit. Their time evolution can be computed from the Lindblad equation of the cavity containing the dispersive Hamiltonian and the cavity photon-loss with a rate κ. In a similar manner than the JPC intra-fields calculation Eq. (2.38) with the difference that here we are in the Schrödinger representation, we get

$$\begin{cases} \dot{\alpha_g} &= i\delta\alpha_g - \frac{\kappa}{2}\alpha_g + \epsilon \\ \dot{\alpha_e} &= i(\delta + \chi)\alpha_e - \frac{\kappa}{2}\alpha_e + \epsilon \ . \end{cases} \tag{B.1}$$

The resolution of these equations is straightforward and considering $\alpha_{g,e}(0) = 0$ we obtain

$$\begin{cases} \alpha_g(t) &= 2\epsilon\frac{e^{(i\delta - \kappa/2)t} - 1}{\kappa - 2i\delta} \\ \alpha_e(t) &= 2\epsilon\frac{e^{(i(\delta + \chi) - \kappa/2)t} - 1}{\kappa - 2i(\delta + \chi)} \ . \end{cases} \tag{B.2}$$

The evolution of the internal states with time is represented in Fig. B.1 when the cavity is driven at $\delta = -\chi/2$ for $\chi = 2\kappa$. The states evolve symmetrically and rotate in time before reaching the steady-state. This rotation in time is due to the dispersive Hamiltonian and sets a practical limit on the speed and fidelity of quantum measurements of superconducting qubits that can be solved if one implements a longitudinal coupling between the qubit an cavity [186].
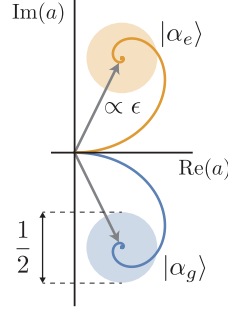
Figure B.1: Evolution of the cavity fields $|\alpha_{g,e}(t)\rangle$ with time represented in phase space, for the cavity initially in vacuum and $\chi = 2\kappa$, $\delta = -\chi/2$. The distance between 0 and the steady-state field is proportional to the drive amplitude ϵ. The quantum fluctuations of vacuum are represented by the plain circles around the steady-states.

B.1.2 *Effect on the qubit: AC-Stark shift and measurement induced dephasing*

The effect of the cavity field on the qubit can be calculated by writing a master equation for the joint system qubit + cavity [187]. Due to the cavity photons the qubit frequency is shifted by AC-Stark shift. When the cavity hosts a Fock state n the qubit frequency is shifted to $\omega_q - n\chi$. More generally when the cavity is probed by the drive ϵ the qubit frequency is shifted to $\omega_q - \omega_{\text{Stark}}$ with

$$\omega_{\text{Stark}} = -\chi \text{Re}\big(\alpha_g^* \alpha_e\big) \tag{B.3}$$

The coherent state in the cavity leaking at a rate κ towards the environment takes information out of the quantum world. Therefore is generates measurement-induced dephasing at a rate Γ_d given by

$$\Gamma_d = \chi \text{Im}\big(\alpha_g^* \alpha_e\big) \ . \tag{B.4}$$

The measurement of ω_{Stark} and Γ_d as a function of the cavity drive frequency allows to compute very precisely the dispersive shift χ and the cavity loss rate κ.

B.2 HIGH-POWER READOUT

When the cavity hosts photons its resonance frequency is shifted due to its non-linearity induced by the qubit. In the limit of large numbers of photons the cavity bifurcates and becomes transparent at the bare cavity frequency. If the qubit is excited bifurcation happens more easily because the system already contains an excitation. Therefore it is possible to find an amplitude point where the cavity bifurcates if the qubit is excited and not if the qubit is in the ground state. By detecting the cavity bifurcation we can perform the so-called High Power Readout measurement [22]. This readout has the advantage of using high drive amplitudes and therefore to achieve a high signal-to-noise ratio even in the absence of a quantum-limited amplifier at cavity frequency. The first interpretation of cavity bifurcation was that quasiparticles were created by the strong drive and thus saturate the superconductor at the level of the transmon junction. In doing so, the non-linearity due to the Josephson junction disappears, causing the cavity to bifurcate to the bare cavity frequency. Recent experimental results by Lescanne and coworkers [127, 188] showed that bifurcation is actually due to the ionization of the junction. The fictive particle moving in the cosine potential energy of the junction (see

Sec. 1.1) jumps to free states above the cosine potential and hence does not feel the cosine non-linearity.

Concretely the readout is performed by sending a strong drive near the bare cavity frequency and measuring its transmission. Figure B.2 shows the experimental evolution of the transmission with the drive amplitude when the qubit is initialized in the ground (blue curve) and in the excited states (orange curve). At cavity bifurcation the cavity transmission is greatly enhanced. The red arrow indicates the selected power for the measurement, which maximizes the distance between the two curves.
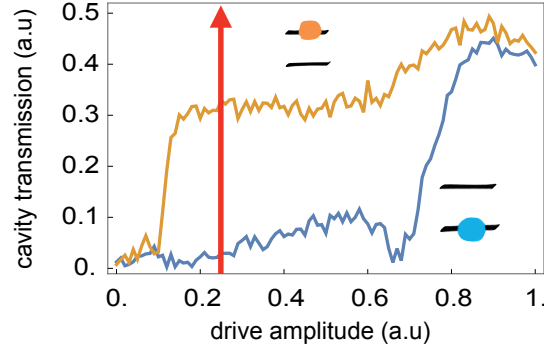

Figure B.2: High Power Readout measurement. The cavity transmission near the bare cavity frequency is measured as a function of the readout drive amplitude when the qubit is initialized in the ground (blue) and excited (organge) state.

THERMAL BATHS OF SUPERCONDUCTING CIRCUITS

Superconducting circuits are mesoscopic objects and are therefore coupled to several uncontrolled degrees of freedom acting as individual thermal baths. The influence of some of these baths on the energy relaxation of fluxonium circuits is discussed in Sec. 5.1. We provide here a more thermodynamical point of view on these effect of the baths on circuits. The question of the temperatures of each baths and their precise coupling to superconducting circuits is still open and actively investigated by the community, hence we will summarize here the results of the literature in order to give a general overview.

The main heat baths identified for superconducting circuits are represented in Fig. C.1. The thermometer of the dilution refrigerator indicates the temperature of the phonons of the metallic base plate and lies generally between 10 and 50 mK [189]. The substrate on which the circuits are build are placed in a sample holder that is thermalized on the plate. Depending on the thermal link between the substrate and the sample holders, the phonon temperature of the substrate T_{ph} can differ from the one of the plate. For circuits embedded in a 3D cavity like the ones used in this thesis the varying circuit thermal occupation (see for instance Appendix A of Ref. [34]) seems to indicate that the substrate phonon temperature can subsequently vary from experiment to experiment. In 2D architecture the thermal occupation of circuits is generally lower, indicating that the phonons might be better thermalized this way. The electromagnetic noise coming from the coaxial cables used to carry the microwave signals is thermalized using attenuators at the different stages of the refrigerator for the driving lines, and dissipated in resistive loads using circulators for the measurement lines (see Fig. A.1). Thus with the proper wiring the temperature of the electromagnetic field T_{em} corresponds to the one of the refrigerator. The contribution of two-level systems (TLS) at the circuit-substrate interface to thermal excitation has not been well explained yet. However their role in energy dissipation is under active scrutiny [190]. Finally if a recent study proved that quasiparticles can be responsible for large parts of thermal excitations [119], the temperature of this bath T_{qp} is still an open question.

In all generality a quantum system represented by the Hamiltonian H and coupled to several heat baths at different temperatures does not equilibrate towards a Gibbs state $\rho = e^{-H/k_B T}$ and it is not possible to assign a temperature to the system at equilibrium. The reason is that the different transitions of the system are sensitive to several frequencies of the baths spectral densities of noise. However when only one frequency describes the system, which is the case for a linear oscillator or a qubit, the coupling to the baths results in a single effective heat bath. Indeed, the system's excitation and deexcitation rates, respectively $\Gamma_\uparrow$ and $\Gamma_\uparrow$, can be expressed by summing over all the baths i

$$\Gamma^\uparrow = \sum_i \Gamma_i n(T_i)$$
$$\Gamma^\downarrow = \sum_i \Gamma_i \Big(n(T_i) + 1 \Big) \tag{C.1}$$
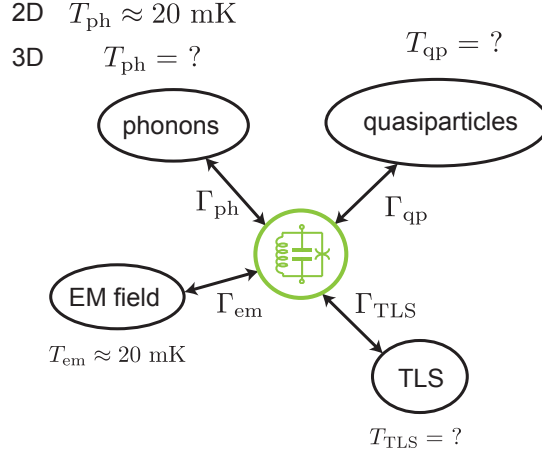
Figure C.1: Main heat baths coupled to superconducting circuits. Depending on the precise experimental setup, the baths temperatures and coupling rates to the circuits can vary.

where $n(T) = \frac{1}{e^{-\hbar\omega_q/k_B T}-1}$ is the number of thermal excitations at temperature T and frequency ω. The effective temperature can be this be expressed as

$$T_{\mathrm{eff}} = \frac{\sum_i \Gamma_i T_i}{\sum_i \Gamma_i} \ . \tag{C.2}$$

In the experiments presented in the thesis the coupling rates of the qubit and cavity to the baths are not equal, thus their effective temperatures are different. This point is important in the quantum-mechanical Maxwell's demon presented in Chap. 7. The transmon and especially the fluxonium circuits are *stricto sensu* not quantum bits but non-linear quantum systems. Therefore assigning them an effective temperature is an approximation based on the assumption that the thermal occupation of the second excited state is much lower than the one of the first excited, which is the case given the frequencies and baths considered in the experiments.

FLUXONIUM MATERIALS

We provide here additional materials about the experiment of fluorescence readout with a fluxonium. The first is an unexplained coupling of the fluxonium circuit to linear modes. The second presents the code used for numerical simulations of the branching ratio.

D.1 COUPLING TO EXTERNAL MODES

The fluxonium spectra showed in Fig. 4.9 present horizontal stripes that are not due to measurement imperfections. Indeed we measure a calibration trace in reflection at 4K before the circuit becomes superconducting and renormalize the raw traces to obtain the reflection coefficient. This method allows to get rid of spurious reflections in the lines and imperfections of the modulation/demodulation setup. However once below the circuit's critical temperature we consistently measure small oscillations of the reflection coefficient independent on the external flux, giving the stripes of Fig. 4.9 and the small residual oscillations seen in Fig. 4.10. We are thus measuring a comb of resonances indicating the presence of multiple modes.
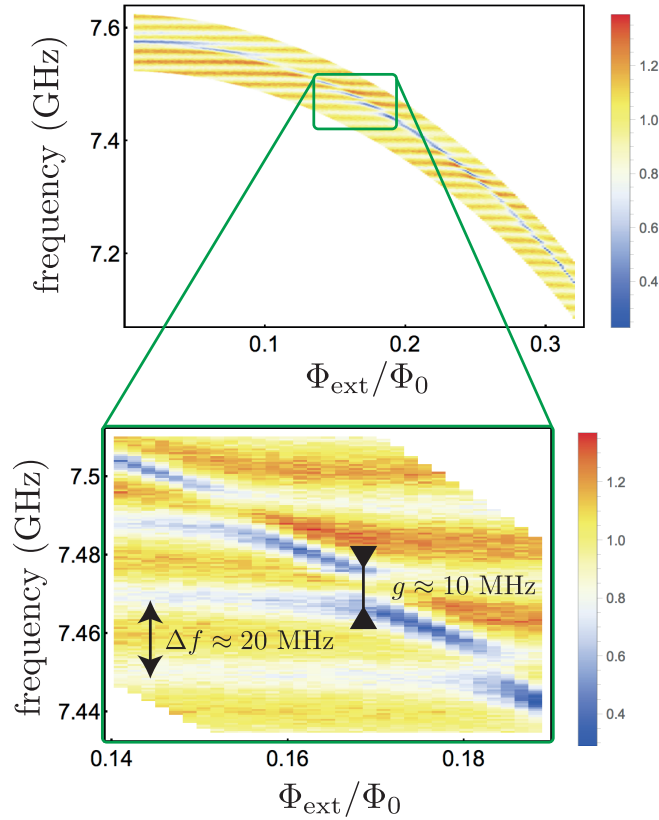

Figure D.1: Anticrossing with unknown modes. When the fluxonium frequency is changed, it goes through a series of avoided crossings with modes spaced every 20 MHz. The coupling rate can be as big as 10 MHz.

When looking more closely at the fluxonium spectrum we find that the fluxonium readout transition presents avoided crossings with all of these modes, as shown in Fig. D.1, measured for the fluxonium A (see Table. 4.1). The coupling between the modes and the fluxonium transition can be as big as $g \approx 10$ MHz, therefore almost as large as the mode spacing $\Delta f \approx 20$ MHz. We studied the possibility that these modes would affect the qubit transition lifetime by Purcell effect and coherence time by measurement induced dephasing due to photon shot noise in the modes and found no influence of these modes on the qubit transition. Surely the qubit matrix elements are too low for the interaction with the unwanted mode to be large enough to affect the lifetime and coherence time.

The interpretation for these modes strongly interacting with the fluxonium is unclear at this time. The possibility of spurious reflections in the microwave cables between the experiment and microwave components such as the circulators (see Fig. A.1) is unlikely. First, these reflections should be present even above the superconducting critical temperature. Moreover the mode spacing indicates that light would have to be reflected over several meters of cables while experimentally we do not have more than a few tens of centimeters between the waveguide and the circulators. A possibility is that we are seeing collective resonances implying the antennas and the chain of junctions realizing the superinductance. The latter is by design a high impedance medium in which slow light propagates and could explain the small mode spacing [191]. However the length of the chain is short compared to the experiments realizing high impedance transmission lines conducted in our group at JQI Maryland [192]. Moreover the role of the antennas and the precise electromagnetic resonances to consider to explain this effect have still to be precised.

D.2 NUMERICAL SIMULATIONS

We simulate the dynamics of the fluxonium by numerically solving the Lindblad master equation containing the circuit Hamiltonian under the drives and the various loss mechanisms. To do so we use the Python package QuTip [180]. We start by defining the fluxonium Hamiltonian and diagonalize it in a large Hilbert space, truncated at $N_1 = 100$. We then reduce the size of the Hilbert space to $N_2 = 10$ and compute the transition frequencies, matrix elements and decay rates. Then we simulate the dynamics of the system under a drive near the resonance between two states $|n_1\rangle$ and $|n_2\rangle$, $n_2 \geq n_1$ using the driving Hamiltonian

$$H_d = \delta \frac{(|n_2\rangle\langle n_2| - |n_1\rangle\langle n_1|)}{2} + \epsilon \varphi_{n_1,n_2}(|n_1\rangle\langle n_2| + |n_2\rangle\langle n_1|) \qquad \text{(D.1)}$$

where we have kept the flux matrix element explicitly to show that some transitions are harder to drive than the other. Physically this Hamiltonian means that we have neglected the possible excitation of higher excited states due to the drive and multi-photons processes. We can do this approximation if the drive amplitude is not too strong and the detuning between the transitions big enough. When it is not the case the whole Hamiltonian in the rotating frame needs to be taken into account, with more computational resources needed.

Listing D.1: Pumping effects in fluxonium circuit

```python
import qutip as qt
import numpy as np
import scipy.linalg as lng
import matplotlib.pyplot as plt


# Physical constants
h = 6.62*10**-34
e = 1.6*10**-19
Rq = h/(8*np.pi*e**2)


# Hilbert space truncature and annihilation operator
N1 = 100
N2 = 10
a = qt.destroy(N1)


# Aluminum superconducting gap and quasiparticles loss
Delta = 82 #in GHz
xqpJunction = input('Quasiparticle population in the junction?')
xqpChain = input('Quasiparticle population in the chain?')


# Dielectric loss
Qdiel = input('Dielectric quality factor?')


# Import measurement transmission of the waveguide (in dB) and
    frequency and interpolate
freq_exp = np.loadtxt('freq.txt')
logS = np.loadtxt('waveguideLog.txt')
def t(f):
    return np.interp(f,freq_exp,10**(logS/20))


# Fluxonium parameters and operators
Ej = 2.045
Ec = 1.177
El = .617


C = e**2/(2*Ec*10**9*h)


n = 1j/np.sqrt(2)*(a-a.dag())/np.sqrt(np.sqrt(8*Ec/El))
phi = 1/np.sqrt(2)*(a+a.dag())*np.sqrt(np.sqrt(8*Ec/El))


# Fluxonium hamiltonian diagonalization
H0 = 4*Ec*n**2 + El*phi**2/2


def V(phiext):
    V0 = -Ej*lng.cosm(phi.full() - phiext*np.identity(N1))
    return qt.Qobj(V0)


phase = np.pi


H = H0 + V(phase)


energies = H.eigenenergies()
states = H.eigenstates()[1]
```

```python
# Rewrite operators and eigenstates in a smaller Hilbert space to
    save memory
phimatrix = phi.full()
phimatrix = phimatrix[:N2-1,:N2-1]
phi = qt.Qobj(phimatrix)
sinmatrix = lng.sinm((phimatrix - phase*np.identity(N2-1))/2)
sine = qt.Qobj(sinmatrix)

states = states[:N2-1]
for i,s in enumerate(states):
    statematrix = s.full()
    statematrix = statematrix[:N2-1]
    states[i] = qt.Qobj(statematrix)

# Compute resonance frequencies, matrix elements, and decay rates
    . The Purcell rate is rescaled to match the experiment
    measurements
freq = np.empty((10,10))
coupling = np.empty((10,10))
couplingn = np.empty((10,10))
couplingsin = np.empty((10,10))

for i,s1 in enumerate(states):
    for j,s2 in enumerate(states):
        freq[i,j] = energies[j]-energies[i]
        coupling[i,j] = np.abs(phi.matrix_element(s1.dag(),s2))
        couplingsin[i,j] = np.abs(sine.matrix_element(s1.dag(),s2
            ))

gammaPurcell = np.zeros((10,10))
gammaJunction = np.zeros((10,10))
gammaArray = np.zeros((10,10))
gammaDiel = np.zeros((10,10))

for i,s1 in enumerate(states):
    for j,s2 in enumerate(states):
        if i>j:
            gammaPurcell[i,j] = freq[j,i]**3*coupling[i,j]**2*t(
                freq[j,i])**2
            gammaJunction[i,j] = couplingsin[i,j]**2*8*(2*np.pi*
                Ej)*10**3/np.pi*xqpJunction*np.sqrt(2*Delta/freq[
                j,i])
            gammaArray[i,j] = coupling[i,j]**2*8*(2*np.pi*El)
                *10**3/np.pi*xqpChain*np.sqrt(2*Delta/freq[j,i])
            gammaDiel[i,j] = coupling[i,j]**2*(2*np.pi*freq[j,i
                ]*10**9)**2*C/Qdiel*Rq*10**-6

gexp = 2.65
gamma = gexp*2*np.pi*gammaPurcell / (gammaPurcell[0,3]+
    gammaPurcell[3,0])

# Compute Lindbladians
c_ops = []
for i in range(10):
```

```python
    for j in range(10):
        if i>j:
            c_ops.append(np.sqrt(gammaPurcell[i,j])*qt.fock(N2,j)
                *qt.fock(N2,i).dag())
            c_ops.append(np.sqrt(gammaJunction[i,j])*qt.fock(N2,j
                )*qt.fock(N2,i).dag())
            c_ops.append(np.sqrt(gammaArray[i,j])*qt.fock(N2,j)*
                qt.fock(N2,i).dag())
            c_ops.append(np.sqrt(gammaDiel[i,j])*qt.fock(N2,j)*qt
                .fock(N2,i).dag())

# Evolution under pulse between |n1> and |n2>, n2 > n1 detuned by
    delta

for p in np.linspace(-1,3,11):
    e = 10**p
    n1 = 0
    n2 = 3

    delta = 0

    Hd = delta*(qt.fock(N2,n2)*qt.fock(N2,n2).dag()-qt.fock(N2,n1
        )*qt.fock(N2,n1).dag())/2. + e*abs(coupling[n1,n2])*(qt.
        fock(N2,n1)*qt.fock(N2,n2).dag()+ qt.fock(N2,n2)*qt.fock(
        N2,n1).dag())

    time = np.linspace(0,200,1001)
    rho0 = qt.fock_dm(N2,0)

    sol = qt.mesolve(Hd,rho0,time,c_ops)
    rho = sol.states

    n = 5
    population = []
    lgd = []
    for k in range(0,5):
        population.append(qt.expect(qt.fock(N2,k)*qt.fock(N2,k).
            dag(),rho))
        lgd.append('p%i'%k)

    # Plot results at each amplitude (if needed)
    plt.figure()
    plt.plot(time, np.transpose(population))
    plt.legend(lgd,loc=0)
    plt.title('Amplitude = %f' %e)
plt.show()
```

SIMULATIONS FOR THE MAXWELL'S DEMON EXPERIMENT
_____

We give here the codes used to compute the cavity Kerr measured in Fig. 7.4 and the simulated Husimi Q-functions showed in Fig. 7.15.

E.1 CAVITY KERR

To simulate the results displayed in Fig. 7.4 we solve the master equation for the system qubit + cavity during the whole measurement sequence. It consists of a cavity displacement whose duration and amplitude can be adapted followed by a π-pulse at qubit frequency f_S with $T_\pi = 96$ ns. We take into account the delays between the displacement and the qubit pulse.

Listing E.1: Kerr simulation

```python
import qutip as qt
import numpy as np
import matplotlib.pyplot as plt
import time

# Hilbert space dimension and number of displacement amplitudes
    and duration
Hilbert_space = 45
num_points = 30
num_durations = 4
sweep_amp = np.tile(np.linspace(0,50,num_points),num_durations)
sweep_t = np.repeat(np.array(range(40,120,20)),num_points)

# Physical parameters
kerr = 0.7 # Kerr
k = 0.77 # Cavity loss rate
ke = kerr*2*np.pi*10**6
kcav = k*2*np.pi*10**6
wc = 2*np.pi*7.913*10**9
wd = wc + 2*np.pi*9*10**6
wq = 2*np.pi*7.09*10**9
chi = 2*np.pi*33.8*10**6
chi2 = 2*np.pi*0.9*10**6
alpha = 2*np.pi*126*10**6

# Qubi pulses
pi_start = 163
T = 96
Tpi = T*10**-9
time_pi = np.linspace(0,Tpi,401)
omega = np.pi/(2.*Tpi)

# Cavity loss
a = qt.destroy(Hilbert_space)
```

```python
c_ops = [np.sqrt(kcav)*qt.tensor(a,qt.qeye(2))]

# Initial state |0><0| x |g><g|
psi = qt.tensor(qt.fock(Hilbert_space,0),qt.basis(2,1).unit())

# Solve master equations for a given displacement duration and
    amplitude and return P(|e>)
def func(t,i):

    # Hamiltonians
    Hcav = (wc-wd)*qt.tensor(a.dag()*a,qt.qeye(2)) - ke*qt.tensor
        ((a.dag()*a)**2,qt.qeye(2))
    Hint = - chi * qt.tensor(a.dag()*a,qt.basis(2,0)*qt.basis
        (2,0).dag()) - chi2*qt.tensor(a.dag()*a*a.dag()*a,qt.
        basis(2,0)*qt.basis(2,0).dag())
    H0 = Hcav + Hint
    amp = 2.0*np.pi*i*10**6
    H = H0 + amp*qt.tensor(a.dag()+a,qt.qeye(2))
    Hq = omega*qt.tensor(qt.qeye(Hilbert_space),qt.sigmay())

    # time arrays
    tdisp = t*10**-9
    tlist = np.linspace(0,tdisp,201)
    twait = (pi_start-t)*10**-9
    twaitlist = np.linspace(0,twait,201)

    # Compute cavity + qubit evolution during the sequence
    # Cavity displacement
    solved = qt.mesolve(H,psi,tlist,c_ops,[],args={})
    state_displaced1 = solved.states[-1]
    # Wait
    solved = qt.mesolve(H0,state_displaced1,twaitlist,c_ops,[],
        args={})
    state_displaced2 = solved.states[-1]
    # Pi-pulse on the qubit
    after_pi = qt.mesolve(H0+Hq,state_displaced2 ,time_pi,c_ops
        ,[])

    return after_pi.states[-1].ptrace(1)

# Parallel solving
if __name__ == '__main__':
    data = qt.parfor(func,sweep_t,sweep_amp)
    z = qt.expect(qt.sigmaz(),data)
    z = np.reshape(z,(num_points,num_durations))

    # Plot data if necessary
    lgd = []
    for k in range(40,120,20):
        lgd.append('displacement time = %i ns'%k)
    plt.figure()
    plt.plot(z)
    plt.legend(lgd,loc=0)
    plt.show()
```

We provide the code used to simulate the Husimi functions presented in Fig. 7.15. We numerically compute the solutions of the master equation for the whole demon sequential sequence of Fig. 7.7a) followed by the measurement sequence of Fig. 7.7d). The outcome is the probability to find the qubit in the excited state.

Listing E.2: Simulation of the Husimi functions measurement

```python
from qutip import *
from numpy import *
from matplotlib.pyplot import *
from time import *

Hilbert_space = 45
num_points = 30
Nmax = 5
kerr = 0.8
k = 0.77
T = 100
t = 5
tw = 10

sweep_amp = tile(linspace(0,399,num_points),Nmax+1)
sweep_n = repeat(array(range(0,Nmax+1)),num_points)

a=destroy(Hilbert_space)
wc = 2*pi*7.913*10**9
wd = wc + 9*10**6
wq = 2*pi*7.09*10**9
chi = 2*pi*32*10**6
alpha = 2*pi*126*10**6
ke = kerr*2*pi*10**6
kcav=k*pi*2*10**6
Tpi = T*10**-9
time_pi = linspace(0,Tpi,701)
width= Tpi/4.
amp_pi = 26./T*10**8
tdisp = t*10**-9
tlist = linspace(0,tdisp,51*max(int(t/10.),1))
twait = tw*10**-9
twaitlist = linspace(0,twait,51*max(int(t/10.),1))

Hcav = (wc-wd)*tensor(a.dag()*a,qeye(2)) - ke*tensor((a.dag()*a)
    **2,qeye(2))
Hint = - chi * tensor(a.dag()*a,basis(2,0)*basis(2,0).dag())

H0 = Hcav + Hint

c_ops = [sqrt(kcav)*tensor(a,qeye(2))]

psi = tensor(coherent(Hilbert_space,0),basis(2,1).unit())

H1 = tensor(qeye(Hilbert_space), create(2))
```

```python
H2 = tensor(qeye(Hilbert_space), destroy(2))

def func(p,i):
    amp = 2.0*pi*i*10**6

    H = H0 + amp*tensor(a.dag()+a,qeye(2))
    solved = mesolve(H,psi,tlist,c_ops,[],args={})
    state_displaced1 = solved.states[-1]

    solved = mesolve(H0,state_displaced1,twaitlist,c_ops,[],args
        ={})
    state_displaced2 = solved.states[-1]

    def ed1(t,args):
        return amp_pi*exp(-(t-Tpi/2.)**2/(2*width**2))*exp(-1j*p*
            chi*t)
    def ed2(t,args):
        return amp_pi*exp(-(t-Tpi/2.)**2/(2*width**2))*exp(1j*p*
            chi*t)

    Hpi = [H0,[H1,ed1],[H2,ed2]]
    after_pi = mesolve(Hpi,state_displaced2,time_pi,c_ops,[])

    return after_pi.states[-1].ptrace(1)

if __name__ == '__main__':
    data = parfor(func,sweep_n,sweep_amp)
    z = expect(sigmaz(),data)
    z = transpose(reshape(z,(Nmax+1,num_points)))
    figure(1)
    plot(z)
    show()
    name = 'Qn(alpha)0detuning_tdisp=%d ns_Tpi=%d ns_ke=%d ns_k=%
        d MHz.txt' %(t,T,10*kerr,k)
    savetxt(name,z)
```

BIBLIOGRAPHY

[1] C. Cohen-Tannoudji, J. Dupont-Roc, and G. Grynberg, *Atom-Photon Interactions* (Wiley-VCH Verlag GmbH, Weinheim, Germany, 1998) (Cited on pages 2, 9, 18, 29, 33, 139, 164).

[2] S. Gleyzes et al., "Quantum jumps of light recording the birth and death of a photon in a cavity.," Nature **446**, 297–300 (2007) (Cited on page 2).

[3] D. Bouwmeester et al., "Experimental quantum teleportation," Nature **390**, 575–579 (1997) (Cited on page 2).

[4] B Hensen et al., "Loophole-free Bell inequality violation using electron spins separated by 1.3 kilometres," Nature **526**, 682–686 (2015) (Cited on page 2).

[5] J.-G. Ren et al., "Ground-to-satellite quantum teleportation," Nature **549**, 70–73 (2017) (Cited on page 2).

[6] M. H. Devoret and J. M. Martinis, "Implementing Qubits with Superconducting Integrated Circuits," Quantum Information Processing **3**, 163–203 (2004) (Cited on page 2).

[7] M. H. Devoret, A Wallraff, and J. M. Martinis, "Superconducting Qubits: A Short Review," arXiv:cond-mat/0411174 (2004) (Cited on page 2).

[8] J. Q. You and F. Nori, "Atomic physics and quantum optics using superconducting circuits," Nature **474**, 589–597 (2011) (Cited on page 2).

[9] M. H. Devoret and R. J. Schoelkopf, "Superconducting Circuits for Quantum Information: An Outlook," Science **339**, 1169–1174 (2013) (Cited on pages 2, 126).

[10] P. W. Anderson and J. M. Rowell, "Probable Observation of the Josephson Superconducting Tunneling Effect," Physical Review Letters **10**, 230–232 (1963) (Cited on page 3).

[11] U. Vool and M. Devoret, "Introduction to quantum electromagnetic circuits," in International journal of circuit theory and applications, Vol. 45, 7 (2017), pp. 897–934 (Cited on pages 3, 4, 10, 32, 78).

[12] E. Flurin, "The Josephson Mixer, a Swiss army knife for microwave quantum optics," Theses (Ecole Normale Supérieure, Paris, 2014) (Cited on pages 3, 36, 42).

[13] H. Ibach and H. Lüth, *Solid-State Physics* (Springer Berlin Heidelberg, Berlin, Heidelberg, 2009) (Cited on pages 4, 100).

[14] F. Pobell, *Matter and Methods at Low Temperatures* (Springer Berlin Heidelberg, Berlin, Heidelberg, 2007) (Cited on page 4).

[15] "Quantum Machines: Measurement and Control of Engineered Quantum Systems," in Lecture notes of the les houches summer school: volume 96, july 2011, edited by M. Devoret et al. (2014), p. 608 (Cited on page 4).

[16] J. Koch et al., "Charge-insensitive qubit design derived from the Cooper pair box," Physical Review A **76**, 042319 (2007) (Cited on page 5).

[17] H. Paik et al., "Observation of High Coherence in Josephson Junction Qubits Measured in a Three-Dimensional Circuit QED Architecture," Physical Review Letters **107**, 240501 (2011) (Cited on pages 5, 126).

[18] Y. Chen et al., "Qubit Architecture with High Coherence and Fast Tunable Coupling," Physical Review Letters **113**, 220502 (2014) (Cited on page 5).

[19] D. C. McKay et al., "Universal Gate for Fixed-Frequency Qubits via a Tunable Bus," Physical Review Applied **6**, 064007 (2016) (Cited on page 5).

[20] V Bouchiat et al., "Quantum Coherence with a Single Cooper Pair," Physica Scripta **T76**, 165 (1998) (Cited on page 5).

[21] E. M. Purcell, "Spontaneous Emission Probabilities at Radio Frequencies," Physical Review **69**, 839–839 (1995) (Cited on pages 7, 79).

[22] M. D. Reed et al., "Fast reset and suppressing spontaneous emission of a superconducting qubit," Applied Physics Letters **96**, 203110 (2010) (Cited on pages 7, 186).

[23] S. E. Nigg et al., "Black-Box Superconducting Circuit Quantization," Physical Review Letters **108**, 240502 (2012) (Cited on page 7).

[24] V. E. Manucharyan et al., "Fluxonium: Single Cooper-Pair Circuit Free of Charge Offsets," Science **326**, 113–116 (2009) (Cited on pages 7, 8, 143).

[25] V. E. Manucharyan, "Superinductance," PhD thesis (2012) (Cited on pages 7, 78).

[26] Y.-H. Lin et al., "Demonstration of Protection of a Superconducting Qubit from Energy Decay," Physical Review Letters **120**, 150503 (2018) (Cited on pages 7, 16, 78, 79, 86, 100).

[27] G. Catelani et al., "Relaxation and frequency shifts induced by quasiparticles in superconducting qubits," Physical Review B **84**, 064517 (2011) (Cited on pages 9, 16, 78, 79, 81, 97, 100).

[28] A. Kou et al., "Simultaneous Monitoring of Fluxonium Qubits in a Waveguide," Physical Review Applied **9**, 064022 (2018) (Cited on pages 9, 81).

[29] U. Vool et al., "Driving Forbidden Transitions in the Fluxonium Artificial Atom," Physical Review Applied **9**, 054046 (2018) (Cited on pages 9, 81).

[30] S. Haroche and J.-M. Raimond, "Exploring the Quantum," Oxford Graduated Text, 616 (2006) (Cited on pages 9, 14, 27, 150, 161).

[31] A. A. Houck et al., "Generating single microwave photons in a circuit," Nature **449**, 328–331 (2007) (Cited on pages 9, 25, 163).

[32] O Astafiev et al., "Resonance Fluorescence of a Single Artificial Atom," Science **327**, 840–843 (2010) (Cited on pages 9, 25, 85).

[33] A. A. Abdumalikov et al., "Dynamics of Coherent and Incoherent Emission from an Artificial Atom in a 1D Space," Physical Review Letters **107**, 043604 (2011) (Cited on pages 9, 25).

[34] P. Campagne-Ibarcq, "Measurement back action and feedback in superconducting circuits," Theses (Ecole Normale Supérieure (ENS), 2015) (Cited on pages 9, 48, 49, 134, 152, 189).

[35] P. Campagne-Ibarcq et al., "Using Spontaneous Emission of a Qubit as a Resource for Feedback Control," Physical Review Letters **117**, 060502 (2016) (Cited on pages 9, 25).

[36] P. Campagne-Ibarcq et al., "Observing Interferences between Past and Future Quantum States in Resonance Fluorescence," Physical Review Letters **112**, 180402 (2014) (Cited on pages 9, 25).

[37] C. W. Gardiner and M. J. Collett, "Input and output in damped quantum systems: Quantum stochastic differential equations and the master equation," Physical Review A **31**, 3761–3774 (1985) (Cited on pages 9, 10, 31).

[38] E Flurin et al., "Superconducting quantum node for entanglement and storage of microwave radiation," Phys. Rev. Lett. **114**, 90503 (2014) (Cited on page 9).

[39] H. Walther et al., "Cavity quantum electrodynamics," Reports on Progress in Physics **69**, 1325–1382 (2006) (Cited on page 14).

[40] A. Blais et al., "Cavity quantum electrodynamics for superconducting electrical circuits: An architecture for quantum computation," Physical Review A **69**, 062320 (2004) (Cited on pages 14, 127).

[41] S Girvin, "Circuit QED: superconducting qubits coupled to microwave photons," in Quantum machines: measurement and control of engineered quantum systems, lecture notes of the les houches summer school: volume 96, edited by M. Devoret et al. (2014), p. 113 (Cited on page 14).

[42] W. Nagourney, J. Sandberg, and H. Dehmelt, "Shelved optical electron amplifier: Observation of quantum jumps," Physical Review Letters **56**, 2797–2799 (1986) (Cited on pages 14, 77).

[43] H. J. Kimble, "The quantum internet.," Nature **453**, 1023–1030 (2008) (Cited on pages 14, 75, 102).

[44] J. I. Cirac et al., "Quantum State Transfer and Entanglement Distribution among Distant Nodes in a Quantum Network," Physical Review Letters **78**, 3221–3224 (1997) (Cited on pages 14, 75).

[45] C Wang et al., "Surface participation and dielectric loss in superconducting qubits," Applied Physics Letters **107**, 162601 (2015) (Cited on pages 16, 78, 99, 100).

[46] M. R. Otto, "Low-temperature characterization of dielectric loss at microwave frequencies in aluminum oxide," PhD thesis (2015) (Cited on pages 16, 105).

[47] I. M. Pop et al., "Coherent suppression of electromagnetic dissipation due to superconducting quasiparticles," Nature **508**, 369–372 (2014) (Cited on pages 16, 78, 79, 97, 100).

[48] K. W. Murch et al., "Cavity-Assisted Quantum Bath Engineering," Physical Review Letters **109**, 183602 (2012) (Cited on pages 16, 97).

[49] S Shankar et al., "Autonomously stabilized entanglement between two superconducting quantum bits," Nature **504**, 419–422 (2013) (Cited on pages 16, 97).

[50] Z. Leghtas et al., "Confining the state of light to a quantum manifold by engineered two-photon loss," Science **347**, 853–857 (2015) (Cited on pages 16, 97, 151).

[51] S. Touzard et al., "Coherent Oscillations inside a Quantum Manifold Stabilized by Dissipation," Physical Review X **8**, 021005 (2018) (Cited on pages 16, 97, 151).

[52] J. C. Maxwell, *Theory of Heat* (Cambridge University Press, Cambridge, 1871) (Cited on pages 19, 117).

[53] K. Maruyama, F. Nori, and V. Vedral, "Colloquium : The physics of Maxwell's demon and information," Reviews of Modern Physics **81**, 1–23 (2009) (Cited on pages 19, 117).

[54] W. H. Zurek, "Maxwell's Demon, Szilard's Engine and Quantum Measurements," in *Frontiers of nonequilibrium statistical physics volume 135 of nato science series b:* edited by G. T. Moore and M. O. Scully (Plenum Press, New York and London, 1986), pp. 151–161 (Cited on pages 19, 117, 121).

[55] S. Lloyd, "Quantum-mechanical Maxwell's demon," Physical Review A **56**, 3374–3382 (1997) (Cited on pages 19, 117, 121).

[56] J. M. R. Parrondo and J. M. Horowitz, "Viewpoint Maxwell ' s demon in the quantum world," Society **13**, 4–6 (2011) (Cited on pages 19, 117).

[57] S Kim et al., "Quantum Szilard Engine," Physical Review Letters **106**, 70401 (2011) (Cited on pages 19, 117).

[58] R. Uzdin, A. Levy, and R. Kosloff, "Equivalence of Quantum Heat Machines, and Quantum-Thermodynamic Signatures," Physical Review X **5**, 031044 (2015) (Cited on pages 19, 117).

[59] P. Campagne-Ibarcq et al., "Observing quantum state diffusion by heterodyne detection of fluorescence," Physical Review X **6**, 1–7 (2016) (Cited on pages 25, 27, 48).

[60] M Naghiloo et al., "Mapping quantum state dynamics in spontaneous emission," Nat Commun **7**, 11527 (2016) (Cited on page 25).

[61] A. O. Caldeira and A. J. Leggett, "Influence of Dissipation on Quantum Tunneling in Macroscopic Systems," Physical Review Letters **46**, 211–214 (1981) (Cited on page 31).

[62] M. A. Castellanos-Beltran and K. W. Lehnert, "Widely tunable parametric amplifier based on a superconducting quantum interference device array resonator," Applied Physics Letters **91**, 083509 (2007) (Cited on page 36).

[63] M Hatridge et al., "Dispersive magnetometry with a quantum limited SQUID parametric amplifier," Physical Review B **83**, 134501 (2011) (Cited on page 36).

[64] J. Y. Mutus et al., "Design and characterization of a lumped element single-ended superconducting microwave parametric amplifier with on-chip flux bias line," Applied Physics Letters **103**, 122602 (2013) (Cited on pages 36, 37).

[65] T. Roy et al., "Broadband parametric amplification with impedance engineering: Beyond the gain-bandwidth product," Applied Physics Letters **107**, 1–12 (2015) (Cited on page 36).

[66] N. Bergeal et al., "Phase-preserving amplification near the quantum limit with a Josephson ring modulator," Nature **465**, 64–68 (2010) (Cited on pages 36, 41, 43).

[67] E Flurin et al., "Generating Entangled Microwave Radiation Over Two Transmission Lines," Physical Review Letters **109**, 183901 (2012) (Cited on pages 36, 37, 152).

[68] B. Abdo, A. Kamal, and M. Devoret, "Nondegenerate three-wave mixing with the Josephson ring modulator," Physical Review B **87**, 14508 (2013) (Cited on pages 36, 158).

[69] P. Campagne-Ibarcq et al., "Persistent Control of a Superconducting Qubit by Stroboscopic Measurement Feedback," Physical Review X **3**, 021008 (2013) (Cited on pages 36, 37).

[70] C. M. Caves, "Quantum limits on noise in linear amplifiers," Physical Review D **26**, 1817 (1982) (Cited on pages 36, 47).

[71] K O'Brien et al., "Resonant Phase Matching of Josephson Junction Traveling Wave Parametric Amplifiers," Physical Review Letters **113**, 157001 (2014) (Cited on page 36).

[72] C Macklin et al., "A near-quantum-limited Josephson traveling-wave parametric amplifier," Science **350**, 307–310 (2015) (Cited on pages 36, 37).

[73] T. C. White et al., "Traveling wave parametric amplifier with Josephson junctions using minimal resonator phase matching," Applied Physics Letters **106**, 242601 (2015) (Cited on page 36).

[74] Y.-F. Chen et al., "Microwave Photon Counter Based on Josephson Junctions," Physical Review Letters **107**, 217401 (2011) (Cited on pages 36, 37).

[75] L. C. G. Govia et al., "Theory of Josephson photomultipliers: Optimal working conditions and back action," Physical Review A **86**, 032311 (2012) (Cited on pages 36, 37).

[76] G. Ribeill, "Qubit readout with the Josephson Photomultiplier," PhD thesis (The University of Wisconsin-Madison, 2016) (Cited on pages 36, 37).

[77] S. Kono et al., "Quantum non-demolition detection of an itinerant microwave photon," Nature Physics **14**, 546–549 (2018) (Cited on pages 36, 37).

[78] J.-C. Besse et al., "Single-Shot Quantum Nondemolition Detection of Individual Itinerant Microwave Photons," Physical Review X **8**, 021003 (2018) (Cited on pages 36, 37).

[79] B. Royer et al., "Itinerant Microwave Photon Detector," Physical Review Letters **120**, 203602 (2018) (Cited on page 37).

[80] J. Govenius et al., "Microwave nanobolometer based on proximity Josephson junctions," Physical Review B **90**, 064505 (2014) (Cited on pages 37, 143).

[81] J. Govenius et al., "Detection of Zeptojoule Microwave Pulses Using Electrothermal Feedback in Proximity-Induced Josephson Junctions," Physical Review Letters **117**, 030802 (2016) (Cited on page 37).

[82] S. Gasparinetti et al., "Fast Electron Thermometry for Ultrasensitive Calorimetric Detection," Physical Review Applied **3**, 014007 (2015) (Cited on pages 37, 143).

[83] D. A. Steck, *Quantum and Atom Optics*, edited by U. of Oregon (2007) (Cited on page 37).

[84] K. Technologies, *UXR1004A Infiniium UXR-Series Oscilloscope: 100 GHz, 4 Channels* (Cited on pages 38, 43).

[85] A. N. Korotkov, "Quantum Bayesian Approach to circuit QED Measurement," in *Quantum machines: measurement and control of engineered quantum systems, lecture notes of the les houches summer school: volume 96, july 2011*, edited by M. H. Devoret et al. (Oxford University Press, 2014) Chap. 17, pp. 533–553 (Cited on page 41).

[86] B. Huard, *Quantum information with superconducting circuits*, HDR thesis (2014) (Cited on page 41).

[87] D. Markovic, "Applications of the Josephson mixer : ultrastrong coupling, quantum node and injection locking in conversion," PhD thesis (Ecole Normale Supérieure, 2017) (Cited on page 43).

[88] B. Abdo et al., "Full Coherent Frequency Conversion between Two Propagating Microwave Modes," Physical Review Letters **110**, 173902 (2013) (Cited on page 44).

[89] C Eichler et al., "Experimental State Tomography of Itinerant Single Microwave Photons," Physical Review Letters **106**, 220503 (2011) (Cited on pages 46, 47, 163).

[90] C Eichler, D Bozyigit, and A Wallraff, "Characterizing quantum microwave radiation and its entanglement with superconducting qubits using linear detectors," Physical Review A **86**, 032106 (2012) (Cited on page 46).

[91] M. S. Kim, "Quasiprobability functions measured by photon statistics of amplified signal fields," Physical Review A **56**, 3175–3179 (1997) (Cited on page 47).

[92] S. Boutin et al., "Effect of Higher-Order Nonlinearities on Amplification and Squeezing in Josephson Parametric Amplifiers," Physical Review Applied **8**, 054030 (2017) (Cited on page 47).

[93] K. W. Murch et al., "Observing single quantum trajectories of a superconducting quantum bit.," Nature **502**, 211–214 (2013) (Cited on pages 48, 126).

[94] K. L. Geerlings, "Improving Coherence of Superconducting Qubits and Resonators," PhD thesis (Yale University, 2013) (Cited on page 49).

[95] F. Binder et al., eds., *Thermodynamics in the Quantum Regime - Recent Progress and Outlook* (Springer, 2018) (Cited on pages 57, 125, 129–133, 145).

[96] I. Shomroni et al., "All-optical routing of single photons by a one-atom switch controlled by a single photon," Science **345**, 903–906 (2014) (Cited on page 57).

[97] T. Aoki et al., "Efficient Routing of Single Photons by One Atom and a Microtoroidal Cavity," Physical Review Letters **102**, 083601 (2009) (Cited on page 57).

[98] I.-C. Hoi et al., "Demonstration of a Single-Photon Router in the Microwave Regime," Physical Review Letters **107**, 73601 (2011) (Cited on page 57).

[99] G. F. Timossi et al., "Phase-Tunable Josephson Thermal Router," Nano Letters **18**, 1764–1769 (2018) (Cited on page 57).

[100] C. J. Axline et al., "On-demand quantum state transfer and entanglement between remote microwave cavity memories," Nature Physics **14**, 705–710 (2018) (Cited on page 75).

[101] P. Kurpiers et al., "Deterministic quantum state transfer and remote entanglement using microwave photons," Nature **558**, 264–267 (2018) (Cited on page 75).

[102] A. A. Clerk et al., "Introduction to quantum noise, measurement, and amplification," Reviews of Modern Physics **82**, 1155–1208 (2010) (Cited on page 78).

[103] M. R. Vissers et al., "Reduced microwave loss in trenched superconducting coplanar waveguides," Applied Physics Letters **100**, 082602 (2012) (Cited on page 79).

[104] J. B. Chang et al., "Improved superconducting qubit coherence using titanium nitride," Applied Physics Letters **103**, 012602 (2013) (Cited on page 79).

[105] G. Calusine et al., "Analysis and mitigation of interface losses in trenched superconducting coplanar waveguide resonators," Applied Physics Letters **112**, 062601 (2018) (Cited on page 79).

[106] G Ithier et al., "Decoherence in a superconducting quantum bit circuit," Physical Review B **72**, 134519 (2005) (Cited on pages 93, 94).

[107] F. Yoshihara et al., "Decoherence of flux qubits due to 1/f flux noise," Physical Review Letters **97**, 167001 (2006) (Cited on pages 93, 94).

[108] K. Kakuyanagi et al., "Dephasing of a Superconducting Flux Qubit," Physical Review Letters **98**, 047004 (2007) (Cited on pages 93, 94).

[109] S. M. Anton et al., "Pure dephasing in flux qubits due to flux noise with spectral density scaling as $1/f\alpha$," Physical Review B **85**, 224505 (2012) (Cited on pages 93, 94).

[110] S. Anton, "Magnetic flux noise in SQUIDs and qubits," PhD thesis (UC Berkeley, 2013) (Cited on page 93).

[111] S. Choi et al., "Localization of Metal-Induced Gap States at the Metal-Insulator Interface: Origin of Flux Noise in SQUIDs and Superconducting Qubits," Physical Review Letters **103**, 197001 (2009) (Cited on page 94).

[112] S. M. Anton et al., "Magnetic Flux Noise in dc SQUIDs: Temperature and Geometry Dependence," Physical Review Letters **110**, 147002 (2013) (Cited on page 94).

[113] P. Kumar et al., "Origin and Reduction of 1/f Magnetic Flux Noise in Superconducting Devices," Physical Review Applied **6**, 041001 (2016) (Cited on page 94).

[114] K. Geerlings et al., "Demonstrating a driven reset protocol for a superconducting qubit," Physical Review Letters **110**, 1–5 (2013) (Cited on pages 97, 106, 169).

[115] P. Magnard et al., "Fast and Unconditional All-Microwave Reset of a Superconducting Qubit," Physical Review Letters **121**, 060502 (2018) (Cited on pages 97, 106, 110).

[116] D. V. Nguyen, G. Catelani, and D. M. Basko, "Dissipation in a superconducting artificial atom due to a single nonequilibrium quasiparticle," Physical Review B **96**, 214508 (2017) (Cited on page 97).

[117] U. Vool et al., "Non-Poissonian Quantum Jumps of a Fluxonium Qubit due to Quasiparticle Excitations," Physical Review Letters **113**, 247001 (2014) (Cited on page 98).

[118] J. Wenner et al., "Excitation of Superconducting Qubits from Hot Nonequilibrium Quasiparticles," Physical Review Letters **110**, 150502 (2013) (Cited on page 99).

[119] K. Serniak et al., "Hot non-equilibrium quasiparticles in transmon qubits," arXiv:1803.00476 (2018) (Cited on pages 99, 189).

[120] J. M. Martinis et al., "Decoherence in Josephson Qubits from Dielectric Loss," Physical Review Letters **95**, 210503 (2005) (Cited on page 99).

[121] J. Aumentado et al., "Nonequilibrium Quasiparticles and 2e Periodicity in Single-Cooper-Pair Transistors," Physical Review Letters **92**, 066802 (2004) (Cited on page 100).

[122] P. J. de Visser et al., "Number Fluctuations of Sparse Quasiparticles in a Superconductor," Physical Review Letters **106**, 167004 (2011) (Cited on page 100).

[123] V. F. Maisi et al., "Excitation of Single Quasiparticles in a Small Superconducting Al Island Connected to Normal-Metal Leads by Tunnel Junctions," Physical Review Letters **111**, 147001 (2013) (Cited on page 100).

[124] X. Y. Jin et al., "Thermal and Residual Excited-State Population in a 3D Transmon Qubit," Physical Review Letters (2015) `10.1103/PhysRevLett.114.240501` (Cited on page 100).

[125] S. Gustavsson et al., "Suppressing relaxation in superconducting qubits by quasiparticle pumping," Science (2016) `10.1126/science.aah5844` (Cited on page 100).

[126] D Ristè et al., "Initialization by Measurement of a Superconducting Quantum Bit Circuit," Physical Review Letters **109**, 050507 (2012) (Cited on page 106).

[127] R. Lescanne et al., "Dynamics of an off-resonantly pumped superconducting qubit in a cavity," arXiv:1805.05198 (2018) (Cited on pages 110, 186).

[128] R. Landauer, "Irreversibility and Heat Generation in the Computing Process," IBM Journal of Research and Development **5**, 183–191 (1961) (Cited on pages 117, 121, 126).

[129] C. H. Bennett, "Notes on Landauer's principle, reversible computation, and Maxwell's Demon," Studies in History and Philosophy of Science Part B: Studies in History and Philosophy of Modern Physics **34**, 501–510 (2003) (Cited on page 117).

[130] C. H. Bennett, "The thermodynamics of computation—a review," International Journal of Theoretical Physics **21**, 905–940 (1982) (Cited on pages 117, 126, 170).

[131] S. Toyabe et al., "Experimental demonstration of information-to-energy conversion and validation of the generalized Jarzynski equality," Nature Physics **6**, 988–992 (2010) (Cited on page 117).

[132] J. V. Koski et al., "Experimental realization of a Szilard engine with a single electron," Proceedings of the National Academy of Sciences **111**, 13786–13789 (2014) (Cited on page 117).

[133] J. V. Koski et al., "Experimental observation of the role of mutual information in the nonequilibrium dynamics of a Maxwell demon," Physical Review Letters **113**, 30601 (2014) (Cited on page 117).

[134] É Roldán et al., "Universal features in the energetics of symmetry breaking," Nature Physics **10**, 457–461 (2014) (Cited on page 117).

[135] M. D. Vidrighin et al., "Photonic Maxwell's Demon," Physical Review Letters **116**, 050401 (2016) (Cited on pages 117, 125).

[136]   P. A. Camati et al., "Experimental Rectification of Entropy Production by Maxwell's Demon in a Quantum System," Physical Review Letters **117**, 240502 (2016) (Cited on pages 117, 125).

[137]   Y. Masuyama et al., "Information-to-work conversion by Maxwell's demon in a superconducting circuit quantum electrodynamical system," Nature Communications **9**, 1291 (2018) (Cited on pages 117, 126, 128, 131, 133, 137, 142).

[138]   M Naghiloo et al., "Information Gain and Loss for a Quantum Maxwell's Demon," Physical Review Letters **121**, 030604 (2018) (Cited on pages 117, 126, 128, 131, 134–136, 142, 145).

[139]   L. Szilard, "Über die Entropieverminderung in einem thermodynamischen System bei Eingriffen intelligenter Wesen," Zeitschrift für Physik **53**, 840–856 (1929) (Cited on page 120).

[140]   J. P. Pekola, D. S. Golubev, and D. V. Averin, "Maxwell's demon based on a single qubit," Physical Review B **93**, 024501 (2016) (Cited on pages 123, 141).

[141]   P. Kammerlander and J. Anders, "Coherence and measurement in quantum thermodynamics," Scientific Reports **6**, 22174 (2016) (Cited on page 124).

[142]   K. Korzekwa et al., "The extraction of work from quantum coherence," New Journal of Physics **18**, 023045 (2016) (Cited on page 124).

[143]   S. Vinjanampathy and J. Anders, "Quantum thermodynamics," Contemporary Physics **57**, 545–579 (2016) (Cited on page 124).

[144]   S. An et al., "Experimental test of the quantum Jarzynski equality with a trapped-ion system," Nature Physics **11**, 193–199 (2015) (Cited on page 125).

[145]   A. Smith et al., "Verification of the quantum nonequilibrium work relation in the presence of decoherence," New Journal of Physics **20**, 013008 (2018) (Cited on page 125).

[146]   J. V. Koski et al., "On-Chip Maxwell's Demon as an Information-Powered Refrigerator," Physical Review Letters **115**, 260602 (2015) (Cited on page 125).

[147]   N. Cottet and B. Huard, "Maxwell's demon in superconducting circuits," arXiv:1805.01224 (2018) (Cited on pages 125, 147, 165, 175).

[148]   A. Roy and M. Devoret, "Quantum-limited parametric amplification with Josephson circuits in the regime of pump depletion," Physical Review B **98**, 045405 (2018) (Cited on pages 126, 139).

[149]   F Mallet et al., "Single-shot qubit readout in circuit quantum electrodynamics," Nature Physics **5**, 791–795 (2009) (Cited on page 126).

[150]   M Hatridge et al., "Quantum Back-Action of an Individual Variable-Strength Measurement," Science **339**, 178–181 (2013) (Cited on page 126).

[151]   R Vijay et al., "Stabilizing Rabi oscillations in a superconducting qubit using quantum feedback.," Nature **490**, 77–80 (2012) (Cited on page 126).

[152]   S. J. Weber et al., "Quantum trajectories of superconducting qubits," Comptes Rendus Physique **17**, 766–777 (2016) (Cited on page 126).

[153]   N. Cottet et al., "Observing a quantum Maxwell demon at work," Proceedings of the National Academy of Sciences **114**, 7561–7564 (2017) (Cited on pages 126, 129, 136–140, 142).

[154] L. Szilard, "On the decrease of entropy in a thermodynamic system by the intervention of intelligent beings," Behavioral Science **9**, 301–310 (1964) (Cited on page 126).

[155] G Wendin, "Quantum information processing with superconducting circuits: a review," Reports on Progress in Physics **80**, 106001 (2017) (Cited on pages 127, 141).

[156] Zurek, "Decoherence, einselection, and the quantum origins of the classical," Reviews of Modern Physics **75**, 715–775 (2003) (Cited on page 128).

[157] P. Talkner, E. Lutz, and P. Hänggi, "Fluctuation theorems: Work is not an observable," Physical Review E **75**, 050102 (2007) (Cited on page 130).

[158] J. Kurchan, "A Quantum Fluctuation Theorem," arXiv:cond-mat/0007360 (2000) (Cited on page 131).

[159] H. Tasaki, "Jarzynski Relations for Quantum Systems and Some Applications," arXiv:cond-mat/0009244 (2000) (Cited on page 131).

[160] A. A. Clerk et al., "Introduction to quantum noise, measurement, and amplification," Reviews of Modern Physics **82**, 1155–1208 (2010) (Cited on page 131).

[161] K. Funo, Y. Watanabe, and M. Ueda, "Integral quantum fluctuation theorems under measurement and feedback control," Physical Review E **88**, 052121 (2013) (Cited on pages 131, 132, 134).

[162] D. I. Schuster et al., "Resolving photon number states in a superconducting circuit," Nature **445**, 515–518 (2007) (Cited on page 136).

[163] G. Kirchmair et al., "Observation of quantum state collapse and revival due to the single-photon Kerr effect," Nature **495**, 205–209 (2013) (Cited on pages 137, 154).

[164] J. Z. Blumoff et al., "Implementing and Characterizing Precise Multiqubit Measurements," Physical Review X **6**, 031041 (2016) (Cited on page 138).

[165] N Roch et al., "Widely Tunable, Nondegenerate Three-Wave Mixing Microwave Device Operating near the Quantum Limit," Physical Review Letters **108**, 147701 (2012) (Cited on pages 139, 152).

[166] J. P. Pekola et al., "Calorimetric measurement of work in a quantum system," New Journal of Physics **15**, 115006 (2013) (Cited on page 140).

[167] H Quan et al., "Maxwell's Demon Assisted Thermodynamic Cycle in Superconducting Quantum Circuits," Physical Review Letters **97**, 180402 (2006) (Cited on page 141).

[168] A. O. Niskanen, Y Nakamura, and J. P. Pekola, "Information entropic superconducting microcooler," Phys. Rev. B **76**, 174523 (2007) (Cited on page 141).

[169] B. Karimi and J. P. Pekola, "Otto refrigerator based on a superconducting qubit: Classical and quantum performance," Physical Review B **94**, 184503 (2016) (Cited on page 141).

[170] M. Campisi, J. Pekola, and R. Fazio, "Feedback-controlled heat transport in quantum devices: theory and solid-state experimental proposal," New Journal of Physics **19**, 053027 (2017) (Cited on page 141).

[171] J. P. Pekola et al., "Decoherence in Adiabatic Quantum Evolution: Application to Cooper Pair Pumping," Physical Review Letters **105**, 030401 (2010) (Cited on page 143).

[172] S. Hacohen-Gourgy et al., "Dynamics of simultaneously measured non-commuting observables," Nature **538**, 491 (2016) (Cited on page 143).

[173] U Vool et al., "Continuous quantum nondemolition measurement of the transverse component of a qubit," Physical Review Letters **117**, 133601 (2016) (Cited on page 143).

[174] C. Elouard et al., "Extracting Work from Quantum Measurement in Maxwell's Demon Engines," Physical Review Letters **118**, 1–6 (2017) (Cited on page 143).

[175] A. Ronzani et al., "Tunable photonic heat transport in a quantum heat valve," Nature Physics, 1–8 (2018) (Cited on page 143).

[176] J. Bohr Brask et al., "Autonomous quantum thermal machine for generating steady-state entanglement," New Journal of Physics **17**, 113029 (2015) (Cited on page 144).

[177] C. M. Caves et al., "Quantum limits on phase-preserving linear amplifiers," Physical Review A **86**, 63802 (2012) (Cited on page 145).

[178] M. A. Castellanos-Beltran and K. W. Lehnert, "Widely tunable parametric amplifier based on a superconducting quantum interference device array resonator," Applied Physics Letters **91**, 83509 (2007) (Cited on page 145).

[179] Q. Ficheux et al., "Dynamics of a qubit while simultaneously monitoring its relaxation and dephasing," Nature Communications **9**, 1926 (2018) (Cited on page 145).

[180] J. R. Johansson, P. D. Nation, and F. Nori, "QuTiP 2: A Python framework for the dynamics of open quantum systems," Computer Physics Communications **184**, 1234–1240 (2013) (Cited on pages 154, 192).

[181] H. M. Wiseman, "Weak values, quantum trajectories, and the cavity-QED experiment on wave-particle correlation," Physical Review A **65**, 032111 (2002) (Cited on page 162).

[182] P. Campagne-Ibarcq et al., "Observing Interferences between Past and Future Quantum States in Resonance Fluorescence," Physical Review Letters **112**, 180402 (2014) (Cited on page 162).

[183] P Six et al., "Quantum state tomography with noninstantaneous measurements, imperfections, and decoherence," Physical Review A **93**, 012109 (2016) (Cited on page 162).

[184] R. H. Dicke, "Coherence in Spontaneous Radiation Processes," Physical Review **93**, 99–110 (1954) (Cited on page 164).

[185] M. Dartiailh, *Exopy: versatile data acquisition software for complex experiments* (Cited on page 179).

[186] N. Didier, J. Bourassa, and A. Blais, "Fast quantum non-demolition readout from longitudinal qubit-oscillator interaction," Phys. Rev. Lett. **115**, 203601 (2015) (Cited on page 185).

[187] J. Gambetta et al., "Quantum trajectory approach to circuit QED: Quantum jumps and the Zeno effect," Physical Review A **77**, 012112 (2008) (Cited on page 186).

[188] L. Verney et al., "Strongly driven quantum Josephson circuits," arXiv:1805.07542 (2018) (Cited on page 186).

[189] *Bluefors Cryogenics LD-Series Cryostats*, 2018 (Cited on page 189).

[190] P. V. Klimov et al., "Fluctuations of Energy-Relaxation Times in Superconducting Qubits," Physical Review Letters (2018) 10.1103/PhysRevLett.121.090502 (Cited on page 189).

[191] J. P. Martinez et al., "A tunable Josephson platform to explore many-body quantum optics in circuit-QED," arXiv:1802.00633 (2018) (Cited on page 192).

[192] R. Kuzmin et al., "Analog simulations of quantum impurity physics with a high-impedance Josephson transmission line," in Aps march meeting (2017) (Cited on page 192).

Résumé

Cette thèse expérimentale explore les aspects énergétiques et informationnels de la fluorescence émise par des circuits supraconducteurs. Un bit quantique échange des quanta d'énergie avec une onde résonante lors de cycles d'émission et d'absorption. Nous avons développé un système de mesure basé sur l'amplification bas bruit et la détection linéaire de la lumière micro-onde pour mesurer l'énergie et l'amplitude complexe du champ de fluorescence, et réalisé trois expériences basées sur la mesure de fluorescence.

Premièrement nous avons réalisé et démontré le transfert d'énergie entre deux impulsions lumineuses résonantes. Grâce aux propriétés de l'émission stimulée, la direction et l'amplitude du transfert d'énergie sont contrôlées par la phase d'une superposition d'états quantiques.

Deuxièmement, nous avons utilisé l'information contenue dans la fluorescence pour réaliser un nouveau type de lecture d'un circuit supraconducteur sans l'aide d'un système quantique auxiliaire. Le circuit, directement couplé à l'environnement, encode l'information quantique dans un sous-espace bien isolé et est lu grâce à la fluorescence d'une transition fortement couplée.

Enfin, nous avons exploré le lien entre information et énergie dans le régime quantique en réalisant un démon de Maxwell autonome. Le démon est une cavité mesurant le système, un qubit supraconducteur. Le travail est extrait sous la forme d'un photon stimulé émis par le qubit et est directement mesurée par notre système de mesure de fluorescence. Il est relié aux variations de l'énergie interne du qubit. Le transfert d'information du système vers le démon est quantifié par des mesures indépendantes. En particulier nous avons démontré la présence de signatures quantique du démon quand le système est initialisé dans une superposition d'états quantiques.

Mots Clés

Mécanique quantique, thermodynamique, circuits supraconducteurs

Abstract

This experimental thesis explores energetic and informational aspects of the fluorescence emitted by superconducting circuits. A quantum bit interacting with a resonant drive exchanges quanta of energy during absorption and emission cycles. Using low-noise amplification and linear detection of microwave light, we have developed a measurement setup to record the energy and complex amplitude of the fluorescence field and realized three experiments based on the record of fluorescence.

First, we have realized and demonstrated a transfer of energy between two resonant drives. Owing to the properties of stimulated emission, the direction and magnitude of energy transfer can be controlled by the phase of a quantum superposition of qubit states.

Second, we have used the information contained in fluorescence to implement a new readout scheme for superconducting circuits without the help of any ancillary quantum system. The circuit, directly coupled to the environment, encodes quantum information in a well-protected subspace and is read using the fluorescence of a strongly coupled transition.

Finally, we have explored the interplay between information and energy in the quantum regime by realizing an autonomous Maxwell's demon. The demon is a cavity measuring the system, a superconducting qubit. Work is extracted in the form of a stimulated photon emitted by the qubit and is directly measured using our fluorescence measurement setup. It is linked with the variations of the system's internal energy. Using independent measurements, the transfer of information from the system to the demon is quantified. In particular, we demonstrated the quantum signatures of the demon when the system is initialized in a quantum superposition.

Keywords

Quantum physics, thermodynamics, superconducting circuits